FACULDADE DE ENGENHARIA DA UNIVERSIDADE DO PORTO

Fibre-Reinforced Thermoplastic Composite Parts Produced by Additive Manufacturing: A Comprehensive Characterization Study

Isaac Alves Ferreira



Doctoral Program in Mechanical Engineering

Supervisor: Jorge Lino Alves

Co-Supervisor: Margarida Machado

March 16, 2020

© Isaac Alves Ferreira, 2020

Fibre-Reinforced Thermoplastic Composite Parts Produced by Additive Manufacturing: A Comprehensive Characterization Study

Isaac Alves Ferreira

Doctoral Program in Mechanical Engineering

March 16, 2020

Abstract

Fused Filament Fabrication (FFF) is an Additive Manufacturing (AM) process, based on the principle of a thermoplastic-based material extruded through a heated dye, and consequently deposited in a layer-wise approach. Currently, the FFF process is not only limited to pure thermoplastics, being possible the addition of reinforcing elements such as particles, and short or continuous fibres to the matrix. Due to its increasing versatility, it is now considered as an industrial fabrication method, instead of a mere prototyping technique. The main factors that are still limiting the industrial uptake of FFF are the inherent anisotropic behaviour of any part manufactured by this method that presents a non-standardized mechanical response, the inferior level of mechanical properties when compared to traditional injection moulding process, besides the low degree of surface finish and dimensional accuracy. Thus, it is considered of main interest to develop appropriate test methods to characterize parts produced by FFF and later complementary post-processed. These shortcomings motivated the present work, which focuses on the characterization of components produced by FFF with non-reinforced and carbon fibre reinforced thermoplastics. This research aims to provide relevant information that allows a reliable evaluation of the competitiveness level of FFF technology over conventional manufacturing techniques.

The first stage of this doctoral study was dedicated to a review of the FFF composites state-of-the-art, as well as a familiarization via experimental activity to the different stages of composite FFF fabrication, particularly the parameterization of key pre-processing parameters (e.g., building orientation, infill pattern, etc.). This preliminary work was supported by some testing experiments, such as dimensional, microscopic, thermal and mechanical characterization analyses of simple parts and feedstock material, which revealed to be of major importance to identify the process variables with more influence on final part's mechanical behaviour.

In order to develop a comprehensive approach to the characterization of parts manufactured by FFF short carbon fibre reinforced and non-reinforced polyamide 12 (PA 12), two topics of scientific relevance and technological complementarity were addressed in detailed throughout this PhD thesis: i) the mechanical performance under mode I loading and multi-axial scenarios, targeting to characterize the interlaminar fracture toughness and the single and combined tensile-shear responses; and ii) the benefit of post processing as a complement of FFF process, regarding dimensional accuracy and surface roughness after finishing the final part by machining, and tensile and flexural behaviours after thermal stabilization by annealing.

For the characterization of the interlaminar fracture under mode I loading, a specific test geometry based on the Double Cantilever Beam (DCB) test specimens was developed, adapting standards used for testing composite structures. Experimental tests were performed on 100% dense samples with reinforced and unreinforced material and numerically validated by finite element analysis (FEA). Multi-axial mechanical performance was assessed by developing Butterfly type specimens, produced with both materials in three different building orientations, tested using Arcan type grip. The applied experimental methodology allowed to characterize the tensile, shear and combined tensile-shear responses and to analyse the reinforcement effect and the importance

of the building strategy on the mechanical behaviour of the component.

The influence of annealing post-processing on tensile and flexural properties was evaluated by submitting the samples to distinct treatment cycles. A design of experiments considering three temperature values at four time intervals was performed, analysing the influence of these parameters combination on both materials mechanical properties. The challenges associated with machining as a surface finishing method of reinforced and unreinforced PA12 FFF printed parts was investigated through surface milling tests. A design of experiments was also developed, considering four types of process variables, namely: tool geometry, building orientation, material (reinforced vs unreinforced) and machining parameters (feed rate, cutting speed and depth of cut).

The comparative analysis carried out between reinforced and unreinforced PA12 in distinct experimental tests showed that the fibre presence in the matrix contributes more significantly to the overall stiffness of the part as well as to increase the fracture toughness. However, there was not observed any substantial improvement in tensile behaviour. Building orientation has proved to be the most critical and influential process variable in the mechanical response of the component, whether in uniaxial loading or in combined load situations. Post processing turned out to be an adequate strategy, promoting a better surface finishing and dimensional accuracy, as well as enhanced mechanical behaviour increase and thermal stability.

Throughout this thesis, a series of mechanical performance evaluation methodologies was developed and demonstrated using FFF printed PA12 based thermoplastics. This testing protocol can be further used as a characterization guide for FFF parts of more advanced polymers and/or thermoplastic composites. It has also been shown that post-processing can become crucial when carried out in sequence with the additive process, resulting in a more accurate and thermally stable part with a good surface quality. This productive chain is directly connected to the overall process enhancement and optimization, which pointed out to the development of hybrid manufacturing solutions.

Keywords: AM, FFF, composites, short fibre reinforcements, thermoplastics.

Resumo

O processo de extrusão por fusão de filamento (FFF) é uma tecnologia de fabrico aditivo que tem como princípio de funcionamento a extrusão de um material de base termoplástica através de uma fieira aquecida e a sua deposição sucessiva por adição de camadas. Atualmente, o processamento por FFF não está limitado só a polímeros puros, sendo possível imprimir filamentos compósitos reforçados com partículas, fibras curtas ou até fibras contínuas. A crescente versatilidade do FFF tem levado a que esta tecnologia seja cada vez mais encarada não apenas como uma técnica de prototipagem, mas sim de fabrico industrial. Os principais fatores que tem condicionado a endogeneização do FFF em contexto produtivo são, a anisotropia inerente a qualquer peça fabricada por este método, a qual confere às peças uma resistência mecânica não padronizada, o nível inferior de propriedades mecânicas comparando processos tradicionais, para alem de um baixo grau de acabamentos superficiais. Neste sentido, considera-se premente desenvolver métodos de teste adequados à caracterização de peças produzidas por FFF, a fim de avaliar o grau de competitividade da utilização desta tecnologia em detrimento de uma técnica convencional. Estas lacunas motivaram o presente trabalho, que se foca na caracterização de componentes produzidos por FFF em termoplásticos não reforçados e reforçados com fibras de carbono.

Os estudos iniciais deste trabalho de doutoramento envolveram naturalmente uma revisão do estado-da-arte do FFF de termoplásticos reforçados, bem como uma familiarização via atividade experimental dos diferentes estágios de fabrico por FFF, em particular a parametrização de parâmetros chave do pré-processamento como a orientação de construção, o padrão de preenchimento, entre outros. A referida atividade experimental de fabrico dos primeiros provetes permitiu também a realização de algumas análises simples de caracterização dimensional, microscópica, térmica e mecânica que se revelaram importantes para a identificação das variáveis do processo com maior influência no comportamento estrutural de uma dada peça.

Com o objetivo de desenvolver uma abordagem inclusiva de caracterização de peças fabricadas por FFF, utilizando poliamida 12 (PA 12) sem e com reforço de fibras curtas de carbono, foram analisados em detalhe dois tópicos de pertinência científica e complementaridade tecnológica, nomeadamente: i) resistência à fratura interlaminar (modo I) e o desempenho estrutural em condições de carregamento uni e multi-axial; e ii) a resposta do componente quando sujeito a pós-processamento por recozido ou acabamento por maquinagem.

Para a caracterização da resistência à fratura interlaminar foi desenvolvida uma geometria específica de teste inspirada nos provetes tradicionais *Double-Cantilever Beam* (DCB), tendo como referência as normas utilizadas para ensaios de estruturas compósitas. Os testes experimentais foram realizados em amostras 100% densas com material reforçado e não reforçado e validados numericamente através de análises de elementos finitos (FEA). O desempenho estrutural foi avaliado utilizando provetes com uma geometria *Butterfly* recorrendo a amarras do tipo Arcan, produzidos com os dois materiais, em três orientações de construção diferentes. A metodologia experimental aplicada permitiu analisar o seu comportamento à tração, ao corte e a esforços combinados de tração-corte para perceber o efeito do reforço e a relevância da estratégia de construção

no comportamento mecânico do componente.

A influência do pós-processamento de recozido nas propriedades de tração e flexão foi avaliada para ciclos distintos de tratamento. Desta forma, foi efetuado um planeamento de experiencias para três valores de temperatura em quatro intervalos de tempo, sendo assim possível analisar a influência da combinação dos parâmetros nas propriedades mecânicas de ambos os materiais. Os desafios associados ao acabamento superficial por maquinagem de peças impressas por FFF em PA12 reforçado e não reforçado foram investigados através de testes experimentais de maquinagem por fresagem de topo, tendo-se estudado a relevância da combinação de quatro variáveis do processo, nomeadamente: a geometria da ferramenta, a estratégia de impressão, a existência de reforço na matriz e os parâmetros de maquinagem (avanço, velocidade de corte e profundidade de corte).

A análise comparativa elaborada entre o PA12 reforçado e não reforçado nos distintos ensaios experimentais permitiu aferir que a presença de fibras curtas na matriz contribui de modo mais significativo para a rigidez geral da peça assim como para a tenacidade à fratura. No entanto, não existiu melhoramento significativo no comportamento de resistência à tração. A orientação de construção revelou ser a variável de processo mais crítica e influente na resposta mecânica do componente, quer em carregamentos uniaxial, quer em situações de cargas combinadas. O pós-processamento revelou ser uma adição positiva ao processo de FFF, na medida em que possibilita uma melhoria do acabamento superficial e tolerância dimensional, assim como um aumento das propriedades mecânicas e uma maior estabilidade térmica da peça.

Nesta tese demonstrou-se uma série de metodologias para testes de desempenho mecânico aplicadas a materiais termoplásticos de base PA12. Esta sequência de ensaios pode também servir como guia para aplicação a outros tipos de polímeros mais avançados ou compósitos de matriz termoplástica. Ficou também demonstrado que o pós-processamento destas amostras pode-se tornar crucial quando efetuado em sequência com o processo aditivo. Desta forma, obtém-se um tipo de peça mais precisa, termicamente estável, melhorando assim o resultado final do produto. Este encadeamento de processos está alinhado com a estratégia de melhoramento do processo, justificando o investimento em tecnologias FFF de fabrico híbrido.

Palavras chave: Fabrico aditivo, FFF, compositos, fibra curta, termoplásticos.

Acknowledgements

First of all, I would like to express my sincere gratitude to Prof. Dr. Jorge Lino Alves, who encouraged me to pursued this work. His mentorship, guidance and support throughout the doctoral period allowed me to improve my capabilities as an engineer.

For Dr. Margarida Machado, as my co-supervisor, I have also the most gratitude. Her guidance allowed me to develop not only as a student, but as a professional in this laboratory. I would like to express the most thankfulness for the patience and most of all understanding.

I would like to acknowledge Prof. Dr. Abílio de Jesus, Prof. Dr. Marcelo Moura and Prof. Dr. Rui Neto, and Prof. Dr. António Torres Marques, which enriched this study through their valuable inputs.

This work would not be materialized without the support of Prof. Dr. Ana Reis, head of the Advanced Manufacturing Technologies group. I would like to reinforce the importance that this group brought to my professional expertises.

To my current and former work colleagues Angela Cardoso, Inês Oliveira, Leonardo Santana, Ricardo Cardoso, Rui Madureira, Santiago Castellanos and Valter Costa, I have to express my gratitude for the cheer and joy brought throughout the years. To my dear friend Armanda Marques, for the ever so kind words and Andreia Durães for the always present sense of humour, I am deeply grateful. To the master students that made part of this work, I leave a word of appreciation.

In the same way, im profoundly grateful to my oldest friends André Costa, João Faria, Pedro Miranda, and Pedro Pereira.

To my girlfriend and partner in "crime" Inês Lima, which I cannot express how thankful I am for the patience and support.

To my Parents, who deserve my deepest appreciation for the constant support and understanding.

Author gratefully acknowledges the funding of Project FIBR3D – Additive manufacturing based hybrid processes for long or continuous fiber reinforced polimeric matrix composites (POCI-01-0145-FEDER-016414), cofinanced by Programa Operacional Competitividade e Internacionalização (COMPETE 2020) and Programa Operacional Regional de Lisboa (LISBOA 2020), through Fundo Europeu de Desenvolvimento Regional (FEDER) and by National Funds through Fundação para a Ciência e Tecnologia (FCT).

Cofinanciado por:

COMPETE 2020 Lisb@20[20] PORTUGAL 2020 UNIÃO EUROPEIA Fundo Europeu de Desenvolvimento Regional FCT Fundação para a Ciência e a Tecnologia

Isaac Ferreira

"There are no pleasures in a fight, but some of my fights have been a pleasure to win."

Muhammad Ali-Haj

Contents

1 Introduction **3**
- 1.1 Motivation and Scope . . . 3
- 1.2 Work purpose and goals . . . 4
  - 1.2.1 Goals . . . 5
- 1.3 Document Structure . . . 5
- 1.4 Scientific contribution . . . 6
  - 1.4.1 Publications . . . 7
  - 1.4.2 Master Thesis Orientations: . . . 9

2 Literature review **11**
- 2.1 Layer based manufacturing . . . 11
  - 2.1.1 Traditional composite Materials . . . 11
  - 2.1.2 Applications . . . 15
- 2.2 Additive Manufacturing . . . 17
  - 2.2.1 Introduction . . . 17
  - 2.2.2 Advantages vs Disadvantages . . . 20
  - 2.2.3 Economic Impact . . . 22
  - 2.2.4 Process chain . . . 22
  - 2.2.5 Additive Manufacturing Technologies . . . 24
- 2.3 Fused Filament Fabrication . . . 26
  - 2.3.1 FFF Processing Parameters . . . 27
  - 2.3.2 FFF parts qualitative features . . . 29
  - 2.3.3 Filament interface wettability . . . 31
  - 2.3.4 Thermal residual stresses . . . 32
  - 2.3.5 Filament production process . . . 33
  - 2.3.6 Polymers . . . 34
- 2.4 Composite Additive Manufacturing . . . 43
- 2.5 A review on fibre reinforced composite printing via FFF . . . 49
  - 2.5.1 Introduction . . . 49
  - 2.5.2 Fibre printing via Material extrusion . . . 50
  - 2.5.3 Research opportunities and final remarks . . . 71

3 Supporting experimental studies **75**
- 3.1 Feedstock Analysis . . . 76
  - 3.1.1 Dimensional Control . . . 76
  - 3.1.2 Feedstock Tensile test . . . 78
  - 3.1.3 Thermal characterization . . . 80
  - 3.1.4 Final remarks . . . 89

3.2 Additive manufacturing of PETG/Carbon fibre composites: an experimental study from filament to printed parts . . . 90
3.2.1 Introduction . . . 90
3.2.2 Materials and Methods . . . 92
3.2.3 Results and Discussion . . . 96
3.2.4 Conclusions . . . 106
3.3 Characterization of thermoplastic matrix composites produced via Markforged® . 107
3.3.1 Introduction . . . 107
3.3.2 Materials and Methods . . . 107
3.3.3 Results and Discussion . . . 110
3.3.4 Conclusions . . . 113
3.4 Effect of layer filling path on mechanical properties of PA and PA reinforced FFF parts . . . 114
3.4.1 Introduction . . . 114
3.4.2 Materials and Methods . . . 114
3.4.3 Results and Discussion . . . 117
3.4.4 Conclusions . . . 120

4 Advanced performance characterization 123
4.1 Study of the interlaminar fracture under mode I loading on FFF printed parts . . . 123
4.1.1 Introduction . . . 124
4.1.2 Materials and methods . . . 126
4.1.3 Numerical analysis . . . 130
4.1.4 Results and discussion . . . 134
4.1.5 Conclusions . . . 139
4.2 Experimental characterization of FFF printed parts under tension, shear and combined shear-tension loads via Arcan test . . . 141
4.2.1 Introduction . . . 141
4.2.2 Experimental details . . . 144
4.2.3 Results and discussion . . . 151
4.2.4 Conclusions . . . 160

5 Post processing of printed samples 163
5.1 Machinability of PA12 and short fibre reinforced PA12 materials produced by Fused Filament Fabrication . . . 163
5.1.1 Introduction . . . 164
5.1.2 Materials and specimens production . . . 167
5.1.3 Research approach . . . 169
5.1.4 Conclusions . . . 194
5.2 Study of the annealing influence on the mechanical performance of PA12 and PA12 fibre reinforced FFF printed samples . . . 196
5.2.1 Introduction . . . 196
5.2.2 Experimental Procedure . . . 198
5.2.3 Results . . . 201
5.2.4 Visual Analysis . . . 202
5.2.5 Conclusion . . . 212

6 Conclusions **215**
6.1 Research Questions 215
6.2 Final Remarks 217
6.2.1 Which are the guidelines for printing the best functional and structural thermoplastic based composites part through FFF? 217
6.3 Future Work 220

A Material and hardware selection **223**

List of Figures

2.1 Composite classification tree [Kar et al., 2016]. . . . 12
2.2 JEC 2003 visitors at various sectors [Friedrich and Almajid, 2013]. . . . 16
2.3 Cost per part AM vs CNC vs Forming [Varotsis, 2018]. . . . 17
2.4 AM evolution time-line adapted from [Narsimlu, K; Pathak G. Arhendu; Mulky G. Avinash; Yavarna, 2017, Goh et al., 2017]. . . . 19
2.5 Process chain adapted from [Cotteleer et al., 2014]. . . . 23
2.6 Schematic of the FFF process indicating components. . . . 26
2.7 FDM process scheme. . . . 27
2.8 FFF cause effect diagram adapted from [Mohamed et al., 2015]. . . . 29
2.9 FFF prototype bonding structure [Bellehumeur and Li, 2004]. . . . 31
2.10 Bond formation process between two beads: (1) surface contacting, (2) neck growth and (3) inter-facial diffusion and final randomization. . . . 31
2.11 FFF process physical phenomena representation [Brenken et al., 2018]. . . . 32
2.12 General view of extrusion line used in the production of filaments [Carneiro et al., 2015]. . . . 34
2.13 Specific volume–temperature curves for a semi-crystalline and amorphous polymers during heating: A-Liquid section, B-viscous liquid with elasticity, C-rubbery region, D-glassy section, E-crystallites in a rubbery matrix and F-crystallites in a glassy matrix [Ebewele, 2000] . . . 36
2.14 Specific volume-temperature curve for semi-crystalline polymer during heating and cooling, indicating crystallization gap and inflection curve, defining T_c [V. and Canevarolo, 2002]. . . . 37
2.15 Polymer division pyramid. . . . 40
2.16 Thermoplastics processing temperature range [Moreira, 2016]. . . . 42
2.17 Schematic of 3DP process. . . . 43
2.18 Schematic of SLS process. . . . 44
2.19 Schematic of SLA process . . . 45
2.20 Continuous Composite Technology Kenneth [2014]. . . . 46
2.21 ATROPOS in mid process [Politecnico Milano 1893, 2014]. . . . 47
2.22 Continuous fibres/matrix in head mixture. . . . 51
2.23 Schematic of the continuous fibres extruder concept, adapted from Prüß and Vietor [2015]. . . . 52
2.24 (a) Adapted extrusion head, (b) Reinforced printed parts [Bettini et al., 2016]. . . . 53
2.25 (a) Continuous fibre depositioning extruder, (b) Printed tensile part, (c) Printed profile [Li et al., 2016]. . . . 53
2.26 Modified extrusion head schematics [Tian et al., 2016]. . . . 54
2.27 (a) Corrugated structure and path planning, (b) Failure mode of the structures [Hou et al., 2018]. . . . 55

2.28 Markforged: (a) Kevlar® fibre bundles, (b) Glass fibre bundles, and (c) Carbon fibre bundles. . . . 56
2.29 Markforged fuctioning principles, adapted from Caminero et al. [2018b]. . . . 57
2.30 3D printing process of tensile specimens with CF (a), and fractured tensile specimens (b) Mori et al. [2014]. . . . 58
2.31 Inclusion of carbon fibres in molten ABS (a), and fractured tensile specimens (b) Nakagawa et al. [2017]. . . . 59
2.32 Path and dimensions of the coupons Justo et al. [2018]. . . . 60
2.33 Prepreg Extrusion Schematic. . . . 63
2.34 Flexural specimen (a), and stress–strain curves of five of the flexural specimens (b) Hu et al. [2018]. . . . 64
2.35 Extrusion and cutting head: (1) Filament extrusion head, (2) Servo, (3) Solenoid, (14) Cutters and (5) 4-bar linkage [Vaneker, 2017]. . . . 65
2.36 Short fibre extrusion process. . . . 66

3.1 Average diameter value of: (a) Commodity, (b) ⌀1.75 mm Engineering Polymers and (c) ⌀3.0 mm Engineering Polymers. . . . 78
3.2 Average diameter value of: (a) High Performance and (b) Reinforced Polymers. . 78
3.3 Filament tensile test: (a) Commodity polymers and (b) Engineering polymers. . . 79
3.4 Filament tensile test: (a) Reinforced polymers, and (b) High performance polymers. 79
3.5 TGA results for commodity polymers; a) Weight loss, and b) Derivative weight. . 81
3.6 TGA results for engineering polymers; a) Weight loss, and b) Derivative Weight. 81
3.7 TGA results for reinforced polymers; a) Weight loss, and b) Derivative weight. . 82
3.8 TGA - Reinforced vs pure PETG (CarbonFill vs HDGLASS). . . . 83
3.9 TGA - Reinforced vs pure PA (FX256 vs CF15). . . . 83
3.10 TGA - Reinforced vs pure PA (CarbonX vs iOn). . . . 83
3.11 DSC curves for commodity, engineering and reinforced polymers 84
3.12 Operating window for Alloy 910 thermoplastic. . . . 87
3.13 MFI results. . . . 88
3.14 Thermal conductivity of different filaments. . . . 89
3.15 Experimental work characterization/graphic abstract 93
3.16 Filamentar testing system 95
3.17 Tensile Samples ISO 527 95
3.18 Flexural Samples ISO 178 96
3.19 TGA results: (a) weight loss %, (b) derivative weight 97
3.20 DSC results: (a) PETGp vs PETGf, (b) rPETGp vs rPETGf, (c) rPETGp vs PETGp and (d) rPETGf vs PETGf 98
3.21 Tensile filament test results: (a) rPETGf and (b) PETGf 99
3.22 Tensile sample test results for: (a) rPETGp and (b) PETGp 100
3.23 Tensile curves for PETGp3 and rPETGp1(a) with the respective sample fractures(b) 100
3.24 Flexural test results for: (a) rPETGp and (b) PETGp 102
3.25 Flexural curves for PETGp1 and rPETGp2 (a) with the respective sample fractures(b) 103
3.26 Micrographs: filament cross section view (a) and axial view (b); Printed specimen cross section (top) view (c) and Printed specimen axial view (lateral) view (d) . . 103
3.27 (a) filament cross sectional view and (b) filament axial view 104
3.28 (a) Fibre length distribution and (b) fibre diameter distribution 104
3.29 Original magnification (75x)(a) and binarized imaged (b) 105
3.30 Fibre bundles after burning: (a) carbon, (b) Kevlar® and (c) glass fibres. . . . 108

3.31 Carbon fibre bundles magnifications with measurements: (a) 150x - bundles and (b) 1500x - fibres. . . . 108
3.32 Carbon fibre bundles magnifications with measurements: (a) 1500x - Kevlar fibres and (b) 1500x - Glass fibres. . . . 108
3.33 Original magnification (150x) (a) and binarized imaged (b). . . . 109
3.34 Fibre distribution for tensile and flexural samples. . . . 111
3.35 Tensile Stress-Strain: a) Pure Nylon samples, b) Reinforced Nylon samples. . . . 112
3.36 Flexural Stress-Strain: a) Pure Nylon samples, b) Reinforced Nylon samples. . . . 113
3.37 Printing orientations and infill: (a) XY45, (b) XZC, (c) XYC and (d) XYCE. . . . 116
3.38 Infill pattern views (top and transversal sections) vs solicitation. . . . 116
3.39 Printed samples organization scheme. . . . 117
3.40 Alloy 910 XY45 and XZC representative curves. . . . 118
3.41 FX256 XY45, XZC and XYCE representative curves. . . . 119
3.42 CF15 XY45, XZC, XYC and XYCE representative curves. . . . 120

4.1 Printing parameters division. . . . 125
4.2 DCB schematic representation. . . . 127
4.3 a) CAD model for the newly developed approach, b) Support and specimen until 6 mm in height, c) Kapton® film application and d) Support enclosing layers and rest of the test sample. . . . 129
4.4 DCB test at the end positions for: a) PA12 b)PA12CF. . . . 129
4.5 Trapezoidal constitutive law for pure-mode I. . . . 132
4.6 Bilinear stress-softening constitutive law for pure-mode I. . . . 133
4.7 $P-\delta$ curve and corresponding state of the numerical DCB specimen at post peak zone (Von Mises Stress). . . . 134
4.8 $P-\delta$ and the corresponding R-curves of DCB PA12 tests. . . . 135
4.9 Fractured surfaces after the DCB test for a PA12 specimen (arrows evidence pull out layer). . . . 135
4.10 Comparison of the numerical $P-\delta$ curve obtained with the average cohesive law with the experimental ones for PA12 considering a nominal a_0=50 mm. . . . 136
4.11 $P-\delta$ and the corresponding R-curves of DCB PA12CF tests. . . . 137
4.12 Fractured surfaces after the DCB test for a PA12CF specimen. . . . 138
4.13 Comparison of the numerical $P-\delta$ curve obtained with the average cohesive law with the experimental ones for PA12 considering a nominal a_0=40 mm for PA12CF. 138
4.14 Comparison of the fractured surfaces for the a) unreinforced and b) reinforced specimens. . . . 139
4.15 Specimens building orientations [Zou et al., 2016]. . . . 142
4.16 Arcan apparatus: (a) components and (b) selected test orientations. . . . 144
4.17 Biaxial state of stress at the gauge region of the test specimen, adapted from Mohr and Doyoyo [2009], Doyoyo and Wierzbicki [2003]. . . . 145
4.18 (a) Original Arcan sample configuration [Arcan et al., 1978], (b) butterfly specimen [Manaia, 2018] and (c) developed geometry. . . . 145
4.19 Von Mises stress simulation results for tensile, combined mode and shear tests. . 146
4.20 Specimen building orientation. . . . 147
4.21 Longitudinal deformation field of a tensile H CF15 sample. . . . 151
4.22 Arcan testing results of H samples at shear, combined mode and tensile loadings. 152
4.23 Arcan testing results of VT samples at shear, combined mode and tensile loadings. 152
4.24 Arcan testing results of VL samples at shear, combined mode and tensile loadings. 152
4.25 Average test values of (a) load and (b) displacement. . . . 153

4.26 Deformation fields: (a) tensile, (b) combined mode and (c) shear for H specimens. 154
4.27 Deformation fields: (a) tensile, (b) combined mode and (c) shear for VT specimens. 155
4.28 Deformation fields: (a) tensile, (b) combined mode and (c) shear for VL specimens. 156
4.29 Fracture examples of CF15 for each type of test. 157
4.30 VT specimens: (a) printing scheme and (b) printed fractured sample. 157
4.31 Obtained material properties: (a) H, (b) VL and (c) VT specimens. 158

5.1 Sample dimensions and deposition strategy. 169
5.2 Work plan schematic. 170
5.3 Approach 1 - Full Factorial DOE test matrix. 171
5.4 Different building orientations considered in this study: a) 0°(Horizontal/Flat position); b) 45° (tilted position) with support structures generated by Simplify3D; c) 90° (Up-right position). 172
5.5 Cutting tools: a) flat end two flute and b) flat end four flute tool 172
5.6 Machining strategy for the first methodology with two distinct parameter sets applied to each face. 173
5.7 Measurement points for Ra,l and Ra,t prior a) and after b) machining. 174
5.8 Main effects plot for *Ra,t*. 176
5.9 Two way interaction plot for *Ra,t*. 176
5.10 Main effects plot for *Ra,l*. 177
5.11 Two way interaction plot for *Ra,l*. 178
5.12 Roughness profile before and after machining: a)longitudinal and b)transversal. . 179
5.13 Surface analysis via SEM: a) Parameters set 1 and 2, b) Magnification of set 1 and c) Magnification of set 2. 180
5.14 Tools wear (1st testing approach): a) two flute tool, b) two flute damage area magnification, c) four flute tool and d) four flute damage area magnification. . . . 181
5.15 CNC setup with Kistler multicomponent dynamometer. 183
5.16 Approach 2 - Taguchi DOE with influential parameters and levels. 184
5.17 Tool path strategy for the second programme. 185
5.18 Measurement points for transversal and longitudinal *Ra* and *Rz*. 186
5.19 Taguchi matrix results: a) *Ra,t*, b) *Ra,l*, c) *Rz,t*, d) *Rz,l* and e) cutting forces. . . . 188
5.20 PA12 main effect plot for *Ra,l*. 189
5.21 PA12 main effect plot for *Rz,l*. 189
5.22 PA12 main effect plot for cutting forces. 191
5.23 PA12CF main effect plot for cutting forces. 191
5.24 Experimental plan. 201
5.25 Tensile FX256 samples after test for each annealing condition. 203
5.26 Flexural FX256 samples after test for each annealing condition. 203
5.27 Tensile results comparison: a) Young's modulus, b) tensile strength and c) strain at break. 204
5.28 Flexural results comparison: a) flexural modulus, b) flexural strength and c) flexural strain. 205
5.29 CF15 - Young's modulus main effects plot. 206
5.30 CF15 - Tensile strength main effects and interactions plots. 206
5.31 CF15 - Strain at break main effects and interactions plots. 207
5.32 CF15 - Flexural strength main effects and interactions plots. 207
5.33 CF15 - Flexural strain main effects plots. 208
5.34 FX256 - Tensile strength main effects and interactions plots. 209
5.35 FX256 - Strain at break main effects and interactions plots. 209

5.36 FX256 - Flexural modulus main effects and interactions plots. 210
5.37 FX256 - Flexural strength main effects and interactions plots. 210
5.38 FX256 - Flexural strain main effects and interactions plots. 211

6.1 Guidelines for functional and structural component production. 219
6.2 Interlaminar strength:(a)specimen and (b)specimen with aluminium bonded grips. 221

A.1 Fibre dimensional analysis: a)cross section at 224
A.2 Magnifications showing porosity in the filament: a)cross section 75x and b)lateral section at 23x. 225
A.3 PrintDry^{TM} (Canada) filament drier. 226

List of Tables

2.1 Carbon fibres classification [da Silva et al., 2013]. . . . 13
2.2 Fibre Properties [da Silva et al., 2013, Hull and Clyne, 1996]. . . . 14
2.3 Typical composite matrix properties [Hull and Clyne, 1996]. . . . 16
2.4 Some expired patents. . . . 18
2.5 AM aplications by select end markets [Cotteleer et al., 2014]. . . . 19
2.6 AM advantages over traditional manufacturing [Attaran, 2017]. . . . 21
2.7 Mass production vs low volume economic impact [Petrick and Simpson, 2013]. . . . 22
2.8 Processes characteristics resume [Ngo et al., 2018, Singh and Singh, 2017, Cotteleer et al., 2014]. . . . 25
2.9 Process characteristics [Guo and Leu, 2013]. . . . 47
2.10 Printing parameters, adapted from Tian et al. [2016]. . . . 54
2.11 Mechanical Properties of Continuous Fibers from ©Markforged [2016]. . . . 57
2.12 Printing parameters adapted from Caminero et al. [2018b]. . . . 61
2.13 Average ILSS for unreinforced and reinforced samples adapted from Caminero et al. [2018b]. . . . 62
2.14 Fibre volume content for impact test samples, adapted from Caminero et al. [2018a]. 62
2.15 Three-factor and three-level central composite design, adapted from Hu et al. [2018]. 64
2.16 Tensile test results for FFF specimens [Zhang et al., 2018]. . . . 69
2.17 Continuous fibres process characteristics resume . . . 73
2.18 Discontinuous fibres process characteristics resume . . . 74

3.1 Commercial details of FFF materials. . . . 77
3.2 Filament tensile test mechanical properties. . . . 80
3.3 DSC test results. . . . 85
3.4 DSC values from the literature review. . . . 86
3.5 Sample nomenclature . . . 92
3.6 Technical specifications . . . 93
3.7 Printing parameters . . . 94
3.8 Glass transition temperature ranges . . . 99
3.9 Filament mechanical properties . . . 99
3.10 Tensile test results . . . 101
3.11 Flexural test results . . . 102
3.12 Imaged based content analysis results . . . 105
3.13 Parameters for sample production. . . . 110
3.14 Tensile Test Results for Pure Nylon and Nylon+Carbon Fibres. . . . 112
3.15 Flexural Test Results for Pure Nylon and Nylon+Carbon Fibres. . . . 113
3.16 Datasheet material specifications [Fillamentum, 2019b,a, Taulman3D, 2019] . . . 114
3.17 Printing parameters for all samples. . . . 115

3.18 Alloy 910 XY45, XZC tensile results and datasheet values. . . . 117
3.19 FX256 XY45, XZC, XYCE tensile results and datasheet. . . . 118
3.20 CF15 XY45, XZC, XYC and XYCE tensile results. . . . 120
3.21 Building orientation comparison . . . 121

4.1 Specimen nominal dimensions. . . . 127
4.2 Real specimen dimensions. . . . 130
4.3 Cohesive parameters obtained for PA12 specimens. . . . 136
4.4 Cohesive parameters obtained for the reinforced specimens. . . . 138
4.5 Datasheet values and material specifications [Fillamentum, 2019b,a]. . . . 149
4.6 Selected printing parameters. . . . 150
4.7 CF15 and FX256 strength and elastic properties. . . . 160
4.8 Anisotropic elasticity relationship. . . . 160

5.1 Datasheet values and material specifications [Fillamentum, 2019b,a]. . . . 168
5.2 Fused filament fabrication parameters. . . . 169
5.3 Literature overview for cutting parameters for polymer machining. . . . 173
5.4 Surface roughness prior to machining tests, average values. . . . 175
5.5 ANOVA *Ra,t* results (1st experimental approach). . . . 175
5.6 ANOVA *Ra,l* results (1st experimental approach). . . . 177
5.7 Optimized processing window for PA12 and PA12CF machining targeting improved finishing - approach 1. . . . 182
5.8 Taguchi L9 orthogonal array used for the second testing programme. . . . 184
5.9 Improvement factor for machined specimens. . . . 187
5.10 PA12 *Ra,l* ANOVA (2nd experimental approach) . . . 189
5.11 PA12 *Rz,l* ANOVA (2nd experimental approach) . . . 190
5.12 PA12 cutting loads ANOVA (2nd experimental approach) . . . 190
5.13 PA12CF cutting loads ANOVA (2nd experimental approach). . . . 190
5.14 Wear analysis for PA12 tools (40x magnification), 2nd testing approach. . . . 193
5.15 Wear analysis for PA12CF tools (40x magnification), 2nd testing approach. . . . 193
5.16 Optimized processing window for PA12 and PA12CF machining targeting improved finishing - approach 2. . . . 194
5.17 Datasheet material specifications [Fillamentum, 2019b,a]. . . . 198
5.18 Selected printing parameters. . . . 199
5.19 FX256 and CF15 DSC results for the control samples. . . . 200
5.20 Full factorial DOE and condition 0. . . . 202
5.21 DSC results for annealed samples t=6h. . . . 202
5.22 Best annealing conditions according ANOVA's analysis. . . . 212
5.23 Mechanical properties overview. . . . 212

A.1 Tronxy X5 3D Printer main specifications. . . . 227
A.2 RatRig V-core 3D Printer main specifications. . . . 228

Abbreviations

3D - Three Dimensional
3DP - Three Dimensional Printing
ABS - Acrylonitrile Butadiene Styrene
ADT - Abstract Data Type
AM - Additive Manufacturing
ANDF - Architecture-Neutral Distribution Format
ANOVA - Analysis of Variance
API - Application Programming Interface
CAD - Computer-Aided Design
CAPP - Computer-Aided Process Planning
CASE - Computer-Aided Software Engineering
CF - Carbon Fibres
CFFFF - Continuous Fibres Fused Filament Fabrication
CFFDM - Continuous Fibres Fused Deposition Modeling
CFRP - Carbon Fibres Reinforced Polymers
CNC - Computerized Numerical Control
CORBA - Common Object Request Broker Architecture
DCB - Double Cantilever Beam
DMA - Dynamic Mechanical Analysis
DLP - Digital Light Processing
DIC - Digital Image Correlation
DIY - Do it Yourself
DOE - Design of Experiments
DSC - Differential Scanning Calorimetry
FDM - Fused Deposition Modeling
FE - Finite Element
FFF - Fused Filament Fabrication
FRP - Fibre Reinforced Plastics
FRTP - Fibre Reinforced Thermoplastics
FTIR - Fourier Transform Infrared Spectroscopy
GF - Glass Fibres

HPP - High Performance Polymer
ILSS - Interlaminar Shear Strength
IT - Information Technologies
LCA - Life-Cycle Assessment
MFI - Melt Flow Index
NDT - Non Destructive Test
PA - Polyamide
PBS - Powder Bed Fusion
PC - Polycarbonate
PEEK - PolyEther Ether Kethone
PEI - Polyetheremide
PET - Polyethylene Terephthalate
PETG - Polyethylene Terephthalate-Glycol
PMC - Polymer Matrix Composites
PP - Polypropylene
PTFE - Polytetrafluoroethylene
PPSU - Polyphenylsulfone
PVA - Polyvinylacetate
VPP - Vat Photopolymerization Process
SFFDM - Short Fibre Fused Deposition Modelling
SCF - Short Carbon Fibre
SLA - Stereolitography
STL - Standard Tessellation Language
TGA - Thermogravimetric Analysis
UV - Ultra Violet

Chapter 1

Introduction

Additive Manufacturing (AM) is a process that dates its origins back to 1986, when Hull [1986] developed and created the first equipment called the "stereolitography apparatus"(SLA) by polymerizing a photopolymeric resin. Since then, several different ways of processing material additively into a desired form where created. Ceramic powders, polymeric resins, carbon fibres reinforced composite materials and metals, among others, were all used as feedstock for these technologies. However, for a long time, industry kept overlooking AM as a solid and capable method for final part fabrication, perceiving it as an inexpensive, yet quick way of producing prototypes. Commonly called Rapid Prototyping, the process went through "dark ages" to get to the stage that is today.

The last decade represented a new era for AM, creating a turning point for how people imagine, develop and design parts for prototyping or even final production. Since these previous years, AM has been growing and two branches have been developed among the technologies. Foremost, professional machines are now reliable, with higher resolution, cheaper to maintain and in general easier to work with. A second branch has been growing since the mid 2000: desktop 3D printers; this happened due to patent expirations, smaller companies have appeared that focused in the concept behind the expensive equipments and created a new era of fabrication available to a broader part of the world [Redwood et al., 2017].

1.1 Motivation and Scope

This study is focused on the extrusion process named Fused Filament Fabrication (FFF) and the characterization of the parts that this technique can produce. This motivation relies on the process performance improvement and in the importance of quantifying how these parts respond in certain situations. FFF is presented in both branches (professional and desktop), and is one of the most embracing when taking into account parts quality and performance, even considering that in terms of these characteristics, the barrier between both categories is getting thinner. Low cost machines can now produce parts with engineering and high performance polymers that previously only high-end equipments could. Nevertheless, the process is evolving and new variables such as

nano particles, short and continuous reinforcing agents are introduced, thus turning blurrier the definition of part property.

FFF is an inexpensive and broad process that allows the use of a vast type of thermoplastics (from PLA to PEEK), which can be easily scaled size wise to higher levels. However, the production of FFF parts with consistent and predictable properties is not straightforward, depending on a variety of intrinsic and external factors. The identification and establishment of the process parameters, creating a data foundation for the test materials, enables the optimization of these properties. Mechanical characterization is then essential, providing the understanding of the part's behaviour and an insight on the performance's variability. Due to the process manufacturing characteristic behaviour, its irregular performance, related to the building orientation (anisotropic behaviour), must be considered at the design and project phase. The process is also limited by its inferior surface finishing, when facing other additive technologies. This limitation is accentuated as the process increases in physical dimension.

Thus, a considerate lack on this scientific field is the understanding of the uncertainties of the FFF process variables, materials and overall process. Considering this problem, evaluation methods must become more capable and fitted with the growth of the technology, comprehending the barriers imposed by the process.

This PhD thesis is under the scope of the FIBR3D[1] project, entitled: Additive manufacturing-based hybrid process, for long or continuous fibre reinforced thermoplastics. The project purpose is the development of a five axis advanced hybrid (additive and subtractive) hardware. In addition, specially defined high performance polymeric formulations were developed, using continuous or long fibres as reinforcing agent. Therefore, it is intended, as our outcome, to develop lightweight, dimensionally accurate, high performance parts that can compete with the traditional methods, while also offering the advantages of the FFF technique [Marques et al., 2017].

1.2 Work purpose and goals

A comprehensive analysis on FFF processing of reinforced thermoplastics in order to develop a robust approach, evaluating evaluate parts mechanical performance is demanded. Furthermore, an analysis focusing on the process mechanical performance variability, taking into account unreinforced and reinforced printed parts, is of major interest. Post processing seems to be essential for the improvement of this technology. As a result, these post operations, should also be investigated as a feasible way to ensure final surface roughness, as well as mechanical performance improvement and residual stress stabilization. The scientific relevance of these topics, motivated the present work to answering of the following open research questions:

Q1 - How much can fibre reinforcement improve the mechanical behaviour of an FFF part?

Q2 - How does the printing conditions affect the mechanical behaviour?

Q3 - How can post processing be a beneficial complement to FFF process?

[1] researchgate.net/project/FIBR3D

1.2.1 Goals

Considering the established purpose of this work, two main areas of concern were defined. Each of these areas is supported by a series of specific goals, which are described bellow.

1.2.1.1 Mechanical Performance

Performance evaluation of feedstock and specifically the development of printed specimens is essential to comprehend the behaviour of functional end-user FFF capabilities to be applied in the industrial level applications. Under this topic, the following scientific goals were established:

G1 - Definition of a test protocol to characterize FFF feedstock in terms of thermal and mechanical behaviour;

G2 - Study of distinct infill and/or building orientations on the mechanical properties of FFF printed samples;

G3 - Analyse the mechanical performance of FFF parts under multiple loading conditions (Arcan);

G4 - Development and analysis of a methodology for interlayer fracture propagation samples (based on laminate composite methodologies);

G5 - Evaluate the challenges and benefits imposed by fibre reinforcement in FFF processing.

1.2.1.2 Post-processing

Motivated by the current trend of process hybridization, two specific objectives were pointed out, regarding post processing treatments, which are described as follows:

G1 - Analyse the annealing influence on the mechanical performance of unreinforced and reinforced short fibre FFF printed parts;

G2 - Investigate the behaviour of short fibre and unreinforced FFF printed parts when submitted to machining operations.

1.3 Document Structure

This document is organized in six distinct chapters. Each of these chapters is initiated by a brief introductory description of the content. The experimental part of this work is presented in independent chapters (3 to 5), which are also divided into standalone sections, presenting an introductory section, methods, results and conclusions as published in the respective journals.

- Chapter 1 - Introduction: This chapter presents the scope of the present work and consequent motivation, also including the document structure and scientific contributions.

- Chapter 2 - Literature review: A theoretical background is presented regarding the additive processes focusing on the FFF technique. Traditional composites layer based manufacturing is briefly summarized, providing contextualization for printing with reinforced materials. FFF technologies using distinct types of fibres are analysed in detail in section 2.5 being presented as published in article form.

- Chapter 3 - Supporting studies: This chapter is divided into four sections, in which in a first stage distinct types of feedstock are analysed providing the essential background knowledge about their processing details. The following three sections present distinct studies, with different materials and types of reinforcement in order to obtain a better practical experience on the different types of reinforcement, as well as the process parameter effect in the mechanical properties.

- Chapter 4 - Advanced performance: Two studies are described in which testing procedures using unconventional methods and specific FFF produced samples are presented. In the first section, the interlaminar fracture behaviour of FFF parts under mode I of both reinforced and unreinforced PA12 materials were studied. In the second section, the anisotropic behaviour of the same type of part is tested, by submitting distinct building orientation parts to different types of loading conditions, thus creating the possibility to evaluate the part's heterogeneity. Section 4.1 and 4.2 are presented in article form as published.

- Chapter 5 - Post Processing of Printed Samples: This chapter is divided into two subsections. In the first section, printed samples are submitted to machining process in order to evaluate the improvements on superficial finishing. The second section presents a methodology in which thermal annealing is applied to printed samples, in order to assess the post processing influence on the mechanical performance and its effect on thermal stabilization. Section 5.1 and 5.2 are presented as an article as published.

- Chapter 6 - Conclusions: The final chapter describes a set of overall conclusions based on the experimental work, answering the research questions previously defined. Some future work and guidelines to production of structural parts through FFF is presented.

1.4 Scientific contribution

Throughout the development of this thesis, the following scientific contributions were achieved:

- Chapter 2: An extensive review about FFF processing of composites was conducted and delivered in a paper form. This contribution gathers information and data on a vast range of studies, being divided by reinforcement type and technology [Ferreira et al., 2019a].

- Chapter 3: A straight forward experimental procedure to characterize mechanical and thermal analysis of feedstock is presented. Complementary information regarding the variability of FFF polymer properties and processing conditions. This work was documented through

MSc dissertations and conference proceedings. Despite being an open topic, the generated knowledge will certainly contribute to the understanding of FFF variability problem. A consequent protocol was delivered in paper form, studying mechanical and thermal behaviour of fibre reinforced and unreinforced PETG thermoplastic parts [Ferreira et al., 2018a].

- Chapter 4 - Advanced Performance testing
  - Section 4.1: A methodology was developed and applied to study the mode I interlaminary fracture behaviour. To complement the experimental work, a numerical approach was pursued, revealing to be suited for the materials tested [Fonseca et al., 2019].
  - Section 4.2: A novel approach to FFF printed specimens was developed by testing a new type of *Butterfly* specimen created based on the Arcan original concept, printed under three different building orientations for multi-axial testing.
- Chapter 5 - Post processing
  - Section 5.1: An analysis concerning the machinability of FFF PA 12 and PA12+CF printed parts was performed, focusing on the final surface roughness and the parameters that led to it.
  - Section 5.2: Advances towards the mechanical improvement of FFF PA 12 based printed parts were made, via thermal treatment. A proof-of concept that annealing is noteworthy of application is reached.

1.4.1 Publications

Some of the results of this PhD thesis have already been published. A list of publications is presented bellow:

1.4.1.1 Journal Articles

- Ferreira I, Machado M, Lino Alves J, Marques AT. A review on fibre reinforced composite printing via FFF. *Rapid Prototyping Journal*. 2019 Jan 1;25(6):972–88. Available from: https://doi.org/10.1108/RPJ-01-2019-0004;
- Ferreira I, Vale D, Machado M, Lino J. Additive manufacturing of polyethylene terephthalate glycol /carbon fiber composites: An experimental study from filament to printed parts. *Proc Inst Mech Eng Part L J Mater Des Appl*. 2019;233(9):1866–78. Available from: https://doi.org/10.1177/1464420718795197;
- Fonseca J, Ferreira I, Moura MFSF De, Machado M, Alves JL. Study of the interlaminar fracture under mode I loading on FFF printed parts. *Composiste Structures*. 2019;214(January):316–24. Available from: https://doi.org/10.1016/j.compstruct.2019.02.005;

- Ferreira I, Madureira R, Villa S, de Jesus A, Machado M, Alves JL, et al. Machinability of PA12 and short fibre–reinforced PA12 materials produced by fused filament fabrication. *International Journal of Advanced Manufacturing Technolies*. 2020; Available from: https://doi.org/10.1007/s00170-019-04839-z;

- Ferreira I, Jesus A, Machado M, Pereira J, Alves JL, Xavier J. Experimental characterisation of fused filament fabrication printed parts under tension, shear, and combined shear–tension loads via Arcan test. *Proc Inst Mech Eng Part L J Mater Des Appl.* 2020 (In press); https://doi.org/10.1177/1464420720908625;

- Ferreira I, Melo C, Neto R, Machado M, Alves JL, Mould S. Study of the annealing influence on the mechanical performance of PA12 and PA12 fibre reinforced printed samples. *Rapid Prototyping Journal* (Approved for publication).

1.4.1.2 International Conference Presentations:

- Isaac Ferreira, Jorge Lino Alves, Margarida Machado, Ana Reis, Rui Neto, António Torres Marques. Mechanical behaviour of thermoplastic based composites processed by additive manufacturing. Materiais 2017. Aveiro, Portugal, 9-12 April, 2017

- Isaac Ferreira, Margarida Machado, André J. Cavaleiro, Rui Neto, Jorge Lino Alves and Ana Reis. A study on the influence of fibre content on the mechanical behaviour of 3D printed thermoplastic parts. EUROMAT2017. Thessaloniki, Greece, 17-22 September, 2017

- Isaac Ferreira, Jorge Lino Alves, and Margarida Machado. Effect of layer filling path on mechanical properties of PA and PA-reinforced FDM parts. PMI2018 - International Conference on Polymers and Moulds Innovations. Guimarães, Portugal, 19-21 September, 2018. DOI:10.13140/ RG.2.2.21586.61124.

- Isaac Ferreira, Ting Ting Shen, Jorge Lino Alves, Margarida Machado, Rui Neto and Ana Reis. Mechanical characterization of FDM parts reinforced with continuous carbon fibres. ICDDMAP2017 - International Conference on Direct Digital Manufacturing and Polymers. Leiria, Portugal, 15-16 May, 2017 DOI:10.13140/RG.2.2.31637.27368/1

- Rui Madureira, Isaac Ferreira, Abílio Jesus, Santiago Villa, Margarida Machado, Jorge Lino Alves. Machining of carbon fibre reinforced thermoplastics produced by FFF. Materiais 2019. Lisbon, Portugal, 14-17 April, 2019.

- Carolina Melo, Isaac Ferreira, Margarida Machado, Rui Neto and Jorge Lino Alves. Enhancement of mechanical properties of 3D printed thermoplastic parts through short fibre reinforcement and annealing post-treatment. EUROMAT2019. Stockholm, Sweden, 1-5 September, 2019.

- Isaac Ferreira, João Pereira, José Xavier, Abílio de Jesus, Margarida Machado and Jorge Lino Alves. Experimental characterization of FFF printed parts under tensile, shear and mixed loads via Arcan-based test. EUROMAT2019. Stockholm, Sweden, 1-5 September, 2019.

1.4.2 Master Thesis Orientations:

Some of the work that has been developed by providing guidance to Master thesis students which resulted in an important contribute for this document. A list of this works is presented bellow:

- Ting Ting Shen, Mechanical Characterization of Polymer Matrix Composites Produced by 3D Printing. Master thesis of MIEM, FEUP, 2017.
- João Fonseca, Inter-laminar fracture study of FDM printed parts. Master thesis of MIEM, FEUP, 2018.
- Rui Madureira, Machining of Carbon fibre reinforced thermoplastics of FDM printed parts. Master thesis of MIEM, FEUP, 2018.
- Carolina Melo. Enhancement of mechanical properties of 3D printed thermoplastic parts through short fibre reinforcement and annealing post-treatment. Master thesis of MIEM, FEUP, 2019.

Chapter 2

Literature review

2.1 Layer based manufacturing

Since the main topic of this work is the behavioural study of AM printed parts, it is important to create a framework of the category in which this technology is inserted and analyse what are the processes behind and before AM. Layer based manufacturing is defined by the production of parts that sequentially add sheets or layers of a material. Traditional methods for composite manufacturing can be included in this category, and the similarity with AM is notorious. Traditional composites are not homogeneous materials and are most commonly fabricated by adding the reinforcement material in the direction of the mechanical solicitation. Some consider FFF process as a producer of a different type of composites. Even though is normally mono material, a structure is created with the feedstock deposition also being made preferentially according the solicitation. Thus, there is a similarity/synergy between both techniques, which is more substantiated by the usage of short or continuous fibres in FFF process.

2.1.1 Traditional composite Materials

A composite is created by combining two or more materials so their distinct properties come together as one improved heterogeneous material. In most cases, one works as a reinforcement component and the other as binding phase, creating a far superior material than its components separated. The matrix is usually a homogeneous material agglutinating the reinforcement part, which normally spreads through the composite. The reinforcement mechanical properties are normally higher than the matrix, giving the material load bearing capabilities that the matrix, which functions as the binding agent, would not have. Therefore, there is a high number of influencing factors when considering composite material mechanical properties, such as fibre type, orientation, percentage, geometry, inter-facial adhesion, among others. Being considered as one of the most influential factors in composites mechanical properties, the geometry defines how it will behave. For a composite to fully benefit from the reinforcement capabilities, the continuity of the fibres must be assured. Since the load is transferred from the matrix to the reinforcement through shear forces, the contact interface between fibre and matrix is much bigger in that dimension than

the others, thus creating a critical aspect ratio within the length and diameter of around 100:1, depending on the degree of bonding [Hull and Clyne, 1996, Friedrich and Almajid, 2013]. To summarize, by disposing the reinforcement in the critical direction, the binding phase allows the cohesion of the material, thus creating a controlled anisotropy. Composites are developed not only to improve mechanical performance, but to enhance other properties such as, electrical or thermal conductivity, optical properties among others, which puts this materials in a class of their own. The possibility of developing a material with a specific purpose considering the type of solicitation that the part is going to be exposed to, is an advantage comparatively to isotropic materials [Kar et al., 2016, da Silva et al., 2013].

The classification of composite materials could be done taking into account several characteristics. Considering matrix materials, this classification divides the composite in metal matrix materials, inorganic nonmetallic materials, which includes ceramics and carbon based matrices. Finally, polymeric matrices, are subdivided into thermosetting resins and thermoplastic resin based. Since this work will be focused in FFF AM process, thermoplastic materials are the only type of matrix to be considered. Reinforcements can also be classified by the material type used (carbon, glass, organic, boron, silicon carbide and hybrid fibres). Currently, industry is demanding for polymer matrix composites (PMC) in higher quantities compared to other types. Fibre reinforced polymers, generally with glass, carbon or Kevlar®, have high specific stiffness, making them attractive for structural parts, in automotive, aerospacial and aeronautical industries. The current trend for metallic matrix composites is to improve thermal properties by adding high temperature resistant particles, as ceramic or titanium to aluminium, creating a more temperature resistant material. Ceramic matrix materials are the most important inorganic non-metallic and are usually reinforced in order to reduce its brittleness, however they are rarely found as its development is still recent. Figure 2.1 is representative of the composite classification by the type of reinforcement.

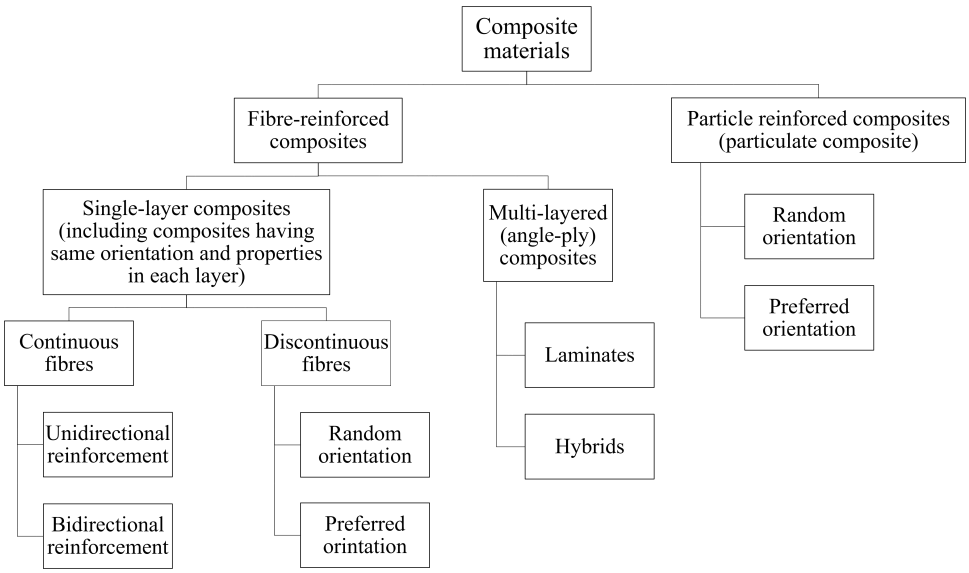


Figure 2.1: Composite classification tree [Kar et al., 2016].

2.1.1.1 Reinforcements

Carbon Fibres: commonly 8 μm diameter and its production is made by the thermal decomposition of several organic components [Hull and Clyne, 1996]. Rayon fibres are produced from cellulose, requiring high grafitization temperatures and are the most expensive. Pan fibres, from polyacrylonitrile and pitch fibres, produced from pitch, present inferior mechanical properties [da Silva et al., 2013]. Polyacrylonitrile fibres production is divided in four different stages:

- **Oxidation** - defined by the heating to 300°C of the fibres in an oxygen enriched atmosphere, suppressing the fibre melting point;
- **Carbonization** - the fibres are heated up to 1100°C in a neutral atmosphere so that carbon atoms can remain;
- **Grafitization** - a pyrolysis is made, again in neutral atmosphere, developing high stiffness;
- **Surface treatment** - in an acidic atmosphere (nitric or sulphuric) where boundary conditions are changed to grant better adhesion between fibres and resins [da Silva et al., 2013, Hull and Clyne, 1996].

Carbon fibres are classified regarding their mechanical behaviour, as seen in Table 2.1:

Table 2.1: Carbon fibres classification [da Silva et al., 2013].

Class	Description
UHM (Ultra High Modulus)	Young's modulus above 500 GPa
HM (High Modulus)	Young's modulus above 300 GPa and ratio thoughness/modulus bellow 1%
IM (Intermediate Modulus)	Young's modulus above 300 GPa and ratio thoughness/modulus 1%
LM (Low Modulus)	Young's modulus bellow 300 GPa
HT (High Tensile Strength)	Tensile strength above 3000 MPa and ratio thoughness/stiffness from 1.5 to 2%

Glass Fibres: considered a high performance, non flammable, heat resistant and electrical insulator with great tensile strength, fabricated from Silicon Dioxide (SiO_2) with additions of other materials. E (Electric) fibres, which are the most used by industry, have high strength, high stiffness, great electrical and environmental properties. C (Corrosion) fibres are the most resistant to corrosion but have the lowest mechanical properties, and S (Strength) fibres are the most expensive, yet having the best mechanical properties [da Silva et al., 2013]. Glass reinforced polymers have become a major player in composite materials industry and are highly used in automotive, construction, electrical and aerospace sectors, among others [Wang et al., 2011].

Other types of Fibres: organic are one of the most used fibres in industry after the previously mentioned ones. Kevlar ® fibres were developed from aromatic PA polymer, technically known as aramide fibres, and are extruded at approximately 200°C, allowing the molecular chain to be aligned, improving mechanical properties. This type of fibre has great chemical wear properties,

resistance to impact and fatigue. However, poor compression and flexural strength are their main flaws. Natural fibres can be processed from several sources: wood fibres, vegetables, animal and mineral fibres and their main weakness is the reduced mechanical properties. In addition, SiC whisker fibres having high strength, stiffness, thermal stability and low density, are produced in a similar environment to the abrasive powder, are used as reinforcement, granting high strength [da Silva et al., 2013, Hull and Clyne, 1996]. Table 2.2 exhibits the properties of these fibres.

Table 2.2: Fibre Properties [da Silva et al., 2013, Hull and Clyne, 1996].

Fibre	Density ρ (Mg/m^3)	Young's Modulus E (GPa)	Poisson's Ratio ν	Tensile Strength (MPa)	Elongation (%)	Thermal expansion coefficient α $(10^{-6}*K^{-1})$	Thermal Conductivity K $(W*m^{-1}*K^{-1})$
SiC Monofilament	3.0	400	0.20	2400	0.6	4.0	10
Boron Monofilament	2.6	400	0.20	4000	1.0	5.0	38
High Modulus Carbon	1.8-2.15	370-830	0.20	2000-2400	0.5-2	-1 to 0.4	80-200
High Strength Carbon	1.75-1.84	224-245	0.20	3400	1.1	-0.1 to 0.4	80-200
E-glass	2.5-2.66	70-85	0.22	2000	≈2.7	4.9	1.2-1.35
Kevlar	1.43-1.48	60-190	0.35-0.37	2500-3600	1-4	-5 to -2	0.2-0.4
Nicalon (SiC)	2.6	190	0.20	2000	1.0	6.5	10
FP (Al_2O_3)	3.9	380	0.26	2000	0.5	8.5	8
Saffil (Al_2O_3)	3.4	300	0.26	2000	0.7	7.0	5
SiC wisker	3.2	450	0.17	5500	1.2	4.0	100
Cellulose(Flax)	1.0	80	0.3	2000	3.0	-	-

2.1.1.2 Matrix Materials

Thermoset Resins: These materials are the most predominant matrices used in composite industry, being epoxies, polyesters and vinyl-esters the most commonly used. Thermosetting resins are initially in liquid state, which is converted to solid via chemical reaction, promoted by a catalyst or hardener, creating a three-dimensional network. Mechanical properties are directly related to its reaction, depending on the number of chemical elements, strength and length of their bonds. The curing process can be improved by adding chemicals at room temperatures, however, increasing the temperature in different stages results in stronger cross-linking and subsequently enhanced mechanical properties. Thermosetting resins have a different behaviour when compared to thermoplastic materials. Due to its chemical structure and curing reaction, thermosettings are brittle, while thermoplastics can sustain high levels of plastic deformation plus having the possibility of being reprocessed. When comparing materials within each class, epoxies are generally tougher than polyesters or vinyl-esters [Hull and Clyne, 1996, da Silva et al., 2013].

Thermoplastics: represent a growing portion of the composite market. Different from the thermosetting cross-linked structure, thermoplastics have their properties defined by their monomers (repeating units) and their molecular weight. The high molecular concentration and level of disorder in amorphous thermoplastics acts similarly to cross-links and semi-crystalline polymers which have the same molecular concentration with high degree of orientation. Heating amorphous polymers will cause the molecular chains to untangle and relax, changing the material phase from solid to liquid state. This relaxation will occur when the glass transition point is reached (or above it). Semi-crystalline polymers behave differently to temperature; when glass transition temperature is reached, the remaining amorphous chains start to move until the melting point is reached. Then, the remaining crystalline phase starts to melt originating a viscous liquid. Depending on the conditions, the material is processed and solidified. Both amorphous and semi-crystalline polymers may have anisotropic properties. In other words, amorphous polymers tend to stretch and align the molecular chains according to the melt flow direction, while semi-crystalline polymers tend to develop laminar units in the flow direction.

Metallic matrices: generally used with aluminium, magnesium and titanium. To improve their mechanical properties, these materials are normally alloyed with other elements, that provide a new and improved set of mechanical properties. Those properties are commonly associated with the thermal treatments that the alloy is subjected. The addition of a reinforcement does not improve toughness and strength, however, wear resistance and thermal stability are enhanced [da Silva et al., 2013, Hull and Clyne, 1996].

Ceramic matrices: divided in four distinct types, glass ceramics are complex oxides namely, borosilicates and aluminosilicates thermally treated to create a precipitation of the crystalline phase, forming a fine dispersion in the glass phase [Phillips, 1991]. This class of material has lower softening points than conventional ceramics, however they are easier to produce. Conventional ceramics like Si_3N_4, SiC, ZrO_2 and Al_2O_3, have a randomly oriented and fully crystalline structure and their main advantage is their easy processability. Another category of ceramic matrices is cement which can be reinforced with short fibres. Finally carbon composites, can be created by vapour infiltration of carbon fibres. Ceramic composites are normally reinforced with the purpose of improving toughness, since they are extremely brittle materials and any improvement in this characteristic is a beneficial factor [Hull and Clyne, 1996].

Table 2.3 indicates the properties for the matrices mentioned above.

2.1.2 Applications

Since composite materials can be tailored accordingly to the specifications, they have been used through the most vast range of applications. From the most advanced industries such as aerospace, automotive, building and construction to consumer products in Figure 2.2 indicates the percentages of visitors in the world largest composite fair (JEC, Paris) that reflects this trend.

Table 2.3: Typical composite matrix properties [Hull and Clyne, 1996].

Fibre	Density ρ (Mg m^-3)	Young's Modulus E (GPa)	Poisson's Ratio ν	Tensile Strength (MPa)	Elongation (%)	Thermal expansion coefficient α (10^-6 K^-1)	Thermal Conductivity K (W m^-1 K^-1)
Thermosets							
Epoxy resins	1.1-1.4	3-6	0.38-0.40	35-100	1-6	60	0.1
Polyesters	1.2-1.5	2.0-4.5	0.37-0.39	40-90	2	100-200	0.2
Thermoplastics							
Nylon 6.6	1.14	1.4-2.8	0.3	60-70	40-80	90	0.2
PP	0.90	1.0-1.4	0.3	20-40	300	110	0.2
PEEK	1.26-1.32	3.6	0.3	170	50	47	0.2
Metals							
Al	2.70	70	0.33	200-600	6-20	24	130-230
Mg	1.80	45	0.35	100-300	3-10	27	100
Ti	4.5	110	0.36	300-1000	4-12	9	6-22
Ceramics							
Borosilicate	2.3	64	0.21	100	0.2	3	12
SiC	3.4	400	0.20	400	0.1	4	50
Al_2O_3	3.8	380	0.25	500	0.1	8	30

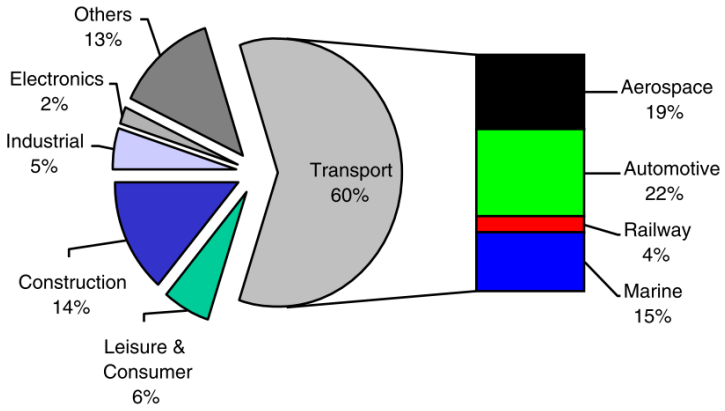


Figure 2.2: JEC 2003 visitors at various sectors [Friedrich and Almajid, 2013].

As a tendency, metallic materials are still dominating in many areas, due to manufacturing difficulties and associated costs, making it difficult to create a competitive market, although composites can grant a better performance. Composite materials are always in evolution and are not being used to their full capabilities due to these economic aspects. Additive manufacturing could be an alternative to traditional processes in a way that is possible to create a combination of high performance materials with a inexpensive, fast and fully customizable process.

2.2 Additive Manufacturing

2.2.1 Introduction

Additive Manufacturing (AM) is defined by the standard ISO/ASTM 52900:2015 [ISO/ASTM, 2015] as "the process of joining materials to make objects from three-dimensional (3D) model data layer upon layer, as opposed to subtractive manufacturing technologies" [ASTM International, 2013]. This technology is also known as additive fabrication, layer manufacturing, rapid manufacturing and rapid prototyping [Guo and Leu, 2013]. The term 3D printing is also defined by the same standard as the method of producing parts by material deposition by means of a printing head, or other deposing technology. In the past, this term has been linked to low cost/performance machines. Currently, this category creation has been dismissed and both terms are considered as the same due to the creation of standards, guides due to the evolution and importance on the market/society of these low end machines [Wohlers et al., 2017].

On the other side of the spectrum, subtractive technologies implicate the use of several techniques and processes into a piece of raw material, removing it, until the desired form is created. Subtractive processes, like machining, are the most widespread metal shaping processes in the industry and parts produced have high dimensional accuracy, better surface finishing and consequently high mechanical properties. However, due to its characteristics, geometric freedom is limited, while being also extremely dependable on human interaction during operations, and creating a high percentage of waste material [Faludi et al., 2014, Campbell et al., 2012]. AM part cost depends on certain parameters such as feedstock cost and manufacturing time, however complex geometries do not implicate increased prices. Other traditional processes, as forming, imply an initial investment in tools and changes on the part add costs, similarly to what occurs with subtractive processes, which are only profitable for high number of parts, as presented in Figure 2.3 [Varotsis, 2018].

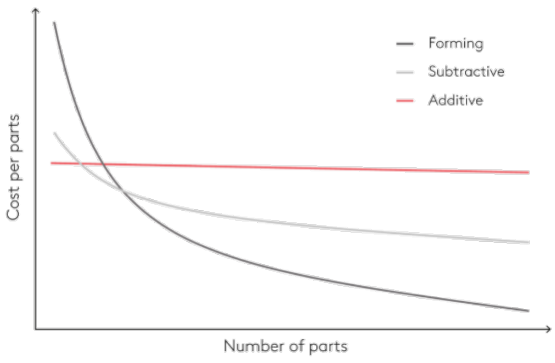


Figure 2.3: Cost per part AM vs CNC vs Forming [Varotsis, 2018].

AM is a process that dates its origins back to 1984, when Charles Hull, co-founder and Vice President of 3D Systems®, created the first equipment called and patented as the "Apparatus for production of three-dimensional objects by stereolithography" by polymerizing a photoplymeric

resin [Hull, 1986]. However, the general opinion of businesses and industry about this type of technology was that these were flawed, expensive equipment to use. Nevertheless, in the last decade, market changed significantly, mostly due to patent expirations as seen in Figure 2.4. The 3D printing boom, or as Prince [2014] and [Barnatt, 2013] described as:

> "The new industrial revolution"

while, the father of the low cost 3D printer, Dr.Adrian Bowyer, described it as:

> "The concept of self-replicating kinematic machines has intrigued some of the world's greatest minds for generations."

The RepRap concept [Jones et al., 2011] led to a worldwide movement consisting in the open source development of extremely low cost machines (when compared to the ones previously sold by Stratasys Ltd.®), that were capable to replicate itself, by producing parts extruding polymer through a heated nozzle and depositing it into a desired shape of form based upon the FFF process developed by Crump [1992] for Stratasys Ltd.® [Schoffer, 2016, Mims, 2013]. Conjointly, the RepRap concept and the FFF patent expiration originated small start-up companies who ended up selling worldwide like Makerbot Industries®, Ultimaker® and Prusa3D, among others, creating one of the most ingrowing market of the decade, the desktop printers [Wohlers et al., 2017]. Since 2009, patents have been expiring one after another as seen in Figure 2.4 and Table 2.4 ushering the next generation of 3D printers.

There is still a doubt whether or not the 3D printer will be as useful as it promises. Nevertheless, the release of the monopolistic control over these processes is now originating the arising of new companies, creating less expensive/desktop equipments, presenting an analogy to the year 2009 when FFF patent expired and thousands of small companies where created, leading to a drop in price from over 10000€ to 1000€ or less, opening new markets and new types of consumers [Schoffer, 2016]. The next generation will be deeply connected to this expiring patents following the desktop trend, using liquid based, power based and metal based type processes.

Table 2.4: Some expired patents.

Patent	Title	Expiration	Assignee	Reference
No. 5,817,206	Selective laser sintering of polymer powder of controlled particle size distribution	Feb 7, 2016	DTM Corp	McAlea and Richard [1998]
No. 5,753,274	Apparatus for producing a three-dimensional object	Mar 26, 2016	EOS GmbH	Wilkening and Lohner [1998]
No. 6,007,318	Method and apparatus for prototyping a three-dimensional object	Dec 20, 2016	Z-Corp	Russell et al. [1999]
No. 5,866,058	Method for rapid prototyping of solid models	May 29, 2017	Stratasys	Batchelder and Crump [1999]
No. 6,085,122	End-of-vector laser power control in a selective laser sintering system	May 30, 2017	DTM Corp	Inc [2000]
No. 6,215,093	Selective laser sintering at melting temperature	Oct 27, 2017	Fraunhofer	Meiners et al. [2001]
No. 6,004,124	Thin-wall tube liquifier	Jan 26, 2018	Stratasys	Swanson and Hopkins [1991]

AM is currently used in totally distinct fields, such as: aerospace, automotive, dental, electronics, furniture, implant and prosthetics, jewellery, gastronomic, sports, surgical devices, textile, tool and mould making, among others types of industries, some of which are presented in Table 2.5 [Gausemeier et al., 2012].

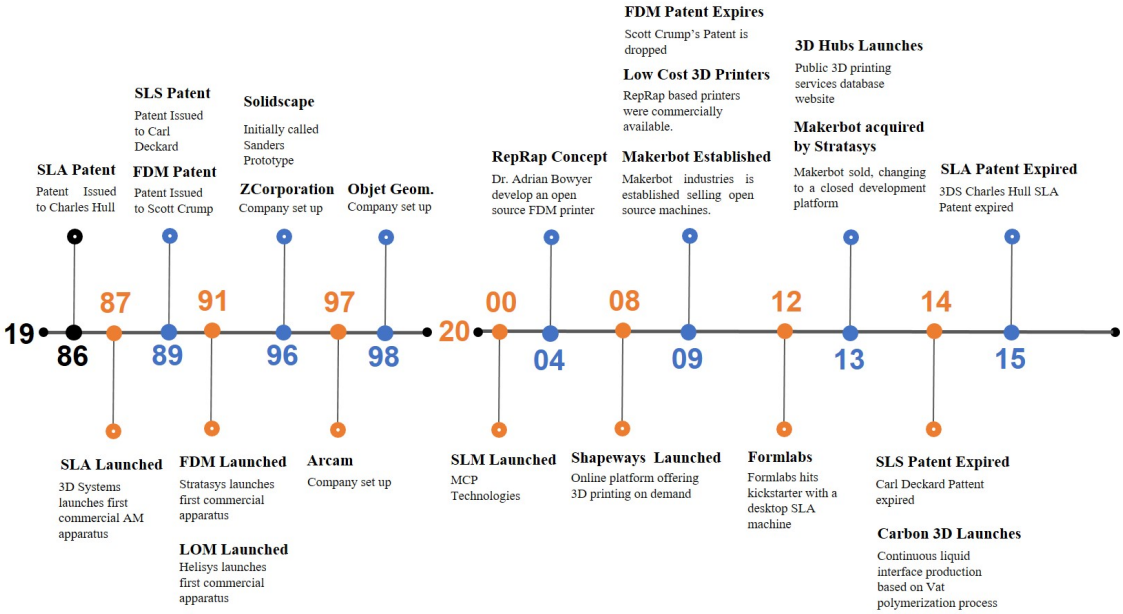


Figure 2.4: AM evolution time-line adapted from [Narsimlu, K; Pathak G. Arhendu; Mulky G. Avinash; Yavarna, 2017, Goh et al., 2017].

Table 2.5: AM aplications by select end markets [Cotteleer et al., 2014].

INDUSTRIES	CURRENT APPLICATIONS	POTENTIAL FUTURE APPLICATIONS
COMMERCIAL AEROSPACE AND DEFENSE[17]	• Concept modeling and prototyping • Structural and non-structural production parts • Low-volume replacement parts	• Embedding additively manufactured electronics directly on parts • Complex engine parts • Aircraft wing components • Other structural aircraft components
SPACE	• Specialized parts for space exploration • Structures using light-weight, high-strength materials	• On-demand parts/spares in space • Large structures directly created in space, thus circumventing launch vehicle size limitations
AUTOMOTIVE[18]	• Rapid prototyping and manufacturing of end-use auto parts • Parts and assemblies for antique cars and racecars • Quick production of parts or entire	• Sophisticated auto components • Auto components designed through crowdsourcing
HEALTH CARE[19]	• Prostheses and implants • Medical instruments and models • Hearing aids and dental implants	• Developing organs for transplants • Large-scale pharmaceutical production • Developing human tissues for regenerative therapies
CONSUMER PRODUCTS/RETAIL	• Rapid prototyping • Creating and testing design iterations • Customized jewelry and watches • Limited product customization	• Co-designing and creating with customers • Customized living spaces • Growing mass customization of consumer products

The tendency is to keep growing and heighten the technology through these specific paths. In the last decade, at least two trends emerged: a) Direct Metal AM with new and significative improvements in the direction of fully-functional components from high strength or high performance alloys, with mechanical properties close to the traditionally manufactured parts; b) Desktop-scale 3D printers appeared shortly after the expired patents for different types of tech-

nologies such as FFF or VATpolymerization that became easily and cheaply available to all types of consumers, which escalated the market, in what was called by some as "the next industrial revolution" [Barnatt, 2013, Prince, 2014]. The evolution is not restricted to these two areas and new process, new technologies and new increments in old technologies are making it more and more relevant.

2.2.2 Advantages vs Disadvantages

2.2.2.1 Advantages

AM is in fact an innovative process, opening new possibilities, streamlining the traditional manufacturing processes. There are several key benefits that AM has over the traditional techniques which are inherent, not to the production of the part itself but, to the complete product development. The intrinsic cost to concept the part's development is significantly reduced with a flexible process capable to iterate and modify prototypes on demand. This translates to high-speed response to demand without sacrificing the quality.

The process offers to remove some of the barriers imposed by traditional methods. Complex parts are as easy to produce as simple parts. Since AM is a layer based process, parts with internal or complex details are created with no different cost to the buyer. Almost everything that can be design by CAD can be produced via AM, allowing for example the possibility of printing moving components in the same job, simplifying the production process by reducing the number of operations and posterior labour [Cotteleer et al., 2014].

Cost is directly related with the production time, quantity of material needed to produce the part and final finishing. As previously mentioned, AM dictates that variety is free, meaning that the CAD file and the produced part can be changed with no significant costs to the final object. In opposition to traditional methods which require new tools, components and consequently longer lead times, added costs if any change in the prototype/part is needed. AM is a powerful tool which creates a quick bridge from the virtual model to the physical part [Attaran, 2017, Holmström et al., 2010]. Table 2.6 illustrates the areas of application where AM can be beneficial over traditional methods.

2.2.2.2 Disadvantages

As the growth and evolution of these technologies take change, one of the major obstacles for the implementation in the industrial sector is the lack of maturity of the process. Even though it is present since the early eighties, only in the recent past it has been considered as a clever alternative, or an intermediate method for manufacturing industry. 3D printers can only produce parts as big as the hardware allows, and even though larger equipments are available, the accommodating spaces requirements can be a restriction. Without this type of machines, objects are produced fragmented, requiring additional time to assemble and finishing. The fabrication time, when compared to mass production techniques is relatively slow, and sometimes, it is justifiable to use traditional methods saving lead time, higher production costs and even feedstock, that can be as cheap as 25 €/kg for

Table 2.6: AM advantages over traditional manufacturing [Attaran, 2017].

Areas of Application	Advantages
Rapid Prototyping	Reduced time to market by accelerating prototyping Reduce the cost involved in product development Making companies more efficient and innovative
Production of spare parts	Reduce repair time Reduce labour cost Avoid costly inventory
Small volume Manufacturing	Small batches are cost-effective to produce Eliminate the investment in tooling
Customized Unique Items	Enable mass customization at low cost Quick production of exact and customized replacement parts on site
Complex Work Pieces	Production of highly complex geometries with no increase in value
Machine Tool Manufacturing	Reduce labour cost Avoid costly inventory
Rapid Manufacturing	Direct manufacturing of finished components Low expensive production of small batches
Component Manufacturing	Enabled mass customization at low cost Improved part quality Shorten the supply chain Reduce the cost involved in product development Reduced number of excess parts
On Site and On-Demand Manufacturing of Replacement parts	Eliminate the storage and transportation costs Considerable reduction in repair costs Shortening of the supply chain Reduced inventory size
Rapid Repair	Significant reduction in repair time Opportunity to modify repaired components to latest design

basic polymers such as PLA/ABS or 400 €/kg for metallic alloys such as Ti6Al4V (Renishaw™) [Attaran, 2017, Martin, 2014].

As mentioned above, AM equipments are not designed for mass production but for customization parts and, unless the processing speeds change, it will continue this way. The initial cost is considered as one of the biggest obstacles, ranging from 100 000 for machines like Metal X from Markforged to 1 million euros (industrial equipments like Renishaw), thus turning the introduction of a new technology, which several are still sceptic about, very difficult. In addition, extensive knowledge of the process parameters is required, often demanding for exclusive operators. Despite the cost of the machines decrease and, in the opposite direction, the quality of the final part improving, this fact is directly related to the patent expiring and new companies taking on their own concepts of technology [Attaran, 2017]. The process often requires the post processing to improve finishing in lower quality parts, so they reach the same quality standards as the traditional methods. Finally, the poor mechanical properties due to multiple interfaces between the

layers which leads to anisotropy is not a positive point for the high performance low weight parts required by manufacturers.

2.2.3 Economic Impact

AM principle goes against traditional methods major principles, creating new possibilities that were not considered until the exploration of this technology. Beyond the technical contrast, there is the economical factor, and how companies are using AM. Let us say that a company wants to produce a single screwdriver with a specific design, the production value of this screwdriver will be in the thousands of euros. The outsourced company has to produce a mould for the handle part and cast the metal component. The creation of one screwdriver with this methodology is unthinkable and expensive, on the other hand, this is the most affordable way of producing thousands of screwdrivers, redeeming the price of specially made tools. For AM, mass production processes have little to no interest, since every screwdriver can be produced differently, the production cost will be the same. On the other hand, companies that produce custom one of a kind parts massively benefit from the technology.

Summing up, manufacturers have to be guided by two rules, mass production is translated by traditional methods as customization is linked to AM processes. Table 2.7 explains how AM is inserted in several business areas [Petrick and Simpson, 2013].

Table 2.7: Mass production vs low volume economic impact [Petrick and Simpson, 2013].

	Mass production	Low volume production
Source of competitive advantage	Low cost, high volume, high variety	End-user costumization
Supply chain	Sequential linear handoffs between distributed manufacturers with well defined roles and responsibilities	Non-linear localized collaborations with well defined roles and responsabilities
Distribution	High volume covers transportation costs	Direct interaction between local consumer/client and producer
Economic model	Fixed costs and variable costs	All costs become variable
Design	Simplified designs dedicated by manufacturing constraints	Complex and unique designs afford customization
Competition	Well-defined set of competitors	Continuously changing set of competitors

According to FIBR3D[1], the current main limitation of 3D printing regarding economic sustainability is the higher cost for large production volumes when compared with injection moulding or other traditional mass production technologies. Besides, the reduced choice of materials can originate higher material costs [Wits et al., 2016]. This barrier, regarding the limited production speed and other technological bottlenecks limit these technologies for smaller production volumes and customized products, but mostly for high value products [Gebler et al., 2014].

2.2.4 Process chain

Despite being simpler than traditional manufacturing, AM is a complex process divided in a sequence of logical operations. The general consensus divides the process in three distinct phases, as

[1] https://www.researchgate.net/project/FIBR3D

seen in Figure 2.5, even though they are subdivided in more complex categories explained ahead .

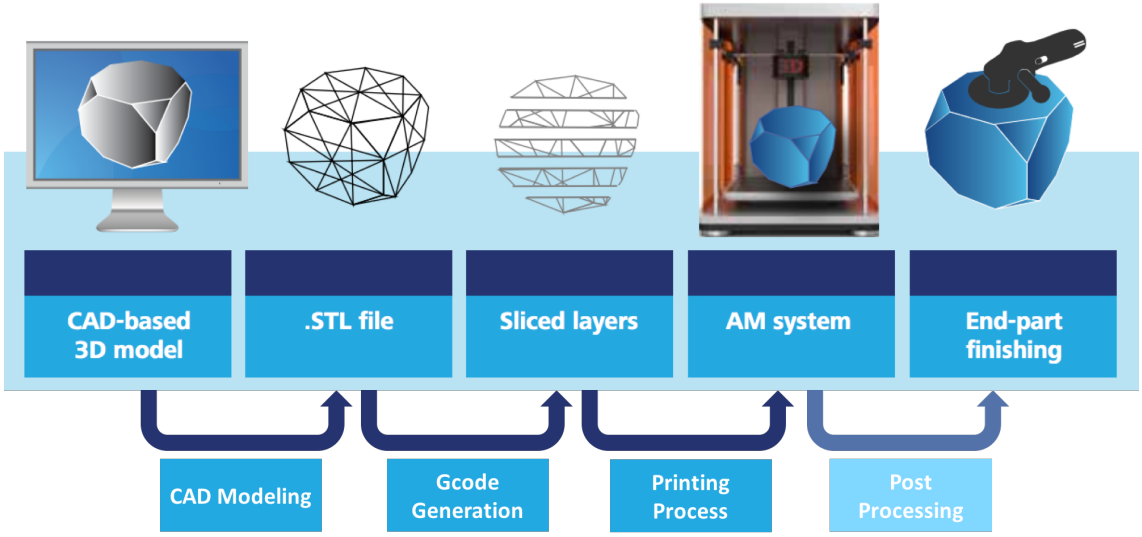


Figure 2.5: Process chain adapted from [Cotteleer et al., 2014].

2.2.4.1 CAD Modeling

This is the first step in every product development; how the part or parts will work together is taken under consideration, and the introduction of ideas or variants for the finished prototype is made. This first conceptualization allows for the user to first visualize the part even though in a virtual model. It is considered that AM would not be born without CAD 3D modeling. There is an infinity of modeling softwares, however the most well known are Solidworks, Inventor, Catia, Autocad, and each one of these tools uses a proprietary type of file/extension. With the birth of the Sterolitography process, came a type of file that would became the universal language for every software, the STL file which is not more than 3D modelled bodies converted in a mesh composed by triangles. Currently every software can export in STL [Gibson et al., 2014]. In alternative, the STL file can be obtained by 3D scanning the model, however it will only be possible in reverse engineering cases when there already is a physical part.

2.2.4.2 Computer-Aided Process Planning (CAPP)

As for CAD modeling, the G-Code generation can be done in several different softwares. A G-Code is a text file, created by the software with each point coordinates making a path throughout the part. It is in this step that each printing parameter is defined using a commonly called, slicing softwares. The output of this step is a file that contains the information about printing routes, layers, velocities, temperatures and energy intensities needed to extrude, depose, polymerize or fuse

the raw material into a desired part. Most-high end machines have their own completely closed pre-defined slicing software, allowing few changes in the print. In contrast, low cost equipments use powerful open source or open source built upon slicing software such as Slic3r[2], Cura[3], MatterControl[4], Craftware[5] or Simplify3D[6].

2.2.4.3 Printing process

Depending on the type of equipment, there is the need to pre-print setup, such as calibration and printing bed surface preparation, among others. Low cost, or simpler equipments require what is called an interface software so that the G-Code can be read and interpreted by the machine. In recent years, there has been an integration of the interface in the slicing software simplifying the process. Previously, softwares such as Octoprint[7], RepetierHost[8] or Pronterface[9] were needed in order to control the machine and read the G-Code file. For high end closed equipments, the printing process might start as soon as the G-Code is ready.

2.2.4.4 Post processing:

Post processing is required by the most of AM processes. More complex processes such as polyjet or even metallic additive technologies among others, require the removal of support components or even surface finishing. Post processing can lead in several processes to mechanical properties improvement or merely aesthetics improvement.

2.2.5 Additive Manufacturing Technologies

Table 2.8 depicts an overview of the most common additive manufacturing processes defining the type of technology as well as some advantages and disadvantages.

[2] slic3r.org
[3] ultimaker.com/software/ultimaker-cura
[4] matterhackers.com/store/l/mattercontrol/sk/MKZGTDW6
[5] /craftbot.com/craftware/
[6] simplify3d.com
[7] octoprint.org
[8] repetier.com
[9] pronterface.com

Table 2.8: Processes characteristics resume [Ngo et al., 2018, Singh and Singh, 2017, Cotteleer et al., 2014].

Category	Technology	Typical Material	Power Source	Advantages/Disadvantages
Material Extrusion	Fused Filament Fabrication	-Thermoplastics; -Ceramic paste; -Metal paste.	Thermal energy	-Inexpensive equipment; -Multi-material usage; -Limited part resolution; -Poor surface finishing.
	Contour Crafting			
Vat Polymeryzation	Stereolitography	Photopolymer with: -Particle; -Fibres.	UV Light	-High speed printing; -High part resolution; -High cost feedstock.
	DLP			
Material Jetting	Inkjet Printing	-Photopolymers -Wax	-Thermal Energy; -Photocuring.	-Multi-Material Print; -Great surface finishing; -Low strength Material.
Binder Jetting	3DP	-Polymer powder; -Ceramic powder; -Metallic powder;	Thermal Energy	-Full colour printing; -Require impregnation during post processing; -Wide material selection; -High porosity parts.
Powder Bed Fusion	Selective Laser Sintering	Polymer powder	High-Power Laser Beam	-High accuracy/detail; -Fully dense parts; -High specific strength/ stiffness; -Powder recyclability; -Support and anchor structure;
	Direct Metal Laser Sintering	-Atomized metal powder; -Ceramic powder.		
	Selective Laser Melting			
	Electron Beam Melting		Electron Beam	
Direct Energy Deposition	Laser Engineered Net Shaping	Metallic powder	Laser Beam	-Repair damaged or worn parts; -Functionally graded material printing; -Require post processing.
	Electron Beam Welding		Electron Beam	
Sheet Lamination	Laminated Objet Manufacturing	-Polymeric film; -Metallic sheet; -Ceramic sheet; -Paper sheet;	Laser Beam	-High surface finish; -Low: material, machine, process cost; -Decubing issues.

2.3 Fused Filament Fabrication

Fused Deposition Modeling is a term coined by Stratays Inc. ©, however, Fused Filament Fabrication (FFF) is the term coined by the open source community. It is a methodology which uses the concept of low melting thermoplastic materials such as, ABS, PLA and PET. Usually the raw materials, which are sold in filament spools, have their temperatures raised during the process, allowing them to flow through a nozzle and being deposited in a flat surface, solidifying, creating a layer and being overlapped by the next, forming a printed part as shown in Figure 2.6. The properties of this printed part will strongly depend on the layer height and width, the infill percentage and the temperatures applied.

The principal drawback of this process is the anisotropy of the printed parts. This constitutes a problem for all AM methods since material is being added in a surface already processed. Since FFF has a larger layer height than the other processes, anisotropy becomes a concern. There are several ways of improving the strength of these parts, like the refinement of the printing patterns, the addition of ribs and internal supports, the development of high strength polymers and the development of new composite materials with the application of fibres in the thermoplastic matrix.

The application of distinct types of reinforcements to the process is now being studied. The addition of carbon fibres as structural material leads to great improvement in mechanical properties. Since FFF is the focus of this review, several examples will be shown in forthcoming section.

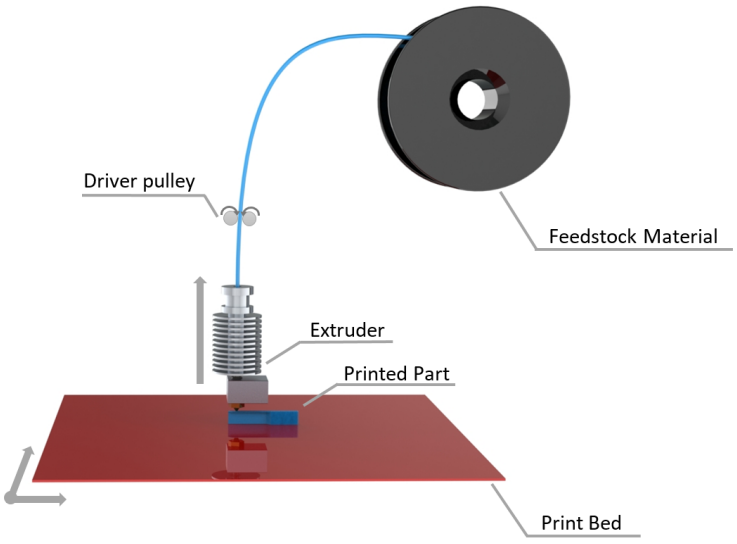


Figure 2.6: Schematic of the FFF process indicating components.

2.3.1 FFF Processing Parameters

From high-end machines to low cost open source equipment, most of the process parameters are the same. Generally, high-end equipments allow partial control of these properties, ensuring the equipment correct functioning, being limited to proprietary software and feedstock. Fully customizable slicing softwares are always associated with low cost/personal machines, where even the hardware can be modified in order to accommodate these characteristics. These process parameters enable the user to produce completely solid or internally patterned with low infill percentages parts, thus varying structural properties, surface quality, amount of used material and process time. The main parameters that will define the part properties are the nozzle diameter, build orientation, job temperatures, layer height, raster width and angle, infill type, percentage and air gaps, among others. For each print job, these parameters are reviewed accordingly with the main purpose of the part.

Summing up, a FFF printing job entails a large set of machine and process-related variables. These variables affect the properties of the final part, especially regarding its dimensional accuracy, surface roughness and mechanical properties. The comprehension of process parameters and the understanding of the process working principles is essential for the production of parts with the desired quality and performance. For a better comprehension of the parameters and their implications on the type of print check Figure 2.7.

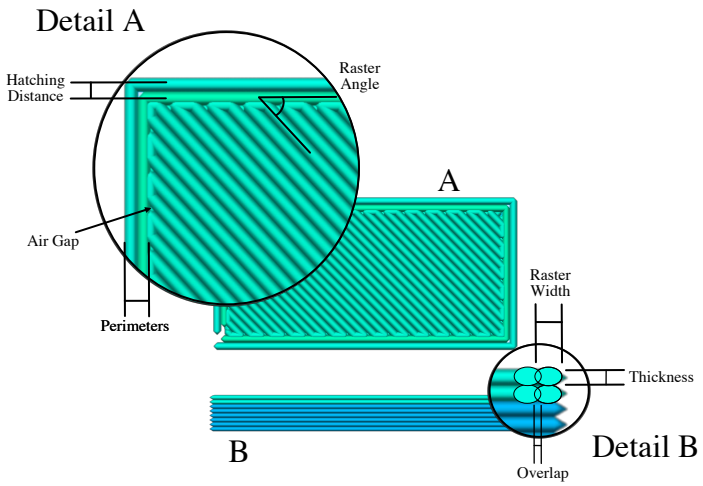


Figure 2.7: FDM process scheme.

Nozzle Diameter: This parameter is initially defined on the hardware, which defines the material flow that will be deposed. Thus, nozzle diameter (from 0.4 to 1 mm) determines the minimum and maximum values for layer height.

Temperatures: There are several heating points that can be defined for the process to operate correctly. Extrusion temperature is a primary value to set and depends on the type of material

that is being used. The heated bed temperature is also defined according to the material, however, some easily processable materials do not require this type of feature. Lastly, more advanced machines use a heated chamber, enabling improved thermal stability and facilitates the usage of high performance materials.

Printing Speeds: The defined speed defines the print quality. If these values are too high, the printed part tend to loose accuracy. When deposing material, excessive velocities will cause adhesion problems between layers and a possible lack of material. A ratio between the movement and deposition speed is always defined, varying this ratio will deteriorate the print.

Layer Height: Layer height parameter defines the thickness for each layer in which the part is divided. This parameter is defined by the incremental gap in Z axis during the process and it can be as small or as big as the printer hardware can allow. In addition, a correlation defines that the layer thickness must be lower than 80% of the nozzle diameter [Carneiro et al., 2015]. Thus, layer height is one of the most influential parameters on the printing time, defining also the level of detail. Using a smaller layer height, a higher definition/resolution is achieved. In addition, mechanical properties are also related with layer thickness, since a higher number of layers will lead to more interfaces, raising anisotropy values, and by increasing the number of layers, more heating and cooling cycles used, leading to more residual stress accumulation [Sood et al., 2010]. Tensile and flexural properties show an inverse relationship with the variation of layer thickness [Narang and Chhabra, 2017].

Number of Perimeters: The number of perimeters delineates how many passes the part will have, creating the contour. Increasing the number of perimeters creates a stronger part.

Raster Width: Raster is the path that the extruder defines while deposing material. The raster width is determined by nozzle diameter and respective extrusion flow linked to the movement speed and layer height. As seen in Figure 2.7, the raster is not perfectly circular but a flattened circle.

Raster Angle: This angle is referred as the entrance angle on the part in relation to the X axis. Typical values are 0/90° and 45/-45°, yet these are customizable values.

Infill Pattern: This pattern defines the type of infill that is used in the interior, top and bottom of the part; this parameter depends on the selected slicing software and pattern geometry.

Infill Percentage: Infill percentage defines the quantity of material deposed in the interior of the part. A low percentage infill will originate bigger air gaps in the part, in contrast, the best tensile strength is obtained with high infill percentage values [Narang and Chhabra, 2017].

Hatching space: Parameter defined by the distance between two deposed lines, the smaller the hatching space, the fewer gaps might occur and higher the quantity of material that can be deposed in the same area.

Overlapping: Overlapping parameter defines the percentage of filament merged between the perimeters and infill or between adjacent raster paths.

Air Gaps: Air gaps are spaces with material that should not be present. During the printing process three types of air gaps can occur: The raster to raster air gap is created between adjacent paths when there is not enough material; the perimeter to raster air gap is created when the overlapping between perimeters and infill is low. Finally, the sparse fill air gap is created with infill low percentages [Masood, 2014].

2.3.2 FFF parts qualitative features

The above mentioned parameters contemplate only one set of variables that influence the obtained print quality. Figure 2.8 presents the input variables in FFF process. Optimizing the conjugation of these parameters plays an important role in improving surface roughness, dimensional accuracy, mechanical properties, material behaviour and job times. An extensive research has been done in the field of process optimization, paying high importance to the study of the improvement in surface roughness, and in consequence, dimensional accuracy and mechanical properties. Some of these studies are described in the following section.

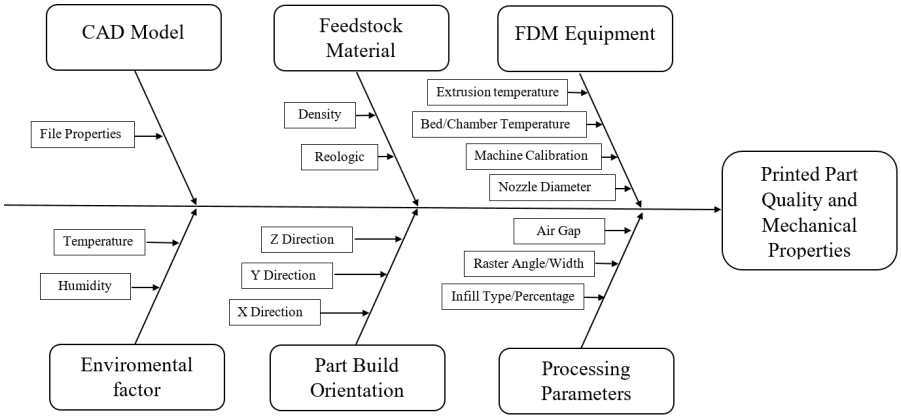


Figure 2.8: FFF cause effect diagram adapted from [Mohamed et al., 2015].

Surface roughness: Surface roughness of FFF printed parts has been extensively studied by several authors. Anitha et al. [2001] analysed the influence of layer thickness, raster width and speed deposition on the surface roughness using the Taguchi method and analysis of variance. The study revealed that the most influential factor on this test was the layer thickness, comparing it with the speed and raster width. Another conclusion was withdrawn, indicating that there is

an inverse relation between layer thickness and the surface roughness. A similar study has been conducted by Nancharaiah et al. [2010], analysing the same input parameters, but also including, the air gap influence. It was proven that surface roughness tends to improve using thinner layers and reducing air gaps by decreasing the voids between the layers. Horvath et al. [2007] included extrusion temperature and infill type of pattern in addition to layer thickness and proved that the last parameter is the most influential in the surface roughness and it was also verified that high temperatures lead to better finishing.

Dimensional accuracy: Santana et al. [2017] studied the influence of layer thickness, infill density, infill/perimeter speeds, as well as extrusion temperature and extrusion multiplier on the part dimensional accuracy. The conclusion, drawn via Taguchi method and analysis of variance (ANOVA), was that infill density and extrusion multiplier are the most influential factors and those the most responsible for distortions along the printed samples. Another approach was used by Sood et al. [2009], analysing the influence of part orientation, raster width, layer thickness, air gap and raster angle on dimensional accuracy. Also using Taguchi method, it was found that sample shrinkage was the most critical defect, with the sample being small in every direction. Ideal parameters were developed according to statistical analysis. Peng et al. [2014] applied the same method in an equipment with fuzzy logic, analysing parameters as raster width, layer thickness, infill speeds and printing speeds, concluding that the most influential factor was raster width, followed by printing speed, layer thickness and infill speeds. In conclusion, dimensional accuracy is an output directly related to the feedstock and its prediction for different types of material is difficult without their full knowledge.

Mechanical Properties: Mechanical properties are inarguably one of FFF main weaknesses and one of the most researched topics. Ahn et al. [2002] studied the anisotropy found in ABS printed parts considering the raster orientation, air gap, raster width, colour and temperature in a factorial DOE approach and compared it with the values from injected samples. It was found that typical tensile strength ranged between 65 and 72 % of the injected parts and the compressive strength ranged from 80 to 90%. Chin Ang et al. [2006] also researched about mechanical properties, surface roughness and dimension accuracy optimization through Taguchi Method and analysis of variance ANOVA with the goal of combining the best properties. Air gap, raster width, build orientation, build pattern and layer thickness were considered the variables in this study, and it was stated that the air gap had the most effect on porosity and mechanical properties. Some of the variables originating the low mechanical properties were studied and a regressive model was used to improve these values. Masood et al. [2010] analysed FFF process parameters as infill percentage, raster width and raster angle effects on the tensile properties of Polycarbonate (PC). It was concluded that the highest value of tensile strength was obtained for samples with 100% infill (solid), and a raster width of 0.6064 mm at 45°. The authors also concluded that mechanical properties of a fully dense printed sample corresponded roughly to 70 to 80% of the injection moulded test part.

2.3.3 Filament interface wettability

FFF parts can differ considerably in quality, due to operational parameters, machine specifications, material properties and part geometry, as previously mentioned. The output is evaluated in terms of dimensional accuracy, mechanical properties and surface finish, which is mainly influenced by the extrusion temperatures [Bellehumeur and Li, 2004, Ferreira and Alves, 2017]. This parameter is what defines the junction among adjacent layers. Bonding formation in FFF process is controlled by the thermal energy of the semi-molten material, and printed parts are considered as anisotropic purely polymeric structures, as seen in Figure 2.9.

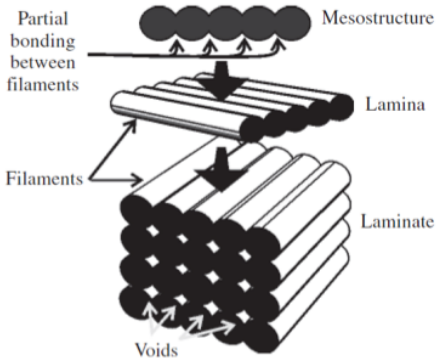


Figure 2.9: FFF prototype bonding structure [Bellehumeur and Li, 2004].

Bond quality among individual deposed filaments or beads relies on the neck growth formed in contiguous filaments and on the molecular connection at interface, considered as interface wetting. This bond formation can be compared to polymer welding, which at a macro level, and properties of each lamina functions as the properties of the filaments, the quality of the bonds among beads, and void density at micro level [Bellehumeur and Li, 2004].

Bellehumeur and Li [2004] studied the bond formation dynamics of sintering data of ABS filaments. The bond formation among polymer filaments in FFF process can be represented according to Figure 2.10.

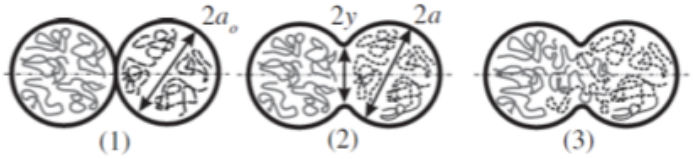


Figure 2.10: Bond formation process between two beads: (1) surface contacting, (2) neck growth and (3) inter-facial diffusion and final randomization.

2.3.4 Thermal residual stresses

To understand some of the FFF process problematic, it is important to consider the physical phenomena behind it. This technology is dependant of several types on parameters that create a decrease in performance if not addressed properly. The induced thermal gradient caused by continuously depose material is directly linked to thermal stress accumulation resulting in the final part lack of dimensional accuracy and warping effect [Zhang and Chou, 2008]. During the process, the part reheats and cools down, due to material deposition on the upper layer, as illustrated in Figure 2.11. These consequent cycles are critical for the bonds created on the adjacent deposition lines, since their bonding is as good as the filament wettability. Higher temperatures and lower printing speeds lead to a better material dispersion of the deposed line, granting improved adhesion, while at lower temperatures, the molecular mobility is limited. Thus, the temperature must be fine tuned to promote better interlayer bonding formation. For semi-crystalline polymers, this bond formation is interrupted as soon as the crystallization takes place, since the viscosity is increased [Brenken et al., 2018].

In the cooling stage, the part solicitation is initiated by convective, radiative and conductive losses to the surrounding areas (chamber, bed and other areas of the part, respectively), being polymer conductivity a factor to be considered. At this point, the thermal expansion coefficient dictates the material shrinkage and internal stresses start to build up, conjugating material stiffness and constraints caused by newly formed bonds. For semi-crystalline polymers, the changes in the behaviour promote higher internal stress levels and consequently warping/deformations [Brenken et al., 2018]. In fully dense parts the number of thermal cycles is higher and consequent distortions are more pronounced.

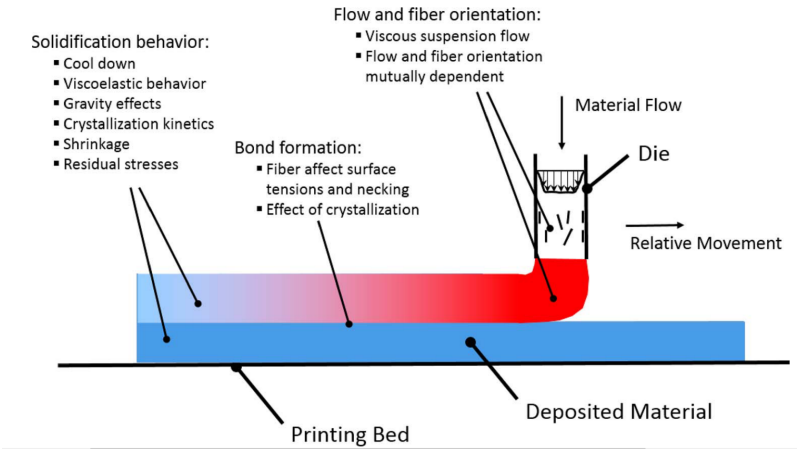


Figure 2.11: FFF process physical phenomena representation [Brenken et al., 2018].

2.3.5 Filament production process

The process of developing specific formulations for FFF has become a big concern in polymeric industries. Initially, the available material on the most expensive machines was ABS, however the industry has evolved and with the open-source movement came along the usage of PLA (Eco friendly - made from corn). This material presents great stability during and after printing. Currently, there is a full range of polymers and co-polymers specially developed for this specific usage, such as Polycarbonate (PC), Polyphenylsulfone (PPSU), Polyetherimide (PEI), Polyvinyl acetate (PVA), among others [Mirón et al., 2017].

Nowadays, feedstock in filament form can be found in several markets, with different specifications, such as colour, diameters (mostly 1.75 and 3 mm), pure or filled with any kind of fibres or particulates, such as specifically developed materials for the creation of medical prostheses or even the materials for pharmaceutical industry, filaments composed of pharmaceutical grade materials [Ronca et al., 2016, Melocchi et al., 2016].

The filament, as it is known, starts its life as pellets. Then, depending on the formulation of polymer that is defined by the producer, and the polymer will respond to the extrusion process with certain properties. There are several types and dimensions extruders for polymers, for example: if the production is dedicated to short carbon fibre (SCF) reinforced polymer, a twin screw extruder is required to create homogeneity and spread the fibres uniformly; if the goal is to mass produce simple pure polymer, industrial 10 meter extruders are recommended.

Carneiro et al. [2015] studied the production of PP filament from two different pellet grades: ISPLEN PP 040 C1E - Repsol (pure) and POLIFOR L6 GF/30 NATURALE - SOFTER (reinforced with 30wt% Glass Fibre (GF)). For both materials numerous extrusion trials were performed with different parameters in order to obtain a 1.75 mm diameter filament. The extrusion setup in Figure 2.12 used forced air instead of water to cool the extruding reservoir in order to prevent voids in the material, an oven at 30°C and a pulling system to grant the correct diameter.

Mirón et al. [2017] used a Filabot^{TM} to produce PLA filament and started by selecting a nozzle that allowed the extrusion of 2.85 mm filament. The temperature was defined in a range from 175 to 195°C and several extrusion speeds were tested, obtaining different outcomes. Slow speed resulted in high diameter, while fast speeds created thin filaments with blisters. The correct configuration of these parameters as previously mentioned, defines the quality of the extruded filament.

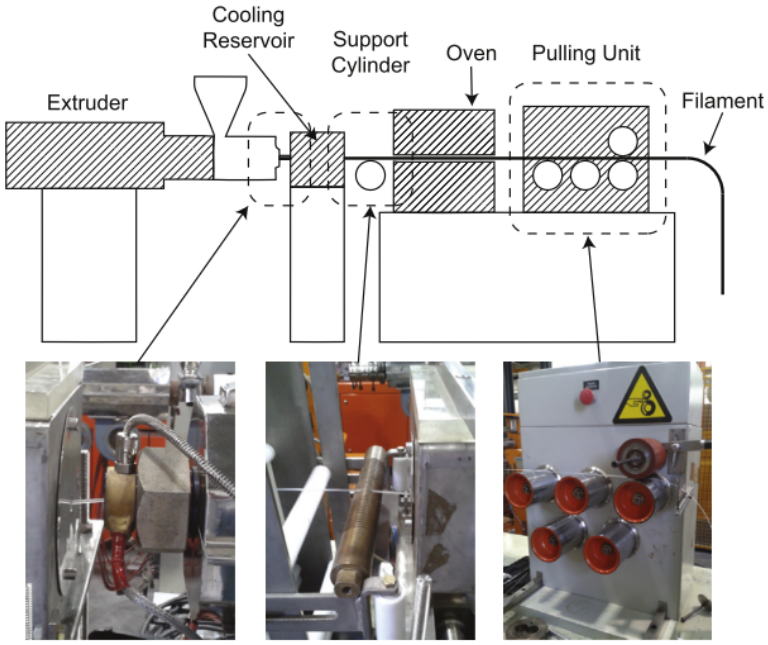


Figure 2.12: General view of extrusion line used in the production of filaments [Carneiro et al., 2015].

2.3.6 Polymers

Polymeric materials can be defined as natural or synthetic, depending on their origin. Synthetic polymers are most common, however, their abundance raises ambiental concerns, since they are petroleum-based materials [Buggy, 2016]. Polymers are composed by a macromolecular union of small units called monomers connected through covalent bonds in which negatively charged electrons are shared. This polarity affects the attraction between the molecular chain, thus affecting the polymer structure [McKeen, 2017]. Polymers can be divided into three distinct classes which reflect their molecular structure: thermoplastics, thermosetting and elastomeric polymers. Since this work is focused on the thermoplastic material group of materials, the remaining types are not analysed with the same depth, however a brief explanation of its internal structure is presented.

Thermoplastic materials represent a growing portion of the composite market. Different from the thermosetting cross-linked structure, thermoplastics have their properties defined by their monomers (repeating units) and their molecular weight. The high molecular concentration and level of disorder in amorphous thermoplastics, act similarly to cross-links and semi-crystalline polymers which have the same molecular concentration with high degree of orientation. Heating amorphous polymers will cause the molecular chains to untangle and relax, changing the material phase from solid to a viscous liquid state. This relaxation will occur when the glass transition point is reached (or above it). Semi-crystalline polymers behave differently to temperature: when glass transition temperature is reached, the remaining amorphous chains start to move until the melting point is reached. Then, the remaining crystalline phase starts to melt originating a viscous liquid. Depending on the conditions, the material is processed and solidified. Both amorphous and

semi-crystalline polymers may have anisotropic properties. In other words, amorphous polymers tend to stretch and align the molecular chains according to the melt flow direction, while semi-crystalline polymers tend to develop laminar units in the flow direction [Hull and Clyne, 1996, da Silva et al., 2013].

Thermosetting polymers are initially in liquid state, which is converted to solid via a chemical reaction, promoted by a catalyst or hardener, creating a three-dimensional network. Mechanical properties are directly related to its reaction, depending on the number of chemical elements, strength and length of their bonds. The curing process can be improved by adding chemicals at room temperatures, however, increasing the temperature in different stages results in stronger cross-linking and subsequently enhanced mechanical properties. Thermosetting resins have a different behaviour when compared to thermoplastic materials. Due to its chemical structure and curing reaction, thermosettings are brittle, while thermoplastics can sustain high levels of plastic deformation plus having the possibility of being reprocessed. When comparing materials within each class, epoxies are generally tougher than polyesters or vinyl-esters [Hull and Clyne, 1996, da Silva et al., 2013]. Due to its inability to be reprocessed, thermosetting materials are not used in FFF process.

Elastomer are amorphous polymers that combine the thermo-plasticity and rubber behaviour. With long polymeric chains, elastomers present a -50 to 180°C T_g. This type of polymers present a high elastic deformation capacity, which is a consequence of its macromolecular reconformation without breaking the covalent bonds [da Silva et al., 2013, V. and Canevarolo, 2002, Melo, 2019].

2.3.6.1 Transition temperatures

The molecular mobility level of a polymer chain determines whether the material will be fragile, rubbery or a viscous fluid. Thus, internal mobility is what dictates the material state and it is induced by temperature. Polymer processing is generally done at higher temperatures at its viscous fluid behaviour and it is commonly used at flexible or rigid state. This variability is important creating a wide range of choice.

Polymer's thermal behaviour is highly complex and differs from materials that have melting and evaporation points. Since polymers are composed by different length chains, there is no constant melting temperature but an interval, which can range from 2 to 10 °C. At higher temperatures polymers generally tend to decompose rather than boil, being denominated as the degradation temperature instead of boiling points. Considering the molecular mobility, which is defined in function of how strong cohesive forces are between the chains, thermal transitions depend also on the structure of the polymer, thus during an heating cycle two important temperature marks where polymers suffer major alterations are identified [Ebewele, 2000, V. and Canevarolo, 2002, Melo, 2019]:

Glass transition temperature (T_g): represents the average value from the amorphous phase of the material start to gain mobility. Bellow this temperature gap, the polymer does not possesses enough internal energy to allow the movement of a chain regarding the others. For semi crystalline

polymers, this type of changes only occurs for the amorphous part of the material. Through specific volume variation it is possible to evaluate the crystalline structure, evaluating the point characteristics. Figure 2.13 depicts both amorphous (ABCD) and crystalline (ABEF) polymers specific volume-temperature behaviour. Amorphous and semi-crystalline regions (D and F, respectively) present a sudden increase in the expansion to a higher level as the T_g is reached [Ebewele, 2000]. From this point on, both type of materials change from hard and solid to a soft rubbery state, which will be maintained onwards for amorphous materials until degradation, or until the melting point for the semi-crystalline polymers.

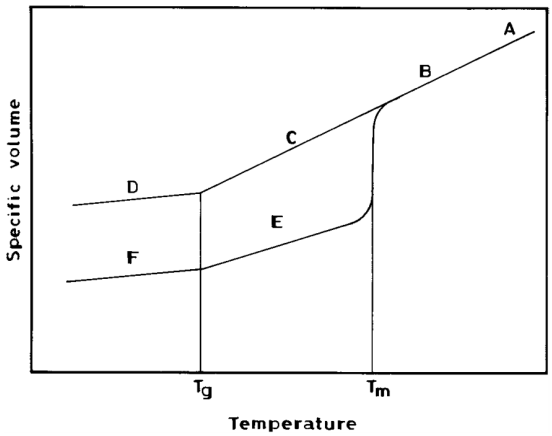


Figure 2.13: Specific volume–temperature curves for a semi-crystalline and amorphous polymers during heating: A-Liquid section, B-viscous liquid with elasticity, C-rubbery region, D-glassy section, E-crystallites in a rubbery matrix and F-crystallites in a glassy matrix [Ebewele, 2000]

Crystalline melting temperature (T_m): is the interval during the heating of a semi-crystalline polymer where it starts to melt. This type of thermoplastics is composed by distinct size crystals causing different effects, therefore T_m is not a specific value but an average. As presented in Figure 2.13, the transition from E to B, shows the abrupt change where the melting occurs, and the material starts to behave like viscous fluid since intermolecular bonds were broken increasing their mobility and creating a sudden rise in the specific volume [Ebewele, 2000].

Crystallization temperature (T_c): is based on the temperature gap that occurs during the cooling phase of semi-crystalline polymers as seen in Figure 2.14 C region. Throughout this phase, the spacial alignment of the molecule chains takes place, in which fold regions are created, called lamellae [V. and Canevarolo, 2002].

Through Figure 2.14 it is possible to observe the changes in specific volume that occur with the temperature during the heating phase and the cooling of a semi-crystalline thermoplastic. Each polymer characteristic temperatures correspond to a variation either during cooling or heating cycle, thus it is possible to conclude that T_g is lower than T_c and both are lower than T_m.

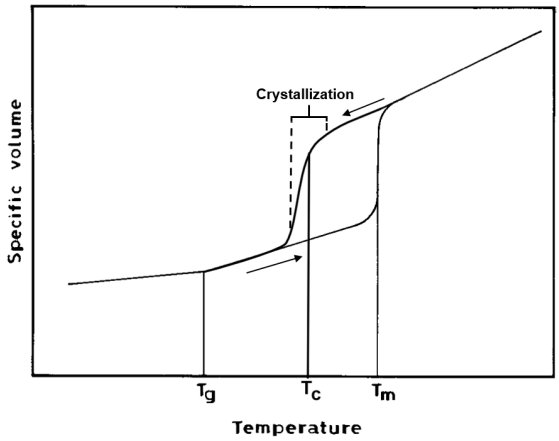


Figure 2.14: Specific volume-temperature curve for semi-crystalline polymer during heating and cooling, indicating crystallization gap and inflection curve, defining T_c [V. and Canevarolo, 2002].

2.3.6.2 Amorphous or Crystalline

In a solid state, a polymer presents a crystalline or amorphous structure depending on how their molecular chains are organized. During the cooling phase, molecules tend to join closely creating a solid form. For some cases, these molecular chains are folded and joined in a pattern, creating a crystalline polymer. Considering that some of these molecules are too long, it is not possible for them to fit in the same disposition, creating an amorphous part [V. and Canevarolo, 2002]. The degree of crystallinity indicates the percentage of the polymer that presents this highly oriented structure. In reality, polymers are never 100% crystalline, being its structure formed by a combination of crystals randomly disposed in the amorphous phase, commonly called as semi-crystalline polymers. In order to crystallization occurs during the cooling, it is demanded that these chains possess enough time so they can acquire the ordered configuration [William D. Callister, 2001, Chanda, 2006, Melo, 2019]. Amorphous polymers are composed by chains that, given the same circumstances, are not capable of the same level of arrangement as the crystalline polymers. This type of material is defined by a short-range repeating units.

In essence, it is possible to sustain that crystalline polymers are characterized by a long range of orderly disposed molecular chains, while amorphous polymers present a short range order of repeating units [Ebewele, 2000].

How is the level of crystallinity important for the FFF process? Before the extrusion, material is kept in an area (heating block) at a temperature over its T_m, and, at the moment the material leaves the extruder, its temperature has already decreased considerably. The presence of a heating chamber, a heated bed or even both are important to prevent rapid crystallization, allowing the chains to properly organize into a crystal structure. For the most part, higher crystallinity polymers present increased density and toughness but inferior strain at break and impact strength [V. and Canevarolo, 2002].

2.3.6.3 Thermal testing

X-Ray Diffraction (XRD): is a technique used to determine the crystalline phases present in a material as well as their chemical composition. This test is performed by focusing an x-ray beam at the sample, causing its diffraction. The diffraction pattern caused the scattering and beam separation indicates the sample's crystalline structure [Klug and Alexander, 1954].

Differential scanning calorimetry (DSC): is one of the most widely used techniques for polymer characterization. In essence this technique determines the amount of heat absorbed by a sample by comparing it with the reference, allowing to identify thermal transition points [Guo, 2016]. DSC testing equipment is constituted by two pans, heated in a measuring area. One of the pans holds the sample material while the second is usually empty, therefore used as a reference. The test consists in the heating or cooling of the sample at a controlled rate of typically 10°C/min, being both sample and control monitored [Mathematisch-naturwissenschaftliche Fakult, 2015]. When a significant temperature variation occurs for the sample, and by comparison with the reference material, it is possible to identify a microstructural transformation. Thus, through this type of analysis it is possible to identify glass transition temperatures (T_g), crystallization temperatures (T_c), melting temperatures (T_m), fusion enthalpy (ΔH_f), crystallization enthalpy (ΔH_c), and consequently the crystallinity percentage (X_c).

Thermogravimetric analysis (TGA): is a widely used technique that measures the rate of change in the mass as the temperature increases along the time. With this type of testing it is possible to identify at which temperature the polymer starts to degrade, as well as its maximum degradation temperature. Therefore, TGA is often used to evaluate the material's thermal stability in a desired range of temperatures. Beyond this, TGA often is also used to evaluate the filler content in polymeric materials. The presence of fillers in a matrix is detectable due to its different degradation temperatures [W.J. Sichina, 2011].

Melt flow index (MFI): is the test that indicates a thermoplastic polymer ability of flow above melting temperature during ten minutes. In order to perform a MFI test, the material is properly stacked inside the barrel in which a piston introduces a force after a pre-heating temperature is reached, which corresponds to the specific thermoplastic. The amount of material that is extruded through the die during those ten minutes corresponds to the thermoplastic MFI. Materials with higher MFI, have lower viscosity at that pre-determined temperature [Singh et al., 2017a].

Rheology: is the study of the flow behaviour of a material, normally in a fluid state. The flow of a material is defined by the shear stress and strain rate, which are calculated accordingly to the torque and flow rate measurements. Several types of flow behaviour are defined depending on its response. A fluid with a Newtonian behaviour presents a linear relationship between stress and strain. A plastic behaviour is presented when the flow of the fluid is initiated over some level of stress, presenting a linear relationship of stress/strain once it starts to move. Pseudoplastic

behaviour is when the fluid viscosity decreases as the strain is increased [Struble and Ji, 2001]. Polymers present a non-Newtonian behaviour in the pseudoplastic class and their properties depend of its strain rate, molecular weight, crystalline structure and additive presence [Gupta, 2000].

2.3.6.4 Polymers in FFF

Since the boom of FFF machines in the early years two thousand, the technology has been evolving, leading to two distinguished categories [Wohlers et al., 2017]. Low cost machines, which have restricted capabilities, are bound to use the common usage polymers, materials with low melting point (mostly bellow 300°C), low shrinkage rate after print, materials that are easy processed and, most importantly, are cheap. Adding to this, the fact that they are built with low end+ materials, leads to lack of accuracy during the printing process. This type of machine is mostly used by hobbyists and enthusiasts, gaining a vast consumer market due to the open source community.

On the other side of the spectrum are the industrial machines. Beyond the high quality, high mechanical accuracy and volume, this type of more expensive equipments allows the usage of engineering and high performance polymers, which have high melting and processing point, and increased mechanical properties. These materials are highly attractive to the industry, however the price per kg increases with its capabilities (mechanical and thermal properties).

FFF is vastly accepted as a promising technology in industrial sector, creating the opportunity for highly customised parts with low production and development time. In addition, the process is slowly moving from the printed prototype part to the final final part as the technology evolves. Thermoplastics can be classified in three different categories beyond its state of amorphous or semi-crystalline as seen in Figure 2.15[10]. The following section describes the most commonly used polymers in the FFF process.

Commodity polymers

Polylactic Acid (PLA): It is arguably the most used polymer in personal FFF machines, with a Young's Modulus of 2.8 GPa and tensile strength of 60 MPa; it is a semi-crystalline polymer, with a melting point between 164 to 178°C. Besides, PLA is a biodegradable material which derivates from corn or maize with very low productive emissions. This material has high mechanical stability and good tensile strength, with low impact strength, low maximum service and heat deflection temperatures. Is easy processable (injection, moulding and thermoforming) and machinable. Beyond filaments for FFF, PLA is used for food packaging, cold drink cups, electronic cases, medical implants and home ware [Wypych, 2012, Design, 2018].

Acrylonitrile Butadiene Styrene (ABS): Was one of the first materials to be used in the FFF process, it has an average Young's Modulus of 2.3 GPa and average tensile strength of 45 MPa.

[10] http://polymers.com.au/thermoplastics/

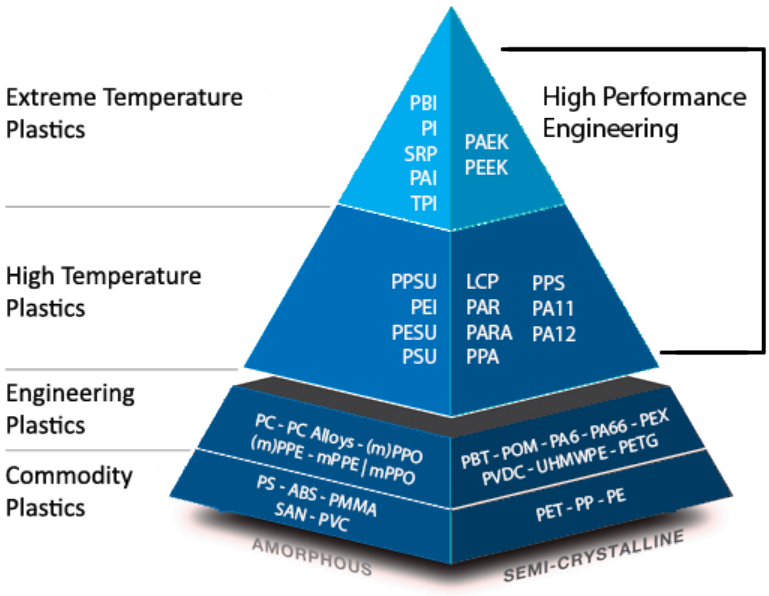


Figure 2.15: Polymer division pyramid.

ABS is an amorphous polymer with a glass transition temperature from 102 to 110°C. This material is easily processable and has a great dimensional stability with good impact resistance, excellent aesthetic properties and it is a low cost material. Usually used for automotive instrument panels, pipe-fittings, for small housing appliances and refrigerator liners, among others [Wypych, 2012, Design, 2018].

Poly (Ethylene Terephthalate)-Glycol (PETG): A variant of PET with added glycol. PETG can be processed by extrusion, injection moulding and blow moulding, among others. It is vastly used for high series/volume production of commercial and consumer applications. The added glycol creates a non-crystallizing, amorphous copolymer [Wypych, 2012, Design, 2018, Dupaix and Boyce, 2005].

Polypropylene (PP): Is simply described as a low cost polymer with good mechanical capabilities and an enormous diversity of applications such as textile industry, domestic appliances, food packaging and automotive industry. PP has good mechanical, thermal, electrical performance, low water absorption values, good chemical and fatigue resistance properties. Nonetheless, this material is particularly brittle at sub-zero temperatures, has high creep, mould shrinkage, thermal expansion, besides poor scratch resistance and toughness. Young's modulus averages 1.4 GPa and tensile strength 33 MPa, proving it presents less interesting properties than the other commodity polymers [Wypych, 2012, Design, 2018, Shen, 2017].

Engineering polymers

Polyamide (PA): Is one of the biggest groups of engineering polymers. The classic PA6 has 1.7 GPa and 70 MPa of average Young's Modulus and tensile strength respectively. This is a semi-crystalline polymer with a melting point between 227 and 238°C, highly sensitive to moisture, causing dimensional and mechanical properties instability. Also, it is not very resistant to strong acids or alkalis, it has poor UV resistance and a relatively high processing temperature. This material has low friction coefficient with good properties to wear, fatigue and they are easily machinable. Moreover, they are frequently is reinforced with glass fibre, to improve its mechanical properties. It is usually used for safety helmet parts, washers, gears, engine and motor parts.

Polycarbonate (PC): Polycarbonate is, after PA, the second most produced engineering polymer due to its high impact resistance, stiffness and strength across a wide temperature range (-150 to 135°C), high transparency and capability of cold bending. However, it is notch sensitive with low long term fatigue strength, presents limited abrasive resistance and it is vulnerable to stress cracking. PC is tougher than ABS and it is used in a vast application field, such as aero-spacial, automotive and medical components. Stratasys filament [Stratasys] presents a Young's modulus of 2.28 GPa and tensile strength of 68 MPa [Wypych, 2012, Design, 2018, Shen, 2017].

High performance polymers

High Performance Polymers (HPPs) are classified by their capacity to maintain its characteristics when submitted to severe conditions, such as chemical environments, high temperature exposure and high mechanical solicitations. With these characteristics, HPPs can be the solution for one of FFF process main flaw, considering that this method is occasionally disregarded due to its low properties. However, these materials are much more expensive and difficult to process than their alternatives, due to their high melting points.

Polyetheretherketone (PEEK): Is a thermoplastic with a Young's Modulus of 3.6 GPa and tensile strength of 170 MPa. This semi-crystalline polymer has a melting point between 350 and 370°C and is highly resistant to high temperatures and chemical environments. The difficult processability and high price are restrictions to its usage; however this is a very easily machinable material. It is commonly applied in medical implants, aeronautics structural parts, and as matrix in fibre pre-pregs [Wypych, 2012, Design, 2018].

Polyetherimide (PEI): Has a Young's Modulus of 3.0 GPa and tensile strength of 96 MPa. It is an amorphous polymer, with a glass transition temperature from 209 to 249°C, high stiffness, dimensional stability and creep resistance. It is flame retardant and resistant to chemical attacks. PEI is cheaper than PEEK, but still requires high temperature and has a high processability cost. It is usually is used in electrical connectors, lamp housings, and microwave cookware [Wypych, 2012, Design, 2018, Shen, 2017].

Polysulfone (PSU): It is an amorphous polymer, with a glass transition temperature from 185 to 190°C and possesses a Young's Modulus of 2.5 GPa and tensile strength of 70 MPa. It has a high degree of transparency, excellent resistance to creep, good stress crack resistance, good electrical insulation properties, poor UV resistance and low impact strength when compared to PC. PEI is easy to machine and to bond.

Polyphenylene Sulfide (PPS): It has a Young's modulus of 10.6 GPa and tensile strength of 64.4 MPa; it is a semi-crystalline polymer, with a melting point from 275 to 285°C. This polymer has high resistance to corrosion to organic solvents, bleaches and strong bases, high dimensional and thermal stability with service temperature at 220°C. It is also, resistant to abrasion, friction and electrically conductive. However, it has high processing temperature, high cost and brittleness.

Figure 2.16 indicates the distribution temperature range (melting point to degradation) and glass transition point for the most part of polymers used for FFF process. It is possible to understand how high performance thermoplastics require high end hardware, due to high-end processing temperature points [Moreira, 2016].

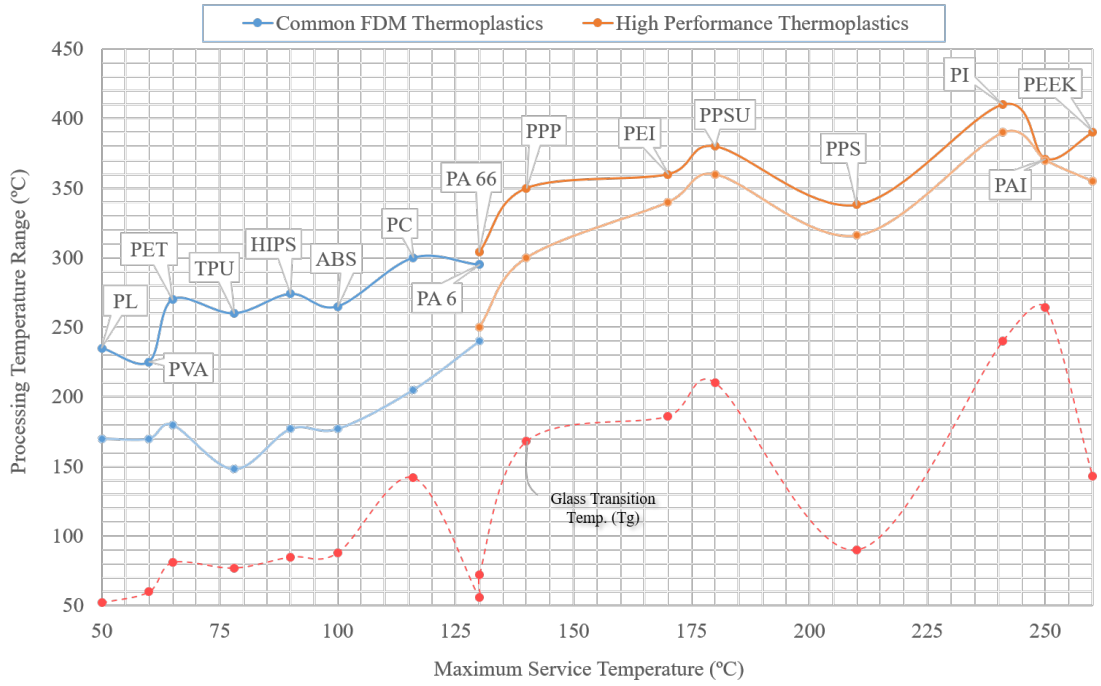


Figure 2.16: Thermoplastics processing temperature range [Moreira, 2016].

2.4 Composite Additive Manufacturing

Currently, polymers are the major base materials used in AM process due to their low processing temperature, low cost and easy processing. Despite these are advantages, their mechanical properties are disregarded for many applications. Along the evolution observed throughout the years, new material formulations, new hardware, and even new techniques have been developed, creating new opportunities for the usage of reinforcements. Currently, beyond the deposition of fused polymers type production method, there are a number of distinct possibilities considering the incorporation of reinforcements in their original feedstock to improve the mechanical performance. Short fibres, particles or even pre-pregs are considered in distinct AM technology type depending on the fabrication methodology. This section presents an overview of some additive techniques, beyond FFF, that have been used to create fibre reinforced parts.

Powder Printing (3DP)

3D printing (3DP) process is a technology based on the usage of powders and liquid binders. The powder is initially spread and compressed in a building platform, and then a moving inkjet creates an internal pattern and silhouette in the plane. The amount of binder as well as the velocity at which it is deposited is a critical factor for the part initial resistance. After this step, the process is repeated until the part is finished [Sachs et al., 1994]. Finally, the part is removed from the bed, and the excess powder is removed. A posterior impregnation is made to promote and increase mechanical properties (Figure 2.17).

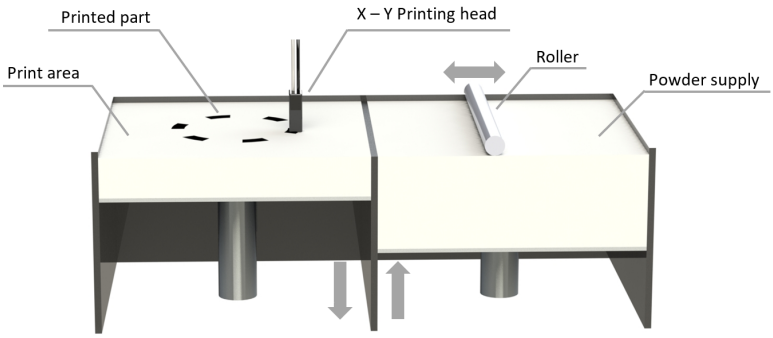


Figure 2.17: Schematic of 3DP process.

Christ et al. [2015] using a ZPrinter 310 investigated the effect of adding increments of 0.5 % up to 2.5%, of 1 to 2 mm fibres to the powder mixture. This blend consisted on a preparation of gypsum and methylcellusose reinforced by four types of fibres: polyacrylonitrile fibre fillers (PAN), polyacrylonitrile short cut fibres (PAN-sc), polyamide fibre fillers and alkali resistant zirconium silicate glass short cut fibres (glass fibre). The equipment did not support a value of fibres

above 2.5% so this is the maximum for reinforcement. The results showed that the green part resistance improved up to 180% for the flexural strength and up to ten times for fracture resistance, compared to the non-reinforced samples. The flexural strength decreased with the introduction of 0.5% of fibre and started to improve from 1% to 1.5%, decreasing afterwards with the following increments, setting 1.5% as the top value for the properties.

Selective Laser Sintering (SLS)

Selective Laser Sintering (SLS) is a technique that requires a similar powder bed setup as the 3DP process. Instead of liquid binder, it uses a laser beam, which scans the area and melts the powder layer upon layer. The printing area is also heated to help the particle fusion, heat dissipation and avoid part distortion. Similar to the previous process, fabrication in SLS does not require support materials since the powder bed is holding the print (Figure 2.18). Since the particles are sintered in the process, a strict range of materials is used, including thermoplastic polymers, ceramics and organic binder. The printing cost is high since a laser is used, which requires high amounts of energy [De Leon et al., 2016].

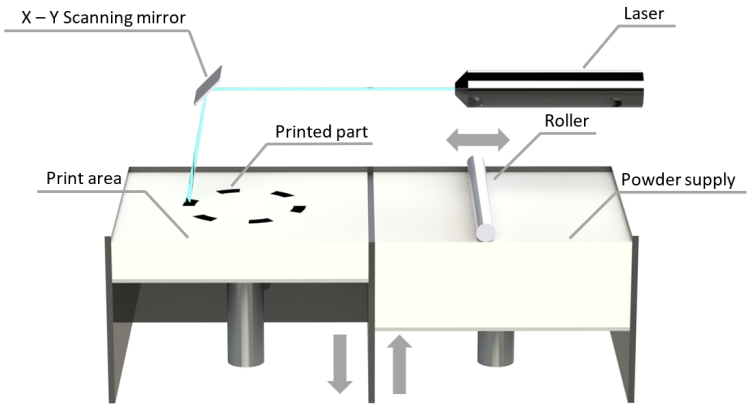


Figure 2.18: Schematic of SLS process.

Jansson and Pejryd [2016] developed a technique using carbon fibre as reinforcement for PA12. The mixture consists in a polymer in powder form with spherical particles, with a granulometry of 50 μm, carbon fibres with 10 μm of diameter, and length varying from 100 to 200 μm. The fibres were chemically treated before the mixture, to improve the adhesion between the fibres and the matrix. In order to investigate the influence of the fibres, three tensile samples for each position starting parallel to X-axis and rotating at 45°increments, were produced in the plane, and in the space. Regarding the comparison between the pure PA12 with the reinforced material, there was an increase of 28% in tensile strength for the x-axis sample and 12% for the y-axis sample.

Stereolithography (SLA)

Stereolithography is a process that uses photo-curable polymers and a controlled UV laser beam to create a desired shape. This UV laser trajectory is controlled by moving mirrors, curing the resin in a tank as its moving through its path. After this layer is cured, the printing platform, which is inside the tank, is moved down, adding a thin layer of resin on top of the previously printed part (Figure 2.19). The materials used in this processes are mainly acrylic and epoxy based resins. Part properties and finishing will depend on the laser power intensity and scanning speed, as well as the post printing cure time. This process has the advantage of printing high volume parts with high resolution; however, this advantage has a high cost, since the resins are expensive, as well as any kind of maintenance.

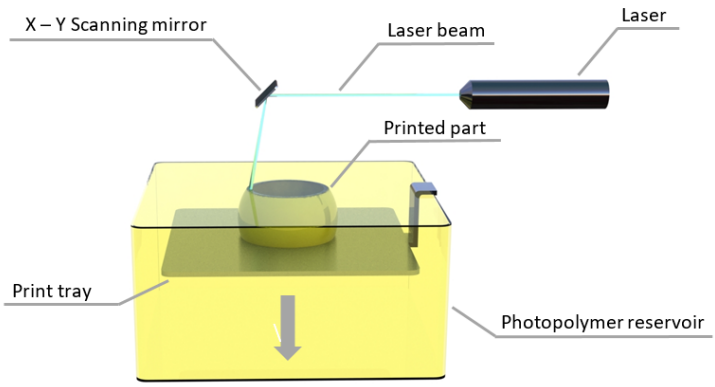


Figure 2.19: Schematic of SLA process

Gupta and Ogale [2002] developed a dual polymerization scheme for curing photo-resin uniformly mixed with carbon fibre reinforced, applied to stereolithography. This dual cure process involved a UV incidence in the first part and posterior thermal treatment, since there was some areas not polymerized due to the carbon fibre tow shadow.

Weng et al. [2016] used organically modified nanofillers loaded into the stereolitography resin. A home-made stereolitography equipment was developed and mechanical testing samples wereLi2016 printed, showing an increase in tensile strength and modulus of 20.6% and 65.1%, not influencing significantly the print quality.

Impossible objects machine (CBAM)

Impossible objects machine or CBAM process (Composite-Based Additive Manufacturing) was patented by Impossible objects, LLC [Swartz et al., 2013]. In this process, composite sheet layers are conducted to the printing area, then a liquid binder is deposed through an inkjet and a polymer powder is added, creating a silhouette of the part. The layers are later manually compressed and

thermally cured in an oven. Afterwards, the excess of the layers is removed through sandblasting. Even though this is a method that is still in prototype phase, this technology promises parts with greater mechanical properties than FFF and other methods that use fibres.

Continuous Composites 3D (CC3D)

Continuous Composites LLC developed a process of deposing continuous fibres embedded in photo-curable resin [Kenneth, 2014]. This machine uses a robotic arm granting six degrees of freedom (Figure 2.20a) and the printing head deposes continuous aramid, glass, carbon fibres and even copper, nichrome wires and fibre optics embedded in an UV-curable resin as binding agent achieving up to 60% vol. (Figure 2.20b). An UV light cures the material at the point of the "extruder" allowing for high-speed printing with a complex shell of curved geometries composites without the need for moulding surfaces or autoclave curing [GARDINER, 2018].

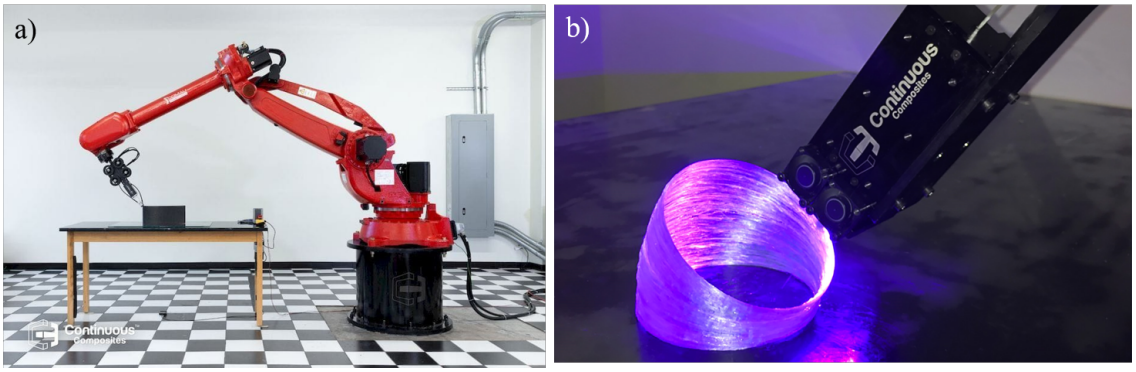


Figure 2.20: Continuous Composite Technology Kenneth [2014].

+LAB

A not significantly different concept from the previous one, the +LAB ATROPOS from Politecnico di Milano, (Figure 2.21), patented by Marinella Levi, Gabriele Natale [2015], promotes the same axial freedom and ability to create parts with similar photo-curable resin matrix and reinforcement. In a press release, the company stated that they are working to expand the reinforcement portfolio from NiTi to natural fibres such as bamboo [Politecnico Milano 1893, 2014].

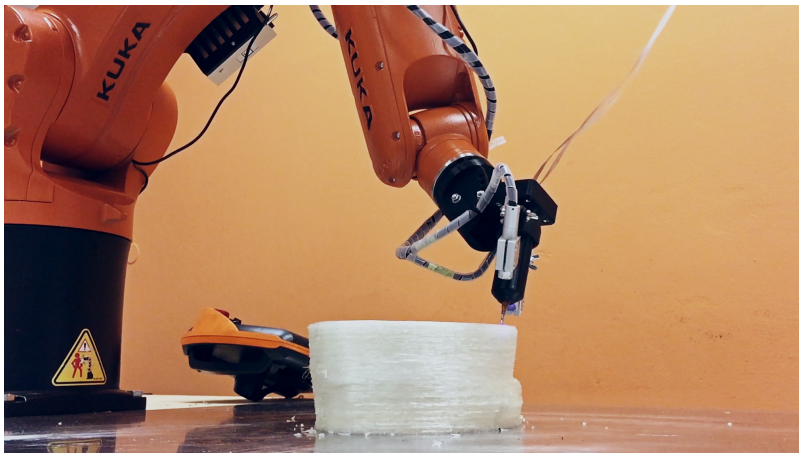


Figure 2.21: ATROPOS in mid process [Politecnico Milano 1893, 2014].

A method and apparatus for additive manufacturing of three-dimensional objects are disclosed. Two or more materials are extruded simultaneously as a composite, with one material in liquid form and one material in a solid continuous strand completely encased within the liquid material. A means of curing the liquid material after extrusion hardens the composite. A part is constructed using a series of extruded paths. The strand material within the composite contains specific chemical, mechanical, or electrical characteristics that grants the object with enhanced capabilities, that would not possible with only one material [Kenneth, 2014].

Table 2.9 depicts an outline of the commercially available processes that can use composite materials for part fabrication. It contains a synopsis of the main process characteristics, advantages and disadvantages, as well as the type of fibre reinforcement.

Table 2.9: Process characteristics [Guo and Leu, 2013].

Process	Material	Material type	Fiber type	Process Characteristics	Advantages	Disadvantages
FFF	PLA, ABS, NYLON	Filament	Particles, short fibres, nanofibres, continuous fibres	Fusing and deposition of thermoplastic material in consecutive layers through a nozzle	Cheap process and material, versatile and open process	Rough part finish, weak mechanical properties, high anisotropy
3DP	Ceramic	Powder	Nanofibres, particles	Agglutination of ceramic powders by deposition of a liquid binder	Capability of printing in different colors, supports not needed	High cost material, low mechanical properties, usage of post print reinforcement agents.
SLS	Polymeric	Powder	Nanofibres, particles	Agglutination of polymeric powders by laser sintering	High resolution and complexity parts, supports not needed.	High cost material and process, material limitations
SLA	Photopolymer	Liquid resin	Nanofibres, particles	Polymerization of photosensitive resin, through the incidence of the UV light beam in successive layers.	High quality finishing, good mechanical properties	High cost material, slow process, involving cure

Metallic matrix composites

According to Kumar and Kruth [2010] and Kruth et al. [2007] there are two main reasons for the usage of composites in processes such as SLS or SLM. The first reason is to facilitate the SLS process by using a liquid phase sintering mechanism. Kruth et al. [2007] states that in Fe-Cu SLS

process, Cu acts as a melted fluid during the sintering process, binding the Fe powders. In this situation, the added copper does not enhance mechanical properties of the iron alloy but helps to create better conditions for the particle consolidation. Secondarily is the emulation of traditional composites by using metal powders as binding agent and fibres as reinforcements [Kumar and Kruth, 2010]. One example of this second approach was taken by Gu et al. [2014] who studied the influence of the SLM parameters on the mechanical properties of AlSi10Mg matrix reinforced with TiC particles.

2.5 A review on fibre reinforced composite printing via FFF

This information compiled in the following section is presented in review article form as published in Rapid Prototyping Journal [Ferreira et al., 2019a].

FFF is a well-known additive manufacturing technique which consists in the feeding of a thermoplastic material in filament form through an heated die, depositing the material in paths and creating a physical part from a CAD file in a layerwise approach. This is a highly adopted AM technology due to its capabilities to produce complex and customized parts without the need of any production tool in an economic manner. In industry, FFF offers flexibility and agility by promoting a reduction in costs and in the lead-time (i.e. time-to-market). Nevertheless, FFF parts exhibit some limitations, such as lack of accuracy and/or lower mechanical performance. As a result, some alternatives have been developed in order to overcome some of these restrictions, namely the formulation of high performance polymers, the creation of fibre-reinforced materials by FFF process and/or the design of new FFF-based technologies for printing composite materials.This work aims to analyze these technologies. These enriched approaches lead a technological evolution of FFF, providing solutions for resolve some main process weaknesses. This work aims to study and understand the advances on the behaviour of 3D printed parts with enhanced performance by its reinforcement with several shapes and types of fibres, from nanoparticles to continuous fibre roving. Thus, a comprehensive survey of significant research studies carried out regarding FFF of fibre-reinforced thermoplastics is provided, giving emphasis to the most relevant and innovative developments or adaptations undergone at hardware level and/or on the production process of the feedstock.

2.5.1 Introduction

AM is defined by the standard ISO/ASTM 52900:2015 [ISO/ASTM, 2015] as "the process of joining materials to make objects from three-dimensional (3D) model data layer upon layer, as opposed to subtractive manufacturing technologies". This same standard divides AM processes in seven distinct categories, in which FFF is inserted in the material extrusion category. FFF was primarilty meant for prototyping purposes, however nowadays is widely applied on manufacturing processes of functional end products in a few fields with high demanded technical requirements, such as automotive and aerospace industries [Liu et al., 2017], electrical [Li et al., 2017, Auyeung et al., 2017] and, biomedical [Norman et al., 2017, Datta et al., 2017]. The progress of this AM technology represents a new era for fabrication (as it is commonly known), changing the paradigm of part design by opening possibilities of creating complex, hollow and/or intrinsic geometries with no substantial waste [Zhai et al., 2014, Lipson and Kurman, 2013]. The process was developed in the 1980's and patented as FDM by Stratasys Inc. USA [Crump, 1992], and has been used since then, due to its wide range of applicability, reliability and cost-effectiveness. FDM or FFF has since the last decade grown in an exponential rate due to patent expiration in 2009. This technique is attracting much attention among scientists and hobbyists, because of its simplicity and wide availability of recyclable feedstock.

In the first ages of this technology, commodity polymers, such as acrylonitrile butadiene styrene (ABS) and polylactic acid (PLA), were the only available materials. The evolution of the technique lead to material development, extending the choice to other categories, which caused an improvement in the process, in its accuracy and consequently an increase in mechanical properties of the 3D printed parts. To become even more competitive, high performance polymers started to be adopted, as well as carbon fibre reinforced polymers (CFRP). Hence, there is a possibility of producing lightweight parts with high specific strength and stiffness using the FFF technique.

A composite material is created by the combination of two of more materials, so their distinct properties come together as one improved material. In most of the cases, one acts as a reinforcing component and the other as a binding agent. Composite's major advantage is that this type of material and its 3D orientation can be tailored according to the load that is going to withstand. FFF uses a similar layer-by-layer approach, with internal pattern configuration, which can be suited to the end use. Considering both technology and material, it is possible to benefit from the geometric freedom and lightweight structure production techniques offered by the FFF process and the mechanical performance offered by the reinforcement.

With this review, the authors intend to compile the information on the developments of the different types of reinforcements added to the thermoplastic processed by FFF method to enhance the properties. Emphasizing the mechanical behaviour and improvements that had been made by employing this new type of material to the process, some researchers describe the development of new types of hardware and others focusing on the material development, combined with the goal of improving the technology, leading to better and stronger parts to reach a more wide range of industrial markets.

2.5.2 Fibre printing via Material extrusion

Because of its simplicity, FFF is commonly used for producing reinforced parts. The addition of fibres is often treated in a slightly similar way to the natural polymeric material. The process allows the use of short fibres and nanocomposites with minimal hardware alteration, such as upgrading the to a harder material nozzle, since the presence of these reinforcements makes the polymer highly abrasive [Rangisetty and Peel, 2017]. The addition of fibres increases the stiffness of the thermoplastics and reduces the material expansion after the extrusion [Shofner et al., 2003]. In some cases, the material becomes brittle and difficult to use in the spool as is supplied; however the ductility can be improved with the addition of a highly molecular oriented linear polymer [Zhong et al., 2001]. Reinforced thermoplastics are made with several different types of reinforcements that can be divided in three different categories, considering their geometry; continuous, short fibres or particles. Some authors, like Thomason [2002], however, have different considerations for what defines each category. They report that short fibres have an average length inferior of 1 mm, long fibres from 1 to 25 mm and continuous fibres are usually in pre-preg bundles or mats. The most common description is defined by the aspect ratio of the fibres. Mahajan and Cormier [2015] consider that continuous fibres have high aspect ratio and a preferred orientation, while discontinuous fibres (short and particles) have lower aspect ratio. In addition to these categories,

nanotubes and nanoparticles must be considered, depending on the aspect ratio at a nanoscale. The lower the aspect ratio, the less oriented are the fibres. Long fibres have high orientation and high interface area, resulting in parts with greater strength and stiffness than those using discontinuous fibres. Nowadays, the market "off the shelf" of thermoplastic FFF filaments reinforced with nanoparticles and/or short fibres is growing, in addition to improvement in their properties. The application of continuous fibres is still restricted, indicating that, the process of printing with continuous fibres is only usable with specific hardware, unlike discontinuous fibre reinforced material. The introduction of these different types and shapes of composite reinforcements in the original materials have been studied, increasing the interest in the improved properties and becoming a more serious consideration by the industry [Mohan et al., 2017]. The research that has been done in this area, is mainly focused in the evaluation and parameter optimization by targeting areas such as mechanical, thermal and dimensional characteristics [Salem Bala et al., 2016].

2.5.2.1 Continuous Fibres

In situ mixture

The approach to this technology relies on embedding the fibres in the extrusion head. The matrix material is supplied traditionally at the head as filament and the reinforcement fibres, as a bundle are embedded in the hot zone, which makes the adjustment of the fibre/material ratio possible. In this specific case, some problems are expected. The merging process between the components is a difficult process to control, and some defects may occur such as air inclusions in the interface (Figure 2.22), low coefficient of embedding and nozzle clogging. Another concern is the fibre feeding, which can be fragile to compression and cannot be pushed into the extrusion head [Prüß and Vietor, 2015].

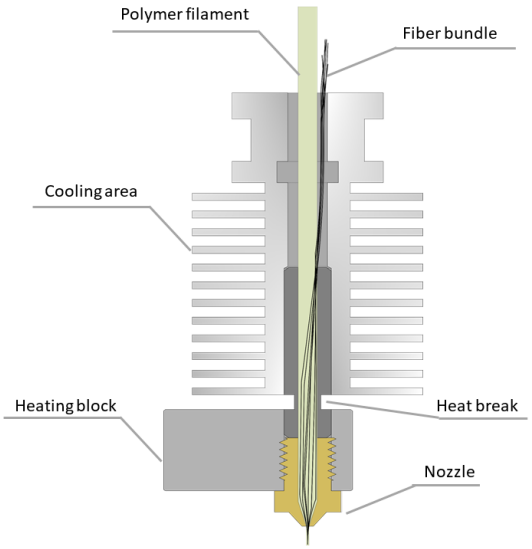


Figure 2.22: Continuous fibres/matrix in head mixture.

Fischer et al. [2013] studied the development of an extrusion nozzle that is capable of mixing the matrix and the fibres together. The 3D Fibre Print Nozzle was produced by Selective Laser Melting (SLM) and although it is similar to a standard version, it has the addition of a slightly curved side channel. The concept developed was based on the principle that the extruded fibres were pulled by the extruded polymer at a similar rate. In this case, the need of feeding mechanisms for the fibres was avoided. The tests were performed using a 3K carbon fibre bundle in a urethane thermoplastic elastomer. Preliminary tests showed good embedding after the extrusion process.

Prüß and Vietor [2015] also defend the idea that the embedding should be done at the head, having developed a prototype using a conventional open source RepRap machine. Their extrusion head consists in three ports, the polymer is supplied laterally through two of the ports (one in each side) and the carbon bundle is supplied vertically by the third port joining the other two in a central mixing chamber. Having two supplies of polymer allows a uniform infiltration in the fibres, as represented in Figure 2.23. No printed results were presented.

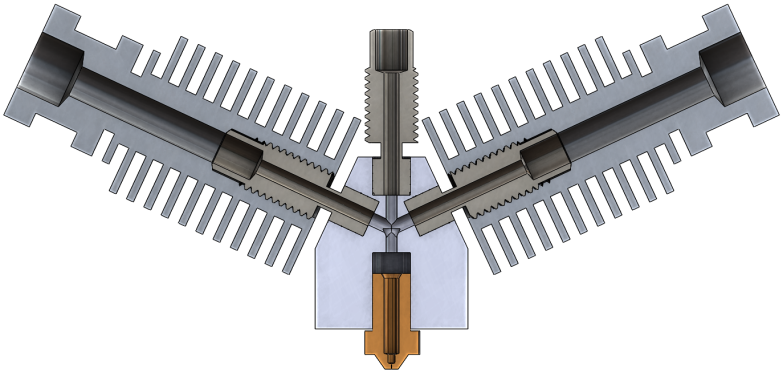


Figure 2.23: Schematic of the continuous fibres extruder concept, adapted from Prüß and Vietor [2015].

Bettini et al. [2016] modified a commercial printer (Blue Tek Strato) extrusion head in order to print PLA reinforced with continuous aramid fibres (Figure 2.24a). This approach is similar to the previous ones because the reinforcing fibres are pulled by the polymer extrusion action. Both PLA and reinforcing fibres feeding is done from the top in the same guide. The processing parameters developed were a crucial factor on printed part properties. Comparison among the usage of aramid, glass and carbon fibres showed that this last two were brittle and much more sensitive than the aramid type, thus increasing the clogging probability. Several samples were created to analyse the mechanical properties, indicating that notable stiffening and strengthening in the direction of the reinforcing fibre deposition, as shown in Figure 2.24b. The tensile modulus is roughly three and six times higher than the original PLA properties.

Li et al. [2016] studied the process of printing with continuous fibres by developing a dedicated extruder for this application. For this research, a 1K carbon bundle was considered as the rein-

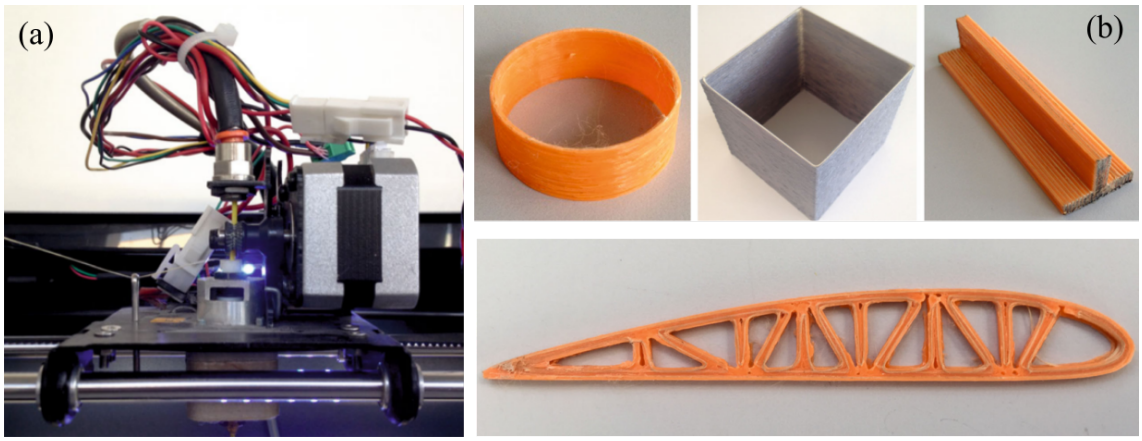


Figure 2.24: (a) Adapted extrusion head, (b) Reinforced printed parts [Bettini et al., 2016].

forcement and PLA as the matrix. Using a technology similar to the previous study, both matrix and fibres were supplied vertically through a common extrusion head. A conical nozzle was used to improve the mixture homogeneity (Figure 2.25a). In addition, a method of pre-impregnating the fibres in a solution for improving the interfacial strength is implemented. Subsequently, a comparison test was made with non-impregnated fibres. A mixture of methylene dichloride and PLA particles was created with a magnetic stirrer, posteriorly filtered, emulsificated, deionized water was added and finally the fibres were inserted.

Samples with unidirectional fibres distribution (Figure 2.25b) and hollow profiles (Figure 2.25c) were printed, as well as test parts with simple PLA, PLA + simple fibres and PLA + modified fibres, to test the flexural and tensile properties. The results shown that modified fibres, tensile and flexural strength were 13.8% and 164% higher than in the PLA + simple fibres, a considerable improvement particularly in flexural behaviour, indicating a better adhesion. Moreover, a scanning electron microscopy (SEM) analysis indicated a presence of a higher volume of voids in the simple fibre mixture than the modified fibres, proving the previous results.

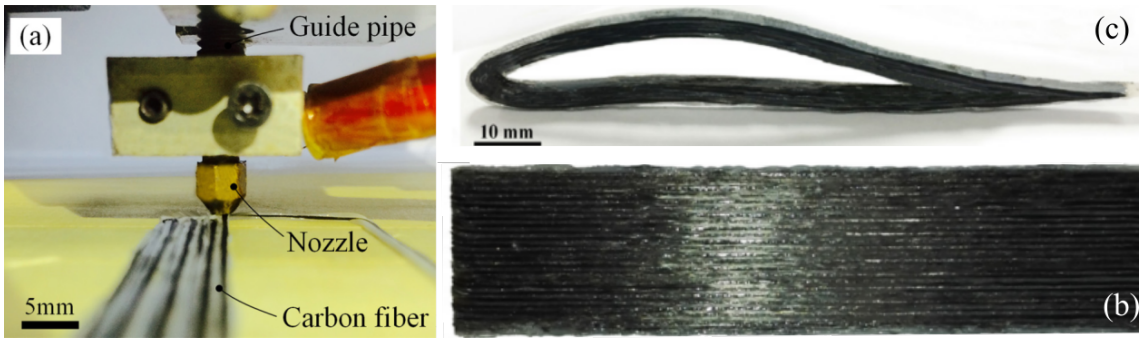


Figure 2.25: (a) Continuous fibre depositioning extruder, (b) Printed tensile part, (c) Printed profile [Li et al., 2016].

Processing temperature is a critical parameter especially in composite printing, as demonstrated by Mori et al. [2014]. Thermal bonding is also, a major factor when taking into account

mechanical properties. Considering the integration of fibres on the printed polymer, several of these previous configurations could determine important properties of this newly processed composite. Interfacial adhesion (filament/fibre) will define the strength of the part. Incorrect fibre volume fractions will create problematic features during the extrusion and erratic patterns can impose wrong fibre distributions, among others effects.

Tian et al. [2016] tested the influence on the mechanical properties by creating several samples in a adapted setup (Figure 2.26), by varying the temperatures between 180 and 240°C. Results showed that both flexural strength and modulus increase almost linearly from the lowest temperature, starting in 110 MPa and 3.5 GPa up to 155 MPa and 8.8 GPa for the highest temperature.

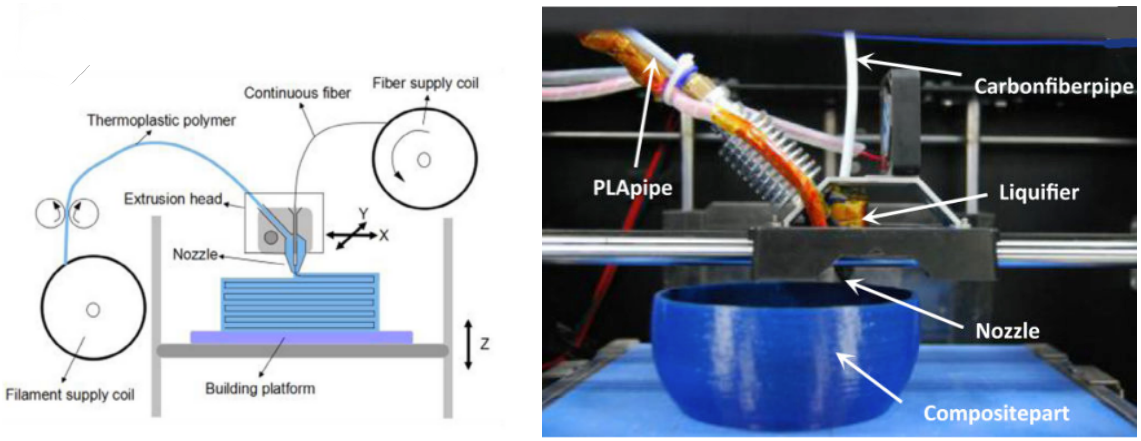


Figure 2.26: Modified extrusion head schematics [Tian et al., 2016].

The second parameter of influence analysed was the layer thickness. Changing the layer height, modifies the fibre percentage in the part. This influence was proven by measuring the flexural strength and modulus, which are doubled when the thickness changes from 0.8 to 0.3 mm. Taking into account the usage of continuous fibres and PLA, as mentioned before, this research was made using the parameters presented in Table 2.10. The results show that a best performance was obtained for 0.3 mm layer thickness, with flexural strength and modulus of 240 MPa and 21 GP. In contrast, 0.8 mm (layer thickness) show a decrease to 92 MPa (flexural strength) and 6.9 GPa (flexural modulus).

Table 2.10: Printing parameters, adapted from Tian et al. [2016].

Target parameter	Range	Complementary Parameters
T - Extruder Temp (°C)	180, 190, 200, 210, 220, 230, 240	L-0.65, V-100, E-150, H-1.2
L - Layer thickness (mm)	0.3, 0.4, 0.5, 0.6, 0.7, 0.8	T-210, V-100, E-100, H-1.2
E - Feed rate of filament (mm/min)	60, 80, 100, 120, 140, 160	T-210, L-0.5, V-100, H-1.2
H - Hatch spacing (mm)	0.4, 0.6, 0.8, 1.0, 1.2, 1.4, 1.6, 1.8	T-210, L-0.5, V-100, E-100
V - Transverse movement (mm/min)	100, 200, 300, 400, 500, 600	T-230, L-0.65, E-150, H-1.2

Feed rate is the amount of filament extruded through the nozzle per minute. A higher value creates more pressure inside the extruder and a better fibre impregnation. Tests showed that the best flexural strength is achieved for the samples printed with the feed rate of 80 mm/min, decreasing slightly its properties for higher rates. Hatching space is the distance between the center of two adjacent deposed lines. Because each line has a filament bundle, it is understandable how gaps can change the mechanical properties. Tests revealed that 0.4 mm of hatching space, resulted in a flexural strength and modulus of 340 MPa and 29 GPa respectively. As for 1.8 mm of hatching, indicated values for flexural strength and modulus of 130 MPa and 6 GPa respectively, which are a lower value than the previous ones. In addition, deposition velocity did not create a significative influence in the properties [Tian et al., 2016]. As shown in this research, printing parameters can be extremely decisive in part properties. In the study, the parts were printed with an unidirectional pattern, and other properties that should be considered are the influence of the infill percentage and pattern strategy.

Hou et al. [2018] used the extrusion system developed by Tian et al. [2016], shown in Figure 2.26 and applied it to an six-axis robot arm, focusing in the production of corrugated structures with structural integrity (Figure 2.27a). For this study, a PLA from FLASHFORGE Corp was considered the matrix material, and continuous aramid-fibres (Kevlar® R) were used as reinforcement without the help of any sizing agent at the surface or further treatment of the bundle. It was studied how printing parameters such as layer thickness and cell length would influence structural integrity in a specimen with 60 x 60 x 15 mm.

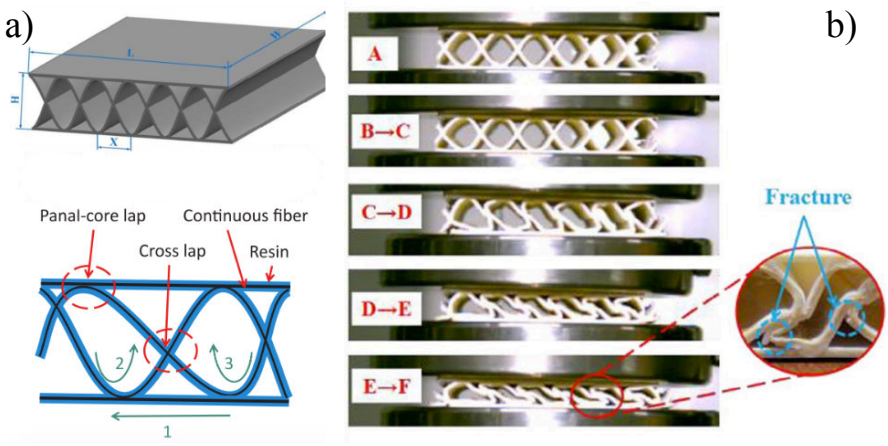


Figure 2.27: (a) Corrugated structure and path planning, (b) Failure mode of the structures [Hou et al., 2018].

The results show that, at higher cell length (x in Figure 2.27a), the compressive strength decays. With the increase of layer thickness it is observed that the same decrease in compressive strength is observed. This can be explained by the fact that each layer contains one bundle of fibres. With thinner layer thickness, more layers are used to print the same geometry. Thus, the volume of glass fibre (GF) is increased, hence, more layers, higher fibre content and higher specific strength. Figure 2.27b shows the corrugated structure failure mode under compressive test.

The ideal parameters were found to be 11.5% vol with a cell length of 9 mm, resulting in a compressive strength of 17.17 MPa, which considering the type and dimensions of the geometry it is a considerable improvement. It is acknowledged by the authors that this improved process has great potential in fabrication of corrugated structures with complex shapes with high mechanical properties corroborating previous tests.

Post extrusion mixture

Post extrusion mixture or fibre embedding in the matrix after the extrusion is a process approached in different ways; however, all of them imply that there is no simultaneous extrusion. In addition, the polymeric matrix deposition is stopped; therefore, the fibres can be inserted, and then it is resumed. This type of process creates a problematic feature, which is the interfacial adhesion between the matrix and fibre. Because the extrusion of both is made at different times, the bonding process becomes harder and the discrepancy between temperatures creates a barrier to the adhesion.

Markforged® Inc. (Massachusetts, USA) MarkOne was considered the only fully automated, commercially available process of printing continuous fibres composites [Mark and Gozdz, 2015] for long time. Carbon (CF), Kevlar® (KF) and Glass (GF) fibre bundles are available as reinforcement and each one has a polymeric sizing about 400 μm in diameter (Figure 2.28) to improve matrix bonding to a proprietary 1.75 mm diameter Nylon® (NYL-AB-1K [©Markforged Inc., 2015]) filament which is used as matrix. Reinforcement mechanical properties can be found in Table 2.11.

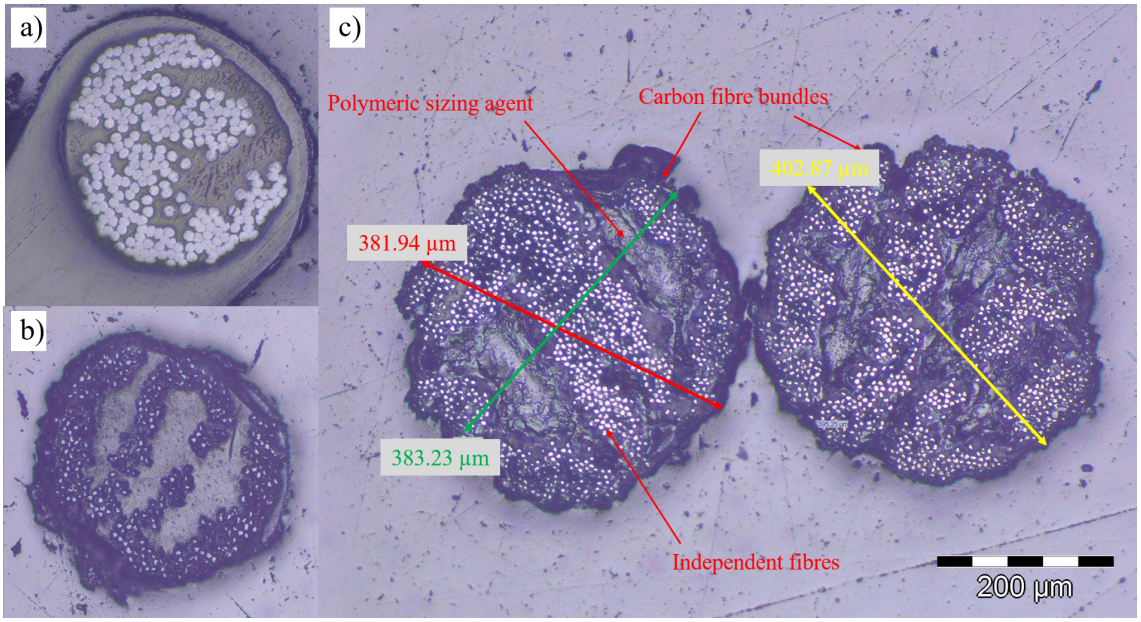


Figure 2.28: Markforged: (a) Kevlar® fibre bundles, (b) Glass fibre bundles, and (c) Carbon fibre bundles.

Table 2.11: Mechanical Properties of Continuous Fibers from ©Markforged [2016].

Property	Standard	Carbon CFF	Kevlar® CFF	Fiberglass CFF	HSHT Glass CFF
Tensile Strength (MPa)	ASTM D3039	700	610	590	600
Tensile Modulus (GPa)	ASTM D3039	54	27	21	21
Strain at Break (%)	ASTM D3039	1.5	2.7	3.8	3.9
Flexural Strength (MPa)	ASTM D790	470	190	210	420
Flexural Modulus (GPa)	ASTM D790	51	26	22	21
Strain at Break (%)	ASTM D790	1.2	2.1	1.1	2.2
Compressive Strength (MPa)	ASTM D6641	320	97	140	192
Compressive Modulus (GPa)	ASTM D6641	54	28	21	21
Strain at Break (%)	ASTM D6641	0.7	1.5	n/a	n/a
Heat deflection Temp (°C)	ASTM D648-B	105	105	105	150
Izod Impact- notched (J/m)	ASTM D256-10-A	958	1873	2603	3117

Marktwo, which contains a few minor changes facing the previous model, includes also a new PA Short carbon fibre (SCF) reinforced matrix (previously unreinforced). This technology uses a two-extrusion head system: one for the matrix polymer and one for the fibre reinforcement bundle that reaches the heated head once pushed by a motor as shown in Figure 2.29. This idea is similar to the polymer FFF extrusion technique; however, it is only possible because of the fibres being pre-impregnated, thus improving their reaction to compression and the adhesion to the matrix [Mark, 2014]. In addition, a fibre cutting mechanism is allocated in the top of the machine, in the first model and near the head in the second model. This allows for some operations as layer changing and feeding stoppage. The similarity between the previous processes is that the polymer deposition should to be stopped so that the fibre can be laid up. The main advantage is that the fibre can be deposed in a bi-directional pattern. The matrix/fibre adhesion problems are minimal since the fibre is pre-impregnated and heated before the contact with the matrix.

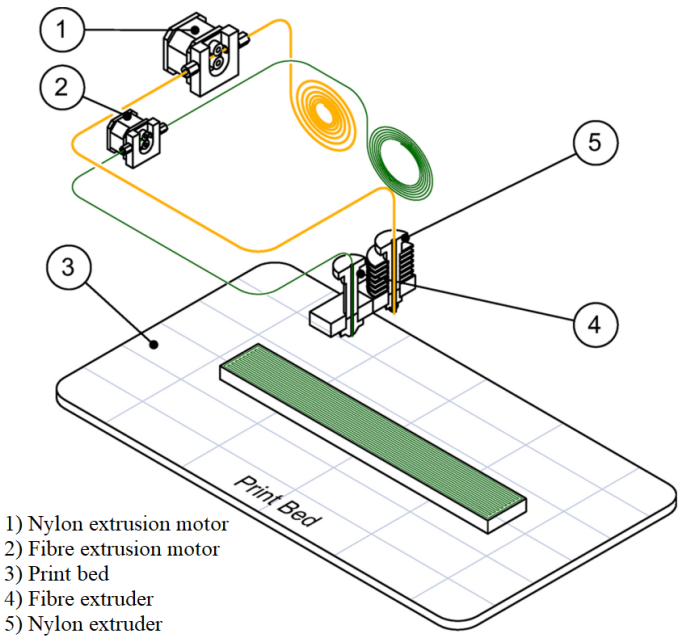


Figure 2.29: Markforged fuctioning principles, adapted from Caminero et al. [2018b].

Anisoprint LLC (Moscow, Russia) Composer is the more recent commercial alternative to Markforged® way of processing continuous fibres via FFF. Anisoprint presents a similar concept to the MarkTwo, by having two distinct print heads, one for polymer (matrix) deposition and other for composite filament co-extrusion (CFC), which deposits and cuts fibre as defined by the machine code [Valerievich et al., 2018]. However, there are two big novelties provided by this system: the continuous carbon fibre reinforcement (Anisoprint CCF-1.5k) is coated by a thermoset resin granting adhesion to a wide range of polymers, opening the possibilities of matrix materials [VALERIEVICH et al., 2017]; and open source characteristics of the software allow for a more manual and selective fibre deposition, improving the part mechanical performance in the desired direction. As this technology is still recent, very little information about mechanical performance is available.

Mori et al. [2014] studied the static and fatigue strength of carbon fibre reinforced PLA by creating samples with a completely new method. This technology uses a three-step process. Half of the sample is printed and the process is stopped, the fibres are manually added and the process is resumed by printing the missing half of the sample on top of the fibres, as shown in Figure 2.30a. The sample is kept in an oven for 15 minutes to improve bonding between the two halves and the fibres. The results showed improved bonding for the samples submitted to the heating process with small fibre pulling (Figure 2.30b), compared to the untreated samples, which translates in an increase from 0.5 kN to 0.85 kN.

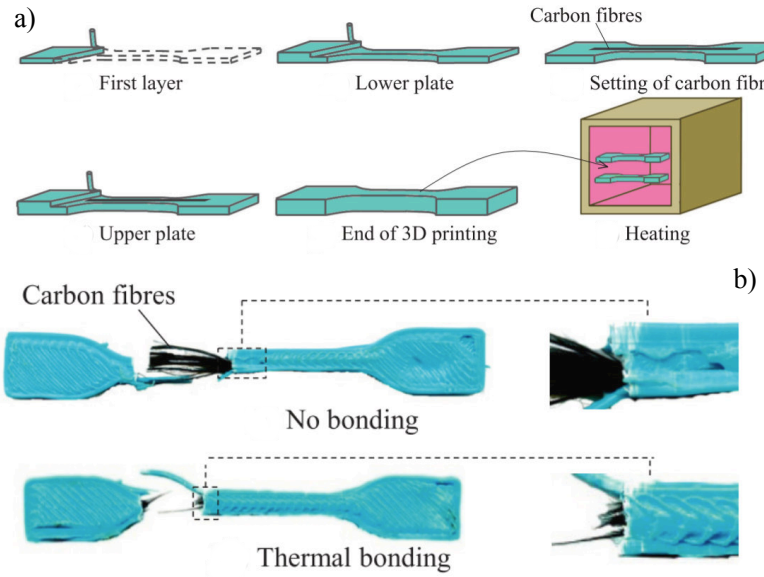


Figure 2.30: 3D printing process of tensile specimens with CF (a), and fractured tensile specimens (b) Mori et al. [2014].

In a following study, Nakagawa et al. [2017] evolved the method previously developed by producing a deposition concept similar to the commercial Markforged® [Mark, 2014]. The process was still divided in three distinct phases; however the middle step changed from manual deposition to the insertion of the fibres in mid extrusion; therefore, they can be embedded with the

thermoplastic matrix (ABS) during the transition from the heating block to the extrusion nozzle (Figure 2.31b). In addition to the thermal bonding that was previously done in oven, the authors added an heated pin, which compresses the layers improving the bonding of the fibres to the matrix. With both of these techniques, tensile (dogbone) and flexural test samples were printed and tested. The results show that both methods of bonding improvement led to the same results with similar maximum tensile strength of 30 MPa. Flexural tests show that there is a slight increase in performance for the heated pin samples presenting a maximum flexural load of 45N, 38N for the microwave treated samples and 20N for the unreinforced ones (Figure 2.31a). Even though there is an increase in performance, the samples do not fully benefit from the inclusion of carbon fibres. Since there is no fibre rupture, only fibre detachment from the polymer, the increase in properties is directly related to the bonding quality and not to the fibre strength.

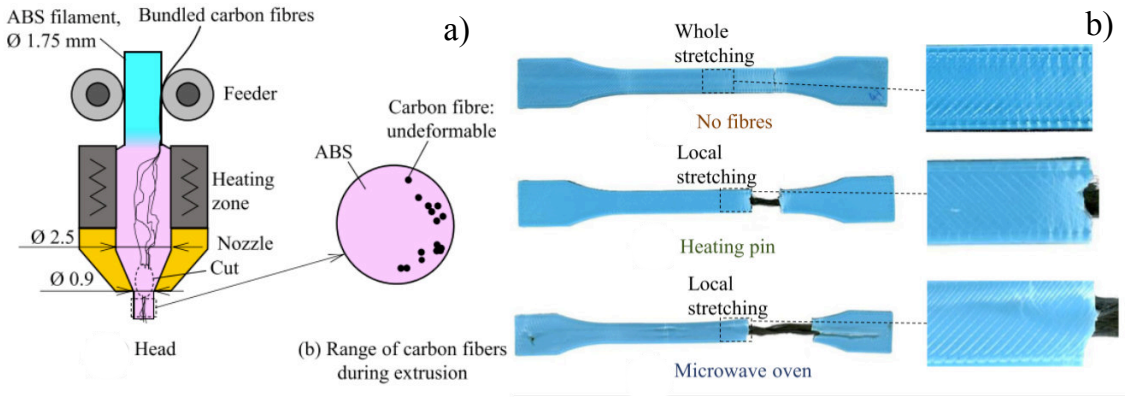


Figure 2.31: Inclusion of carbon fibres in molten ABS (a), and fractured tensile specimens (b) Nakagawa et al. [2017].

The advantage of this process is that no specific hardware is needed, although there is only reinforcement in one direction and the fibre/polymer bonding force is not ideal. With a similar approach, Yao et al. [2016] developed a technique for reinforcing PLA sample parts with continuous carbon fibres. However, the fibres serve not only as structural reinforcement but also as sensory agents, thus monitoring the changes in the fibre electric resistance along the deformation. In addition, reduction of the weight and printing time, maintaining, or even improving the structural strength using PAN carbon fibre bundles of 3K, 6K and 12K, aligned and stabilized uniaxially with epoxy resin. Three-point bending and tensile samples were produced with 20%, 40%, 60%, and 100% of fibres added manually during the print. The process was resumed with the printing of the rest of the sample over the fibres. After the print, the samples were left curing for 7 hours at 40°C in an incubator. The results show an increase of 70% in tensile and 18.7% in bending strength, with weight reduction of 26% and 11.41% in printing time.

Klift et al. [2016], using a Markforged® Inc. Mark One, evaluated the tensile properties, following the Japanese JISK7073 standard, creating three types of samples. The first type consisted of 100% Nylon®, the second one contained six concentric intermediate layers of carbon fibre and the third one containing two concentric intermediate layers of carbon. The results shown that,

in the samples using two layers of carbon fibre, the ultimate tensile strength was 149.5 MPa and the strain is 1.05%. As for the samples with six carbon layers, the ultimate tensile strength was 464.4 MPa and the average strain was 1.65%. This result clearly shows an improvement in the part strength with the increase of carbon layers. As the fibre is deposed in a pattern, discontinuities are created (entry and exit point of fibre deposition), which in some cases led to premature failure.

Melenka et al. [2016], also using the Mark One machine, evaluated the elastic properties of FFF samples reinforced with Kevlar® fibres produced accordingly with ASTM D638-14. Four sets of samples with no fibres, two, four and five concentric rings, were produced with an infill percentage of 10%. The experimental procedure demonstrated that the increase in fibre volume raises stiffness and ultimate strength. In addition, a mathematical model was created, simulating the sample properties. The model shown that the results are similar, especially in the high fibre samples.

Justo et al. [2018] used the Markforged® Mark One created fully reinforced coupons (Figure 2.32) with CF and GF, for mechanical characterization of plane strength and stiffness with tensile and compression load rates. GF and CF coupons were cut from the original printed sample with dimensions 250 x 12.5 x 1 mm for the fibres in longitudinal direction, and for perpendicular direction. GF with 175 x 25 x 2 mm were taken for tensile test (ASTM D3039). Compression tests were carried out according ASTM D695-02a standard in both direction and perpendicular to the fibres with 80 x 12.5 x 2 mm samples and in-plane shear tests were carried out following ASTM D3518 with 175 x 20 x 2 mm only for GF due to Markforged® incapabilities to produce CF samples with these dimensions. For all these tests, a comparison was made with traditional CF pre-preg (AS4 CF/Epoxy) 69 Vol.% and GF pre-preg (Eglass/Epoxy) 65 Vol.% The results show that the behaviour of the respective pre-preg for each test was far superior than the printed sample. These results are explained by the samples low fibre volume fractions (40% vs 69% for CF) and (50% vs 65% for GF) and the low mechanical properties of the PA matrix against epoxy resin. The authors refer that at the present stage the product obtained by continuous fibre FFF (CFFFF) via Markforged® One is not at the same level as the ones provided by traditional methods, however the type of properties that can be obtained by this type of machine represents a great improvement in comparison to simple FFF parts. Considering the limitations imposed by the software (preventing sharp deposition angles for carbon fibres), the coupon methodology, used by the authors is simple way of bypassing this type of restriction, maximized the fibre content in the part.

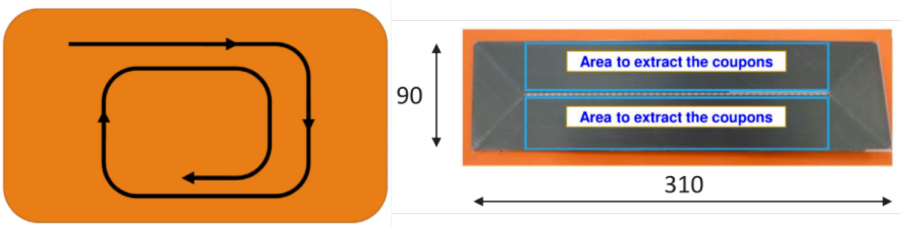


Figure 2.32: Path and dimensions of the coupons Justo et al. [2018].

Goh et al. [2018] characterized the mechanical properties and fracture mode of CF and GF

Table 2.12: Printing parameters adapted from Caminero et al. [2018b].

Parameter	Value
Layer thickness of unreinforced samples(Lt)(mm)/Number of layers(Nl)	Lt=0.1/Nl=60, Lt=0.125/Nl=48, Lt=0.2/Nl=30,
Layer thickness of fibre reinforced samples(Lt)	Lt^{CF}=0.125, Lt^{GF}=0.1, Lt^{KF}=0.1
Fibre Volume Fraction(%)	CF Type A / CF Type B 26.8/72.4 KF Type A / KF Type B 27.5/73.8 GF Type A / GF Type B 22.7/73.4

composites via FFF to understand how to compare them to traditional composites. For this study a Markforged® MarkOne was used with branded Markforged® pre-impregnated fibres and a PA thermoplastic matrix material, printing fully dense samples with fibre deposition at 0°. A density analysis was made according ASTM D3171-15, indicating that the CF amount was 41 Vol.% and the GF was 35 Vol%. For tensile tests (ASTM D3039/D3039M-14), samples with 25 x 250 x 2.5 mm were produced with 23 layers of fibres, laid unidirectionally at 0°. Flexural samples were printed with the same unidirectional pattern following the ASTM D790 with dimensions of 13 x 154 x 4 mm. In addition, a quasi-static indentation test was perform according to ASTM D6264 with samples 100 x 100 x 16 mm. The results show that all values were inferior to the manufacturer's data-sheet, with specially low values for the GF. Tensile strength for GF FFF and CF FFF test samples was much higher than the conventional materials; however, the flexural behaviour had the opposite tendency. The authors acknowledge that using this type of process allows some barriers to be broken, such as the part production with the desired mechanical characteristics, without the need for big machinery tooling. However, note that this type of fabrication will not replace traditional composites because its low deposition rate, making this method one of the biggest obstacles to the development of the process.

In a study conducted by Caminero et al. [2018b], the inter-laminar bonding performance of CFFFF printed parts was evaluated using short beam shear test (ISO 14130) to obtain the inter-laminar shear strength (ILSS), considering layer thickness and fibre volume content as variables. This study uses a Markforged® MarkTwo, using Nylon® as matrix, and Kevlar®, glass and carbon fibres as reinforcement. In addition, a comparison of the inter-laminar bonding performance between pure Nylon® and reinforced samples was conducted. Table 2.12 indicates the used fibre percentages and layer thickness in which five samples of each type were produced with 100% fill density, rectangular pattern for the unreinforced samples and isotropic fibre infill style at 0° for the samples containing fibres.

The results in Table 2.13 indicate that the layer thickness variation for unreinforced samples does not affect the ILSS coefficient. CF exhibited the best inter-laminar shear performance. KF shows poor improvement for both percentages of fibres, presenting extensive delamination due to

Kevlar® fibres poor wettability. The authors explain how promising is the technology since there is a lack of experimental data in this field of research; however, it is necessary to create new methods for structural and mechanical property characterization.

Table 2.13: Average ILSS for unreinforced and reinforced samples adapted from Caminero et al. [2018b].

Interlaminar shear strength of unreinforced samples	
Lt=0.1 mm	10.19 MPa
Lt=0.125 mm	9.79 MPa
Lt=0.2 mm	9.33 MPa
Interlaminar shear strength of reinforced samples	
CF Type A / CF Type B	22.19/31.94 (MPa)
KF Type A / KF Type B	13.65/14.28 (MPa)
GF Type A / GF Type B	13.87/20.99 (MPa)

In a following study, Caminero et al. [2018a], using the same previous hardware, studied the effect of the building orientation, layer thickness and fibre volume content influence on the impact performance (Charpy ASTM D6110). It is important to consider that the printing parameters were the same as the previous work (Table 2.12). Unreinforced samples with varying layer height, and reinforced test specimens with Kevlar, carbon and glass continuous fibres were used. The samples were printed in two different orientations, flat and on edge and different fibre volume fractions as seen in Table 2.14.

Table 2.14: Fibre volume content for impact test samples, adapted from Caminero et al. [2018a].

		Type A	Type B	Type C
Fibre Volume Fraction (%)	Carbon Fibre			
	Flat	3.44	24.94	53.18
	On-edge	3.38	24.82	33.16
	Kevlar Fibre			
	Flat	8.60	29.50	56.06
	On-edge	3.38	29.53	34.65
	Glass Fibre			
	Flat	8.40	29.15	55.60
	On-edge	7.82	29.68	34.30

The results show a gradual improvement in properties for the unreinforced flat samples as the layer thickness increases; however, the opposite tendency was found for on edge samples. The reinforced test specimens presented an improvement in behaviour as the fibre content is increased for the three types of reinforcing agents, both for flat samples and on edge, thus contradicting the pure samples test. In addition, the values were higher for all of the on edge samples. It is shown

that there is in fact an increase in impact performance of FFF printed parts through the addition of continuous fibres; however, this technology is still subpar from traditional composites when considering this property.

Pre-Impregnated Filaments

Pre-impregnated filaments, or pre-pregs, are specific filaments for 3D printing with the inclusion of continuous fibres. To use this type of filament, a specific hardware with different features from the stock extruder is used, such as a fibre cutting system and a special extruder nozzle (Figure 2.33).

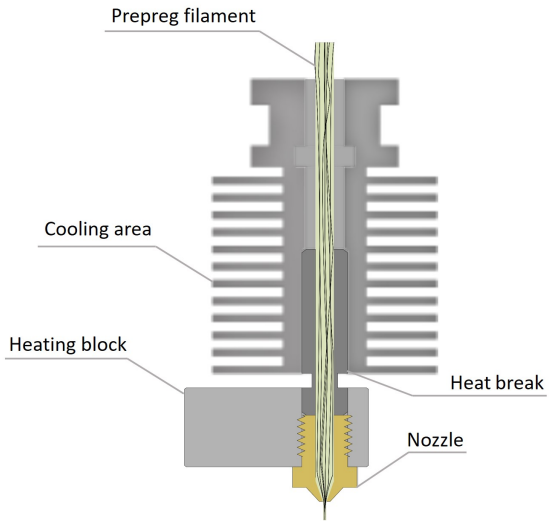


Figure 2.33: Prepreg Extrusion Schematic.

A methodology for manufacturing and testing 3D printing continuous fibre pre-preg filament was developed by Hu et al. [2018], thus aiming to improve FFF parts characteristics. Considering both *In situ* mixture and post extrusion mixture, the authors defined that both methods were flawed. The first did not grant the best matrix/fibre bonding during extrusion, whereas the second method, because of a problematic lack of pressure and temperature, did not grant the best interfacial adhesion. The research presents a feedstock production method ensuring a proper adhesion between both compounds. No fibre cutting mechanism was considered in this work.

To produce a single screw extruder, coaxial extrusion dies were used. The pressure caused by thermoplastic being pushed by the screw against the fibre creates a proper impregnation. The filament is then entered into water for solidification and posteriorly dried at a constant rate. Regarding the extruder head, no significant alterations were made, the entrance was made via PTFE tube and the nozzle was replaced for one with a wider diameter in order to prevent cloggings. For this study, NatureWorks 4043D PLA and Toray T300-T1000 were used, and a range of parameters was considered in order to grant the best fitting filament. Regarding printing parameters, a three-factor and three-level central composite design was used (Table 2.15).

Table 2.15: Three-factor and three-level central composite design, adapted from Hu et al. [2018].

Factors	Coded Levels		
	-1	0	1
T: Printing Temp (°C)	200	215	230
S: Printing Speed (mm min^{-1})	60	90	120
L: Layer Thickness (mm)	0.6	0.9	1.2

For the flexural test, a 60 x 11 x 3 mm specimen (Figure 2.34a) was created, and, in total, twelve tests were carried out. The results presented in Figure 2.34b, show that the highest flexural strength was achieved with sample twelve, corresponding to printing parameters of T=215°C, S=60 mm/min and L=0.6 mm. Note that only by changing printing parameters the properties can decay to 1/5th of the maximum value (sample fifteen: T=215°C, S=60 mm/min and L=1.2 mm). In this case, the problem is caused by the excessive diameter of the extrusion height; however the second cause of decrease in flexural strength is divided by the other two factors.

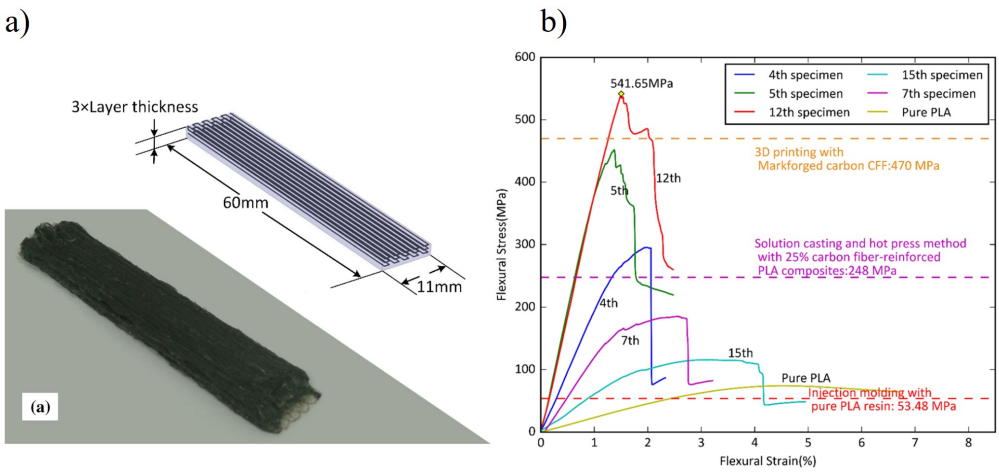


Figure 2.34: Flexural specimen (a), and stress–strain curves of five of the flexural specimens (b) Hu et al. [2018].

A similar approach to the problem was done by Vaneker [2017], in a follow up study to a master's thesis [Rietema, 2015], which used a pultrusion system to create a commingled filament from a PP matrix material and E-Glass as reinforcing agent. The developed pultrusion apparatus contains a heater embedded brass mould with 1.3 mm diameter hole in which the yarn comes out and is pulled by a servomotor with a pull wheel. The integration of this concept in a low-cost FFF equipment consisted of the development of an extrusion head and a cutting mechanism actuated by a solenoid and a servomotor, as seen in Figure 2.35. The cutting mechanism goal is to interrupt the fibre deposition, directly above the deposed surface as the extrusion head goes up in a scissor like movement, which is done at an angle in order to avoid leftover fibres in the printed area. Moreover, the following restrictions were imposed to the software: the print speed has to be constant with a constant flow rate. Slic3r Software was modified adding new features to the G-Code. Thus, giving

the indication for the actuation of the cutting head, every time that the head moves to a different location without extruding material, if an 120° angle is performed or if a radius inferior to 6mm occurs in two adjacent lines.

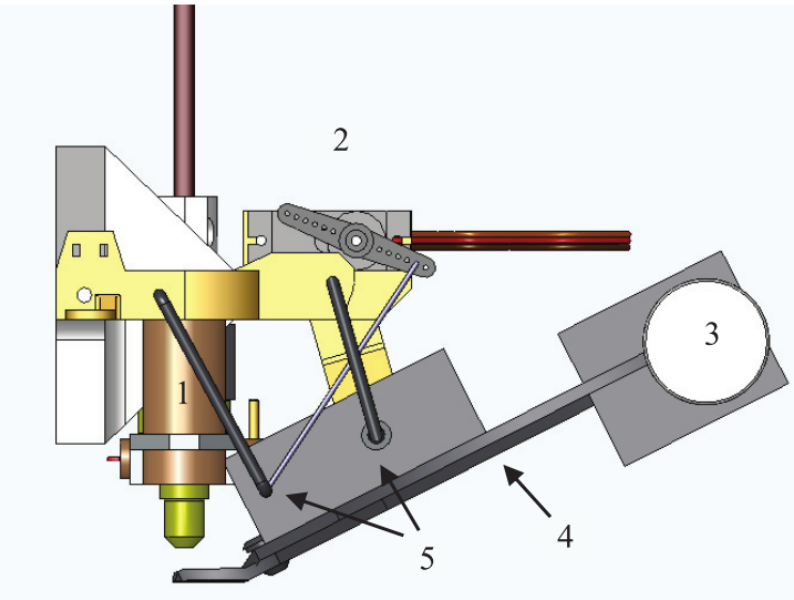


Figure 2.35: Extrusion and cutting head: (1) Filament extrusion head, (2) Servo, (3) Solenoid, (14) Cutters and (5) 4-bar linkage [Vaneker, 2017].

Void analysis showed that the air gaps were aligned in horizontal lines indicating an insufficient consolidation between subsequent layers due to some of the parameters. Flexural samples (ISO 14125) were produced for several parameters and the best combination achieved at T=210°C, L=0.5mm and S=90mm/min with a flexural modulus of 12.37 GPa.

2.5.2.2 Discontinuous fibres

Short fibres

Short fibre reinforced thermoplastics have been around for decades to produce high end products via moulding or extrusion processes, showing prominent results. However, printing thermoplastics with short fibre can be an hard task. For example, formulations with high fibre content may lead to unpleasant difficulties during the process, such as thermal degradation of the matrix due to viscous dissipation, and/or extruder cloggings [Kishore et al., 2016]. Short fibre reinforcements, unlike the continuous fibres process, need minimal hardware alteration because these fibres are extremely abrasive, and hardened nozzles are recommended for high usage [Rangisetty and Peel, 2017]. Figure 2.36 shows an example of short fibre filament extrusion during the FFF process, which also illustrates the fibre disposition throughout its path.

The production process of a thermoplastic reinforced filament comprises several steps. The raw material is supplied in pellets, which are mixed with carbon fibre powder and posteriorly extruded in filament form. This process could be repeated by grinding the filament if the fibre

distribution is not according with the requested standard or if there are any production defects. These filaments are commercially available with several matrices; usually the same materials that can be processed by the FFF process are charged with short fibres, improving its properties.

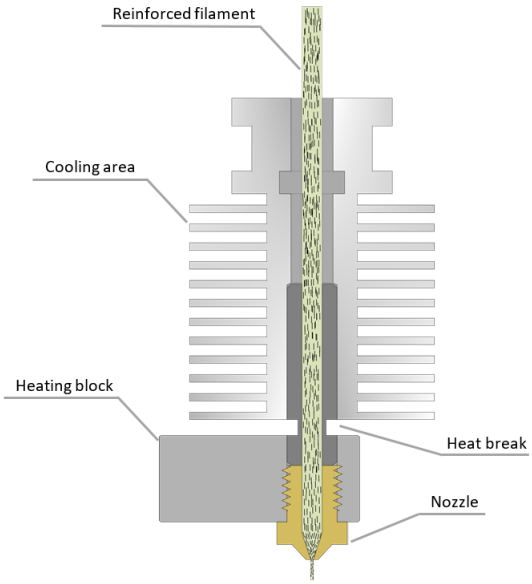


Figure 2.36: Short fibre extrusion process.

Several studies have been conducted regarding the fibre length and content influence on mechanical properties of printed samples. The properties obtained through printed parts with short fibres, are not as much associated with the printing process properties as continuous fibres are. Instead, these properties are defined by the fabrication of the feedstock (mixture percentage, fibre orientation and size) in which a major part of the research is focused.

Hull et al. [2015] focused their studies on the effects of process variables such as, fibre content, expansion percentage and extrusion rate on filament diameter. For this work, ABS pellets from ExtrusionBot, LLC (Chandler AZ, USA) and 100 μm carbon fibres were mixed and extruded in a filament form in a Extrusion Bot EB-1 (3 mm diameter nozzle) with 0, 5, 10 and 15wt.%. The results show that there is a decrease in diameter when the fibre content is increased up to 10%, increasing (diameter) when raised to 15%. The extrusion rate increased with the fibre content; however not in a linear way. Moreover, if temperature and diameter are increased, the expansion values decrease, and the opposite effect is found for extrusion rate. It is shown that there is in fact a relationship among these parameters and the filament properties and future studies aim to test mechanical properties.

Nikzad et al. [2011] studied the thermo-mechanical properties of a highly filled, self-produced polymeric composite filament. ABS material was considered as matrix of the composite, while iron (45 μm) and copper (10 and 45 μm) particles, were considered as reinforcements, in amounts of 5, 10, 20, 30, 40 Vol.%. Part of the mixture for filament production material was injected moulded. Thermal conductive tests show that higher percentages of reinforcement leads to higher

conductivity. Dynamic mechanical analysis (DMA) tests indicate that copper mixture with 10 μm in 30 Vol.% has the better performance among the samples with same dimension reinforcement. For 45 μm copper the best results were obtained for the 10 Vol.% and, among iron-reinforced samples, 30 vol% have slightly better results than 20 vol%. In conclusion, the results indicate that an easy printable composite showed thermally and mechanically better performance for the reinforced materials.

Ning et al. [2015] used pellets of ABS thermoplastic to produce filaments by varying the percentage of fibres and length to study the influence on the mechanical properties of 3D printed samples. The fibre content was 3, 5, 7.5, 10 and 15 wt.%, with an average length of 100-150 μm, and a common diameter of 7.2 μm. Posteriorly, they were mixed with ABS and extruded in a 2.85 mm diameter filament. This filament was then printed in 100% infill and 0.2 mm layer height with ASTM D638-10 and ASTM D790-10 geometries for tensile and flexural testing. Through the analysis of the 150 μm fibre length samples, from 0 to 5 wt.% there was a considerable increase in the tensile strength, stabilizing at 7.5 wt.%. At 10 wt.% and 15 wt.% the values were closer to the 0 wt.% ones. For the Young's modulus, the behaviour was similar, increasing up to 7.5 wt.%, dropping at 10 wt.% and maintaining a low value at 15 wt.% fibre content. It was found that ductility decreased from 4.14% for the pure polymer samples to 2.74% for 10 wt.%, with a slight increase at 15 wt.%. Comparing (100 and 150 μm at 5 wt.% carbon fibre content, the average values for tensile strength for 150 μm were higher. The ductility was improved with the shorter fibres and the yield strength was similar for the two types.

Tekinalp et al. [2014] also used short fibre reinforced ABS to create tensile (ASTM D638) and compressive samples (D4703) via compression moulding and AM. Several mixtures were made, containing 10, 20, 30 and 40 wt.% of carbon fibre with lengths between 0.2 mm and 0.4 mm. The samples were printed using a commercial model with specification of 0.2 mm layer height and 0.5 mm extrusion nozzle. Clogging problems were found when printing the 40 wt.% samples, indicating that, for this fibre values, a higher diameter nozzle is required. The results show that no visible voids were found in compression-moulded samples; however, in the printed samples, voids in the material and between the deposed lines were evident. Although the gaps between the lines decreased with the fibre amount, FFF samples show a higher level of fibre alignment than the compression-moulded samples. Bearing in mind the tensile strength and modulus, FFF samples presented an increase in properties, reaching 115% and 700% respectively.

Mahajan and Cormier [2015] developed an unconventional technique to produce parts using 14 wt.% aligned short fibres and epoxy-based resin. The fibres used were 100μm in length and 7.2μm diameter, which were mixed with the epoxy resin for 20 minutes before the extrusion. An nScrypt Smart Pump micro-extrusion system was used for the printing process. After the extrusion, a UV cure time of 30-60 s was applied. Sets of five ASTM D638-10 samples with longitudinal and transversal fibre orientation were printed. The results showed an increase of 44.12% in tensile strength and 42.67% in modulus for the longitudinal aligned fibres. The tensile strength is 44% higher when using longitudinal fibres rather than with transversal orientation.

Liao et al. [2018] studied the variations on thermal and mechanical properties of CF/PA composite parts via FFF by fabricating filaments with different wt.%. For this study, PA12 (Vestamid L1670) was considered as matrix material and the reinforcement was made by continuous fibres with diameter ranging between 6 and 7 μm, which were posteriorly cutted into 15 to 20 mm length fragments. Subsequently, mixtures with 2, 4, 6, 8 and 10 wt.% were created and 1.75 $\pm$ 0.05mm filament was produced by a twin screw extruder equipped with a 5 mm die at 240°C. Tensile (ASTM D638-10/type IV), Flexural (ISO 14125) and Impact samples (ISO 180-2000) were produced with the following printing parameters: 0.4 mm nozzle diameter, infill at 100%, 0.2 mm layer height, 30 mm.s^{-1} printing speed, 250 °C extruder temperature and 120°C bed temperature. DSC results exhibited that, an incremental increase in temperature for T_c (crystallization temperature) from 141.3$\pm$ 0.2 for the pure material to 144.7$\pm$ 0.2°C, melt flow index (MFI) values decreased from 5.5 for the pure to 3.3 g/10 min for the 10 wt.%. The T_{outset} and T_{max} increased with the fibre content, in addition thermal conductivity also showed an increase of 277.8% (0.221 to 0.835 W/m/k). Tensile strength and modulus exhibited a linear increase from 44.6 MPa and 0.978 GPa respectively, for the unreinforced material to 93.8 MPa (102.2% increase) and 3.581 GPa to 10 wt.%, decreasing the elongation at break from 192.1% to 8.1%. Flexural strength increased linearly from 35.6 MPa to 124.9 MPa and the modulus from 1.178 GPa to 5.257 GPa. Finally, the impact properties stayed roughly the same for both 0 and 10 wt.%, keeping at 24.8 kJ/m^2. The obtained improvement can be explained by the good dispersibility and preferential orientation in the deposing direction of the fibres found in the printed parts.

Hofstätter et al. [2016] analysed the fibre distribution and orientation by investigating the inner configuration of PLA thermoplastic as matrix material reinforced with short carbon. The printed parts were analysed in SEM and with Radiological Imaging in order to define the position and fibre orientation. The feedstock used contained 15 wt.% of virgin short carbon fibres, averaging 7.2 μm in diameter and 100 μm in length which was extruded by a 0.4 mm diameter nozzle resulting in the orientation to follow along the deposition path. SEM showed that a polished cut through the extrusion line exhibited no gaps between the fibre and matrix or cracks in the matrix. It is possible to understand that the fibre alignment is due to a two step process. First an extrusion to create the filament and a second extrusion when printing the part, thus aligning the fibres in the deposition direction. Ellipsoidic holes where found, also with the major dimension in the extrusion orientation, possibly reducing the part tensile strength. In addition, the interconnection of deposed lines creates bonding among them, allowing for orthogonally oriented fibres to be interconnected. A further analysis to a tensile tractioned sample showed that more than 40% of the fibres were ripped out during the process.

Zhang et al. [2018] studied the interfacial bonding strength of both ABS reinforced with short fibres (14 wt.%) and carbon nanotubes (8 wt.%), supplied by 3DXTech Inc. (Michigan, USA), with in-plane tensile shear (ASTM D3518/D3518M-13), for raster orientations of 0, $\pm$45° and 90°, emulating traditional laminates. As for double notch shear tests (D3039/D3039M-14) a $\pm$45° was used. A set of samples was produced with different printing speeds (60 /80 /100 mm/s), same layer height of 0.24 mm and the speed of 80 mm/s. The layer height varied among 0.18, 0.25 and

0.3 mm for another combination of samples. The samples were used for the double notch test. In addition unreinforced ABS samples were produced for property comparison, and Table 2.16 exhibits comparative values obtained for each set of samples.

Table 2.16: Tensile test results for FFF specimens [Zhang et al., 2018].

Specimen	Raster Orientation	Tensile Strength [MPa]	Tensile Modulus [MPa]	Poisson's ratio	Porosity [%]
ABS	0°	27.69±2.39	2245±141	0.41±0.03	0.82
ABS	±45°	23.95±3.55	2061±5	0.38±0.01	0.49
ABS	90°	22.31±1.24	1952±60	0.37±0.01	1.87
CNTABS	0°	29.64±0.17	2522±53	0.38±0.01	0.85
CNTABS	±45°	29.20±0.42	2196±106	0.38±0.01	2.39
CNTABS	90°	21.46±0.98	2017±13	0.34±0.01	1.39
CFABS	0°	39.05±3.98	5899±215	0.37±0.01	4.18
CFABS	±45°	29.23±2.38	2830±80	0.44±0.01	8.54
CFABS	90°	13.74±3.12	2193±91	0.20±0.01	6.93

By examining the samples via X-ray, the authors concluded that, the different raster angles originate distinct microstructures and porosity levels. The highest amounts of porosity were found in SF ABS set, and ± 45° raster angle presented the maximum value. It is possible to conclude that the deposition direction is a major factor in tensile strength values, because the highest value for each sample is the 0° orientation (solicitation direction), then ± 45° and finally 90°. Values of in-plane shear strength for ±45° are higher in the reinforced samples. Double notch test revealed that the strength drops with the increase of printing speed and layer thickness. Matrix fracture, fibre pull-out and fibre-matrix interfacial debonding were found as failure modes.

Nanocomposites

Polymer nanocomposites comprise a polymer matrix reinforced with fillers that have at least one dimension smaller than 100 nm and exhibit a significantly better performance comparatively to the matrix at low filler loadings. Polymer nanocomposites have caught the attention of the industrial and scientific communities because of their potential for developing novel, cost-effective and high-performance materials for advanced engineering applications, namely where high thermal and electrical conductivity are necessary. Electrically conductive nanocomposites are quite interesting for FFF applications, due to their properties that fulfil the requirements of the process and the necessary functionalities. Efficient dispersion of carbon nanoparticles in polymeric matrices is considered a critical matter that has created an obstacle in its application. In its primitive state, carbon nanoparticles tend to agglomerate in clusters with strong cohesive forces. The preparation of polymer nanocomposites can be approached in three different ways. Firstly, *In-situ* monomer polymerization in the presence of nanoparticles, this means that the polymer is already divided in monomers in which the nanocomposites are mixed, occurring then the polymerization. This type

of solution rely on the capacity of a low viscous medium to intercalate the particles. With this technique, it is expected to be obtained higher levels of dispersion. However, this method is oriented for batch scale and require the use of solvents and catalysts that can compromise the purity of the final composite [Wang et al., 2011]. The second technique is the dissolution of the polymer in a solvent followed by mixing and nanoparticle dispersion. Finally, melt mixing of a thermoplastic polymer with the carbon nanoparticles using a batch or continuous mixing equipments [Hu et al., 2014, Song et al., 2011]. This technique uses conventional polymer compounding techniques such as twin screw extrusion, batch mixers or micro-compounders, however it becomes a complex process due to high level of parameters and the not being easy to establish clear correlations between material properties process conditions and final dispersion levels.

García-Tuñon et al. [2015] processed graphene nanoparticles in a suspension by robotic assisted deposition, and Kim et al. [2015] printed successfully graphene oxide nanowires colloidal mixture using a micropipette.

Shofner et al. [2003] developed a nanocomposite material for the FFF process by combining the vapor-grown carbon nanofibres with ABS copolymer. For this work, ABS pellets were mixed with 100 nm in diameter and 100 μm in length fibres with a maximum content of 10 wt%. Tensile test samples (ASTM D638 Type V) were made for pure ABS and ABS filled with fibres. Dispersion analysis, porosity values, fibre alignment and comparison between filled and unfilled models was made. The results showed that there was high dispersion and distribution of fibres with minimal porosity in the matrix. Tensile strength increased from 26.9 to 37.4 MPa and tensile modulus also increased from 0.49 to 0.79 GPa (ISO 17296). It was observed that the fracture change from ductile to brittle, indicating that the matrix/fibre and layer/layer bonding was not ideal.

Gardner et al. [2016a] studied the application of a continuous carbon nanotube yarn with Ultem® as matrix material. This approach to composite printing has a similar method to continuous fibre FFF pre-impregnated filaments. Although carbon nanotubes make the reinforcement, they are processed in a printable yarn/filament form, with Ultem® (PEI) material coating. A substrate was previously added in the deposition area in order to the yarn adhere properly. Beyond this, a cutting mechanism was developed and added to the system to terminate the deposition in a desired point, allowing the start of the forthcoming layer in another area. No structural tests were made; however the results showed that with this method it is possible to print fully functional high strength parts.

Weng et al. [2016] studied the mechanical and thermal properties of ABS/ montmorillonite (OMMT) nanocomposites in a traditional FFF process approach. Beyond the control of pure material, three types of ABS composites were made with 1, 3 and 5 wt.% of OMMT, to be injected and compared with FFF produced parts. Tensile strength results indicate that injected parts have approximately 40% higher properties than printed parts. For each value of fibre content there was also an increase in strength of approximately 15% for the both types of process. The elastic modulus was also higher in injected parts, as well as the strain percentage, quadruplicating its value for printed parts (control samples).

2.5.3 Research opportunities and final remarks

As an evolving technology, FFF is being applied to new and different sectors. However, this AM technique is not considered suitable for other purposes than prototyping by many researchers and engineers, due to its inferior mechanical properties when compared to traditional processes. The inclusion of fibres in this type of additive process is mostly pointed out as a strategy to improve the performance of FFF thermoplastic parts. Thus, it is possible to produce, in an economic and fast way, robust and reliable D parts that can compete with the ones fabricated by convectional techniques, and hence spread out the application of FFF technology in key manufacturing industries.

The present survey shows that composite materials can be produced/processed via FFF in several ways and with different outcomes. Nevertheless, each type of fibre reinforcement have its own processing issues and limitations, which lead to distinct research opportunities. Tables 2.17 and 2.18 show an overview of the most relevant studies undergone for continuous and discontinuous fibres, respectively.

To print with discontinuous fibres, normal FFF hardware can be easily applied without any significant changes, being the most important stage in this scenario, the material production. Indeed, creating 3D parts with enhanced properties using thermoplastics reinforced with discontinuous fibres is not guaranteed and several studies had demonstrated that it is very dependent on the amount of fibre and its distribution onto the matrix. Discontinuous fibres exhibit low superficial areas for contacting the matrix material surrounding it. As a result, a non-adequate fibre amount/distribution can lead to a lower mechanical performance when compared with the unreinforced material. For instance, a too high percentage of short fibres lead to more fibre interactions and, at the same time, to some defective interfacial connections between them and the surrounding matrix, which may cause conflicting effects on material behaviour. Therefore, detailed experimental studies should be carried out in order to determine ideal amounts of short fibres to include in FFF thermoplastic filaments. These quantities depend on the chemical composition of the fibres and the matrix, as well as the filament diameter and the adopted procedure for the feedstock production.

In the case of continuous fibres, the benefits of using these type of reinforcements on FFF printing are generally exhibited as a significant increase on the mechanical performance of a 3D part. Hence, the load is mostly supported by the fibres, being the thermoplastic matrix a mean of joining them together in the desired shape. Nevertheless, the process of producing FFF printed parts with continuous fibres is not straight forward, as it is for the discontinuous fibres, and implies the use of a distinctive FFF printer devoted for that purpose, which only a few companies can provide. To surpass this hardware limitation and the possibility to fabricate 3D printed parts reinforced with continuous fibres in an economic way for research characterization purposes, some authors had developed customized equipment based on the reconfiguration and upgrade of low-cost FFF printers and/or lab-scale extrusion devices.

The emerging improvement in material development was the focus of the present work, which portrays that a great effort has been done in this area to evolve and create a more robust outcome. Nevertheless, it was noticed that the majority of the performed studies so far are dedicated to com-

modity polymers (such as PLA or ABS). Hence, further investigations are needed to successfully print 3D parts with engineering plastics (such as PA or PC) and high-performance polymers (such as PEEK or PEI), as well as with reinforced versions of these more advanced matrices.

Regarding characterization, only tensile and flexural responses have been evaluated as a function of printing input parameters and anisotropic features of the FFF process have been considered. Despite the valuable results, some more properties should be analysed to supplement this characterization work, namely, interlayer strength and shear behaviour.

Table 2.17: Continuous fibres process characteristics resume

Author [Date]	Disposition	Fibre type	Matrix	Fiber content	Process type	Focus	Properties Inc.
Bettini et al. [2016]	Continuous	Aramid fibres	PLA	9.5 wt.%	*In Situ*	Ext. Head development, mechanical properties comparison	●●●●●
Li et al. [2016]	Continuous	1K CF	PLA	34% Vol	*In Situ*	Ext. Head development, interface bonding agent, SEM analysis, mechanical properties comparison	○○○○○
Matsuzaki et al. [2016]	Continuous	CF/Jute fibres	PLA	40, 50% Vol	*In Situ*	Ext. Head development, high diameter nozzle, mechanical properties comparison, fracture analysis	●●●●○
Melenka et al. [2016]	Continuous	Kevlar® fibres	Nylon®	-	Post extrusion	Markforged® MarkOne, comparison between predictive mathematic model and mechanical tests	-
Tian et al. [2016]	Continuous	1K CF	PLA	27% Vol	*In Situ*	Ext. Head development, mechanical properties comparison, printing parameters influence on fibre/matrix bonding	-
Yao et al. [2016]	Continuous	3K, 6K, 12K CF	PLA	-	Post extrusion	No fibre extrusion, manual fibre insertion and incubator curing, mechanical properties	●●●○○
Prüß and Vietor [2015]	Continuous	CF	-	-	*In Situ*	Ext. Head development, no results shown, design for fibre reinforcement, curve layer deposition strategies	-
Klift et al. [2016]	Continuous	CF	Nylon®	-	Post extrusion	Markforged® MarkOne, evaluation of properties	●●●●●
Bade et al. [2015]	Continuous	CF	PLA	-	*In Situ*	Extrusion of fibres through the original nozzle, comparison with compression moulded part, mechanical properties	●●●○○
Mori et al. [2014]	Continuous	CF	ABS	-	Post extrusion	No fibre extrusion, manual fibre insertion, thermal bonding effect, mechanical properties	●●●●●
Namiki et al. [2014]	Continuous	1K CF	PLA	1% Vol	*In Situ*	Ext. Head development, mechanical properties, SEM analysis	●●●○○
Fischer et al. [2013]	Continuous	1K CF	-	-	*In Situ*	Ext. Head development, fibre extrusion problematic	-
Hou et al. [2018]	Continuous	Kevlar® R	PLA	2,10,11.5% Vol	*In Situ*	Ext. Head application to an 6-axis robot, corrugated structure development, mechanical property analysis for each different parameters	●●●○○
Nakagawa et al. [2017]	Continuous	CF	ABS	-	Post extrusion	No fibre extrusion, manual fibre insertion, thermal bonding effect with heated pin and oven, mechanical properties	●●●●●
Justo et al. [2018]	Continuous	CF,GF	Nylon®	-	Post extrusion	Markforged® MarkOne, cutted coupons in plain strength and stiffness, comparison with traditional Epoxic matrix composites	●●●●●
Goh et al. [2018]	Continuous	CF,GF	Nylon®	35/41 Vol%	Post extrusion	Markforged® tensile, flexural, quasistatic indentationt tests and density analysis	-
Caminero et al. [2018b]	Continuous	CF,GF,KF	Nylon®	20 to 70 Vol%	Post extrusion	Markforged® tests for inter-laminar bonding with variations in layer thickness, number of layers and fibre Vol%	-
Caminero et al. [2018a]	Continuous	CF,GF,KF	Nylon®	3 to 50 Vol%	Post extrusion	Markforged® tests, layer thickness, number of layers and fibre Vol% fraction influence on impact performance	●●●●●
Hu et al. [2018]	Continuous	CF Toray T300-T1000	PLA	-	Pre-Impregnated	Pre-preg filament development, ext. head modification, printing parameter variation, mathematic model and flexural tests	-
Vaneker [2017]	Continuous	CF	PP	-	Pre-Impregnated	Pre-preg filament fabrication, ext. head development, fibre cutting system addition, software modification, void analysis and flexural samples	-

Increase in Properties - Increase in strength ○○○○○ - up to 20% ●○○○○ - over 20% ●●○○○ - over 40% ●●●○○ - over 60% ●●●●○ - over 80% ●●●●● - over 100%

73

Table 2.18: Discontinuous fibres process characteristics resume

Author [Date]	Disposition	Fiber type	Matrix	Fiber content	Process type	Focus	Properties Inc.
Ning et al. [2015]	Short	100 and 150 μm CF	ABS	3, 5, 7.5, 10, 15 wt.%	Filament + CF	Composite development and analysis, mechanical properties comparison	●○○○○
Mahajan and Cormier [2015]	Short	100 μm	Epoxy Resin	14 wt.%	Resin + CF	Micro-extrusion system, UV reinforced resin, mechanical properties	●●○○○
Hull et al. [2015]	Short	100 μm	ABS	5, 10, 15 wt.%	Filament + CF	Composite development, physical(properties, expansion, extrusion rate)	-
Tekinalp et al. [2014]	Short	200 and 400 μm	ABS	10, 20, 30, 40 wt.%	Filament + CF	Composite development, voids and gap analysis, fibre bonding and count, mechanical property comparison (printed vs molded)	●●●●●
Nikzad et al. [2011]	Short	20 and 45 μm Cu and Fe	ABS	5, 10, 20, 30 and 40% Vol	Filament + Cu and Filament + Fe	Filament development, thermo-mechanical behavior analysis	○○○○○
Zhong et al. [2001]	Short	Glass fibre	ABS	-	Filament + CF	Filament fabrication, introduction of plasticizer and compatibilizer, SEM analysis	-
Gardner et al. [2016a]	Nano tube yarn	CF	Ultem®	4.7 wt.%	Filament + CF	Fabrication of a nanotube yarn, mechanical, conductive properties	●●●●●
Weng et al. [2016]	Nano tubes	Montmorillonite (OMMT)	ABS	1, 3, 5 wt.%	Filament + CF	Filament fabrication with organic modified montmorillonite, mechanical property comparison, flexural, thermal expansion and dynamic tests	●●●○○
Shofner et al. [2003]	Nano fibre	L=100 μm, D=100 nm	ABS	10 wt.%	Filament + CF	Filament fabrication with Vapor-grown carbon fibres, SEM analysis, mechanical property comparison	○○○○○
Liao et al. [2018]	Short	CF 15mm	PA	2, 4, 6, 8 and 10 wt.%	Filament+CF	Filament development, printing parameters definition, DSC, MFI, tensile and flexural tests	●●●●●
Hofstätter et al. [2016]	Short	CF 100μm	PLA	15 wt.%	Filament +CF	Commercial filament and printed part Radiological Imaging and SEM, orientation and dispersion analysis	-
Zhang et al. [2018]	Short and nano tubes	CF	ABS	14 and 8 wt.%	Filament+CF	Interfacial bonding strength for printed samples with different infill angles (0,45,90°), tensile and double notch test	-

Increase in Properties - Increase in strength ○○○○○ - up to 20% ●○○○○ - over 20% ●●○○○ - over 40% ●●●○○ - over 60% ●●●●○ - over 80% ●●●●● - over 100%

Chapter 3

Supporting experimental studies

This chapter presents a group of supporting studies that were performed in order to provide a better understanding of the material's mechanical and thermal characteristics, consequent processability from filament to part and difficulties of printing reinforced materials. Section 3.1 describes a set of thermal and mechanical tests performed to a large group of materials from the distinct classes in filament form. Through this study, the most influential properties of each material were identified, thus recognizing restrictions at the processing level. Section 3.2 describes a first study with a short fibre reinforced material by comparing printed parts with its unreinforced version, at mechanical and thermal level. This analysis was performed using PETG based materials, since both reinforced and pure versions were easily obtained in addition to the ease of process that they provided at fabrication. In Section 3.3 a study in which mechanical testing of continuous carbon fibre reinforced PA samples using Markforged® was performed, presenting the benefits and limitations of continuous fibre deposition. In Section 3.4 three distinct PA were compared in different printing orientations/patterns allowing a better comprehension of the resultant distinct mechanical performance.

3.1 Feedstock Analysis

This section presents an analysis of the feedstock as provided by the supplier. Since the material is produced in an industrial environment in large batches, it is expected that imperfections might occur. These flaws may become from factors such as interferences in the production process, ageing of the material, climate alterations, contamination during its process, resulting in variation of properties, even in the same production batch. Thus, an analysis of the material proved to be of relevance in order to obtain better quality parts, regarding print quality, mechanical performance and correspondent ease of process. Table 3.1 presents a number of commercially available filaments, divided into four sections; commodity, engineering, reinforced (several matrices, including some of high performance) and high performance polymers, presenting the processing temperatures among other details. Focusing on the engineering and the reinforced group of material, a thermal, mechanical and dimensional characterization was performed.

3.1.1 Dimensional Control

Dimensional control of the feedstock was performed by taking diameter measurements with a calibrated calliper each 200 mm in a total of 15 sections, in order to best evaluate the uniformity of the material along its length. A higher or lower (constant) filament diameter, along other parameters, such as extrusion speed and nozzle diameter, dictates the flow of the material that is going to be extruded. Diameter measurements allow to adjust and prevent printing issues that might be associated with over or under extrusion. The diameter variation or irregular dimensions prompt printing issues such as nozzle clogging, irregular flow and consequently uneven surfaces. In fact, a quality filament might not have the announced dimension but present a low level of diameter variation. Tolerance values defined by the material manufacturers are regularly in ± 0.10 and ± 0.05 mm for 2.85 mm and 1.75 mm filaments correspondingly.

The results presented in Figure 3.1 and 3.2, which are divided in the same categories as suggested in the Table 3.1, show the differences in diameter. Commodity polymers (Figure 3.1a), present a consistent diameter throughout the length, proven by the low values of the standard deviation. Engineering polymeric feedstock show higher levels of divergence from the original dimension as well as increased standard deviation. The worst results were obtained for Taulman3D PA6/69 Alloy 910 with a diameter 94% the reference value and a standard deviation exceeding the manufacturers tolerance. Fillamentum PA12 FX256 is 96% of the reference diameter, however presents low values of deviation.

Considering the high performance polymers (Figure 3.2a), beyond PEI material from Indmatec, which presents a high standard deviation, there are no relevant values to consider. Reinforced materials class (Figure 3.2b) present no considerable irregularities throughout all the tested samples. However, PA 66 + 4 wt.%CNT and PEEK + 4 wt.%CNT materials (as stated in Table 3.1) were developed by the University of Minho's (UM), Institute of Polymers and Composites (IPC) in the scope of FIBR3D Project, thus being prototype materials and consequently not commercialized. Therefore, by analysing the diameter results, PEEK materials present a closer value

Table 3.1: Commercial details of FFF materials.

Commodity Polymers			
Base Material	Comercial Reference	Manufacturer	Printing temperatures [ºC]
PLA	PLA BQ	BQ	200-220
PLA	Premium PLA	Formfutura	190-225
ABS	ESUN ABS	ESUN	220-260
PETG	HDGLASS	Formfutura	230-265
Engineering Polymers			
Base Material	Comercial Reference	Manufacturer	Printing temperatures [ºC]
PA 12	STYX-12	FormFutura	240-270
PA 6/69	Aloy 910	Taulman3D	250-255
PA 12	Nylon FX256	Fillamentum	235-250
PA 6/66	Tough Nylon	Markforged	270
PA Alloy	iOn Nylon Alloy	3DXtech	240-270
Reinforced Polymers			
Base Material/Reinforcement	Comercial Reference	Manufacturer	Printing temperatures [ºC]
PLA + CF[2]	Proto-pasta PLA	Proto-pasta	210-230
PETG + CF[2]	CarbonFill	Formfutura	230-265
ABS + CNT[3]	3DXSTAT ESD ABS	3DXtech	220-240
PA 6 + CF[2]	CarbonX	3DXtech	240-270
PA 12+CF[2]	Nylon CF15	Fillamentum	235-260
PA 66 + 4%CNT[3]	PA66	Developed by IPC[1]	-
PEEK + 4%CNT[3]	PEEK	Developed by IPC[1]	-
PEEK + 2%CNT[3]	PEEK	Developed by IPC[1]	-
High Performance Polymers			
Base Material	Comercial Reference	Manufacturer	Printing temperatures [ºC]
PEI	PEI - Ultem 9085	Indmatec	330-350
PEI	PEI - Ultem 9085	3D4MAKERS	340-360
PEEK	PEEKQ	3D4MAKERS	360-400
PEEK	PEEK	3D4MAKERS	360-400

[1] Material developed for FIBR3D project (https://www.researchgate.net/project/FIBR3D
[2] Carbon Fibres
[3] Carbon Nano Tubes

to 1.75 mm and a higher variation, while PA 66 differs from this same announced value and lower variation throughout its length.

Depending on the material and its density, 1 kg spool can hold from 300 to 400 meters of 1.75 mm of filament. This analysis was performed along a small portion of its length, being representative of the shifts in short segments. However, it is estimated that bigger ones might occur for higher lengths.

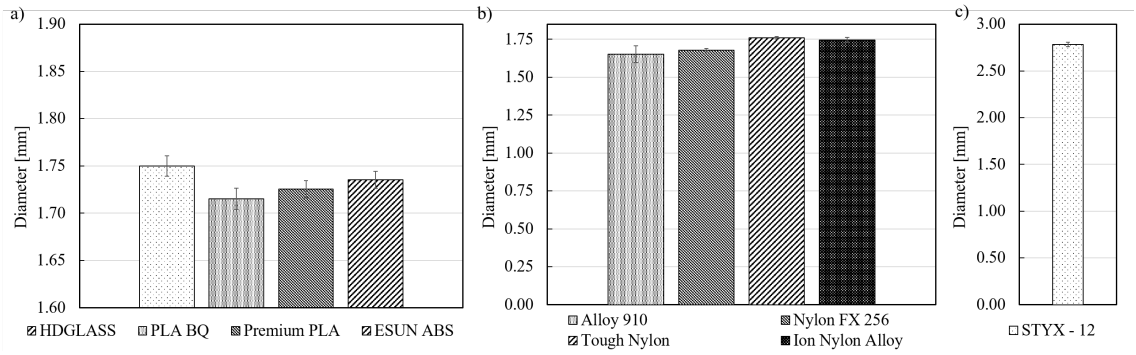


Figure 3.1: Average diameter value of: (a) Commodity, (b) ⌀1.75 mm Engineering Polymers and (c) ⌀3.0 mm Engineering Polymers.

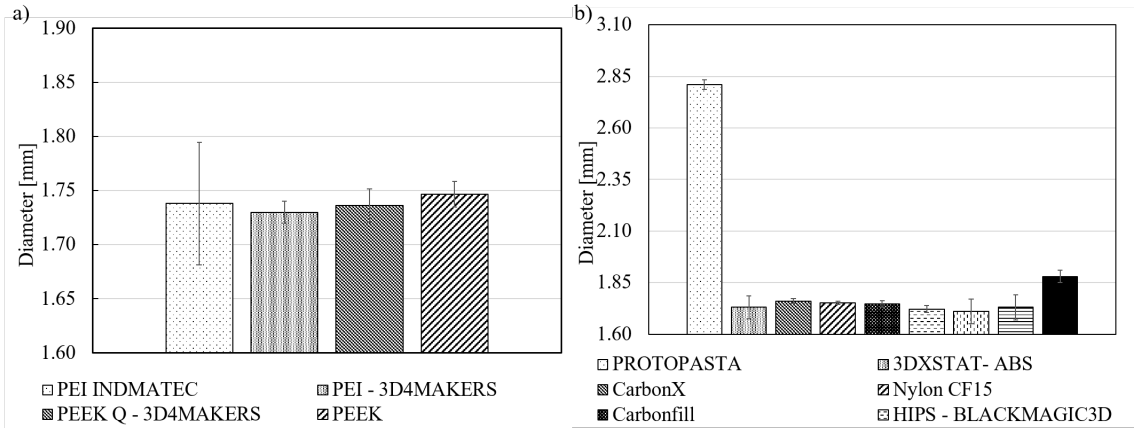


Figure 3.2: Average diameter value of: (a) High Performance and (b) Reinforced Polymers.

3.1.2 Feedstock Tensile test

Considering that each printed part can be associated as a structure instead of a homogeneous sample, a simple way to understand the material behaviour is to test the filament itself in a tensile manner. Therefore, the testing of a homogeneous sample is possible without the need of laborious and expensive processes of granulating filament, mould fabrication and injection moulding it into the dogbone shape. It is also important to disclaim that for polymeric filaments there is no associated standardized test. A set of bollard grips was developed, considering this type of test, despite suitable for higher performance materials such as metallic wires, carbon/kevlar and glass fibres due to the alignment position needed. Considering the inferior mechanical properties of the filaments, a set of clamp grips was used with a 5kN load cell and a test speed of 1 mm/min. The different behaviour of the materials is depicted in Figures 3.3 and 3.4, while the summary results is presented in the Table 3.2.

Given the mechanical response of these four groups of materials depicted in Figures 3.3 and 3.4, different patterns are delineated. Commodity polymers show maximum stress averaging 40 to 50 MPa and low levels of strain when compared to the other material categories, as can be observed in Table 3.2. Engineering Polymers, which in this case consists only in PA materials,

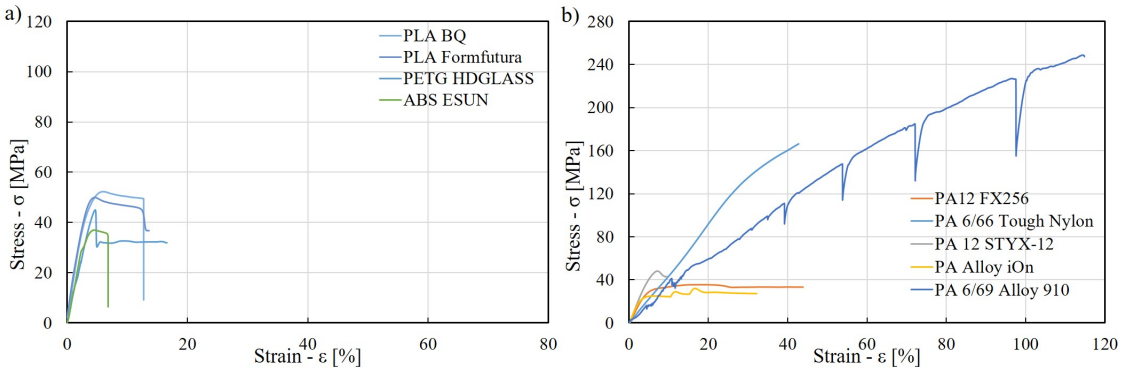


Figure 3.3: Filament tensile test: (a) Commodity polymers and (b) Engineering polymers.

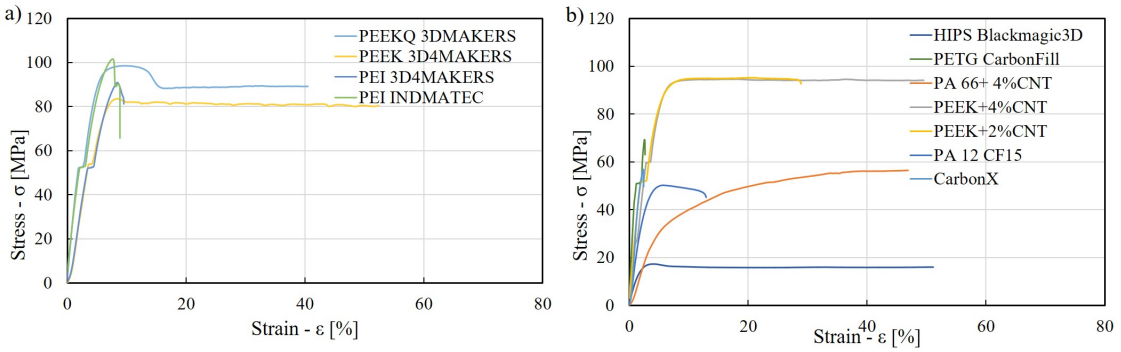


Figure 3.4: Filament tensile test: (a) Reinforced polymers, and (b) High performance polymers.

are confirmed as having a more ductile behaviour, even though the maximum stress remains similar to commodity polymers. However, Tough Nylon presented a non expected behaviour with a normal strain at break but an abnormal maximum stress, putting itself in the high performance polymer range. Alloy 910 also presented atypical behaviour, with a maximum stress of 240 MPa, and the highest strain at break of approximately 115%. Through its curve, it is possible to verify that several neck areas were developed, thus the high levels of strain. High performance polymers (Figure 3.4a), show two distinct behaviours, PEI based materials present much less ductile behaviour than PEEK based ones. Since the reinforced polymers (Figure 3.4b) consist in different matrix materials and distinct types of reinforcements, the results cover three types previously discussed.

Taking into account the discussed results, through Table 3.2 it is easily identifiable that pure polymers and their respective reinforced versions present different properties. By comparing PETG HDGLASS vs CarbonFill, the presence of fibres is notorious by the decrease in ductility and increase in maximum stress. The same behaviour is observed by comparing PA 12 FX256 vs PA 12 CF15 and PA Alloy iON vs PA6 CarbonX, even though the matrix is not exactly the same in this last pair. Considering that due to lack of availability of some materials, a distinct number of samples was tested for different materials, therefore, only the average value is presented, being merely indicative of the materials properties.

Table 3.2: Filament tensile test mechanical properties.

Commodity Polymers		
Reference	Maximum Stress [MPa]	Strain at break [%]
PLA BQ	52.27	12.72
PLA Formfutura	49.96	13.61
ABS ESUN	36.95	6.80
PETG HDGLASS	44.99	16.56
Engineering Polymers		
Reference	Maximum Stress [MPa]	Strain at break [%]
PA 12 STYX-12	48.11	9.54
PA 12 FX256	35.49	43.89
PA 6/66 Tough Nylon	166.30	42.77
PA 6/69 Alloy 910	248.76	114.83
PA Alloy iOn	32.01	32.22
High Performance Polymers		
Reference	Maximum Stress [MPa]	Strain at break [%]
PEI Indmatec	101.54	8.86
PEI 3D4MAKERS	90.83	9.51
PEEKQ 3D4MAKERS	98.45	43.55
PEEK 3D4MAKERS	83.47	52.44
Reinforced Polymers		
Reference	Maximum Stress [MPa]	Strain at break [%]
PETG + CF CarbonFill	69.31	2.63
PA 6 + CF CarbonX	56.80	2.38
HIPS+CF+Graphene	17.27	70.25
PA 12 + CF CF15	50.21	12.92
PA 66 + 4 wt.%CNT	56.43	46.90
PEEK + 2 wt.%CNT	95.19	28.90
PEEK + 4 wt.%CNT	94.57	49.53

3.1.3 Thermal characterization

3.1.3.1 TGA

Thermogravimetric analysis (TGA) is a method used to determine the polymers' thermal stability, in which the mass of a sample is measured over time with changes in temperature. This type of equipment is equipped by a precision balance inside of a furnace which raises the temperature and consequently measures the difference in mass with temperature. Tests were performed in a Q500 gravimetric balance from TA instruments (USA). A ramp of 10 °C/min was used, starting at 30°C

until 700°C with nitrogen atmosphere. Considering the available equipment range, the main focus of this work is focused on engineering thermoplastics and its fibre reinforced versions, therefore, not all of the materials presented in Table 3.1 were thermally analysed. Figure 3.5 shows the weight loss diagram (a) and respective derivative weight (b).

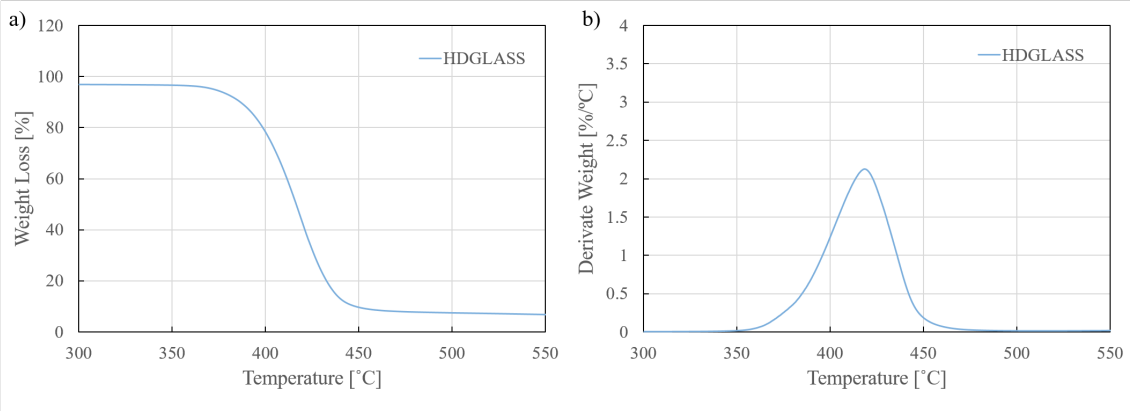


Figure 3.5: TGA results for commodity polymers; a) Weight loss, and b) Derivative weight.

It is possible to verify that HDGLASS material degradation starts at 370°C, reaching its maximum degradation rate at 420°C.

Through Figure 3.6a it is possible to observe that even though the materials are all unreinforced PA, there is a significant difference in degradation rates. Tough nylon and iOn nylon start their degradation (around 350 °C), earlier than the other polyamides, in a longer range of temperatures, reaching degradation peak at 404 and 422°C respectively (Figure 3.6b). Alloy 910, FX 256 and STYX-12 show a more pronounced step, and a shorter range of degradation, starting around 370°C for the first and 400°C for the others. Through the derivative weight curves, it is possible to observe that the maximum values occur at 438, 447 and 452 °C for Alloy 910, FX 256 and STYX-12 respectively.

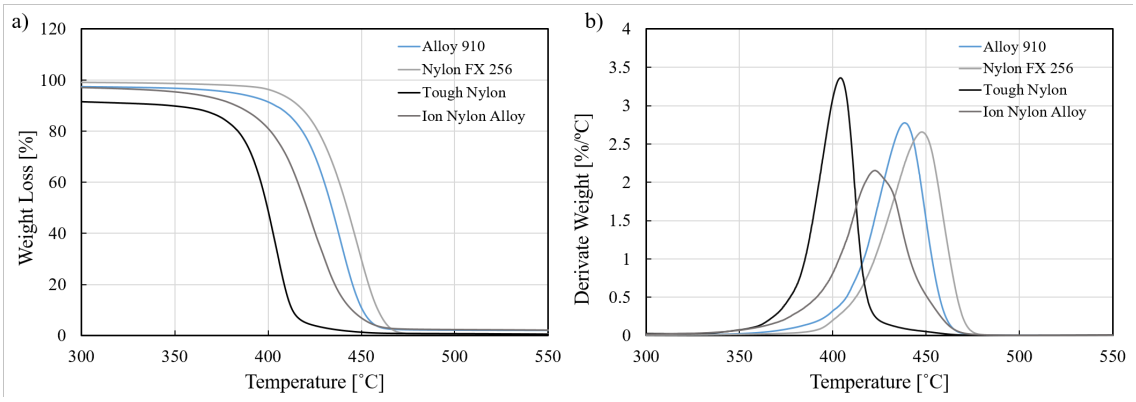


Figure 3.6: TGA results for engineering polymers; a) Weight loss, and b) Derivative Weight.

By analysing the reinforced materials TGA results (Figure 3.7), it is possible to confirm that

Proto-pasta's polymeric matrix (PLA) it is processed at lower temperatures since it starts its degradation at 310 °C and reaches its peak at 350 °C. The other three materials present similar temperature ranges. CarbonFill (PETG matrix) degradation starts more abruptly than CF15 and CarbonX altering the slope in midcurve, indicating a rate change. Maximum degradation rates are at 416 °C for CarbonFill, 433 °C for CarbonX and 443 °C for CF15. While in the previous material categories the final weight of the samples, is approximately 0 %, in reinforced materials it presents a residual value of 12 to 20% that is related with the fibre percentage.

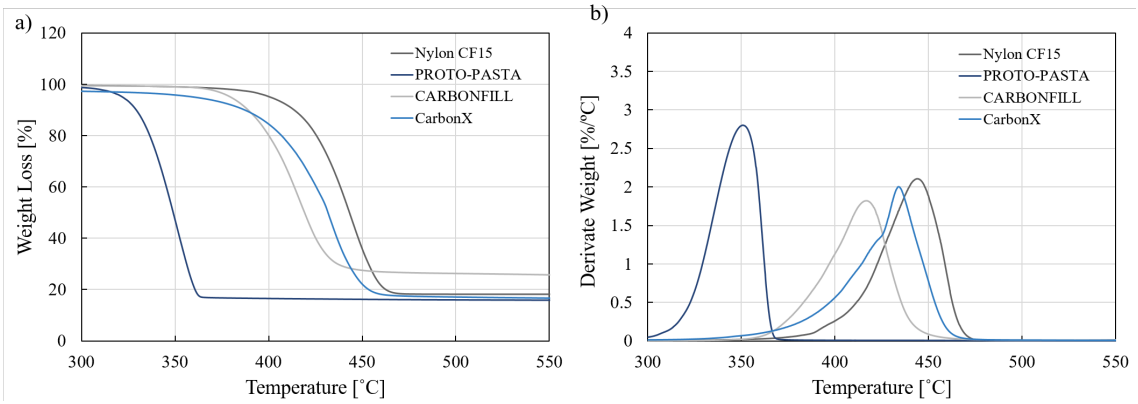


Figure 3.7: TGA results for reinforced polymers; a) Weight loss, and b) Derivative weight.

3.1.3.2 Fibre reinforced vs unreinforced materials TGA

The difference in weight loss final values indicates the fibre content by weight present in the reinforced sample, making the assumption that both polymer compositions are similar. In HDGLASS vs CarbonFill (Formfutura) (Figure 3.8a), the curves present the same profile, roughly similar degradation peaks at 418 and 416°C (Figure 3.8b), respectively, at lower percentages for the reinforced. Through this analysis, the fibre content present in CARBONFILL is 19 wt.%, which is near the 20 wt.% as presented in datasheet [FormFutura, 2019]. Comparing FX 256 and CF15 from Fillamentum (Figure 3.9), the results confirm the above-mentioned, same profile curve and peaks at 447 and 443°C respectively. These results show that pure thermoplastic filament is similar to the reinforced version for both cases. Difference in weight loss indicate a fibre content of 15 wt.% as presented in the datasheet [Fillamentum, 2019a]. A different scenario is presented for the iOn Nylon vs CarbonX from 3DXTECH (Figure 3.10a), in which the curve have distinct profiles, reaching its maximum degradation at 422 and 433°C, indicating that there is a difference in the material composition. Even though, the fibre content calculated is 15 wt.%.

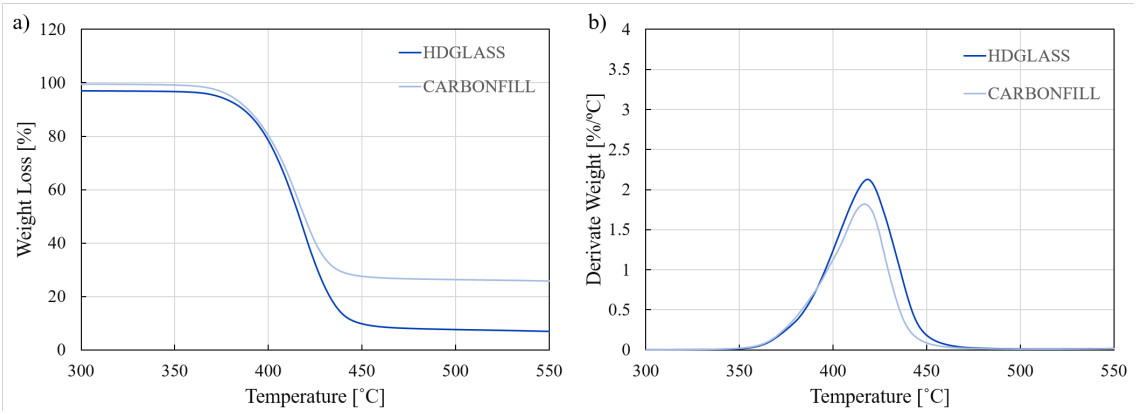


Figure 3.8: TGA - Reinforced vs pure PETG (CarbonFill vs HDGLASS).

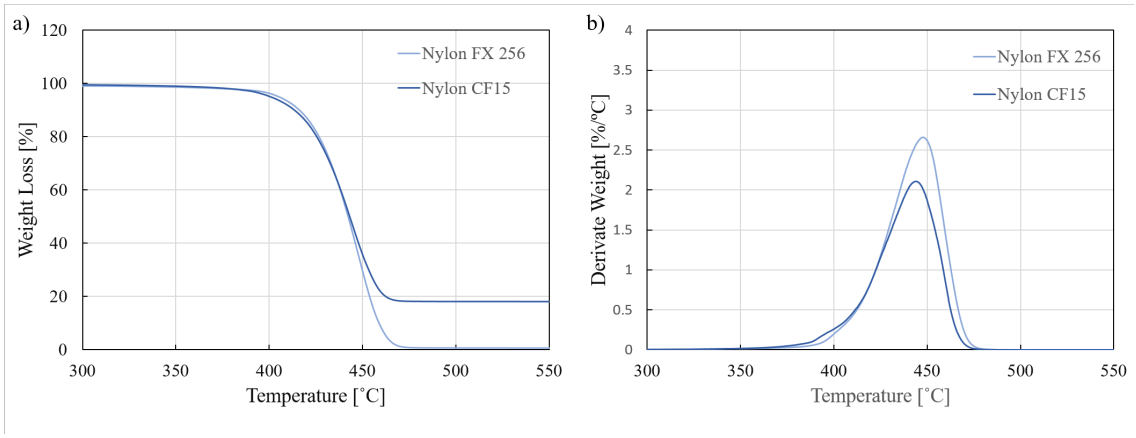


Figure 3.9: TGA - Reinforced vs pure PA (FX256 vs CF15).

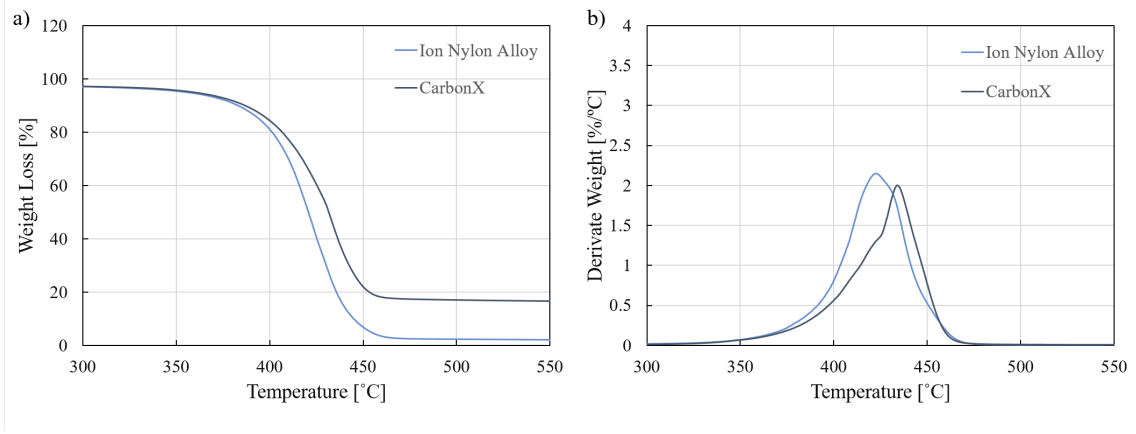


Figure 3.10: TGA - Reinforced vs pure PA (CarbonX vs iOn).

3.1.3.3 DSC

Differential scanning calorimetry (DSC) is a material characterization technique in which the differences in the heat flux are compared between a controlled sample and the testing sample during a gradual temperature increase and consequent decreased. The principal outputs of this technique are glass transition (T_g), melting (T_m) and crystallization (T_c) temperatures for polymeric based materials. Other values such as fusion enthalpy (ΔH_f), crystallinity percentage (%X), specific heat (C_p) among others can be obtained. For the filament analysis, DSC measurements were carried out in a 200 F3 equipment from Netzsch® (Germany), under nitrogen purge, using a range of temperatures from 30°to 300°and two heating cycles along with the cooling scanning. For analysis purposes, the first heating cycle was not represented as it was performed to eliminate any possible effects of thermal history. Figure 3.11 presents heating and cooling curves of each filament divided into the previously defined groups. Apart from HDGLASS and CarbonFill, which are PETG based polymers, thus presenting an amorphous behaviour (with no fusion or crystallisation points), all the other materials present their semi-crystalline behaviour and respective peaks.

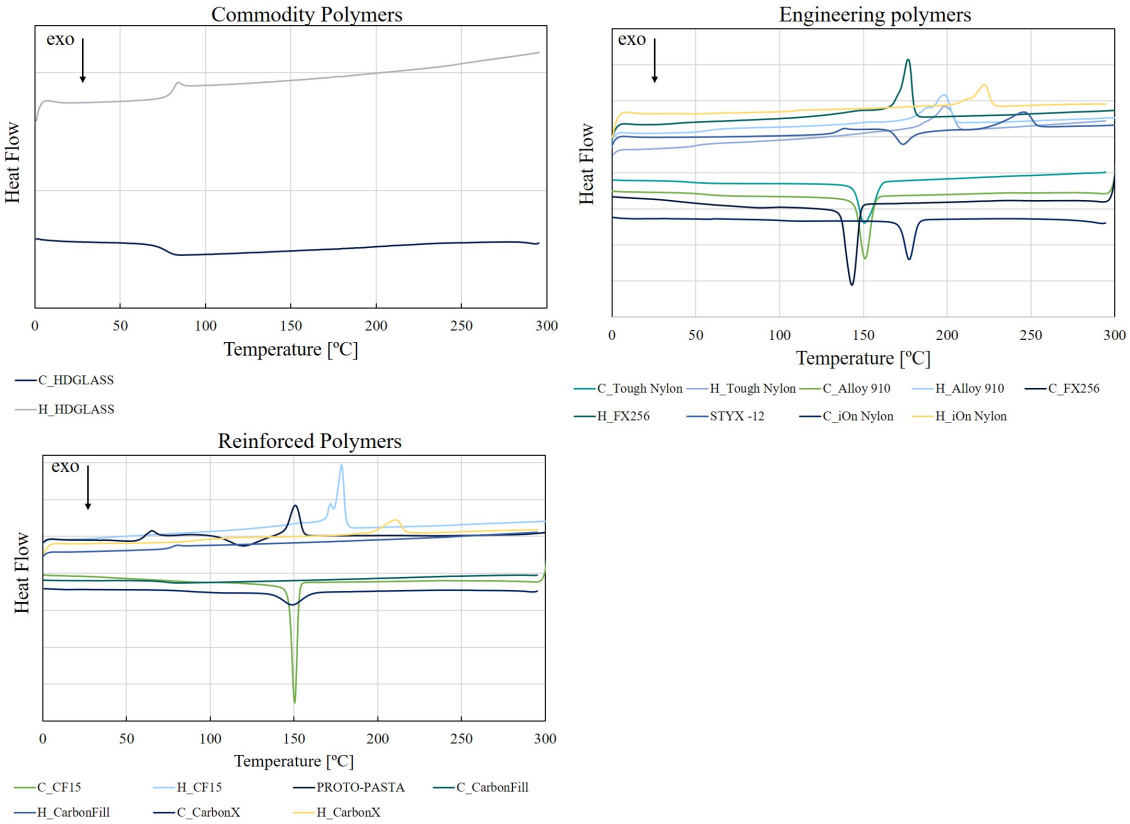


Figure 3.11: DSC curves for commodity, engineering and reinforced polymers

Table 3.3 depicts the most relevant values obtained from the DSC curves. In order to calculate the crystallinity percentage (X[%]), the following equation was used:

$$X[\%] = \frac{\Delta H_f}{\Delta H_f^*} \tag{3.1}$$

Where ΔH_f is the material fusion enthalpy and ΔH^*_f is the fusion enthalpy of the 100% crystalline, values which can be found in literature [Blaine, 2002, Fehri et al., 2016].

Table 3.4 depicts the values obtained from the literature review. Some of these values were already available from previous researches, others from material datasheet and CES Edupack material database [Design, 2018]. However, none of these provided any information about crystallization temperature. In addition, the CES Edupack provided values that do not reflect the actual values of the specific commercial reference, but only the type of material (i.e. PA 12, PA 6 and others). This alternative was only considered when there was no other source of data for the material.

For both PETG based materials, it is possible to observe coherence in the obtained values, considering reinforced vs pure matrix, which can be roughly inserted in the literature temperature range. Focusing on the engineering materials, there is still no comparative value for crystallization points.

Table 3.3: DSC test results.

Commodity Polymers

Details		DSC Results				
Base Material	Commercial Reference	T_c [ºC]	T_m [ºC]	T_g [ºC]	ΔH_f [J/g]	X [%]
PETG	HDGLASS	-	-	79.9	-	-

Engineering Polymers

Details		DSC Results				
Base Material	Commercial Reference	T_c [ºC]	T_m [ºC]	T_g [ºC]	ΔH_f [J/g]	X [%]
PA 12	STYX-12	173.4	245.5	58.4	21.7	8.9%
PA 6/69	Alloy 910	151.0	197.7	61.3	34.1	13.2%
PA 12	Nylon FX256	143.2	176.3	44.7	35.5	14.5%
PA 6/66	Tough Nylon	151.0	198.8	50.6	33.9	15.0
PA 6 Alloy	iOn Nylon Alloy	177.5	222.3	110.4	17.5	-

Reinforced Polymers

Details		DSC Results				
Base Material	Commercial Reference	T_c [ºC]	T_m [ºC]	T_g [ºC]	ΔH_f [J/g]	X [%]
PLA+CF	PROTO-PASTA	119.8	150.9	59.3	19.4	20.7
PETG+CF	CarbonFill	-	-	76.4	-	-
PA 6+CF	CarbonX	148.5	210.7	94.6	14.9	6.5%
PA 12+CF	Nylon CF15	150.4	178.5	52.9	14.9	6.1%

Literature refers that, as the level of crystallinity grows for a certain polymer, its Young's modulus, strain at break and hardness increase [V. and Canevarolo, 2002]. This is valid for the same material, even if processed in different conditions. Considering that STYX-12 and FX 256

Table 3.4: DSC values from the literature review.

Commodity Polymers

Details		Literature values			
Base Material	Commercial Reference	T_c [ºC]	T_m [ºC]	T_g [ºC]	Ref
PETG	HDGLASS	-	-	76-79	Ferreira et al. [2018a]

Engineering Polymers

Details		Literature values			
Base Material	Commercial Reference	T_c [ºC]	T_m [ºC]	T_g [ºC]	Ref
PA 12	STYX-12	-	240-260	-	datasheet[1]
PA 6/69	Alloy 910	-	196-215	54-62	Design [2018]
PA 12	Nylon FX256	-	171-174	40-43	Design [2018]
PA 6/66	Tough Nylon	-	210-220	44-56	Design [2018]
PA 6 Alloy	iOn Nylon Alloy	-	-	105	datsheet[2]

Reinforced Polymers

Details		Literature values			
Base Material	Commercial Reference	T_c [ºC]	T_m [ºC]	T_g [ºC]	Ref
PLA+CF	PROTO-PASTA	-	145-175	52-60	Design [2018]
PETG+CF	CarbonFill	-	-	75-78	Ferreira et al. [2018a]
PA 6+CF	CarbonX	-	-	70	datasheet [2]
PA 12+CF	Nylon CF15	-	160	-	datasheet[3]

[1] https://www.formfutura.com, access date:5/4/2019;
[2] https://www.3dxtech.com, access date:5/4/2019;
[3] https://www.fillamentum.com, access date:5/4/2019.

are both PA12 materials, it is difficult to included them in the previous statement, since they come from different manufacturers. In addition, other influential factor is the difference in diameters (STYX-12 - 2.8 mm and FX 256 - 1.75 mm), implying that in the manufacturing process, the smallest diameter is more strained than the previous, creating longer and better aligned crystals.

Amorphous polymers are usually easier to print since they do not present a crystalline phase. Due to their low level of molecular orientation, less contractions and residual stresses occur in the material when cooled. The same does not happen for semi-crystalline polymers, where the crystalline phase is denser and tends to reorder their molecules, contracting more than the amorphous phase, creating a great deal of residual stresses in the part after being extruded through the nozzle (cooling cycle). As a result of this phenomenon, warping and other defects can be minimized by identifying T_m, T_c and T_g, ensuring the ideal processing conditions, controlling crystallization, shrinkage and consequent stresses by regulating the cooling rate through the entire part. Figure 3.12 depicts Alloy 910 heating and cooling curves. The operation window is defined by T_m onset, which is the point where the material starts to melt and, under the T_g onset (which happens at lower

temperatures than the T_g offset), is where the polymeric chains lose their molecular mobility [V. and Canevarolo, 2002]. In order to manage crystallization rates, shrinkage and residual stresses, it is important to control the cooling rate of the part. In the FFF specific case, the control of these rates is directly related to the introduction of an heated bed or chamber in the process, which will allow a more perfect spherulites. For certain cases, crystallization only occurs if the temperature remains in the appropriate range for a certain period of time, which translates to the growth of crystallites being much slower than the cooling rate [Sorrentino et al., 2007, Frankland, 2013].

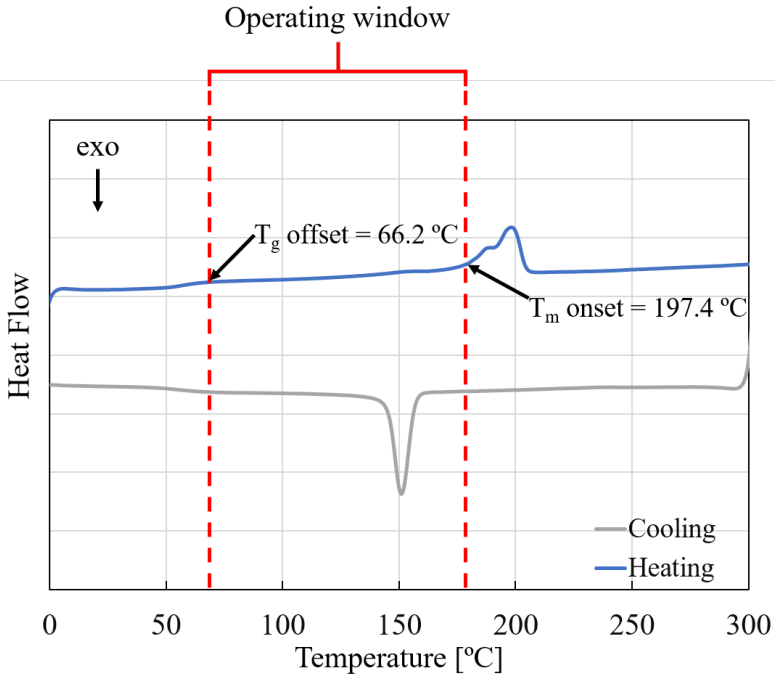


Figure 3.12: Operating window for Alloy 910 thermoplastic.

3.1.3.4 MFI

Melt flow index (MFI) consists in the measurement of the material flux through a small orifice under pre-defined load and temperature conditions during ten minutes, representing the polymer flow index. The tests to the commercial materials were performed using a MFI Daventest (UK) equipment following International Organization for Standardization [2011]. The material was pushed through a capillary by means of the application of 2.16 kg after a pre-defined period of time. The temperatures at witch these tests were conducted were defined according to the printing temperature range provided by the manufacturer data-sheet. Therefore, STYX-12 was processed at 275°C, Alloy 910, CF15 and FX256 at 250 °C and Protopasta at 210 °C.

MFI results (Figure 3.13) indicate how fluid the material becomes at ideal printing temperature. Therefore, the most fluid material is STYX-12, which contrasts with Alloy 910 with the lowest MFI, and consequently higher viscosity. Proto-pasta is the second less viscous material. To finalize, both PA 12 from Fillamentum present similar behaviours, being the unreinforced (FX256)

more fluid than the reinforced version (CF15), thus leading to believe that the presence of fibres makes the material more viscous.

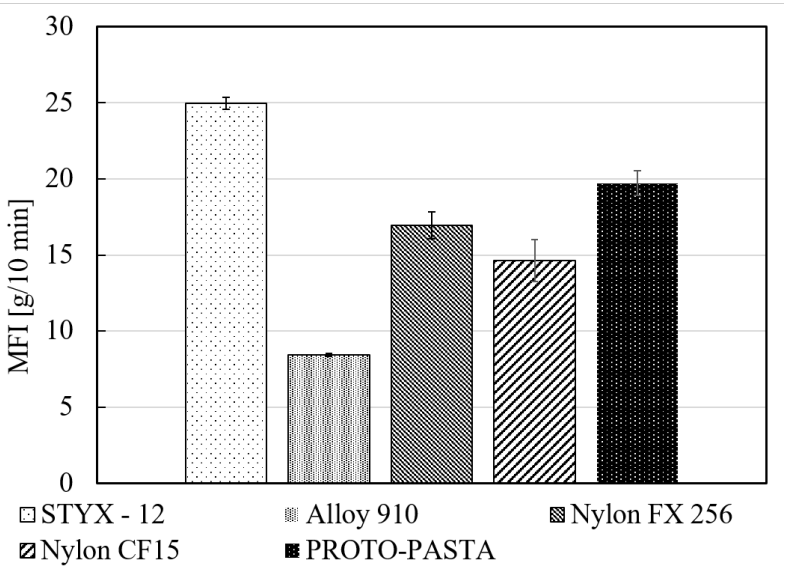


Figure 3.13: MFI results.

As previously stated, FFF process consists in the extrusion of a polymer through a small dimension nozzle. This nozzle consists in a highly conductive piece of metal with an internal section reduction, which usually has the diameter of the filament of 0.5 mm. An highly viscous material will create higher pressure in the nozzle than a more fluid material, for this reason it is harder to print. High viscosity materials lead to poor adhesion among layers and extruded lines, which consequently results in lower mechanical properties. Since the material is more viscous it is difficult for it to reach some of the more confined areas, resulting in higher levels of air gaps in the part. In essence, the level of viscosity is highly relevant for the final part performance, despite the fact that this value can be changed according with processing temperatures [Khaliq et al., 2017].

3.1.3.5 Thermal conductivity

Thermal conductivity was measured using an Alambeta apparatus in which the feedstock needed to be converted into a disc shape with 40 mm diameter and 3 mm thickness respectively, via granulation and consequently hot pressing. Figure 3.14 depicts the thermal conductivity results.

It is shown that all PA materials have roughly similar values, being Alloy 910 the most conductive material. In contrast, Proto-pasta, which is a PLA based material, is the less conductive, even though containing short carbon fibres as reinforcement (which promotes conductivity). This conclusion is confirmed by the fact that CF15 conductivity value is significantly higher than its unreinforced version.

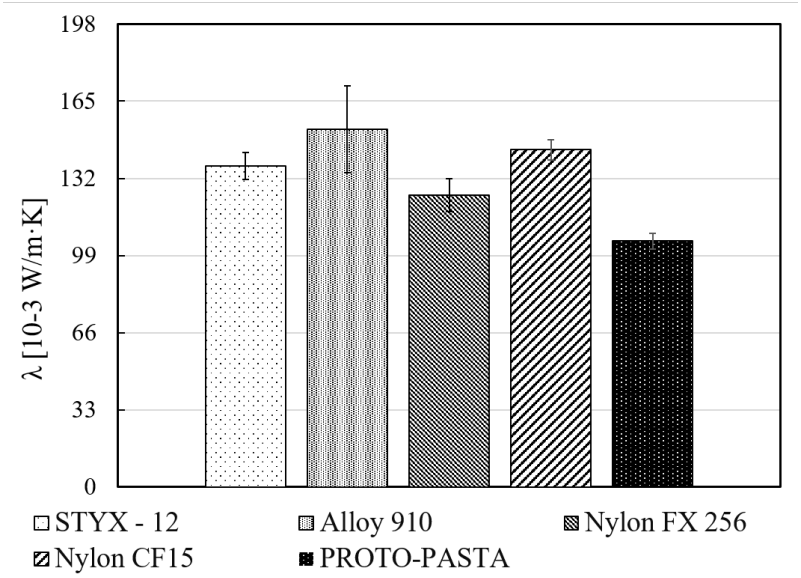


Figure 3.14: Thermal conductivity of different filaments.

3.1.4 Final remarks

With the FFF process uprising, new types of enhanced polymers have been formulated, to specifically accommodate the technology characteristics. This section focuses in the analysis of commercial types of feedstock in order to better understand their capabilities, leading to an improved printing process. Beyond the data provided by each material datasheet, which in some of the cases has proven to be unreliable, it is important to categorize and properly understand how these polymers behave in terms of mechanical performance and thermal properties, which is related to the ease of printing process. This analysis focused in the study of dimensional, mechanical and thermal differences among the same category polymers, and outside the group.

A feedstock dimensional analysis, provided an insight to the variability along its length as well as the deviation from the original dimension, indicating that if even the measured average value is not the same as announced diameter for the most materials, the variation is, however, mostly inside the manufacturers range. A feedstock tensile test was performed in order to comprehend how much the performance varies within categories. It was shown that some of the engineering polymers presented an above average strength, surpassing even high performance polymers. The thermal analysis was performed to the materials. This analysis was based upon the processing temperatures provided by the manufacturers datasheet, which were capable of being processed by the available hardware, thus being disregarded the high performance group. Through DSC, the studied polymers critical transition points were determined, presenting a foundation for the following studies. By comparing reinforced vs unreinforced materials in the TGA test, it was possible to obtain the true (wt.%) fibre content. Overall, it was possible to create an understanding of the tested polymers behaviour, knowing before hand their properties and, consequently, how to minimize problems related to the printing process.

3.2 Additive manufacturing of PETG/Carbon fibre composites: an experimental study from filament to printed parts

This study was previously developed in the curricular phase of this work and published in Proceedings of the Institution of Mechanical Engineers, Part L: Journal of Materials: Design and Applications [Ferreira et al., 2018a]. The current section is presented in article form, as published.

By selecting the reinforced PETG, it was possible to take advantage of the the easy processability/printability of this material, and in order to comprehend how short fibre reinforced materials can behave, several types of experiments were performed. PA material is an engineering thermoplastic which has a more irregular behaviour, requiring higher processing temperatures and a more profound knowledge of the process, thus, not being considered for this first study. This research is focused on a characterization methodology to determine not only mechanical, but thermal and morphological properties of both reinforced PETG and pure matrix material.

This research focuses on the definition and application of a characterization methodology to determine the characteristics of FDM 3D printing materials. Commercial short fibre reinforced and unreinforced PETG parts were tested achieving comparison terms. The presented methodology is composed in three classes: the thermal analysis, mechanical testing and material morphology. Filament was tensile tested with specially developed setup in order to determine raw material's mechanical properties. Standardized flexural and tensile samples were printed 100% dense in both materials and tested. DSC results showed that thermal properties of both materials do not change with successive heating cycles. TGA analysis allowed to understand the thermal stability of the materials and to quantify the amount of fibre in the matrix. Tensile tests indicated that the addition of fibres increase the Young's modulus by 70.10% but withstanding 28.21% less in stress. Flexural tests exhibited an increase in flexural modulus of 191.38% and 5.14% in flexural strength for the reinforced PETG, due to fibre presence. Microscopy analysis revealed a 12% of void spots and the fibre alignment accordingly to the deposition path.

3.2.1 Introduction

The advances in additive manufacturing (AM) represent a new era for fabrication, considered a turning point for how people imagine and design parts for prototyping. The possibility of creating complex, hollow and intrinsic geometries efficiently with virtually no waste is one of the most meaningful features [Zhai et al., 2014, Lipson and Kurman, 2013]. Although, AM was traditionally meant for rapid prototyping purposes, in nowadays it finds application on many research fields as a technique to produce functional end products, such as automotive/aerospace [Liu et al., 2017], electrical [Li et al., 2017, Auyeung et al., 2017], and, biomedical [Norman et al., 2017, Datta et al., 2017]. Within the range of AM technologies currently available, Fused Deposition Modelling (FDM) [Crump, 1992] or Fused Filament Fabrication (FFF) has attracted much attention among scientists and hobbyists, due to its simplicity, the possibility to use different types of feedstock, recyclability of the printed products, and total cost (hardware and feedstock). For instance, due

to FFF's flexibility, Volkswagen Autoeuropa Lda (Portugal) is already using Ultimaker® (Netherlands) printed parts to create customized tools to help maximize efficiency in production lines. These low cost machines can also provide this type of services, due to its capability of producing completely different parts with no need for expensive moulding or machining services for short-term disposable tools. The conventional FFF machine comprises: i) an extrusion head, and, ii) a building plate. The former is responsible to melt and extrude a thermoplastic material (in filament form) through a small dimension nozzle (with diameter ranging 0.1-0.8 mm).

The extrusion produces and deposits a molten strand over a building plate, which accommodates the part that is being produced. Simultaneously, the relative motion between the extrusion head and the building plate assures the layer-by-layer shaping of the printed part. Despite the simplicity of the process, new features are constantly emerging [Kruth et al., 1998, Wohlers et al., 2016] to turn this technology more robust, accurate and efficient, and new materials are being formulated for FFF in order to fulfil the requirements demanded by many applications. Thermoplastic materials commonly used in FFF are Acrylonitrile Butadiene Styrene (ABS), Polylactic Acid (PLA), and, Polyethylene Terephthalate-Glycol copolymer (PETG). Aming to obtain improved performance materials, researches have been conducting studies regarding the influence of fibre percentage and length on the mechanical properties of printed samples. These properties are strictly related to the feedstock fabrication, namely amount, orientation and size of fibres [Fu, 1996, Ning et al., 2015] produced ABS thermoplastic filaments, varying the fibre amount and length, identifying the mechanical properties of 3D printed standardized samples. It was found that there is an optimal fibre percentage, with properties increasing (tensile and Young's modulus) from zero to 7.5 wt% of fibres, decreasing incrementally until 15 wt%, and consequently, a decrease in ductility. Comparing fibre length, they have reported that samples with longer fibres obtain improved strength but lower ductility. The authors characterized the parts using flexural and tensile tests. [Tekinalp et al., 2014] analysed the mechanical properties of printed vs compressed moulded samples, concluding that the fibres can fill the voids caused by the roundness of the overlay of the extrusion paths. Furthermore, the fibre alignment is more evident in the printed samples than the compressed moulded, as expected. [Nikzad et al., 2011] proved that it is possible to obtain a semi conductive material by incorporating 10% of Fe in an ABS matrix, showing a higher stiffness with a small decrease in tensile properties. Other type of reinforcement are nanotubes/particles which, in similarity with short fibres, the reinforcement is made with dispersed, low volume fraction of particles [Gardner et al., 2016b, Weng et al., 2016, Shofner et al., 2003]. The process of printing with continuous fibres requires the development of specific new hardware. Since there is an introduction of a new component in the form of a continuous bundle of fibres, it is necessary to find a way of processing both components together [Bettini et al., 2016, Li et al., 2016, Ryosuke Matsuzaki (Tokyo University), 2013]. The previous present different approaches to this challenge, though the only commercial FFF equipment available is Markforged® supporting Kevlar, Carbon and Glass fibres [Mark, 2014].

To the best of the author's knowledge, the conducted studies with similar feedstock focuses in the characterization and improvement of the mechanical properties. The above-mentioned studies

focused in the filament development with several types of reinforcements (geometries) or process of reinforcement and consequent mechanical testing for validation. This work intends to define a more complete methodology, subjecting raw and processed material to testing, by creating a sequence of experiments, analysing several types of properties such as thermal, mechanical and morphological, as represented in Figure 3.15. Thereby, it will be possible to comprehend and evaluate the thermomechanical properties and the effect of the fibres on the material general behaviour. For this work were selected PETG and PETG+CF as basis material for characterization due to its in printing stability (no warping and easy processability) [Lam et al., 2005].

This manuscript contains four main sections. Followed to this introductory section, Section 3.2.2 addresses the materials and experimental methods used. Details of the processing conditions used to fabricate the samples and the setup for the mechanical, thermal and microscopy characterization are provided. Section 3.2.3 refers to the presentation of the results obtained and corresponding discussion. Finally, the highlights of major achievements of this work in Section 3.2.4.

3.2.2 Materials and Methods

3.2.2.1 Materials

Table 3.5 shows the abbreviation list used to differentiate which sample for each test.

Table 3.5: Sample nomenclature

Nomenclature	Designation
rPETGp	Printed reinforced PETG+CF samples
PETGp	Printed PETG samples
rPETGf	Filament reinforced PETG+CF samples
PETGf	Filament PETG+CF samples

Figure 3.15 depicts a schematic representation of the characterization methodology proposed herein. Several areas are analysed, such as thermal, mechanical and microscopical (morphological). The test sequence is logically defined in order to complement and provide better comprehension of the obtained results.

PETG is a copolymer based on PET that is composed by replacing some of the ethylene glycol with secondary glycols (connected along the backbone of the copolymerizing agent [Dupaix and Boyce, 2005]), creating an amorphous co-polyester, which has low levels of crystallinity. The added glycol prevents the material from crystalizing and becoming breakable. These are ideal properties for FFF printing, benefiting from high stability [Lam et al., 2005]. Kattan et al. [2002] studied the difference of crystallinity between PET and PETG and found that the first can crystalize up to 40% while PETG can barely go up to 3%. PETG is used in several areas such as injection moulding applications including, toys, chairs, medical device parts, face shields, display racks, containers and appliances parts [Rosato and Rosato, 2012].

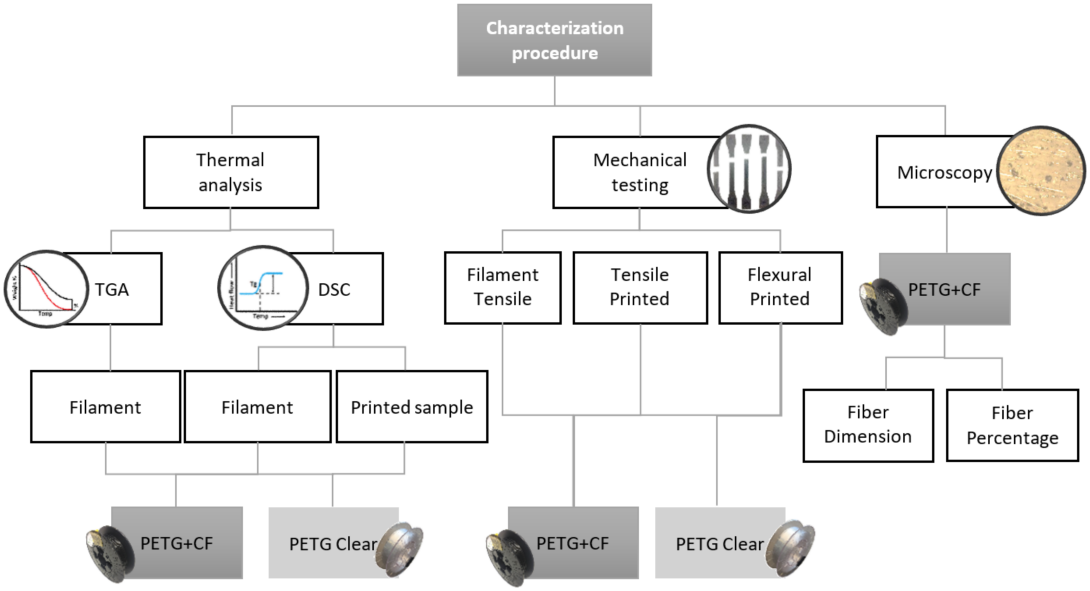


Figure 3.15: Experimental work characterization/graphic abstract

Since one of FFF flaw is the lack of geometrical/dimensional stability (contractions and warping), PETG contradicts these problems since its low crystallinity makes it an ideal material for 3D printing. This work was developed around a short fibre reinforced PETG + 20 wt% carbon content (Carbonfill^{TM}) and PETG pure filament (HDglass^{TM}) from Formfutura[1]. Table 3.6 indicates the filaments technical specifications and considering the overlap in temperatures the same values were selected.

Table 3.6: Technical specifications

rPETG	PETG
Diameter: 1.75 mm	Diameter: 1.75 mm
Printing temp: 225 – 245°C*	Printing temp: 215 – 250°C*
Colour: Natural (black)	Colour: Clear
Fibre content: 20%	Fibre content: 0%

*Typical range of temperatures

3.2.2.2 Sample production procedure

The printing process was conducted in an open-source FFF equipment (Tronxy X5[2]) considering two different types of nozzles for the process. For the reinforced material, a 0.4 mm diameter stainless steel hardened nozzle was used since the carbon fibres are extremely abrasive and for the unreinforced material, a same diameter common brass nozzle. Both materials used the same slicing parameters and temperatures as shown in Table 3.7. For sake of comparison, the same

[1] formfutura.com
[2] tronxy.com/x-series

set of printing parameters was used for both materials (Table 3.7). These values were selected after some preliminary tests and taking into consideration the overlap of printing temperatures recommended by each datasheet (Table 3.6). The selected infill of 100% ensure a minimum void presence, as is an injected/homogeneous like approach, way to produce samples and obtain more accurate results as demonstrated with PP by Carneiro et al. [2015]. Bed temperature of 65°C was chosen considering the literature value of the glass transition temperature (Tg) of 77°C which must not be exceeded [Lam et al., 2005]. This value considers the time for the material to cool off, the printing speed and number of layers. The conducted tests revealed that at 65°C the deposited material did not warp or contract in the lower layers ensuring a good adhesion to the printing surface [Wang et al., 2007]. Even though, printing with 100% infill is normally an hard task in materials such as ABS, PLA and PA, since there is the tendency to contract and detach from the surface [Shen, 2017]. Nonetheless, in this work PETG showed no warping defects or difficulties in printing distinct geometries, namely cubes with 10 mm length wall, tensile and flexural standard specimens.

Table 3.7: Printing parameters

Layer type	Temperatures and features	Infill
Nozzle diameter: 0.4mm	Bed temp: 65°C	Raster: 45°
Layer height: 0.20mm	Ext. temp: 240°C	Infill: 100%
Perimeters: 2	Bed surface: glass + glue	

3.2.2.3 Thermal Analysis

Thermogravimetric Analysis (TGA) was performed in a Q500 gravimetric balance from TA instruments (United States of America). A ramp of 10°C/min was used, starting at 30°C until 500°C with nitrogen atmosphere, to avoid oxidative degradation of carbon fibres. The samples used were obtained from the purchased filament with weight between 10 and 20 mg. Residual carbon was evaluated to determine the fibre percentage (wt%).

Differential Scanning Calorimetry (DSC) measurements were carried out in 200 F3 equipment from Netzsch® (Germany) at a heating rate of 2°C/min under nitrogen purge. The samples used were obtained from filament and printed parts with weights in the 10 to 20 mg range. The temperatures used were 30 to 300°C and two heating cycles were performed along with cooling (crystallization) scanning. For analysis purposes, the first heating cycle was not represented as it was performed to eliminate any possible effects of thermal history.

3.2.2.4 Tensile Filament Setup

The first step of this methodology was the filament tensile test. The lack of information about tensile tests for polymeric filaments, specifically for 3D printing, led to the authors to the development of a set of grips for this experiment based on standards concepts for composites (ISO 3341)

and metallic wires (BsS EN 10218-1:2012). The designed grip consisted in a clamping mechanism to fix the filament and a bollard, where the filament is rolled around three times as seen in Figure 3.16. Five samples of each material were used for statistical purposes. This system was design accordingly with the available tensile testing machine (INSTRON® 4507 (United States of America)). The testes were performed with a 100 kN load cell at 5 mm/min for both material samples (reinforced and unreinforced). This test was conducted as an exploratory method for testing material tensile properties for homogeneous samples, in opposition to the printed samples.

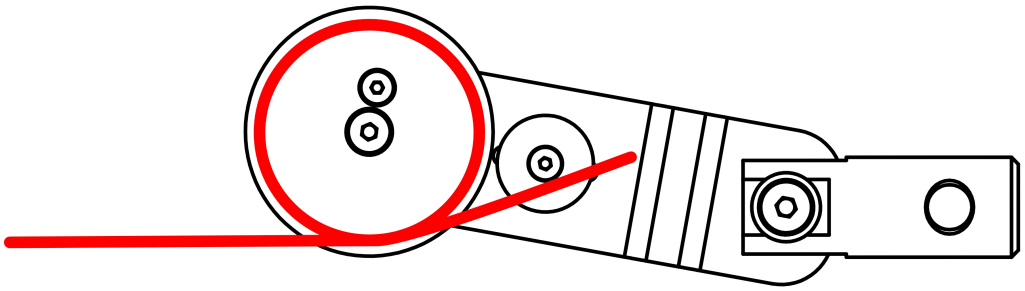


Figure 3.16: Filamentar testing system

3.2.2.5 Tensile Samples

Tensile samples were produced accordingly with ISO-527 Standard (Figure 3.17). The test was performed in an INSTRON 4507 (United States of America) machine with a 100 kN load cell, at 1 mm/min with a distance between clamps of 50 mm.

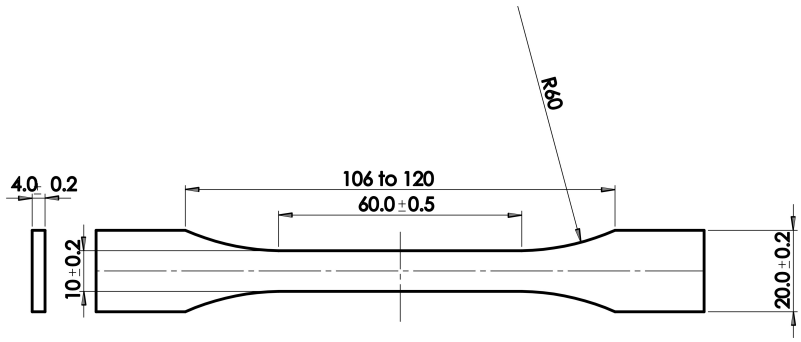


Figure 3.17: Tensile Samples ISO 527

3.2.2.6 Flexural Samples

Flexural samples were produced accordingly with ISO-178 Standard (Figure 3.18) and tested in a TIRAtest® 2705 (Germany) apparatus. The test velocity was 1 mm/min with a distance between spans of 64 mm and a 100 kN load cell.

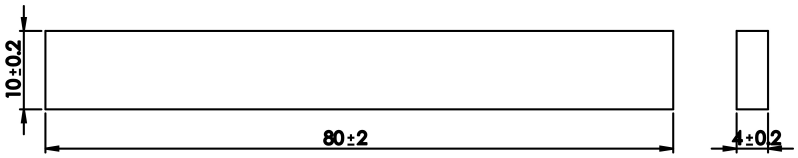


Figure 3.18: Flexural Samples ISO 178

3.2.2.7 Microscopical Characterization

Microscopic analysis was performed using an Olympus® PMG 3 (Japan) inverted microscope with reflection light and an Olympus® DP12 software and DP12 digital camera to capture magnifications at 23x, 150x and 300x of filament and printed samples. Two types of samples were prepared, three 100% infill cubes (10x10x10 mm) and three filamentar samples. Both were inserted in epoxy resin and posteriorly polished, filamentar samples were placed in axial and in cross sectional view and the printed samples were positioned in two different orientations. With these images, it was determined material properties such as fibre orientation, distribution and dimensions, using ImageJ software measuring tools [Schneider et al., 2012]. Regarding fibre content, whenever TGA test is not available/possible, an alternative methodology based on image analysis can be applied, which was also carried out herein.

3.2.3 Results and Discussion

3.2.3.1 Thermal Analysis

TGA Analysis

TGA analysis is commonly used to study the thermal stability of polymeric materials. In this work, a comparison study was carried out between pure and reinforced materials in order to quantify the fibre content of the composite samples.

The difference between the residue of the pure and reinforced material is directly related to the amount of carbon fibre that does not degrade at the highest test temperature (425.8°C), since the reinforcement material is composed by high modulus fibres, which degrade at 800-900°C [Thostenson et al., 2002]. It was determined an average value of 13.7% of carbon fibre incorporation in the matrix. Note that these tests were conducted only for the filament material.

Figure 3.19 depicts the weight loss and derivative weight for the tested filaments. The first derivative of the weight loss/temperature curve provides information about the temperature at the maximum degradation rate, which is similar for both materials. However, the thermal degradation of the reinforced material occurs later than the pure material, which can be observed by the

slight deviation of the curve to the right side (higher temperatures) in Figure 3.19a and by the low intensity of the first derivative peak in Figure 3.19b.

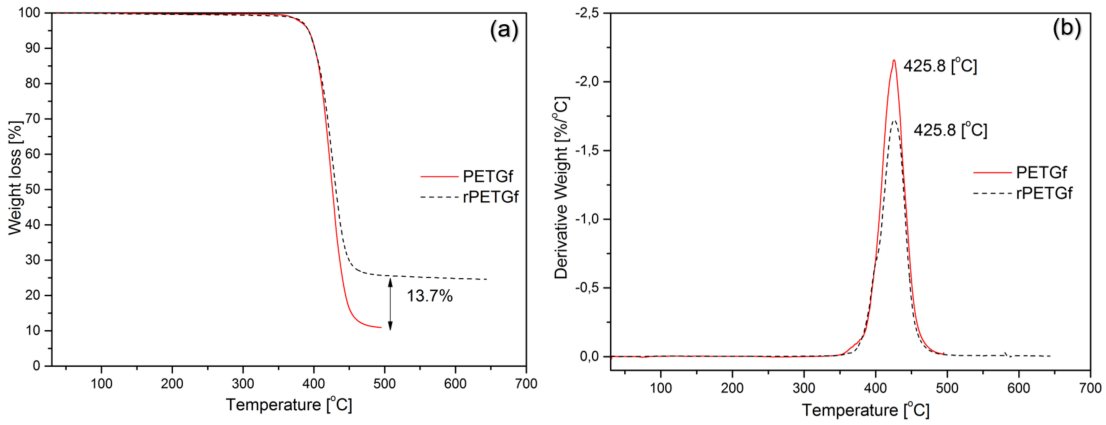


Figure 3.19: TGA results: (a) weight loss %, (b) derivative weight

DSC analysis

Figure 3.20 shows the DSC curves of four material combinations: (a) PETGp vs PETGf, (b) rPETGp vs rPETGf, (c) rPETGp vs PETGp and (d) rPETGf vs PETGf. With these combinations, it is possible to understand the difference between printed samples and its corresponding filament material, and compare printed/filament pure with printed/filament with carbon fibres.

Considering all plots, in the heating cycle it is found an exotermic peak that allows for the identification of the glass transition temperature. Up to this point the behaviour is roughly the same for the all the samples. The cooling cycle reveals no endotermic peak, indicating that the material is completely amorphous, also proven by the absence of melting peak in the heating cycle [Lam et al., 2005, Kattan et al., 2002].

All the curves show a similar profile to the ones found in literature for the pure PETG [Greco et al., 2010], for the filament and printed part, which means that the polymer characteristics do not change with the consecutive heating cycles due to successive reprocessings. The four types of samples presented similar values with an average temperature of 75.32±1.90°C (seen in 3.8), which corresponds to the value found in the literature for the glass transition temperature [Lam et al., 2005]. PETGf presented the highest value with 77.20°C while the printed part (PETGp) showed 73.85°C. The rPETGf presented a value of 73.53°C and the rPETGp 76.70 °C, thus not creating any pattern in temperature oscilations. Since these values are the average obtained from the range of Tg, it is considered that these differences are not significative to prove once again the thermal stability of the materials.

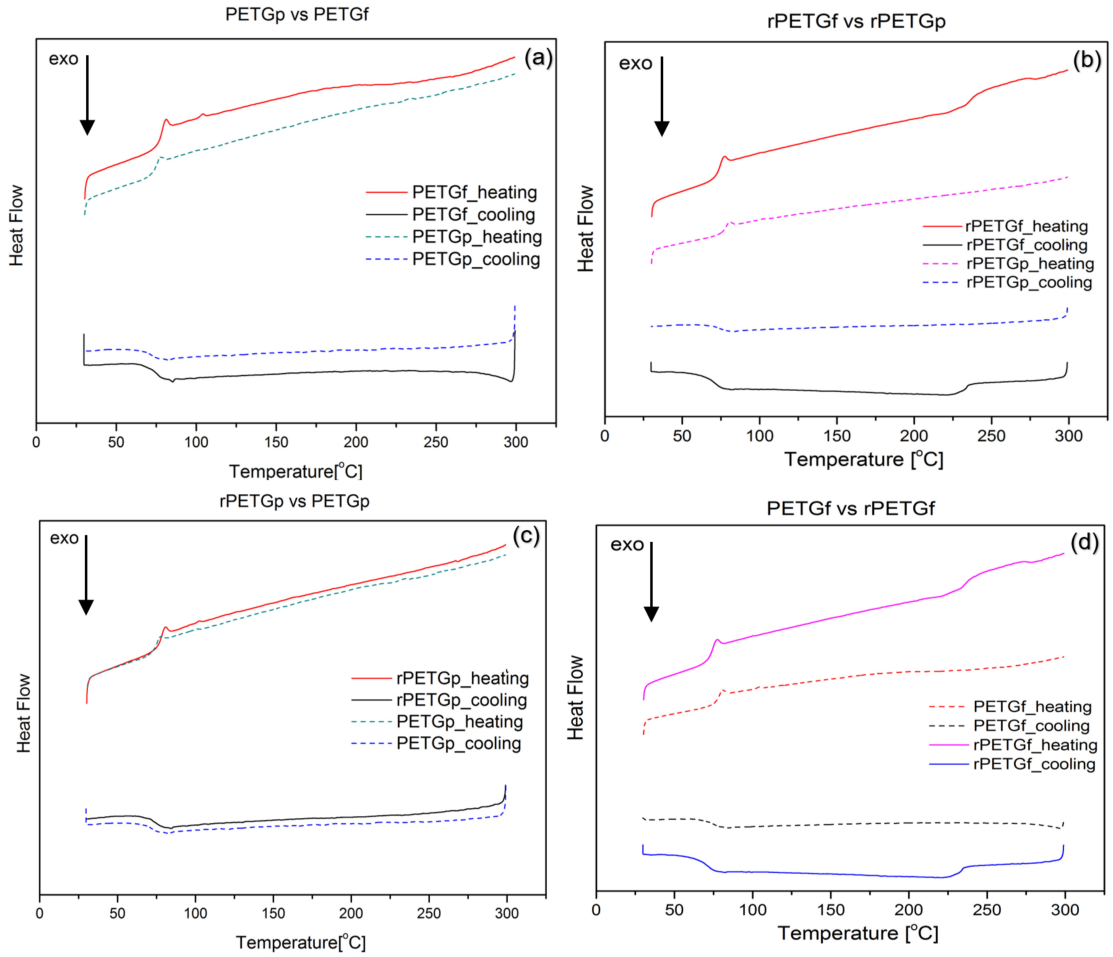


Figure 3.20: DSC results: (a) PETGp vs PETGf, (b) rPETGp vs rPETGf, (c) rPETGp vs PETGp and (d) rPETGf vs PETGf

3.2.3.2 Mechanical testing

Tensile filament test

The preparation of the test setup revealed to be a difficult process on rPETGf, since reinforced thermoplastics, tend to be more brittle than the matrix itself, and the winding of the filament around the bollard had to be made carefully, in order to avoid fractures during the tensile test. This fragility and lack of ductility allied to a small diameter (1.75 mm) could be the cause of the result disparity among the rPETGf samples. However, and apart from rPETGf1 the behaviour was similar for all the curves. The unreinforced material represented in Figure 3.21 shows a different pattern, with similar behaviour amongst themselves and a low value of deviation for all the samples. Since this process was specially developed for this study and the tensile test of polymeric filaments, some calibration issues have been found. It is visible that in each test there is pre-tension applied. This tension does not affect the stress values, but could change minimally the strain results.

Table 3.9 lists the average values obtained from the curves. Regarding the maximum stress, rPETGf samples presented a decrease of 6.13% when compared to PETGf samples. However, the

Table 3.8: Glass transition temperature ranges

Sample	T_g[°C]
PETGf	[75.45 - 78.94]
PETGp	[71.85 - 75.85]
rPETGf	[72.10 - 74.96]
rPETGp	[74.99 - 78.41]

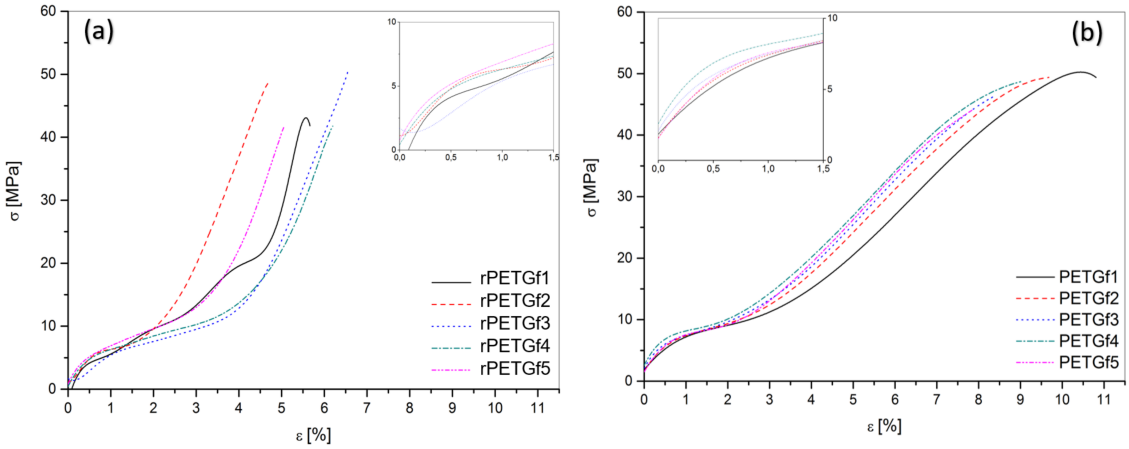


Figure 3.21: Tensile filament test results: (a) rPETGf and (b) PETGf

standard deviation among rPETGf samples was much higher. Since, no standard was followed, the modulus was obtained by the tangent method, which showed similar results for both materials. Finally, the strain at rupture showed that rPETGf is 43.94% less ductile than the reference material (PETGf), which is the only predictable result since fibre reinforced materials are generally less ductile than its matrix materials Ning et al. [2015], Schneider et al. [2012]. All the curves present the same rupture and maximum stress except for rPETGf1 and PETGf1.

Table 3.9: Filament mechanical properties

	Tmax(MPa)	E(GPa)	Strain(%)
PETGf	47.76±2.48	0.716±0.110	10.06±0.56
rPETGf	44.83±3.76	0.749±0.119	5.64±0.69
EF*	-6.13%	4.61%	-43.94%
*Enhancement factor			

Tensile Specimen Test (ISO 527)

Figure 3.22 depicts tensile specimen test results for reinforced and unreinforced material. In Figure 3.22a, a fragile fracture is visible for rPETGp, which may be justified by the short values of strain at the fracture point. Moreover, a high Young's modulus is also perceptible for all samples, except

for rPETGp4 whereas a premature fracture occurred. Figure 8b shows the results for PETGp, and it is possible to see different points of rupture.

It can be highlighted the curve smoothness and linear extension after yield of PETGp1 and PETGp3. Both samples show a similar behaviour when compared to an injected (homogeneous) part, as seen by the neck extension in Figure 3.22b. The samples PETGp2 and PETGp4 show a clear "staircase" behaviour representing the delamination between the deposition strands and layers material accordingly with tests provided by Ziemian et al. [2015].

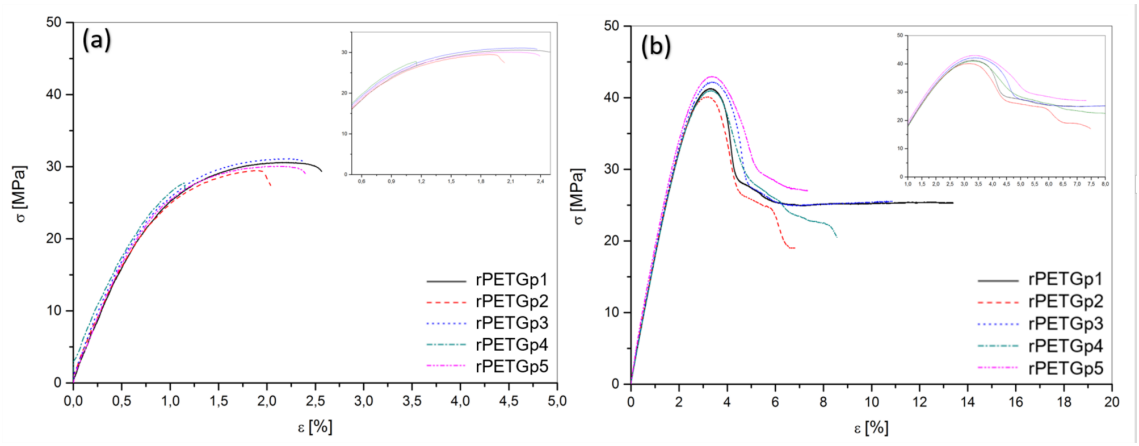


Figure 3.22: Tensile sample test results for: (a) rPETGp and (b) PETGp

Figure 3.23 shows tensile curves for PETGp3 and rPETGp1 with the respective sample fractures. By analysing Figure 3.23b, it is noticeable the difference between the fractures and how they are related to the respective curves in Figure 3.23a. Both sample fractures are represented with magnification (40x) of the damaged area. rPETGp1 shows a fragile fracture (represented by a typical curve of a fragile material), unlike PETGp3 which presents a stretched neck (i.e., a ductile fracture).

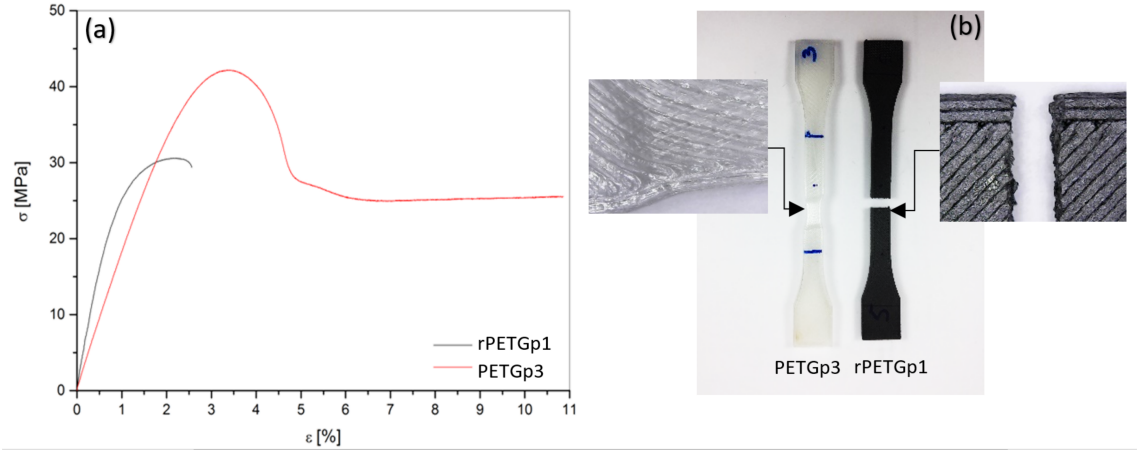


Figure 3.23: Tensile curves for PETGp3 and rPETGp1(a) with the respective sample fractures(b)

Table 3.10 summarizes the average comparative values obtained from the mechanical test for both materials. The maximum stress values for rPETGp were 28.21% lower than the unreinforced material, while the rupture stress was 27.16% higher. Young's modulus revealed an improvement of 70.1% for rPETGp and the strain at break lost 78.82% of its value (values acquired accordingly with the standard IS0 527). Ferreira et al. [2017b] proved this elasticity at break reduction by testing samples of PLA and PLA+20% carbon fibre in several printing orientations. Comparing the tensile filament results (Table 3.7) with the values from Table 3.10 it is possible to analyse some tendencies. Although maximum stress values were lower for the reinforced filament, the printed sample presented a decrease of 6.13% (filament) to 28.21% (tensile sample). Regarding Young's modulus, the improvement factor revealed an increase of 65.49% facing the filament results. Finally, the strain at break decreased 43.94% (filament) to 78.82% (printed sample). The comparison between filament and tensile samples showed that the main tendency was kept, with no contradictory results.

This trend indicates that reinforced samples present a decrease in maximum stress and strain at rupture, and an increase in Young's modulus when facing unreinforced material. This behaviour can be explained by two main aspects: the short fibre length and the quality of fibre sizing and/or fibre-matrix interface. It is also noteworthy that this interface can be also affected by the material conditioning (i.e., moisture presence). This result was expected since the presence of fibres contributes to an increase in stiffness and, simultaneously, to constrain the natural material expansion after extrusion (creating voids in the 3D structure).

Table 3.10: Tensile test results

	σmax(MPa)	σrot(MPa)	E(GPa)	Strain(%)
PETGp	41.51±0.99	21.87±5.15	1.94±0.12	9.87±2.26
rPETGp	29.80±1.30	27.81±2.41	3.30±0.12	2.09±0.60
EF*	-28.21%	27.161%	70.10%	-78.82%

Flexural Specimen test (ISO 178)

Figure 3.24 depicts flexural specimen test results for reinforced and unreinforced material. Figure 3.25 shows two typical flexural curves for PETGp and rPETGp with the respective sample fractures, where it is visible the brittle behaviour of the reinforced material in comparison with the pure material. In Figure 3.24a, it is observed a more pronounced dispersion of results. The curves rPETGp2, rPETGp4 and rPETGp5 present similar behaviour, with comparable strain at break, though with different maximum stress points. Curves rPETGp1 and rPETGp3 show slightly different behaviour from the previous ones. The first one show an higher maximum stress while the other depicts a higher strain at break. Figure 3.24b shows very consistent results regarding maximum stress and strain at break. Comparing both plots, it is clearly visible that the unreinforced material is much more ductile than the reinforced one, as the strain at break increases two times its value.

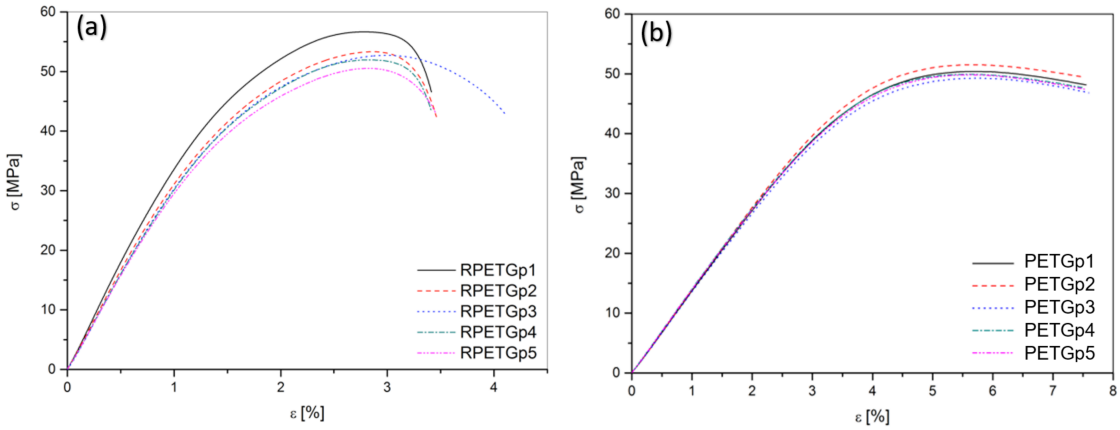


Figure 3.24: Flexural test results for: (a) rPETGp and (b) PETGp

Considering the values in Table 3.11, rPETGp samples showed an increase in flexural strength of 5.14%. The flexural modulus presented an increase of 191.38% for the reinforced material, which was verified by the analysis of the slopes, indicating a better interlayer adhesion. However, the strain at break for unreinforced material is nearly double of the rPETGp values. Flexural modulus is expected to be different from Young's modulus since these are anisotropic materials and each variation in processing parameters can imply a different mechanical response. Short fibre reinforcement has a positive effect on the flexural behaviour in contrast with tensile performance. This can be explained by the behaviour of the fibres during the extrusion process, which tend to move towards to the deposited bead surface [Brenken et al., 2018]. This peripheral fibre arrangement may promote the interlayer adhesion and, hence, the mechanical response.

Table 3.11: Flexural test results

	σmax(MPa)	E(GPa)	Strain(%)]
PETGf	50.56±1.06	1.16±0.17	7.53±0.04
rPETGf	53.16±2.31	3.38±0.17	3.74±0.33
EF*	5.14%	191.38%	-50.33%

*Enhancement factor

3.2.3.3 Microscopical Analysis

Image-based fibre dimension analysis

A critical factor of reinforced printed FFF parts is the fibre orientation. In an ideal scenario all the fibres are aligned with the desired extrusion path. Figure 3.26 show micrographs of filament and printed samples from cross section and axial views with 300x magnification. Figures 3.26a and b indicate that the majority of fibres are aligned along the filament. The sample that is shown in Figure 3.26c and 3.26d is a cube (10x10x10mm) printed with the parameters in Table 3.7. Figures

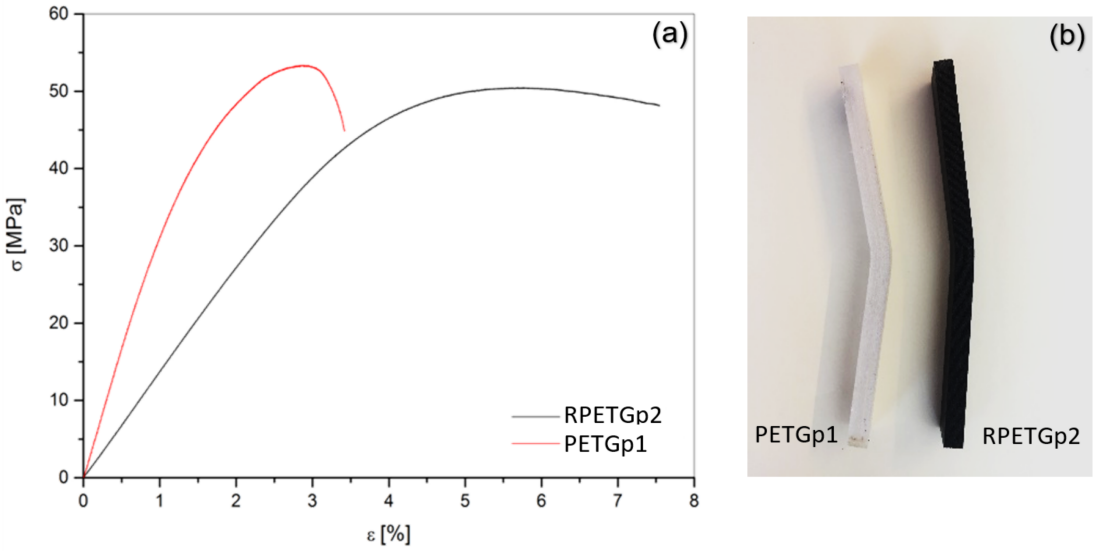


Figure 3.25: Flexural curves for PETGp1 and rPETGp2 (a) with the respective sample fractures(b)

3.26c and d depict that fibres are aligned with the extrusion direction even when the material is extruded through a 0.4 mm diameter nozzle.

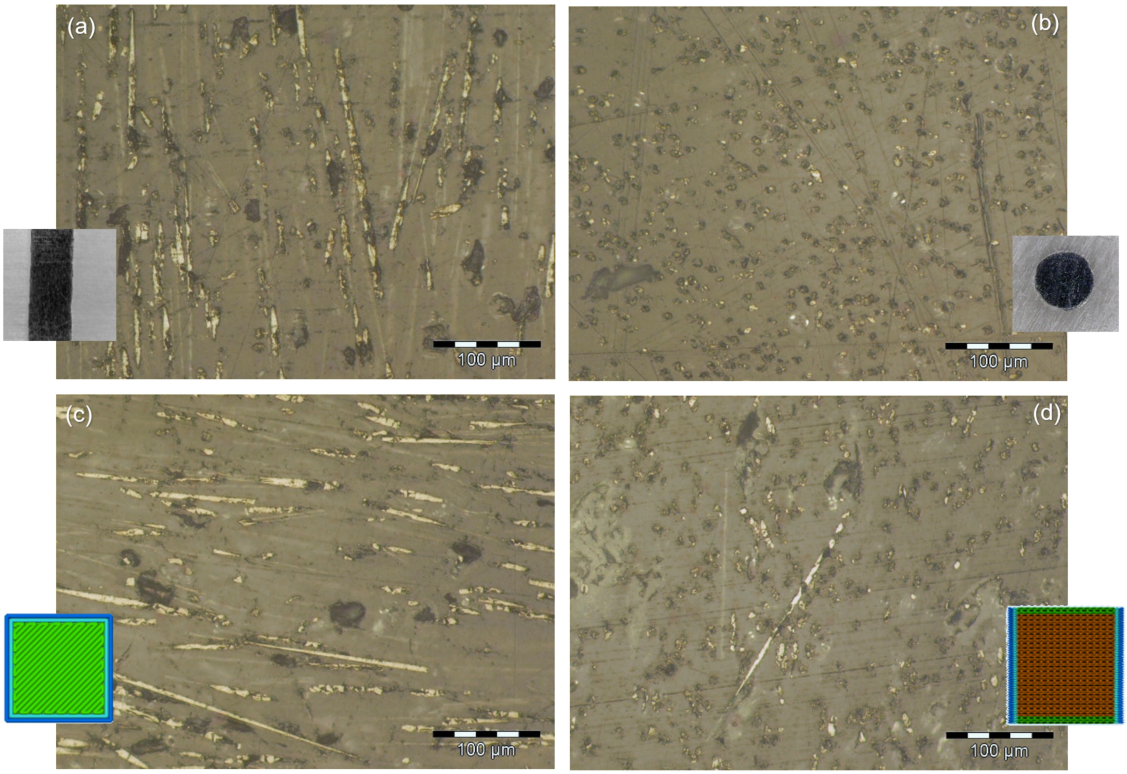


Figure 3.26: Micrographs: filament cross section view (a) and axial view (b); Printed specimen cross section (top) view (c) and Printed specimen axial view (lateral) view (d)

For fibre dimension evaluation purposes, two 150x magnification images of a filament sample

were used(Figure 3.27). Figure 3.27a shows cross sectional fibre positioning, with an average length of 117.67±66.55 μm and an average angle of 49.45±5.64°. Figure 3.27b (300x magnification), shows an axial view providing measurement for fibre diameter, averaging 7.54±1.90 μm. Figures 3.28a and b show histograms of the fibre length with corresponding number of measurements. For the cross sectional image (Figure 3.27a) 40 measurements were taken, and the average length values are presented (24.47 μm). For Figure 3.27b, 120 measurements were taken also presenting the average value (±0.63 μm). The higher number of fibres measured in length are located in the 45.45±24.47 μm range and the interval with the most amount of measurements of the diameter is 6.56±0.63 μm.

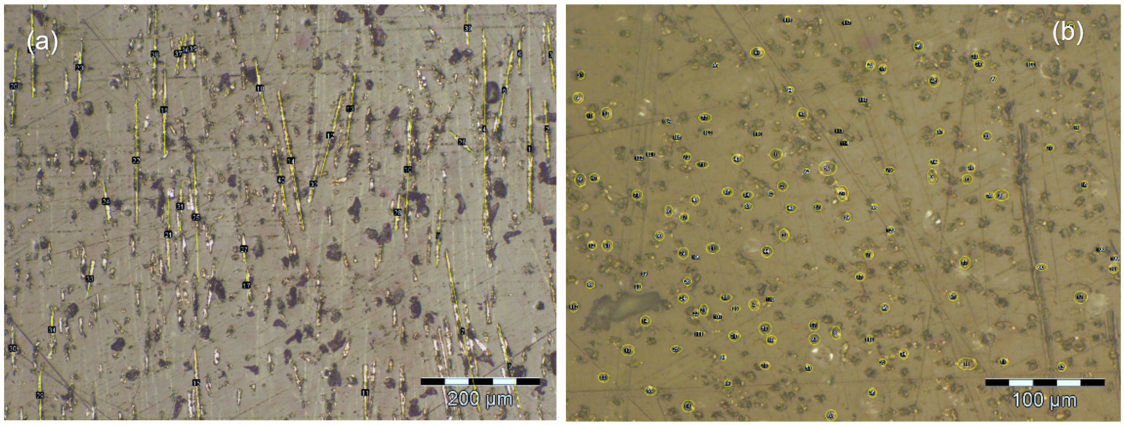


Figure 3.27: (a) filament cross sectional view and (b) filament axial view

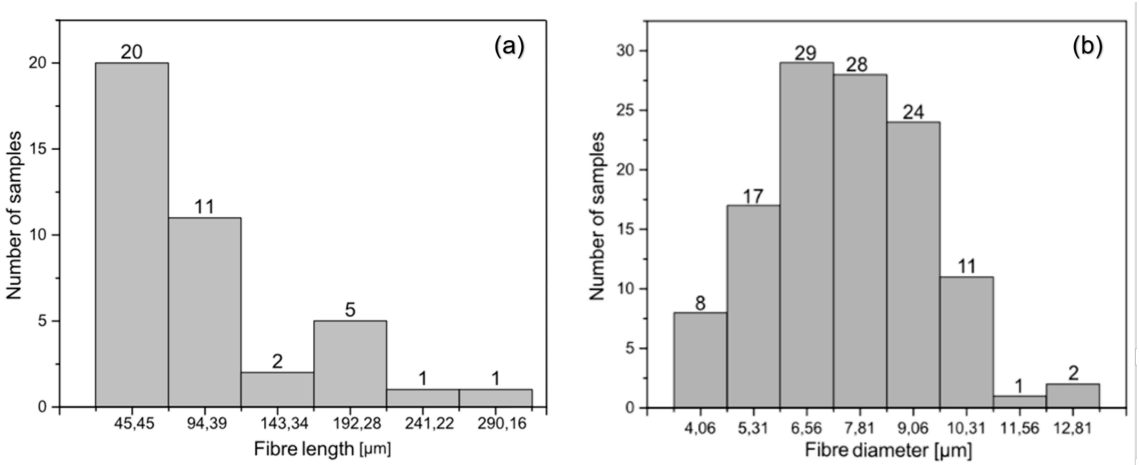


Figure 3.28: (a) Fibre length distribution and (b) fibre diameter distribution

Image-based fibre content analysis

A test was developed using an optic microscope to capture a 75x magnification from the transversal section of six samples in different zones of the filament as seen in Figure 3.29a. Using ImageJ software, a binary segmented image of the interest area was created, detecting the percentage of

white pixels/fibres (AF%) (Figure 15b).The results showed that the average percentage of white pixels is 4.82±1.20 %.

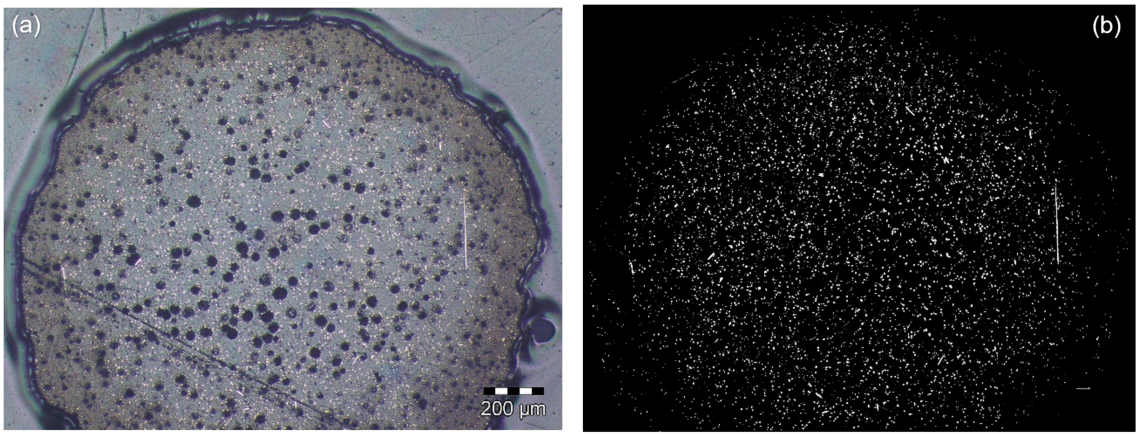


Figure 3.29: Original magnification (75x)(a) and binarized imaged (b)

These results are complementary to the TGA values indicating only the percentage of fibre in a transversal section. Considering the fibre percentage obtained, the following calculations were made:

ρ - Density(g/mm^3)

v - Volume(mm^3)

$$w_t\% = \frac{\rho_{cf} V_{cf}}{\rho_{cf} V_{cf} + \rho_m V_m} \quad (1)$$

Table 3.12: Imaged based content analysis results

Property	AF%-1.20%	AF%	AF%+1.20
ρ PETG*	0.0012	0.0012	0.0012
ρ High mod. fibre**	0.0018	0.0018	0.0018
Fibre Area [mm^2]	2.4053	2.4058	2.405
Fibre Length [mm]	0.1100	0.1100	0.1100
Fibre Volume [mm^3]	0.2646	0.2646	0.2646
Matrix Volume [mm^3]	0.2550	0.2487	0.2487
Fibre volume [mm^3]	0.0096	0.0159	0.0159
wt.%	5.17	7.10	8.51

*Material datasheet

**[Hull and Clyne, 1996]

By using equation 1 it is possible to calculate de wt% from the percentual fibre area. Calculations which are presented in Table 3.12. There is a discrepancy in values even when comparing

the highest value of 8.51 wt% with the 13.75 wt% obtain in TGA analysis, being this the most accurate method. The area analysis method is not the most accurate principle, since there are several variables to consider. Looking into Figure 3.29a it is possible to find several dark holes, these holes could be caused by the exposition of the filament to moisture after extrusion. The area of these holes correspond roughly 12% of the filament area and the fibres in these areas were not detected, presenting a reason for the final values to be lower than TGA results.

3.2.4 Conclusions

The main goal of this work was to characterize at mechanical, thermal and microscopical level the reinforced material comparing it to its matrix. Filament tensile test, developed specially to study 3D printing filaments defined a trend in behaviour that the tensile samples (ISO 527) confirmed later. This type of test is not perfectly calibrated but enables an exploratory and preliminary capability of testing the material in its raw state. With these tests, it was possible to confirm that the improvement factor in both tensile tests matched, even though the values were far superior for the printed samples. Tensile tests indicated that the addition of fibres increase the Young's modulus by 70.10% but withstanding 28.21% less in stress. Flexural tests exhibited an increase in flexural modulus of 191.38% and in flexural strength of 5.14%, for the reinforced PETG indicating a better interlayer adhesion, without any sign of delamination. The usage of short fibre reinforced filament, suggests that this material is indicated for low ductility higher stiffness applications. DSC curves proved that these are amorphous materials with similar behaviour, before and after processing, and when comparing reinforced with unreinforced material. In TGA analysis, it was verified by comparison of both rPETGf and PETGf, that the difference between carbon residues is 13.7 Wt%. This method allowed the identification of an approximate percentage of carbon fibre in the matrix. Through microscopy analysis of printed samples, it was observed that there is in fact fibre alignment following the extrusion path. Regarding the filament analysis, it was found a presence of void spots in approximately 12% in the total area analysed. The Wt.% of fibre calculated by means of area analysis is inferior than the TGA value possibly due to the void percentage.

3.3 Characterization of thermoplastic matrix composites produced via Markforged®

Part of this work was presented at the International Conference on Direct Digital Manufacturing and Polymers (ICDDMAP) 2017 in Leira, Portugal [Ferreira et al., 2017a].

3.3.1 Introduction

As previously mentioned in chapter 2, Markforged® is one of the few commercially available equipments capable to print reinforced thermoplastics with continuous fibres. This preliminary work reports the evaluation of the carbon fibre presence influence on the mechanical performance of a part by comparing it with non reinforced samples. Tensile (ISO 527 [International Organization for Standardization, 2012a]) and flexural (ISO 178 [International Standards Organization, 2010]) were produced considering Eiger software limitations, being posteriorly tested, so it can be possible to understand how reinforced printed specimens behave facing pure polymer samples. Since the feedstock of this type of hardware is limited to the one provided by the manufacturer, the considered matrix material was Nylon MF (Tough Nylon) and carbon fibre with polymeric coating as the provided reinforcement. In addition, a morphological analysis was performed for the distinct types of fibre available bundles.

3.3.2 Materials and Methods

3.3.2.1 Markforged® Fibre Analysis

At this point, Markforged® provides three different types of reinforcements for the MarkOne equipment. Carbon, Kevlar® and Glass fibres are provided, each one in a small spool which is inserted in a extrusion head similarly to the polymeric matrix material, pushed by a stepper motor and deposited in the part. Since a major problematic is the matrix/fibre adhesion (as discussed in section 2.5.2.1), Markforged® provides their fibre bundles seized by a polymer with similar processing temperatures than the matrix. This temperature value is automatically defined by software, and presented in the equipment information panel. Beyond granting an improved adhesion to the polymeric matrix, the fibre coating allows the pushing of the fibre towards the extrusion head, otherwise, the fibre bundle would not have the necessary stiffness to be extruded. Figure 3.30 depicts a magnification of the three distinct samples after being subjected to a flame during five seconds originating the polymer degradation and consequently showing loose fibres.

Figures 3.31a) and b) depict carbon fibre tows cross section magnifications at 150x and 1500x respectively. By means of ImageJ [Schneider et al., 2012], it was possible to measure the bundle and each fibre's individual diameter. The results show that the average bundle diameter is 376,75$\pm$11.49 μm, while the fibre presents an average area of 45$\pm$5.84μm^2 and consequently a diameter of 7.58$\pm$2.73 μm. Figure 3.32a) depicts a 1500x magnification of a Kevlar fibre bundle, in which fibre area measurements were taken. This magnification presents a higher average area dimension of 185.81$\pm$18.11 μm^2 and a virtual approximated diameter of 15.38$\pm$4.80 μm. Figure

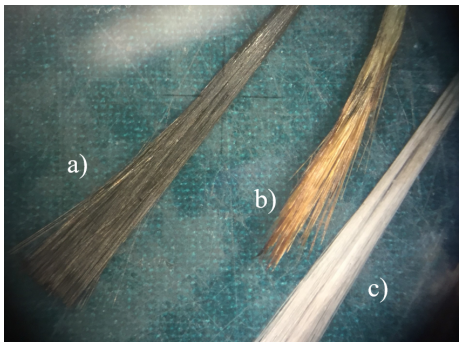


Figure 3.30: Fibre bundles after burning: (a) carbon, (b) Kevlar® and (c) glass fibres.

3.32a) depicts a 1500x magnification of glass fibre bundle. The measurements indicate an average area dimension of 48.15±9.77μm^2 and diameter of 7.83±3.52 μm. Through these results it is possible to understand that even though Kevlar fibres are bigger, they present shape flexibility, which neither carbon or glass can do.

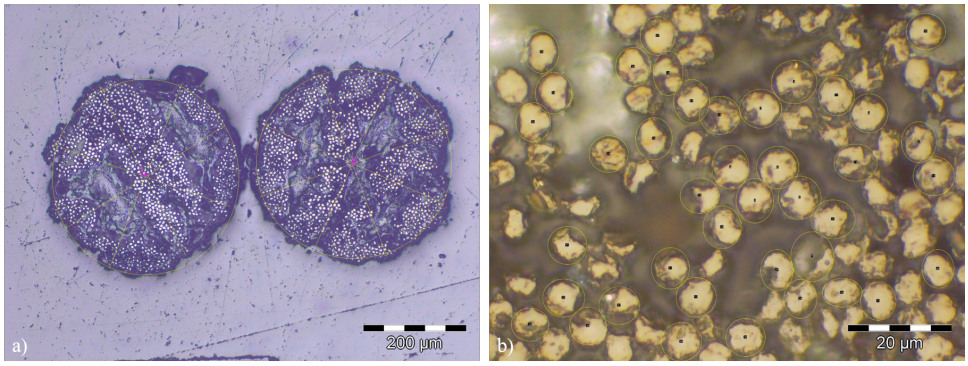


Figure 3.31: Carbon fibre bundles magnifications with measurements: (a) 150x - bundles and (b) 1500x - fibres.

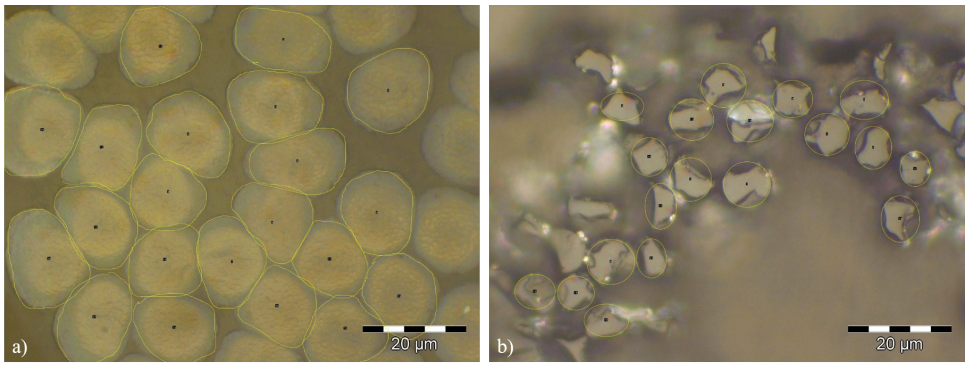


Figure 3.32: Carbon fibre bundles magnifications with measurements: (a) 1500x - Kevlar fibres and (b) 1500x - Glass fibres.

A second analysis was performed to identify the cross sectional fibre content of the bundle. Once again ImageJ software was used to transform the original picture (3.33a) in a binary segmented image (3.33b), and a Matlab script was created to identify the percentage of white areas

(fibres) inside the bundle circular shape. The results indicate that only 15.23% of the internal area of the bundle is occupied by fibres.

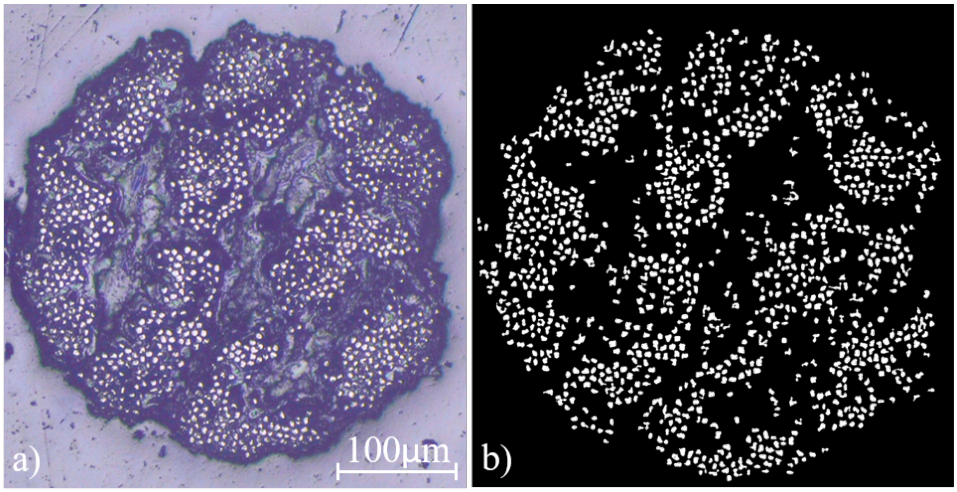


Figure 3.33: Original magnification (150x) (a) and binarized imaged (b).

Since Markforged® slicing software (Eiger[3]) imposes different process parameters for the unreinforced and reinforced parts, the samples had to be produced considering these limitations, as depicted in Table 3.13. As presented in Figure 2.28, the reinforcing agents have similar overall diameters of approximately 400 μm, yet distinct morphology, which reflects the process limitations regarding the printing job, more precisely, layer height. Eiger software imposes a layer height of 0.125 mm for carbon fibre while for Kevlar and Glass fibres this parameter changes to 0.100 mm. This limitation is imposed in order to grant layer adhesion and fibre compaction. Eiger software offers the possibility of laying the fibre in three distinct types of patterns: (1) Isotropic, in which the fibre is deposited rectilinearly with 180° change of directions; (2) Concentric pattern, creating rings from the outside of the part to the inside; (3) Full fibre, which is similar to the isotropic, rotating each layer of fibre 45°. From these three patterns, only concentric is available for carbon fibre type, which can be explained by the fragility of the bundle. Figure 3.34 presents Eiger software interface, with the concentric disposition of the fibres in the layer as well as their position on the overall height of the sample, among some other parameters.

3.3.2.2 Test Specimens

For tensile testing ISO 527-2 [International Organization for Standardization, 2012b] type 1A samples, with overall 150x4x10(neck) mm geometry was selected. As for the flexural testing ISO 178 [International Standards Organization, 2010], a bigger geometry was selected (120x15x6 mm) instead of the normal 100x10x4 mm, otherwise software would not allow the fibre deposition.

Due to software limitations, during the four layers in which the fibre is deposited concentrically (as presented in Figure 3.34), the interior pattern is not 100% dense as the rest of the

[3]https://www.eiger.io

Table 3.13: Parameters for sample production.

Setting	Pure Nylon Samples	CF Reinforced Samples
Layer height (mm)	0.2	0.125
Fill density (%)	100	100
Top and bottom pattern	45°	45°
Infill patern	Triangular	Triangular
Perimeters	2	2
Others	Usage of Brim	Usage of Brim
Reinforcement settings		
Fibre fill type	-	Concentric pattern
Fibre layers	-	4
Fibre concentric rings	-	3

part. Instead, in there, a default percentage of 10% is used, lowering the mass values. Due to this limitation, fibre content is only possible to obtain through the theoretical vol.% presented by the software. According to Eiger software, tensile samples are presented a 4.6 vol.%, while the flexural specimens showed a 3 vol.% of carbon fibre content.

3.3.2.3 Testing Method

Six tensile samples were tested on a MTS Systems 810 (Minnesota, USA) with a 15kN load cell at a speed of 2 mm/min for the unreinforced samples, while the reinforced was tested at 10 mm/min. Also six flexural samples were tested in a TIRAtest 2705 TIRA GmbhH (Germany) with a load cell of 500 N at 5 mm/min.

3.3.3 Results and Discussion

In order to accurately test the mechanical properties, fully dense samples are necessary. However, during this work, it was found that this feature originates warping of the samples and consequently detachment from the printing tray, leading to print fail. To ensure the control of the warping effect, specific glue (Cube glue, 3Dsystems, USA) was used in addition to a brim in each specimen, increasing the contact area.

3.3.3.1 Mass and dimensional analysis

Weight analysis revealed that for six tensile samples of pure Nylon, the average mass value was 8.78±0.21 g and 8.96±0.06 g for the reinforced tensile samples. Flexural samples presented a value of 9.88±0.07 g and 10.76±0.07 g for unreinforced and reinforced samples respectively. These low deviations in mass values indicates great hardware accuracy and high levels of repeatability. Regarding the dimensional analysis, the deviation from the reference value was always

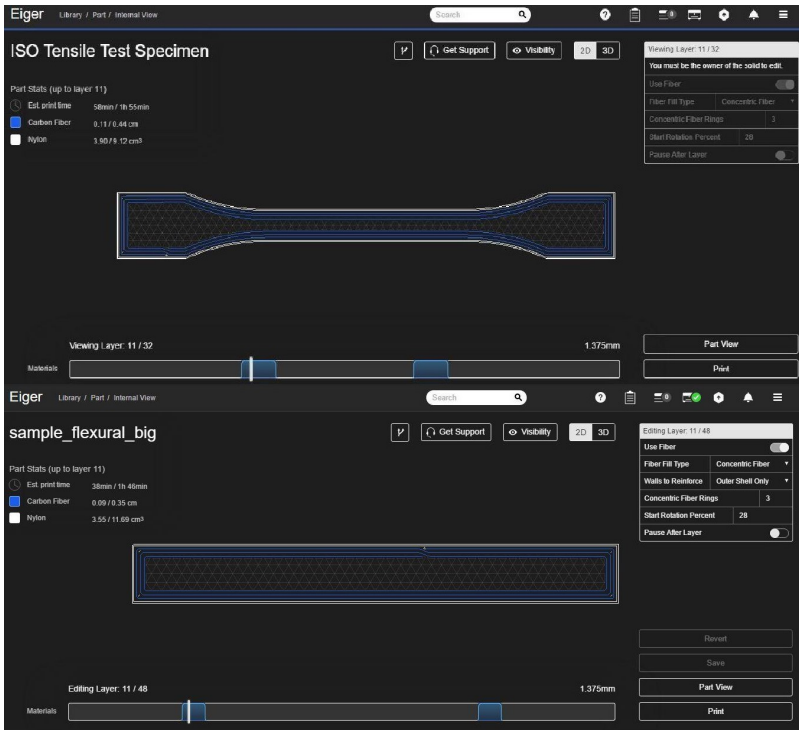


Figure 3.34: Fibre distribution for tensile and flexural samples.

bellow 2% and, considering the common irregularities and lack of repeatability in the process, the presented values are extremely positive.

3.3.3.2 Tensile tests

Figure 3.35 depicts the tensile results, both for unreinforced (a) and reinforced samples (b). Considering the obtained results (Table 3.14), it is possible to understand how a 4.6 vol.% of carbon fibre can impact the part mechanical performance. For the pure polymer specimens, it is shown a typical ductile behaviour with strain values upwards 50%. These samples present a maximum strength of 32.65±0.83 MPa, obtained at roughly 5% strain and 1.11±0.04 GPa Young's modulus. Reinforced samples presented an increase in tensile strength to 61.29±5.67 MPa and a Young's modulus of 6.00±0.29 GPa almost 6 times greater than the unreinforced samples, being the strain at break reduced to 1.11±0.12%. This indicates that the behaviour has become brittle, making the fibres the predominant element in the specimen. It is shown that by applying 4.6 vol.% of fibre or 12 fibre tows in the solicitation direction results in a material capable of sustaining the double of the force. Taking into account Markforged's datasheet [©Markforged, 2016], it is observed that the experimental values are inferior. This might occur due to improper material conditioning post printing process, since PA is an highly hygroscopic material. Since the filament is hermetically sealed in a box, previous to the print job, the exposure to moisture, might have occurred after printing. In addition, the print process is affected when there is moisture in the filament by creating voids due to its evaporation, which leads to a worst surface finish.

Table 3.14: Tensile Test Results for Pure Nylon and Nylon+Carbon Fibres.

Nylon				Nylon+Carbon Fibers			
Part	Tensile Strength (MPa)	Young's modulus (GPa)	Strain at break (%)	Part	Tensile Strength (MPa)	Tensile Modulus (GPa)	Strain at break (%)
1	-	-	-	1	62.80	6.06	1.10
2	32.10	1.15	No fracture	2	58.66	5.96	1.00
3	34.10	1.14	No fracture	3	56.98	6.36	1.22
4	32.42	1.10	No fracture	4	54.05	6.05	0.98
5	32.47	1.06	No fracture	5	68.29	6.08	1.23
6	32.13	1.12	No fracture	6	66.93	5.48	1.14
Average	32.65	1.11	-	Average	61.29	6.00	1.11
St. Dev	0.83	0.04	-	St. Dev	5.67	0.29	0.12

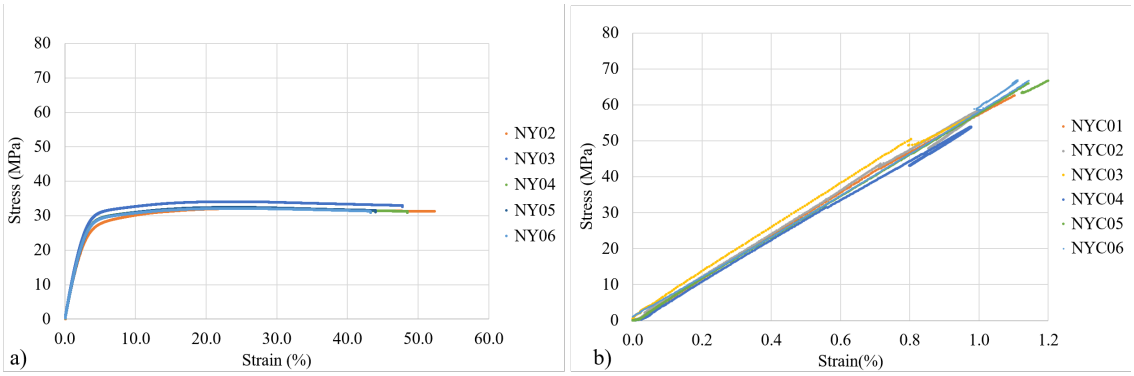


Figure 3.35: Tensile Stress-Strain: a) Pure Nylon samples, b) Reinforced Nylon samples.

3.3.3.3 Flexural tests

Figure 3.36 depicts curves for the flexural results, both for unreinforced (a) and reinforced samples (b). In Table 3.15 the results for both unreinforced and reinforced samples are presented. Pure Nylon samples indicate approximately half of the flexural strength of the reinforced samples. Young's modulus for the unreinforced samples is 43.2% of the reinforced flexural samples, and the strain at break of the pure nylon is 1.7 higher of the value of the reinforced ones. Through the curves depicted in Figure 3.36a, it is possible to observe a ductile behaviour, with a strain averaging 11.68%±1.53% without the occurrence of delamination. As for the reinforced samples, all the curves present an oscillating behaviour above 30 MPa (indicating fibre rupture), with an increase in strength until final fracture. No delamination was observed, and even despite the higher stiffness; after the fibre rupture, the samples behaved as the pure polymer ones.

Table 3.15: Flexural Test Results for Pure Nylon and Nylon+Carbon Fibres.

Nylon				Nylon+Carbon Fibers			
Part	Flexural Strength (MPa)	Flexural modulus (GPa)	Flexural Strain (%)	Part	Flexural Strength (MPa)	Flexural modulus (GPa)	Flexural Strain (%)
1	21.26	0.58	11.38	1	42.86	1.25	7.06
2	20.44	0.51	11.13	2	44.83	1.27	6.46
3	21.12	0.58	11.56	3	40.45	1.28	5.15
4	18.80	0.49	9.54	4	43.05	1.21	8.72
5	19.31	0.52	14.21	5	43.50	1.24	7.92
6	19.22	0.54	12.27	6	39.44	1.23	4.89
Average	20.03	0.54	11.68	Average	42.36	1.25	6.70
St. Dev	1.05	0.04	1.53	St. Dev	2.01	0.03	1.68

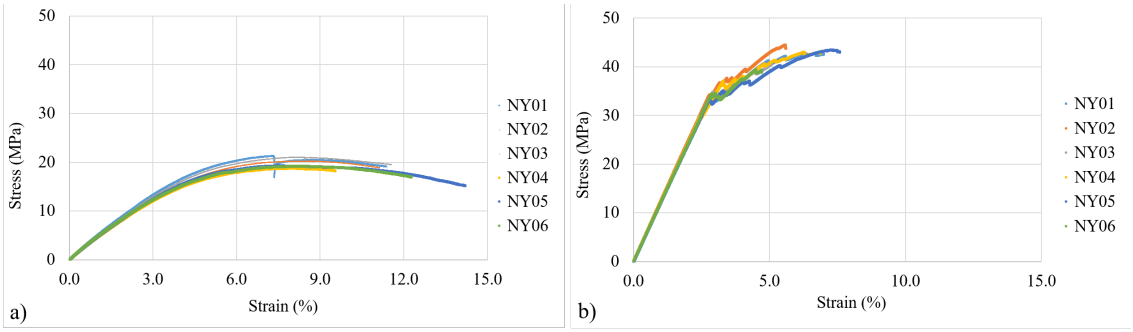


Figure 3.36: Flexural Stress-Strain: a) Pure Nylon samples, b) Reinforced Nylon samples.

3.3.4 Conclusions

This study revealed that Markforged equipment can print samples with a dimensional error percentage bellow 2% in almost every orientation. It was found that printing with 100% infill is a difficult process, since contrarily to PETG and other materials such as PLA, the printed PA sample tends to warp, requiring the addition of brim and high quantities of specific adhesive in order to stick to the machine tray. With this preliminary study, it was intended to understand how the addition of continuous fibres improves the performance of a part. In this work, the presence of 4.6 and 3 vol.% of fibre for tensile and flexural samples presented a significant increase of 88% and 112% for tensile and flexural samples respectively. It is important to consider that in real life applications, fully dense parts are typically not used. By locally adding continuous fibres it is possible to obtain stronger parts with low infill percentages, corresponding to less polymer usage. This concept is not valid for short fibre reinforced materials, in which the strength is increased with higher infill percentages. Due to several software limitations imposed for the carbon fibre usage, other fibre infill patterns could not be tested.

3.4 Effect of layer filling path on mechanical properties of PA and PA reinforced FFF parts

The following study was presented at Polymers Moulds and Injection (PMI) Conference in September of 2018 [Ferreira et al., 2018b] in Guimarães, Portugal.

3.4.1 Introduction

This work main focus was the study of FFF mechanical properties of printed parts and how they change with simple layer filling features. For this study, three types of PA filaments were selected: PA6/69, PA12 and PA12 with short carbon fibers. Dogbone ISO 527 [International Organization for Standardization, 2012a] samples were produced with 100% infill, varying the number of perimeters, the printing starting point in the part, and the orientation of the sample in the printing bed (xy – on flat, xz – on edge). The results obtained confirm the anisotropy of the process, revealing distinct properties for each feature tested and exposing the most sensitive parameter and, hence, a critical factor. The mechanical properties increased with number of layers and/or perimeters. This study aims to contribute to the creation of a correct strategy for the material deposition in order to sustain localized mechanical solicitations.

3.4.2 Materials and Methods

3.4.2.1 Materials

For this work, three types of feedstock were considered. Two pure (unreinforced) versions of polyamides, namely PA 6/69 Alloy 910 [Taulman3D, 2019] from Taulman3D (Missouri, USA) and PA 12 FX256 [Fillamentum, 2019b] from Fillamentum© (Hulin, Czech Republic). PA 12 CF15 [Fillamentum, 2019a], a reinforced version of the same PA 12 provided by Fillamentum©, so a direct comparison can be made. Some of the properties that are described in the datasheets are presented in Table 3.16.

Table 3.16: Datasheet material specifications [Fillamentum, 2019b,a, Taulman3D, 2019]

Property	PA12 - FX256	PA12 - CF15	PA 6/69 Alloy 910
Density (g/cm^3)	1.01	1.08	-
Tensile strength (MPa)	45.5	54.5	55.8
Tensile Modulus (MPa)	1400	500	503
Strain at break (%)	>50	>103	31
Printing temperatures (°C)	235-260	235-260	250-260
Bed/chamber temperature (°C)	80-105	80-105	30-100

3.4.2.2 Production Strategy

The sample production was performed in a Tronxy X5 3D printer from Shenzen Tronxy Technology Co. Ltd and the slicing configuration was performed with Simplify3D®4.0.1. Table 3.17 lists the parameters used in the production of the samples. The choice of printing temperatures was made considering the datasheets, with the purpose of finding a common value for all three materials. The remaining of the test parameters was chosen taking into account preliminary experiments, revealing to be the best combination, thus being possible to find the best overall setup of process variables, that provide the least warping and improved visual appearance.

Table 3.17: Printing parameters for all samples.

Parameter	Description
Nozzle diameter	0.4 mm
Extrusion multiplier	1.05
Layer height	0.3 mm
Infill pattern	±45°and concentric
Infill percentage	100%
Extrusion temp.	260°C
Bed temp.	90°C
Printing speed	40 mm/s

Figure 3.37 presents the internal scheme and building orientation of each type of sample. In Figure 3.37a it is presented a horizontal sample (XY) with an internal infill pattern of ±45°and two exterior perimeters per layer, which from now on will be referred as XY45. Figure 3.37b, designated by XZC (concentric pattern on edge), was printed with the maximum number of perimeters (4) that the slicing software allowed, thus creating a concentric structure. This type of samples were produced with resourcing to support material in the neck area. Due to software limitations, an internal ±45°is also mandatory as the nucleus of the sample. The last two types of samples presented in Figure 3.37(c and d) were printed horizontally (XY), with a concentric pattern that deposes the filament along the sample instead of a cross pattern (as found in the first type of sample). The only difference between the concentric samples is that the entry point of the extruder in the first one (c) is located in the beginning of the neck (XYC samples), while the second concentric sample (d), extruder entry is made at 0° in the grip end area (XYCE). It is important to consider that the feedstock was dried (according to what is presented in Annex A) previous to printing process, and conditioned in closed bags with silica gel.

It is expected that XZC, XYC and XYCE will have a similar behaviour and a better response than XY45, as it deposited lines are aligned with the loading direction. Figure 3.38 explains the basis of this assumption by showing the neck and transversal area of each type of sample in which it is visible that even XZC (printed on edge), shows a number of longitudinal lines similar to XYC/E.

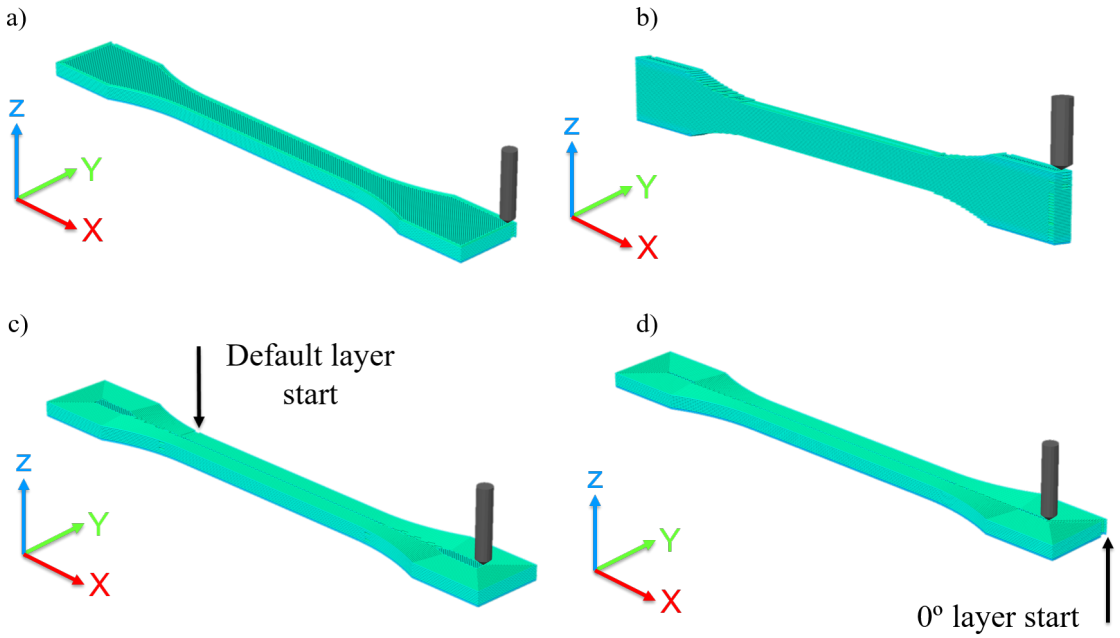


Figure 3.37: Printing orientations and infill: (a) XY45, (b) XZC, (c) XYC and (d) XYCE.

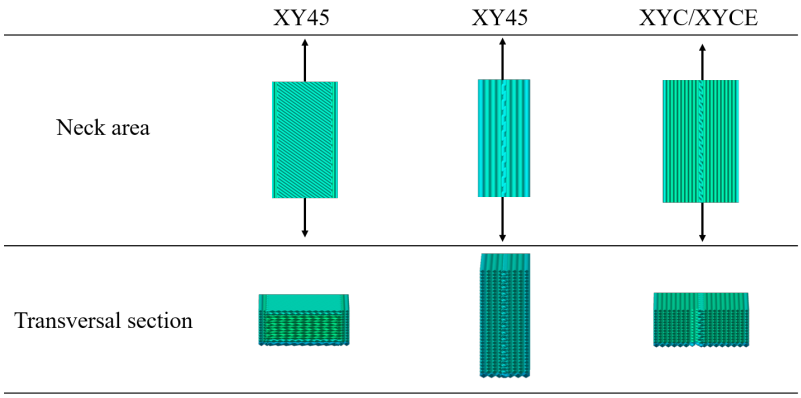


Figure 3.38: Infill pattern views (top and transversal sections) vs solicitation.

Due to a lack of feedstock availability at the time of this work, the four types of samples were not produced for all the materials. Considering the available set of samples, two types of comparisons can be done. Firstly, it is possible to compare the difference in properties for the same material with different orientations/strategies. It is also possible to compare distinct materials in same type of samples. The scheme depicted in Figure 3.39 indicates the printing orientation that each material.

Five tensile samples were fabricated in accordance with ISO 527-2 standard [International Organization for Standardization, 2012a] per each orientation. The test was performed in an Instron 4507 (USA) machine with a 5 kN load cell, at 1 mm/min with a distance of 50 mm between the clamps.

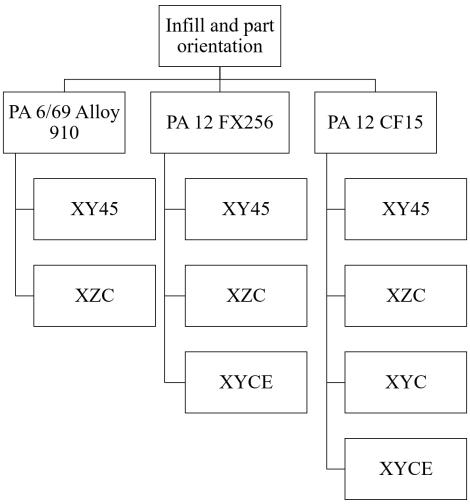


Figure 3.39: Printed samples organization scheme.

3.4.3 Results and Discussion

3.4.3.1 Orientation comparisons

PA 6/69

Table 3.18 depicts the results from tensile tests of Alloy 910 XY45, XZC and the datasheet values, while the comparison for the tested samples is presented in Figure 3.40 by the representative curves. From Table 3.18, it is possible to verify that even though the strain at break is practically the same for both building orientations, maximum stress was higher for XZC samples, while the Young's modulus value surpassed the double of the XY45 printed part. The datasheet results indicate that independently of the building orientation, the modulus is lower, while the maximum stress values and strain are higher than the ones obtained. By analysing Figure 3.40 representative curves, both sets present a slight waviness, when the plasticity area is reached, which may indicate that intralaminar detachment has occurred. These results clearly indicate that a better mechanical performance is obtained when the samples are printed in XZC, which might occur because the built on edge sample has are more layers, and consequently more perimeters deposited in the loading direction enhancing the material strength.

Table 3.18: Alloy 910 XY45, XZC tensile results and datasheet values.

PA 6/69 Alloy 910			
	XY45	XZC	Datasheet
E [MPa]	796.80±8.61	1707±26.92	503.00
σmax [MPa]	24.96±0.30	36.91±1.06	55.80
ε [%]	17.96±0.02	17.93±0.02	31.00

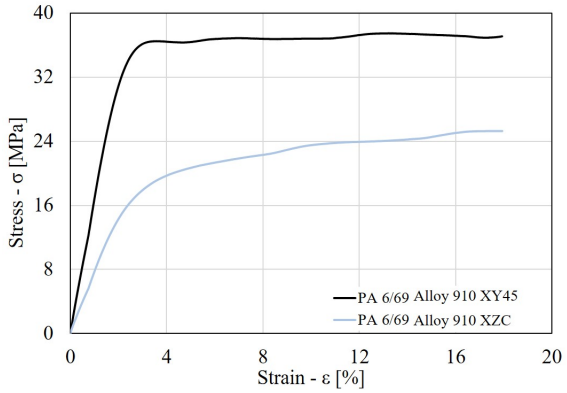


Figure 3.40: Alloy 910 XY45 and XZC representative curves.

PA 12 FX256

Through Table 3.19 it is possible to verify that unlike Alloy 910, FX256 presented an inferior behaviour for the XZC samples relatively to XY45. These results show an increase in modulus of about 38% more than the XY45 samples, while the tensile strength and the strain at break are 14% and 25% inferior correspondingly. When comparing XZC and XYCE, the results are roughly the same considering the standard deviation values. This can be explained by the fact that, even though one is printed on edge and the other flat, there is a similarity in the number of longitudinal lines (along the sample – solicitation direction) creating this resemblance in behaviour. As far as the data sheet results are concerned, the modulus is roughly similar to XY45 and XYCE values, however the maximum stress and strain are lower than any other samples.

Table 3.19: FX256 XY45, XZC, XYCE tensile results and datasheet.

PA 12 FX256				
	XY45	XZC	XYCE	Datasheet
E [MPa]	1565 ± 36.97	1130 ± 27.55	1296 ± 131.70	1400.00
σmax [MPa]	36.97 ± 0.40	32.48 ± 0.84	32.33 ± 0.28	45.00
ε [%]	17.13±0.58	13.63±1.36	12.77± 0.52	>50.00

Considering the representative test curves in Figure 3.41, it is possible to observe that even though XY45 presents higher values of tensile strength and stiffness, similar behaviour is identified. In this case, the three curves show yielding occurring at similar strain values (≈3%). Strain hardening is found above the yielding point until the maximum stress is reached, (roughly 8% of the strain), maintaining the stress value, necking and/or fracturing at the end.

PA12 CF15

The results obtained from the mechanical testing of the PA 12 CF15 samples are presented in Table 3.20. Young's modulus results indicate that XY45 samples present the lowest values (unlike

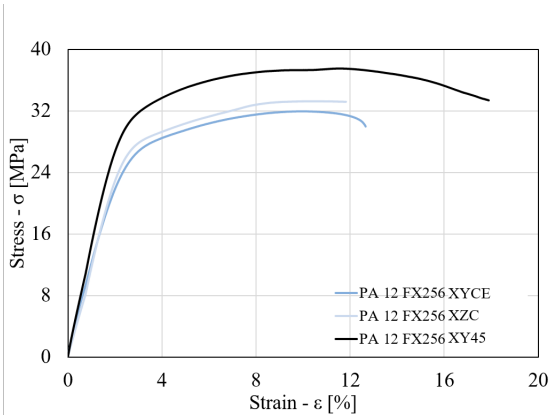


Figure 3.41: FX256 XY45, XZC and XYCE representative curves.

FX256), while roughly similar results are found for XZC and XYC, even considering a much higher dispersion in XZC results. Due to fibre presence, an increase in modulus (and decrease in strain) is expected. The fibres are aligned with the extruder deposition direction (material flow), thus concentric samples take greater advantage of their presence than the $\pm 45°$samples. For tensile strength, results indicate once again the highest value for XZC samples, even though high levels of dispersion.

In this case, the fibre presents an increase in overall performance facing FX256 of approximately 3 MPa (XY45 and XYCE). However it is not possible to conclude how it impacts XZC due to the high results dispersion. For strain at break, it is shown that the XY45 samples present the higher value followed by the XYCE, XZ and XYC. Since the only difference in parameters between XYC and XYCE is the extruder entry area, it might be possible that the strain is lower due to an existence of a discontinuous deposition or merging area of the entry and exit of the extrusion head, originating in a premature rupture of the sample. Similarly to the unreinforced material, higher strain was expected for XY45 samples due to its pattern. Considering that, XYC and XYCE present the exact same internal pattern, besides the distinct entry point. In theory the mechanical properties should be similar, if not greater for the second case, which was not confirmed by the results. By testing these two types of samples it was possible to understand how the entry point at the beginning of the sample's neck could lead to a premature fracture, thus incorrectly influencing the results.

By analysing XZC vs XYC, it is understandable the similarity in modulus and tensile strength, due to the resemblance in the internal scheme. Even though they are printed in different directions, the number of longitudinal lines deposited is similar, as it can be seen in Figure 3.38. As far as datasheet results, it is possible that this data has been provided incorrectly. By comparing it with FX256 datasheet it is possible to observe that CF15 the modulus is lower than the unreinforced version, and the strain is almost the double. As far as maximum strength, all the tested orientation/schemes fail to meet the datasheet values.

Figure 3.42 depicts CF15 representative curves for each set of samples, in which it is possible to observe similar profiles even though there is a difference in the final properties.

Table 3.20: CF15 XY45, XZC, XYC and XYCE tensile results.

PA 12 CF15					
	XY45	XZC	XYC	XYCE	Datasheet
E [MPa]	1907 ± 98.69	2969 ± 601.2	2952 ± 36.2	2243 ± 6.43	500.00
σmax [MPa]	39.47 ± 0.41	45.96 ± 9.11	38.45 ± 3.81	35.45 ± 1.33	54.50
ε [%]	7.90± 0.58	5.02 ± 0.94	2.6 ± 0.84	6.59 ± 1.42	>103.00

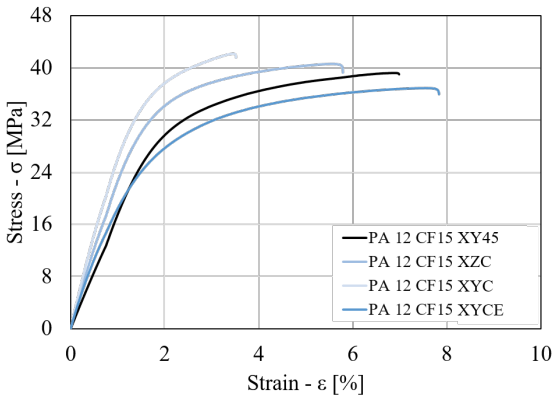


Figure 3.42: CF15 XY45, XZC, XYC and XYCE representative curves.

3.4.3.2 Material comparisons

Table 3.21 depicts the summarized results by printing orientation, making it possible to compare different materials. For XY45 specimens, a highest modulus was presented by the reinforced (CF15). As far as tensile strength, the same reinforced material is only 6.7% higher than its pure version (FX256). Strain values are similar for FX256 and Alloy 910, while CF15 is much inferior due to the fibre presence. XZC results indicate, once again, that higher modulus and tensile strength are achieved with the reinforced samples even considering high levels of standard deviation. However, Alloy 910 and FX256 present contradicting values when facing the XY45 results. For the flat samples (XY45), FX256 presented superior behaviour in terms of modulus and tensile strength, while Alloy 910 presents the best performance between the two for XZ. Considering the concentric samples (XYCE), the obtained results indicate that CF15 is a stronger, stiffer and less ductile behaviour as it would be expected for a short fibre reinforced material.

3.4.4 Conclusions

Through this work it is possible to verify that beyond the feedstock material original properties, the internal part pattern and build orientation are a major factor when considering mechanical performance. A major goal of this preliminary study was to understand how these printing properties influence the final part property. By subjecting different materials to distinct printing conditions it was possible to understand if these changes affect equally all the materials. This way, it was

Table 3.21: Building orientation comparison

XY45			
	FX256	Alloy 910	CF15
E (MPa)	1564.55±20.37	796.78±8.61	1907.44±98.69
σmax (MPa)	36.97±0.40	24.96±0.30	39.47±0.41
ε (%)	17.13±0.58	17.96±0.02	7.90±0.58
XZ			
	FX256	Alloy 910	CF15
E (MPa)	1130.37±27.55	1706.75±26.92	2968.56±601.23
σmax (MPa)	32.48±0.84	36.91±1.06	45.96±9.11
ε (%)	13.63±1.36	17.93±0.02	5.02±0.94
XYCE			
		FX256	CF15
E (MPa)		1296,03±131,69	2243,16±66,43
σmax (MPa)		32,33±0,28	35,45±1,33
ε (%)		12,77±0,52	6,59±1,42

possible to understand that printed parts act more like a structure than a homogeneous material, thus proving the lack of isotropy.

Even though no data about sample production parameters is given in the datasheet, it was shown that tested samples stress values are lower than what is presented by the manufacturers. Young's modulus are also different from the datasheet values, hence, for this case, it is completely disproved that FX256 presents higher modulus than CF15. Considering these two materials, it is possible to conclude that, the fibre becomes a predominant element regarding material stiffness, in which its effect is maximized if its deposition is done in the solicitation direction.

Considering the global set of results, it is possible to conclude that the mechanical performance depends on the feedstock's original property and its internal scheme. Higher modulus and strength will reflect its properties if deposited in the solicitation direction. For non longitudinal pattern dispositions, the interface between two deposed lines will have a distinct behaviour than the longitudinal, i.e., ±45°is generally less stiff, when considering higher modulus materials.

FFF process is one of the most simple and rudimentary AM technologies, thus being susceptible to several influential uncontrollable factors such as: moisture in the filament which leads to air gaps and material bubbling at the extruder, difference in temperature for distinct tray areas, extruder temperature oscillations and distinct properties throughout the batch. These are some of the influential variables which might lead to distinct performance of the same feedstock,throughout each printing batch, which presents an obstacle to obtain similar results with a few different samples.

Chapter 4

Advanced performance characterization

In this chapter, unconventional/non normalized tests are described in detail, allowing the analysis of properties that with typical tensile and flexural type tests would not be possible. Two distinct methodologies are presented in this chapter. Section 4.1 presents a study concerning the interlaminar fracture behaviour off FFF parts under mode I. For these tests, a method for double cantilever beam (DCB) production is developed, in which the samples are posteriorly tested and compared to a numerical analysis. In section 4.2, the mechanical properties variation according the building orientation is analysed by means of the modified Arcan test for distinct types of solicitation. A specific type of sample was also developed considering the production process and the testing apparatus. Through this work, it was possible to quantify the lack of isotropic behaviour.

4.1 Study of the interlaminar fracture under mode I loading on FFF printed parts

The work described in the forthcoming section is presented in original article format, as published by Composite Structures Journal [Fonseca et al., 2019].

The present study aims the development of a methodology for the analysis and evaluation of the fracture toughness under mode I loading of 3D printed parts, produced by the fused filament fabrication (FFF) additive technology. This work is motivated by the urgent need of improvement in this area, in order to extend the reliability of this process to applications which require high mechanical performance. For this purpose, a specific geometry was developed, taking into account the inherent characteristics of both, the applied material and process used for the production of DCB tests. A set of experimental tests was performed with pure and short fibre reinforced Polyamide 12 (PA 12), and, in parallel, a numerical analysis was also followed. Posteriorly, an inspection on the fracture surfaces was made, by microscopy, in order to refine the conclusions obtained and furtherly comprehend the variables in play. The obtained results provided a consistent value for the fracture toughness for only one of the cases studied, being this the unreinforced

material. However, for the reinforced material, a set of conclusions which justify its behaviour was also able to be attained. The followed approach for the numerical analysis also revealed to be as suitable for this specific combination of material and additive process.

4.1.1 Introduction

Fused Filament Fabrication (FFF) is one of the most popular additive manufacturing (AM) techniques, which has been regarded as an effective method for the creation of complex geometries. However, as it can be understood from the production process, which rely on creating the desired geometry layer by layer, the interfacial bonding strength between the mentioned layers plays an important role on the mechanical properties of the resulting part. Since each layer is created by deposition of a line of extruded filament in a defined orientation, this process is also prone to induce manufacturing defects, such as voids or air gaps. In fact, one of the major issues when applying this technique is the highly anisotropic behaviour exhibited by the produced parts, which is undesirable when the demanded application requires a high mechanical performance. This effect is considered to be one of the major limitations in the current state of art for FFF process, since it limits its applicability to aesthetic and low load bearing components. The type of tests developed in this work, consider two different of feedstock materials. A pure PA 12 and a reinforced version of the same material were used for sample production, introducing the fibres as another variable process uncertainty. As it can be perceived by this conclusion, it is important to develop solutions from which higher mechanical properties can be obtained, in order to increase its viability for this type of applications.

Thus far, conducted researches are primarily focused in the mechanical performance identification by associating the feedstock material, the process and the type of printing settings that are used. The influence of correct parametrization of FFF printed parts is key in defining how capable is the mechanical response, when submitted to a solicitation. Studied parameters are mainly defined by three categories (Figure 4.1): material-related for printing temperatures; geometric-related, with properties like infill orientation/width, air gap and layer height, and process-related, for printing speeds, extrusion flow among others. Those also define the level of anisotropy taking into account the part orientation when printed [Ahn et al., 2002, Chin Ang et al., 2006, Masood et al., 2010, Ziemian et al., 2015]. Most of these studies focuses in tensile properties of printed parts, leaving a characterization gap when considering the interlayer mechanical performance.

Other resultant property is the dimensional accuracy. Studies show the influence of these parametrization on the definition of how exact or not the initial CAD geometry can become after printing [Sood et al., 2009]. It was proven that parameter such as extrusion multiplier is one of the most responsible factors for distortions in the printed sample [Santana et al., 2017]. In a similar set of experiments, Peng et al. [2014] proved that raster width and thickness were the most influential factors when considering dimensional accuracy [Young et al., 2018, in Park et al., 2018, Spoerk et al., 2017].

Regarding fracture toughness, few studies have been conducted. In Young et al. [2018] research, a modified DCB sample, version of the ASTM D5528 [ASTM D5528-01, 2014] is applied

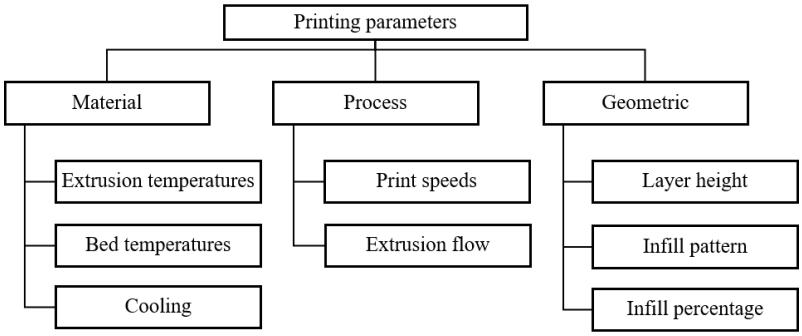


Figure 4.1: Printing parameters division.

for the experimental tests, followed by the use of the Compliance Calibration Method (CCM) data reduction scheme. The authors concluded that this standard is an adequate methodology for the characterization of the interlayer performance of FFF components, filling in part of the existent characterization gap, which may prove essential for the development of the technology. Furtherly sustaining this conclusion, a study presented in Park et al. [2018] attempted to characterize the fracture behaviour of DCB specimens created with Acrylonitrile butadiene styrene (ABS), employing cohesive damage models. The authors concluded that this type of approach can be used as an effective tool to capture the interlayer fracture behaviour of the FFF components, as well as to improve the fracture energy estimation procedure of the final components. In Spoerk et al. [2017], a DCB test is conducted on samples manufactured with Polylactic acid (PLA) supplied by Prirevo e.U., Austria. It was concluded that the layer design parameters, such as layer thickness or raster orientation specific for the type of load applied, are key aspects in enhancing the interlaminar strength of the final component. It was also stated that the DCB test is an appropriate methodology to perform studies for this type of technology.

Due to being created with a layer-by-layer step process, the parts obtained from the FFF technology can be regarded in the same light as laminate composites. As result, they tend to exhibit the same type of problems as these composites. Among them, the possible delamination effect between adjacent layers is one of the most severe types of damage that can occur, being its consequence a reduction on the mechanical properties, resulting in an early failure of the component [Islam and Prabhakar, 2017]. This effect is due to a crack propagation phenomenon, which is a typical application of the fracture mechanics concepts. The same problems are susceptible to occur between adjacent layers of the FFF components, since the process itself is responsible for the separation of the layers.

Taking into account the previously mentioned discussion, this work intends to study the bond connection between layers, i.e., the interlaminar strength and toughness under mode I loading at these critical interfaces, of components created by the FFF process. In order to do this, an analysis via fracture mechanics concepts will be applied, for the characterization of the crack propagation behaviour presented by a series of experimental tests. This is done in order to study and adequate a method from which the correct measurement of the fracture toughness can be obtained. By using

a test geometry based on the DCB test, portrayed by ASTM D5528-01 [2014] standard for unidirectional fibre reinforced polymer matrix composites, a methodology for sample creation was developed avoiding the usage of reinforcing doublers. The aim is to present measures that can be taken to enhance it, since it is the main property responsible for characterization of the fracture between layers. As stated previously, this work presents a newly developed approach to fracture toughness under mode I, by defining a new test geometry, including an also printed disposable supporting structure that allows for a more accurate pre-crack creation, using reinforced and unreinforced FFF printed PA 12 parts, in parallel with numerical simulations for result validation.

4.1.2 Materials and methods

4.1.2.1 Material Selection

Two types of 1.75 mm diameter PA12 from Fillamentum ©, Parzlich s.r.o (Czech Republic) materials were selected. A pure version of PA12 (Nylon FX 256) and a composite one (CF15), reinforced by short carbon fibres (15 vol.%), with approximately 100 μm in length and 10 μm diameter, both obtained in filament form. This selection was made based on research requirements in this area, which is the implementation of reinforced composites in the FFF process [Zhang et al., 2018, Islam and Prabhakar, 2017]. This type of polymer is widely regarded as an engineering plastic, being suitable for applications which require load bearing. The interest in applying this material to the FFF technology is understood as a need for further advancement in the mechanical properties, which are able to be obtained from it. Furthermore, the same type of investigations is also currently being conducted for other polymers, for instance ABS [Ziemian et al., 2012, Aliheidari et al., 2016] and PLA [Tymrak et al., 2014]. However few studies have been conducted with engineering thermoplastic such as PA 12, which reinforces the appropriateness of searching a suitable testing methodology.

4.1.2.2 Development and fabrication of DCB printed samples

Definition of DCB overall dimensions

As a first approach, the specimen dimension procedure applied in Young et al. [2018] was considered. Those authors decided, due to the low stiffness of the material (ABS), to apply glass/epoxy doublers as a way to prevent the deflection of the specimens during the DCB test. While this can be an effective method of reducing the deflection, it can also increase the overall fracture toughness of the specimen, since when solicited, damage can develop at interfaces between the doublers and the specimen which dissipates fracture energy. This circumstance leads to erroneous estimations of material fracture toughness, which is difficult to keep account. Even if this type of over estimation can be made negligible by considering the use of a strong adhesive, it must be taken into account that there is no reference for the expected fracture toughness values of the specimens, which makes difficult the assessment of the relevance of spurious energy being dissipated. For these reasons, another approach was followed based on dimensioning of specimens taking into consideration the

low Young's modulus (E_1) of the material. The bending stiffness ($E_1 * I$) imposed for the specimen's arms was based on previous works [Dias et al., 2013, Spoerk et al., 2017] using DCB tests which have pointed to values of the order of 10^6 N/mm^2. Another condition was imposed, which was the specimen standards for the dimensioning presented in [ASTM D5528-01, 2014]. For the materials used, Nylon FX256 (PA12) and Nylon CF15 Carbon (PA12CF), the mechanical property values were obtained from previously performed tensile tests on specimens created by the same FFF equipment and settings used to produce the DCB samples. For fully dense, ±45° infill, ISO 527 dogbones presented an average Young's modulus for PA12 of 1564.6±20.4 MPa, and for the PA12CF, 1907.4±98.7 MPa. In both cases, the specimen arms are thick balanced laminates and the propagation is mainly resin controlled at the pre-cracked interface. These conditions minimize the presence of spurious modes of loading (mode II and mode III) thus leading to predominant mode I [De Morais et al., 2003, Samborski, 2016]. From the array of combinations obtained, the decision on the final dimensions was also made based on the possible warping effect which can take place due to the thermal gradient induced by the continuous deposing of filament. The defined specimen dimensions were then obtained, being presented in Table 4.1 with the schematic representation in Figure 4.2.

Table 4.1: Specimen nominal dimensions.

Specimen Material	Length L [mm]	Width B [mm]	Height h [mm]	E_1 [MPa]	I [mm^4]	Pre-crack a_0 [mm]	$E_1.I$ [N*mm^2]
PA12CF	125	25	6	1907.4±98.7	450	50	8.5x10^5
PA 12	115	25	6	1564.6±20.4	450	40	7.0x10^5

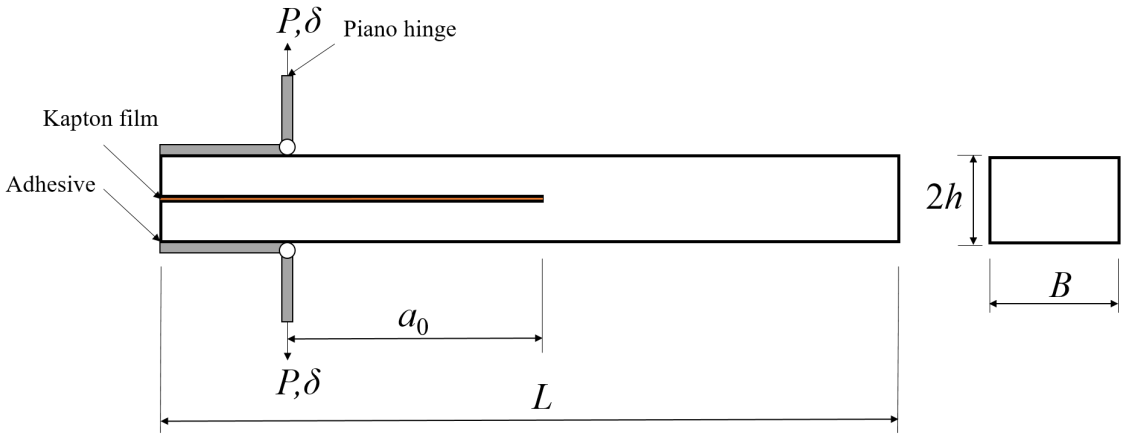


Figure 4.2: DCB schematic representation.

DCB printing strategy and production settings

The DCB specimens were manufactured accordingly the dimensions shown in Table 4.1, following a methodology for pre-crack creation iteratively developed. In order to match the mechanical

properties obtained via tensile tests, ensuring the bending stiffness and toughness needed for a correct crack propagation, 100% dense infill was used, also minimizing the part voids presence. For the production process, a commercially available Tronxy X5 3D printer from Shenzen Tronxy Technology Co. Ltd was used, in which the extrusion process was performed with 0.4 mm diameter stainless steel nozzle, layer height of 0.3 mm and raster orientation $\pm 45^{\circ}$. Considering process temperatures, an extrusion temperature of 260°C and a print bed temperature 90°C were utilized. As a consequence of the high infill percentage applied, the amount of deposited material in each layer and the time needed to complete it also increases. This heavily influences the thermal gradient of the specimen, leading to a higher warping effect. In addition, another issue was found while printing the specimens, being it when creating the pre-crack during the printing. A Kapton® film was applied between the layers adjacent to the mid-plane of specimen. Being the specified height for each layer of the specimen 0.3 mm, the specimen then contains 40 separate layers, corresponding to its total height of 12 mm, which means the film is applied between the 20th and 21st layers.

However, due to the inexistence of adhesion between the newly deposed layer and the Kapton® film, this process was not straightforward. Several attempts were performed in order to be able to insert the Kapton® film without affecting the printing of the specimen. In order to solve this problem, a new geometry was created, containing a disposable part solely for the film support, which was used to prevent the film and specimen from warping, by depositing 2 extra layers on top of the film. Also, the increase in adhering area to the heated bed is also beneficial since it counteracts the thermal contraction effect. The appearance of the new geometry is shown on Figure 4.3a, and it consists in three different parts combined. The printing starts with parts 1) and 2) representing the support structure and DCB specimen which are both printed until reaching the height of 6 mm, and at this point the print is paused and the Kapton® film is applied in order to create the pre-crack, continuing with the enclosing layers 3) and the rest of the sample 2). This allows the Kapton® film to be sealed, while also preventing the layers deposed on top of it from warping, since part 3 also adheres to a part of the support which is not covered by the Kapton® film. After the printing job, the resulting part is taken out of the bed, and the support and film are cutted out, originating on a DCB specimen.

Two piano hinges were bonded to the end of each specimen, following the procedure presented in the ASTM D5528 [ASTM D5528-01, 2014]. Prior to bonding, the surfaces of the hinges and the specimens were smoothed with sandpaper and cleaned with isopropyl alcohol to ensure the load transfer without debonding. After the application of the adhesive, a clamp was placed in each specimen, to prevent the hinges from moving and to guarantee an optimal cure process of the adhesive, which lasted 48 hours.

Following this methodology, the production process, took approximately 2 hours and 20 minutes for each sample. Table 4.2 presents the real dimensions of the created samples.

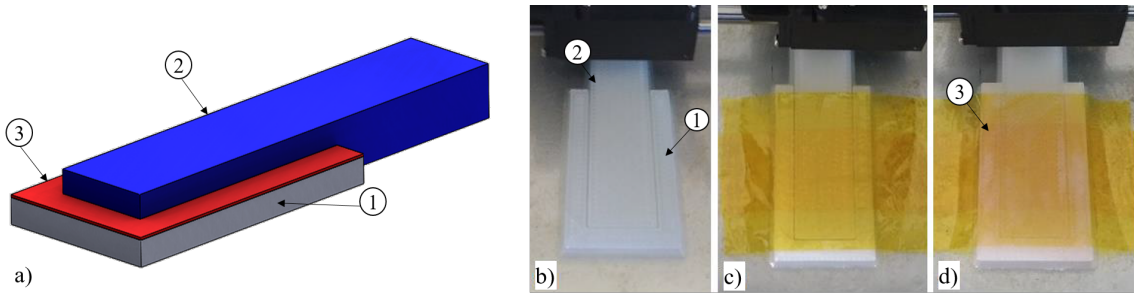


Figure 4.3: a) CAD model for the newly developed approach, b) Support and specimen until 6 mm in height, c) Kapton® film application and d) Support enclosing layers and rest of the test sample.

4.1.2.3 Testing procedure

After the completion of the cure process, the specimens were tested using an Instron Model 4208 universal testing machine with 5kN load capacity and an opening rate of 5 mm/min at environment temperature (≈25°C). From Figure 4.4 it is possible to understand that for both PA12 and PA12CF crack propagation at the pre-cracked plane was able to be achieved, however it is distinguishable in between a) and b) the difference in flexibility. Since both samples have the same geometry, this is due to an inferior Young's modulus for the unreinforced material.

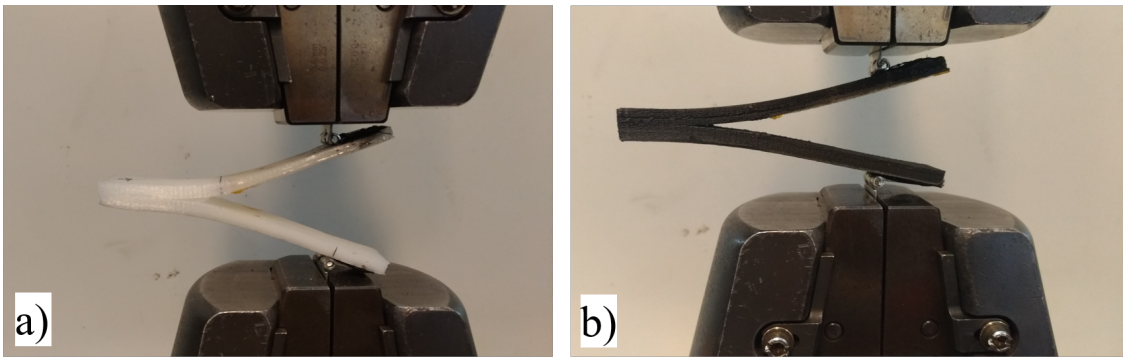


Figure 4.4: DCB test at the end positions for: a) PA12 b)PA12CF.

4.1.2.4 Data reduction scheme

An equivalent crack length based procedure was followed to get the *Resistance*-curve (*R*-curve) as a function of load-displacement data. This method is particularly advantageous since crack length monitoring is difficult to be performed with the required accuracy due to unstable crack growth, and accounts indirectly by the energy dissipated in the fracture process zone (FPZ) [de Moura et al., 2008].The method relies on specimen compliance ($C = \delta/P$) determined through Timoshenko beam theory which can be expressed as [Dias et al., 2013],

$$C = \frac{8a^3}{E_1 B h^3} + \frac{12a}{5BhG_{13}} \tag{4.1}$$

Table 4.2: Real specimen dimensions.

Specimen	Length L [mm]	Width B [mm]	Height h [mm]	Pre-crack a_0 [mm]
PA12-1	123.4	25.1	5.51	46.3
PA12-2	124.5	25.2	5.57	47.4
Average	123.9	25.1	5.54	46.9
St. Dev.	0.8	0.1	0.04	0.8
PA12-3	114.0	25.7	5.54	37.5
PA12CF-1	114.9	25.8	5.58	37.6
PA12CF-2	114.5	25.7	5.61	37.7
PA12CF-3	115.5	25.7	5.51	37.2
Average	115.0	25.7	5.57	37.5
St. Dev.	0.5	0.1	0.05	0.2

where E_1 and G_{13} are the material elastic properties, a the crack length and B and h specimen dimensions (Figure 4.2). This equation can be solved aiming to get the equivalent crack length a_e as a function of the current compliance, C using the Matlab® software [de Moura et al., 2008, Dias et al., 2013]. Combining the Irwin-Kies equation

$$G_{\mathrm{I}} = \frac{P^2}{2B}\frac{dC}{da} \tag{4.2}$$

with equation 4.1, yields

$$G_{\mathrm{I}} = \frac{6P^2}{B^2 h}\left(\frac{2a_e^2}{h^2 E_1} + \frac{1}{5G_{13}}\right) \tag{4.3}$$

Following this procedure, an estimation of the mode I energy release rate G_{I} as a function of the equivalent crack length a_e (R-curve) can be obtained, only requiring the data ensuing from the load-displacement curve. The only issues faced when applying this data reduction scheme were the values used for E_1, the Young's modulus, and G_{13}, the shear modulus, which were not available. The Young's modulus was determined by an inverse procedure fitting the initial stiffness of the numerical load-displacement curve to the experimental observed one. In order to get accurate values, each specimen was simulated considering its real dimensions instead of the nominal ones. In the case of the shear modulus, it can be observed from equation 4.3 that its importance is quite low when regarding the overall result. Consequently, a typical value was assumed for it, considering that in a generic orthotropic material the shear modulus is typically ten times lower than the Young's modulus, for the referred direction.

4.1.3 Numerical analysis

Finite element analyses considering cohesive zone modelling (CZM) were performed aiming to identify softening laws representative of fracture behaviour of the tested materials. These models allow reproducing material fracture behaviour assuming two distinct stages. Before the occurrence

of any damage, the model is in the linear elastic regime, being characterized by the following equation,

$$\sigma = \mathbf{E}\delta_r \tag{4.4}$$

in which σ and δ_r are the stress and relative displacements vectors that develop between homologous points belonging to the surfaces of the cohesive element, and **E** is a diagonal matrix containing the interface stiffness. The values inputted in this matrix aim to satisfy two requirements: first, the value should be as high as possible in order to minimize unwanted interpenetrations when compression occurs [de Moura et al., 2008]; second, the value is limited in order to avoid numerical problems. These circumstances led to a compromise giving rise to a value normally in the range $10^6 - 10^7$ N/mm^3, usually known as the penalty parameter. After reaching the local strength, damage occurs, and the equation 4.4 turns into

$$\sigma = \mathbf{(I\text{-}D)E}\delta_r \tag{4.5}$$

where **I** is the identity matrix, and **D** is a diagonal matrix containing the damage parameter, d, which is function of the softening law utilized. Two different cohesive laws were considered in this work, the trapezoidal and the trilinear one. In both cases, inverse procedures where used to identify the cohesive law (CL) representative of the material fracture behaviour. The CL is iteratively adjusted aiming a good fitting between the numerical and experimental load-displacement curves.

4.1.3.1 Trapezoidal cohesive law

The trapezoidal law is particularly adequate when non-linear fracture behaviour is present, thus being appropriate for PA12 whose load-displacement curves revealed some non-linearity after the peak load. This behaviour is a symptom that some plasticity is associated to the fracture process, which is properly accounted for in the trapezoidal law (Figure 4.5).

In the plateau region ($\delta_{1,I} \leq \delta_I \leq \delta_{2,I}$) the damage parameter becomes,

$$d = 1 - \frac{\delta_{1,I}}{\delta_I} \tag{4.6}$$

being δ_I the current relative displacement and $\delta_{1,I}$ obtained from the local cohesive strength σ_U and the initial stiffness value. The size of the plateau is given by $\delta_{2,I}$ and governs the plastic behaviour associated to fracture. After the second inflexion point ($\delta_{2,I}$, σ_U) a linear stress softening occurs till complete failure ($\delta_{2,I} \leq \delta_I \leq \delta_{u,I}$) by means of the following damage parameter,

$$d = 1 - \frac{\delta_{1,I}(\delta_{u,I} - \delta_I)}{\delta_I(\delta_{u,I} - \delta_{2,I})} \tag{4.7}$$

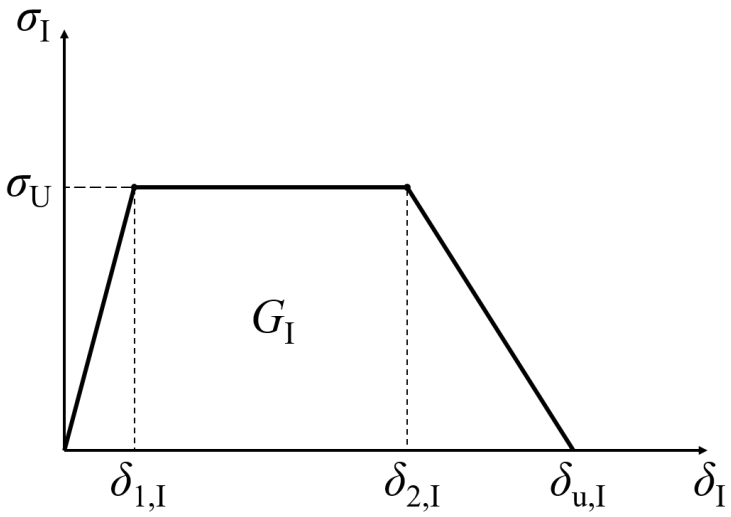


Figure 4.5: Trapezoidal constitutive law for pure-mode I.

The ultimate relative displacement value $\delta_{u,I}$ is obtained equating the area of the trapezoid to the critical strain energy release rate,

$$\delta_{u,I} = \frac{2G_{Ic}}{\sigma_u} - \delta_{2,I} + \delta_{1,I} \tag{4.8}$$

In this case, the iterative procedure involves alteration of the parameters $\delta_{2,I}$ and σ_u till good agreement is achieved.

4.1.3.2 Trilinear cohesive law

This law is characterized by a bilinear softening relationship thus being suitable for materials revealing different fracture mechanisms ahead of the crack tip, as is the case of micro-cracking and fibre bridging [de Moura et al., 2008]. This fracture behaviour usually reflects on remarkable non-linearity of the load-displacement curves before the peak load (Figure 4.6), which was observed in the PA12CF material.

In the first softening branch ($\delta_{1,I} \leq \delta_I \leq \delta_{2,I}$) the damage parameter writes,

$$d = \frac{\delta_{2,I}(\delta_I - \delta_{1,I})(1-\phi)}{\delta_I(\delta_{2,I} - \delta_{1,I})}, \delta_{1,I} \leq \delta_I \leq \delta_{2,I} \tag{4.9}$$

being ϕ=$(\sigma_{2,I}.\delta_{1,I})/(\sigma_U.\delta_{2,I})$. For the final branch the damage parameter yields

$$d = 1 - \frac{\phi\,\delta_{2,I}(\delta_{u,I} - \delta_I)}{\delta_I(\delta_{u,I} - \delta_{2,I})}, \delta_{2,I} \leq \delta_I \leq \delta_{u,I} \tag{4.10}$$

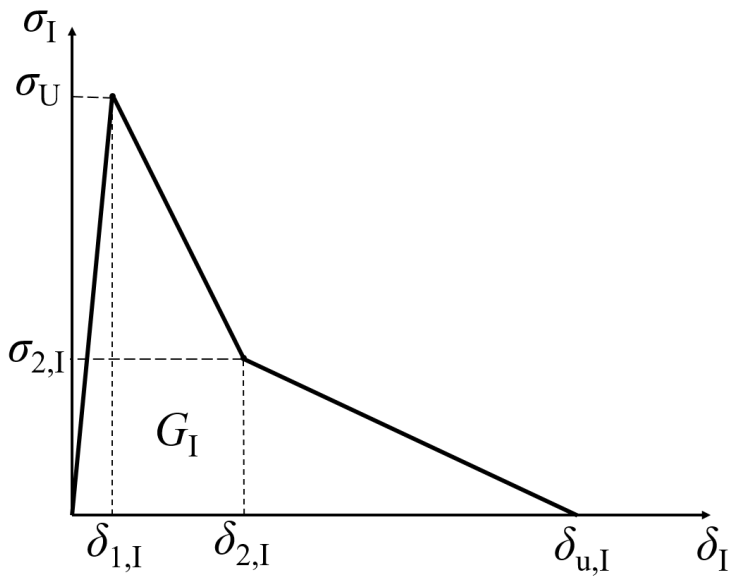


Figure 4.6: Bilinear stress-softening constitutive law for pure-mode I.

where the ultimate displacement $\delta_{u,I}$ is given by the area under the stress– relative displacement softening model,

$$\delta_{u,I} = \frac{2G_{Ic} + \sigma_{2,I}\sigma_{1,I} - \sigma_{u,I}\delta_{2,I}}{\delta_{2,I}} \tag{4.11}$$

In this model, an additional parameter ($\sigma_{2,I}$) is included in the inverse procedure in order to fit the numerical and experimental load-displacement curves.

4.1.3.3 Finite element analysis

The models described earlier were implemented as a user subroutine, in ABAQUS® software. Plane strain analysis was assumed, owing the width of the specimens, considering 8-node solid isoparametric rectangular elements with mesh refinement in the region where crack propagation occurs, aiming to get more accuracy. The cohesive zone, where damage is susceptible to occur (the mid-plane of the specimen), was modelled by 106 6-node cohesive elements compatible with the solid elements as seen in Figure 4.7.

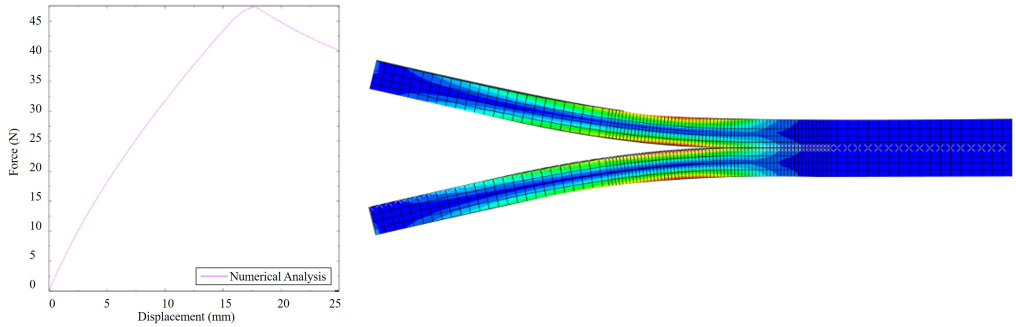


Figure 4.7: $P-\delta$ curve and corresponding state of the numerical DCB specimen at post peak zone (Von Mises Stress).

4.1.4 Results and discussion

The experimental load-displacement curves were registered in the course of the DCB tests. Subsequently, the data reduction scheme described in Section 4.1.2.4 was applied aiming to get the corresponding resistance-curves. The critical strain energy release rate was obtained from the plateau region of these curves and used as input in the numerical analysis in order to determine cohesive laws representative of materials fracture behaviour. Three experimental results were obtained for each material.

4.1.4.1 Nylon FX256 (PA12)

Figures 4.8 shows the experimental load-displacement curves and the corresponding *R*-curves obtained for PA12. It can be observed that after peak load the load decreases smoothly meaning that nonlinear fracture phenomenon is occurring. Typically, the ensuing *R*-curves reveal two main regions. Initially, a gradual rising trend is observed until a plateau develops. The first branch corresponds to FPZ development and its large extension is a symptom of substantial FPZ, which reinforces the idea of a nonlinear fracture mechanics behaviour. Two initial tests with a nominal a_0=50 mm were performed. Since large displacements were observed the third one was executed with a nominal a_0=40 mm. However, no remarkable influence of the initial pre-crack length or measured toughness was observed. In fact, the values of strain energy release rate of the three tests converge to values around 0.8 N/mm revealing consistency. It was observed that the trapezoidal law is appropriate to deal with fracture behavior of PA12. The inverse procedure originates numerical load-displacement and *R*-curves in agreement with the experimental ones (Figures 4.8). The found discrepancies are due to spurious experimental effects related to pull-out layers occurring occasionally (Figure 4.9), leading to the observed irregular pattern on load-displacement and *R*-curves.

Table 4.3 lists the cohesive parameters obtained for each specimen as well as the respective average values.

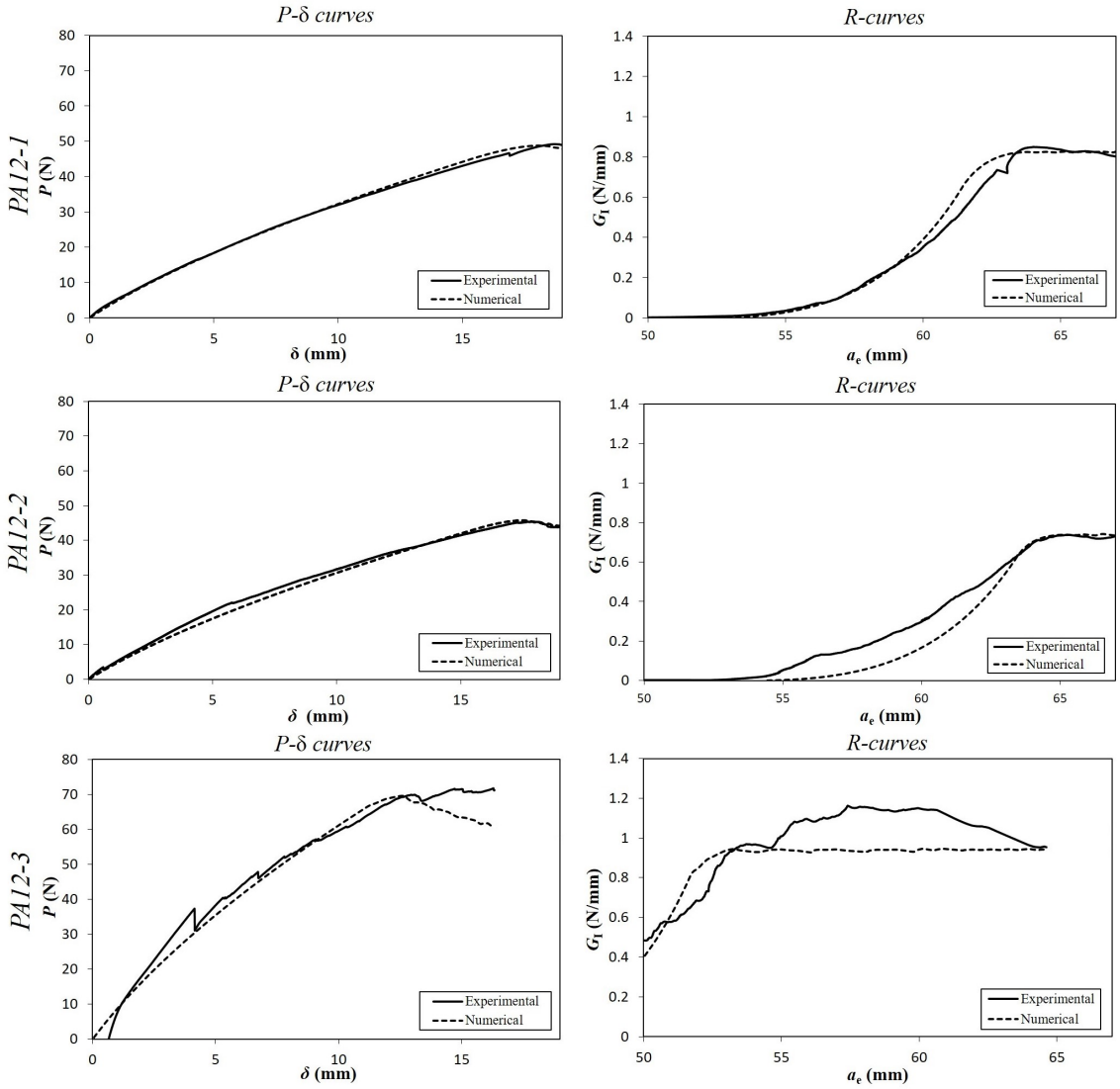


Figure 4.8: $P-\delta$ and the corresponding R-curves of DCB PA12 tests.

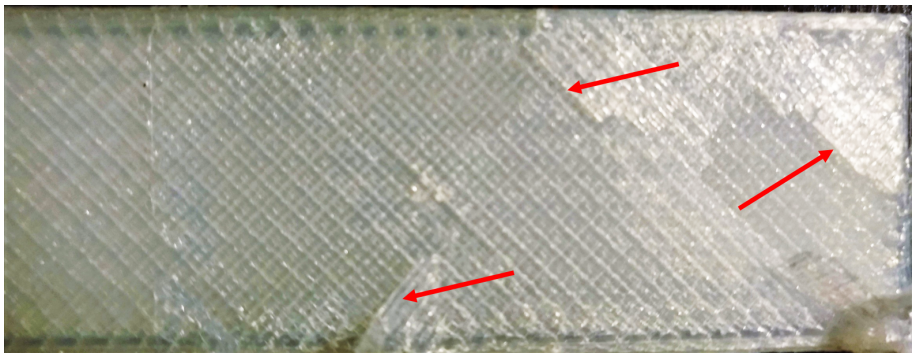


Figure 4.9: Fractured surfaces after the DCB test for a PA12 specimen (arrows evidence pull out layer).

The average cohesive law was used to obtain a typical load-displacement curve of PA12 and

Table 4.3: Cohesive parameters obtained for PA12 specimens.

Specimen	σ_u [MPa]	$\delta_{2,I}$ [mm]	G_{Ic} [N/mm]
PA12-1	0.48	1.35	0.81
PA12-2	0.45	1.38	0.73
PA12-3	0.75	1.00	0.86
Average	0.56	1.24	0.80
CoV [%]	29.5	17.0	8.2

the ensuing curve was compared in Figure 4.10 with the experimental ones respecting to tests with a nominal a_0=50 mm. It can be concluded that the numerical $P-\delta$ curve reproduces the experimental ones, meaning that the obtained CL represents well the fracture behaviour of PA12.

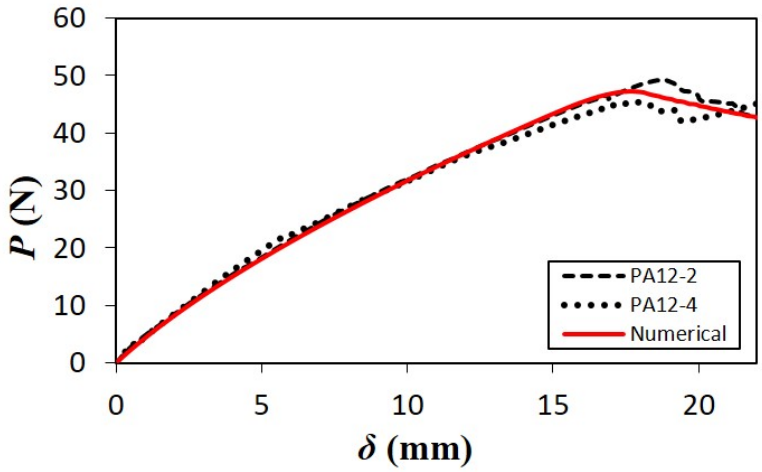


Figure 4.10: Comparison of the numerical $P-\delta$ curve obtained with the average cohesive law with the experimental ones for PA12 considering a nominal a_0=50 mm.

4.1.4.2 Nylon CF15 Carbon (PA12CF)

The experimental load-displacement curves and the respective *R*-curves of the three performed tests are plotted in Figures 4.11. All the tests were executed with a nominal a_0=40 mm owing the statement that much higher toughness was obtained when compared to PA12. In fact, higher initial pre-racks would lead to unwanted quite large displacements. The initial stiffness increased markedly (approximately twice) relative to unreinforced material; the longitudinal elastic modulus (E_1) obtained by an inverse procedure points to 2973 MPa instead of the 1474 MPa found for PA12.

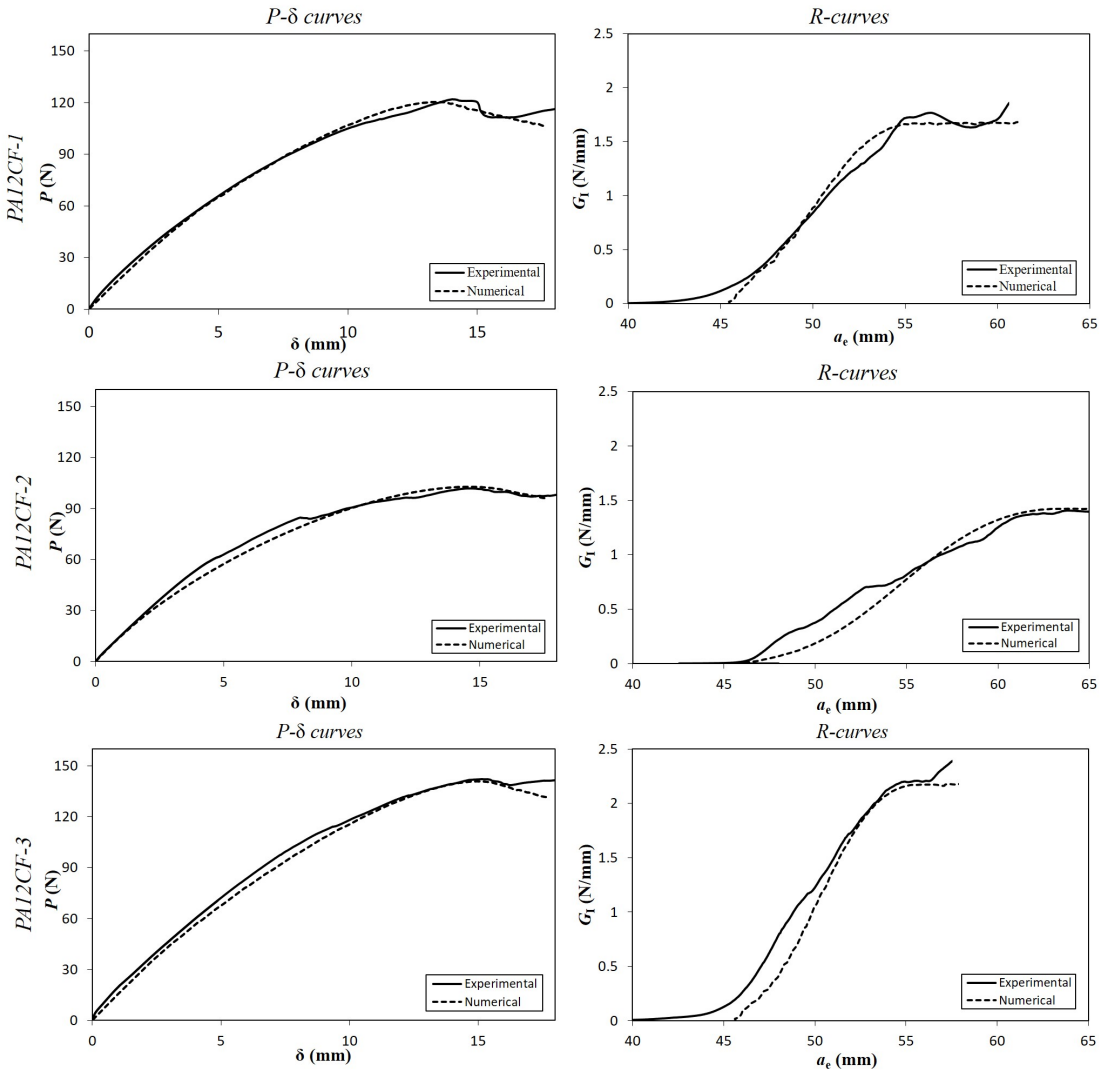


Figure 4.11: $P-\delta$ and the corresponding R-curves of DCB PA12CF tests.

Characteristically, the load-displacement curves revealed a pronounced non-linear behaviour before peak load is attained, which makes more adequate the trilinear CL with bilinear softening relationship. Although the phenomenon of pull-out layers leading to sporadic intralaminar failure is also present in this material (Figure 4.12), its effect on irregular pattern of experimental curves is less pronounced. Overall, good agreement was achieved in load-displacement as well as in R-curves, proving the appropriateness of the trilinear cohesive law to reproduce fracture behaviour of PA12CF.

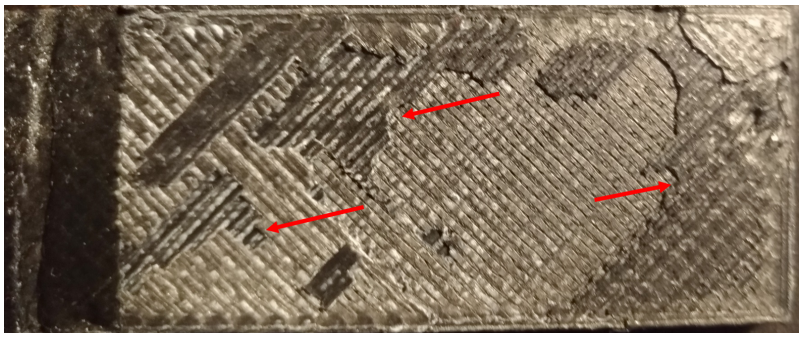


Figure 4.12: Fractured surfaces after the DCB test for a PA12CF specimen.

The cohesive parameters are listed in Table 4.4. Although some scatter can be observed, a special remark should be pointed concerning the high value of G_{Ic} comparatively to PA12. The average values were used as input in a numerical simulation and the resulting $P-\delta$ curve replicates the overall trend of the experimental ones (Figure 4.13).

Table 4.4: Cohesive parameters obtained for the reinforced specimens.

Specimen	σ_u [MPa]	$\delta_{2,I}$ [mm]	$\sigma_{2,I}$[MPa]	G_{Ic} [N/mm]
PA12CF-1	3.25	0.13	1.50	1.70
PA12SC-2	1.00	0.10	0.77	1.44
PA12CF-3	3.40	0.07	1.85	2.21
Average	2.55	0.10	1.37	1.78
CoV [%]	52.7	30.0	40.1	22.0

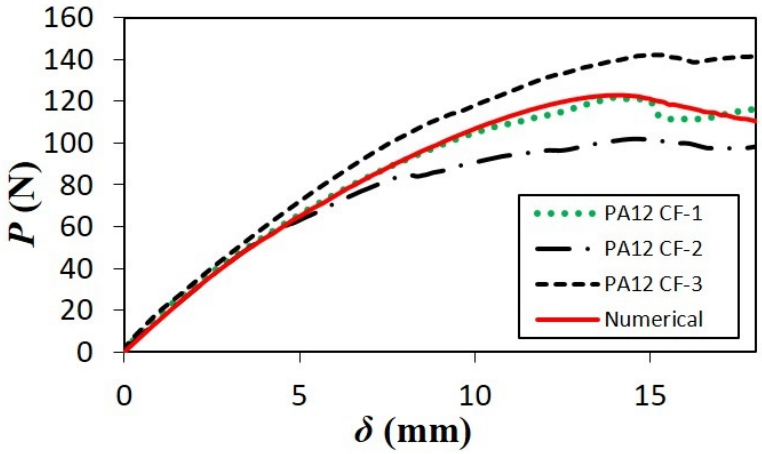


Figure 4.13: Comparison of the numerical $P-\delta$ curve obtained with the average cohesive law with the experimental ones for PA12 considering a nominal a_0=40 mm for PA12CF.

4.1.4.3 Scanning electron microscopy (SEM) analysis

For a better understanding of the behaviour differences observed for each type of material and test, a SEM analysis was conducted. Figure 4.14 shows the resulting surfaces of each type of material. Overall, it is possible to observe that the reinforced specimen exhibits an irregular surface while on the other hand the unreinforced displays a much smoother one. The presence of fibres in fractured surface of reinforced specimen indicates that the fibres were effectively loaded during the test, which explains the higher fracture toughness of PA12CF relatively to PA12.

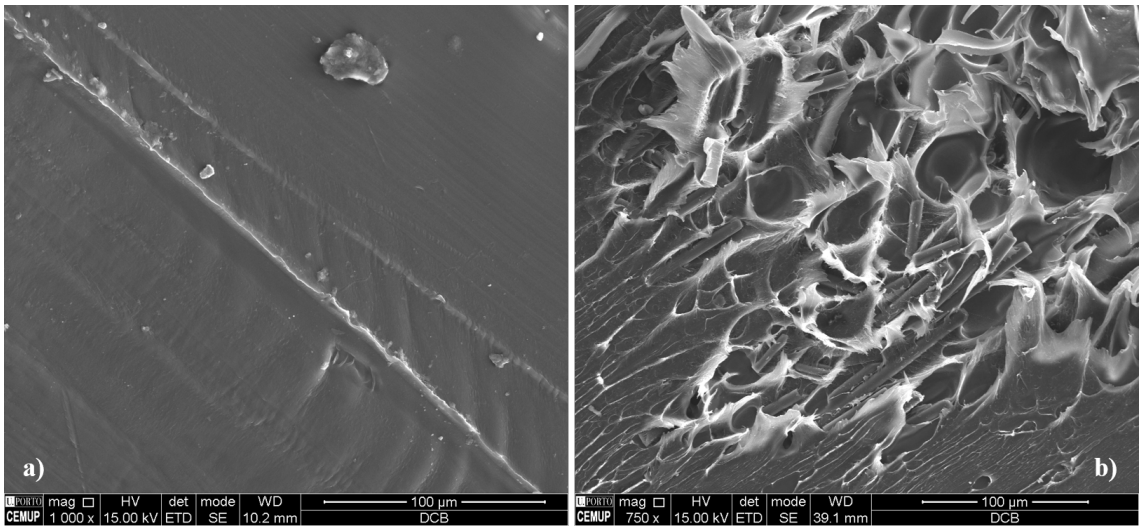


Figure 4.14: Comparison of the fractured surfaces for the a) unreinforced and b) reinforced specimens.

4.1.5 Conclusions

Interlaminar fracture characterization under mode I loading of FFF printed components fracture was studied in this work. Double cantilever beam (DCB) tests were performed considered unreinforced (PA12) and reinforced materials (PA12CF) and a suitable data reduction scheme based on equivalent crack length method was applied. In spite of some scatter, it was verified that reinforcing fibres contributes to increase markedly material toughness. A scanning electron microscopy (SEM) was performed and it was concluded that fibres were effectively loaded during the test, thus explaining the higher fracture toughness. A finite analysis including cohesive zone modelling was performed aiming to determine cohesive laws (CL) representative of the fracture behaviour of both materials. An inverse procedure was followed by iteratively adjusting the cohesive parameters in order to get numerical load-displacement curves in agreement with the experimental ones. It was concluded that the trapezoidal and trilinear CL are appropriate for PA12 and PA12CF, respectively. In fact, the average cohesive laws were used in numerical simulations and the ensuing load-displacement curves were compared with the experimental ones. In both cases it was concluded that resulting numerical load-displacement curve replicates the overall trend of the experimental ones. The average toughness values obtained in this work for the two materials deserve

a special comment. In fact, it is verified that these materials reveal a quite low cohesive strength and Young's modulus when compared with traditional composites. However, a special remark should be done about the fracture toughness under mode I loading, whose values are in the range of 0.8-1.8 N/mm. These values are much higher than the ones of typical thermoset composites, usually in the range of 0.3-0.5 N/mm [de Morais et al., 2015]. This reveals that these materials have a potential of application, namely when interlaminar fracture behaviour under mode I loading is a crucial design parameter to take into account.

4.2 Experimental characterization of FFF printed parts under tension, shear and combined shear-tension loads via Arcan test

4.2.1 Introduction

Similarly to traditional composites, AM produced parts, particularly FFF manufactured parts, if considering the production orientation or internal parametrization, present an anisotropic mechanical behaviour. Due to its in planar infill strategy, the mechanical performance may vary according to the selected property, indicating that anisotropy is present even at layer level. Correspondingly to traditional laminate composites, AM parts are built layer-by-layer. Unlike most traditional composite conformation methods in which shell type parts are obtained, AM/FFF parts are built in a layer-wise manner until an enclosed 3D shape is obtained. Therefore, building directions must be considered in the design stage. Functional parts produced by this technology be subjected to different loading in distinct directions, also resulting distinct mechanical responses. Anisotropic behaviour related to internal pattern and building orientation is characteristic of AM produced parts. Consequently, it is of the most importance understanding the effects caused by these parameters on the part final performance.

Koch et al. [2017] focused their study on the evaluation of the impact in mechanical performance caused by the use of three distinct infill patterns - 0° (longitudinal, concentric samples), ±45° (alternate, diagonal) and 90°(transverse samples) - when compared with injection moulded tensile specimens using acrylonitrile butadiene styrene (ABS) material. In addition, the compaction rate effect (caused by bed adjustment parameters) on the mechanical performance of the specimens was evaluated. The tests indicate that the tensile strength of longitudinal samples was 92.3% of the injected material, while the worst behaviour was presented by the transversally printed samples, with 72% of the injected parts tensile strength. It is demonstrated that high compaction levels lead to improved mechanical results. Jiang and Smith [2017] studied the anisotropic mechanical properties of carbon filled feedstock by printing tensile samples according to 0°, ±45° and 90° infill orientations. Beyond the infill strategies, a comparison was also made with the unreinforced versions of each material. The results showed that beyond the increase in mechanical strength due to the fibres presence, the best behaviour was always observed in the longitudinal direction. Similar results were also found by Ahn et al. [2002] and Casavola et al. [2016], that adopted the same infill strategies. These results showed, that even in xy plane, distinct patterns result in different performances.

Due to its layer-by-layer nature, which is more pronounced in FFF process than other technologies, Z or upright build direction is the least favourableas regards the mechanical performance. Chacón et al. [2017] studied the effect of process parameters on mechanical properties by varying the layer thickness, printing orientation and speeds. Tensile samples were printed horizontally (90° - flat), on edge (90°) and upright (0°), being this way possible to quantify the differences in mechanical performance of these orientations. Tensile results showed that between the flat and on edge samples there was no significant difference in strength, even considering different layer

thickness and printing speeds. However, for upright specimens, the tensile strength increased with the increasing layer thickness, indicating that, smaller layers results into less interfacial contact and higher number of interfaces. Even though, upright samples presented an average of 45% decrease in tensile strength (for the best layer thickness parameters) compared to flat samples. Rybachuk et al. [2017] studied the anisotropic behaviour of ABS printed parts through tensile and compressive tests. Dogbone specimens were produced horizontally (90°-flat), on edge (90°) and vertically (0°), while the compressive tests were performed with cylindrical samples printed vertically, horizontally and at 45°. It was shown that, between flat and on edge type specimens there is not relevant differences in the tensile behaviour, while the vertical specimens' tensile strength is rougly half of the previous. As concerns the compressive specimens, there is no significant changes in performance for the three orientations, indicating that compressive mechanical performance are less sensitive to the printing orientation. Zou et al. [2016] studied the anisotropic behaviour of tensile specimens printed upright (0°) and at angles of 30°, 45°, 60° and 90° (on edge samples), as seen in Figure 4.15. The results showed that the worst mechanical performance (strength) was achieved for the 0° for the same material, being increased gradually as this angle increases.

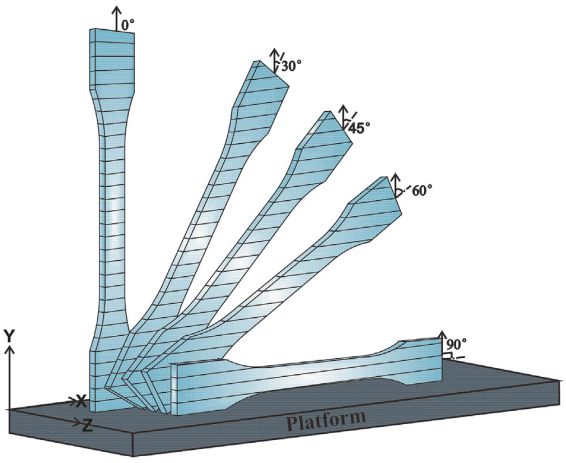


Figure 4.15: Specimens building orientations [Zou et al., 2016].

The anisotropy of AM parts has been studied through different approaches, being the comparison of tensile behaviour of vertically and horizontally printed specimens the most common. However, this approach is not ideal, as the tensile samples are usually long, which implies long printing times, resulting in large thermal gradients. Beyond this, there is the fact that printing imperfections are prone to occur vertically, since the specimen in cause is not adequate for this type of operations. Therefore, it is essential to identify a type of sample that would reduce this type of problem, and allow several building directions.

The Arcan testing method [Arcan et al., 1978] was developed to analyse uniform combined plane-stress in fibre reinforced materials. The original developed Arcan specimen was a circular plane, with opposite cut outs and a centralized small test area. These samples were extracted from a plate, and tested on a universal test machine. A second version of the test was then developed

by Voloshin and Arcan [1980], transforming the sample into a re-usable metallic apparatus or grip setup for composite samples. Currently, the Arcan test is based on two components: a specimen, which might be presented in different shapes [Hoffmann et al., 2015, Hachour et al., 2014, Xavier et al., 2018, Alfonso et al., 2018, Manaia, 2018, Manaia et al., 2019] and two semi-circular gripping plates, holding the test sample. Each metallic grip has a set of holes which allows the apparatus to test a combination of biaxial loads such as, combined shear and tension, or just tension or pure shear [Manaia, 2018, Manaia et al., 2019]. This type of apparatus has been used to test distinct types of materials since then. Alfonso et al. [2018] studied the strength of bonded assemblies for automotive applications by subjecting these samples to a series of tests ranging from 0° (tensile), 45° (tensile–shear), 90° (shear) and 135° (compression–shear). Créac'hcadec et al. [2015] evaluated an epoxy adhesive mechanical response with a modified Arcan method for the same range of orientations. Fibre reinforced composites are the most common material tested using the Arcan apparatus. An investigation of combined-mode delamination of carbon fibre reinforced Polyetherimide (CF/PEI) samples under different stress combinations, varying the loading angle from 0 to 90° was conducted by Choupani [2008]. Gning et al. [2010] used the Arcan apparatus to test two distinct types of glass fibre/epoxy composites, using the pure tension, shear and tension/shear loadings. Hung and Liechti [1997] analysed the shear behaviour of laminated specimens, in which the samples were cut off from a continuous carbon fibre reinforced Polyether ether ketone (AS4/PEEK) unidirectional laminate composite. Considering the literature review on testing methodologies for anisotropic materials, only limited types of data can be provided by common tensile tests. The purpose of this work is to develop a type of sample that avoids the major problems found in previous researches. Samples created in distinct build orientations and subjecting them to different types of loading combinations, are proposed to provide a better understanding of the anisotropy on the mechanical behaviour. Digital image correlation (DIC) is an optical method, capable of providing full-field displacements of a specimen through the comparison of the images captured at distinct mechanical states [Dias et al., 2013]. Therefore, it is widely used as part of distinct types of mechanical tests, which in some of the cases the traditional contacting measurement methods are not capable [Caminero et al., 2012, 2014, Dias et al., 2013]. The Arcan method is one of these types of test which could be enriched in association with DIC due to its capability to measure displacements in distinct orientations, thus being part of this study [Xavier et al., 2018, Alfonso et al., 2018, Hachour et al., 2014].

To the best of the author's knowledge, this testing methodology was not yet applied to FFF printed samples. Therefore, an experimental approach for assessing the mechanical response of FFF specimens under multiaxial loadings is presented, coupling the Arcan fixture apparatus with full-field deformation measurements via DIC. An Arcan test-based geometry was designed considering the limitations of FFF process (e.g., to print wall angles greater than 45° without supports structures). Regarding the material, two compositions were used, namely polyamide 12 (PA12) and short fibre reinforced polyamide 12 (CF15). Testing samples were produced according three different build orientations namely, Horizontal (H), Vertical-Transverse (VT) and Vertical-Longitudinal (VL), and tested under three distinct loading directions, 90°- tensile, 45°- combined

tensile-shear and 0°- pure shear.

4.2.2 Experimental details

4.2.2.1 Arcan test

The Arcan apparatus used in this study, was also applied by Manaia [2018] and it is based on the Doyoyo and Wierzbicki [2003] concept, an evolution of the original Arcan et al. [1978] test. As presented in Figure 4.16a, this setup consists of two semi-circular steel plates with clamping bars held by a screw in each end. In order to avoid the test specimen slipping, two extra central clamps were added, allowing better pressure distribution throughout the sample. Each semi-circular plate presents an array of holes 15° apart from each other, ranging from 0 to 90°, being the 90° tensile and 0°, pure shear. Each steel plate is then fixed with machine loading axis by two pins. Considering the setup specifications, three positions were analysed for the purpose of this study, corresponding to shear (α=0°), combined tension and shear (α=45°) as well as pure tensile loading (α=90°) as presented in Figure 4.16b, in which a global coordinate system is also proposed.

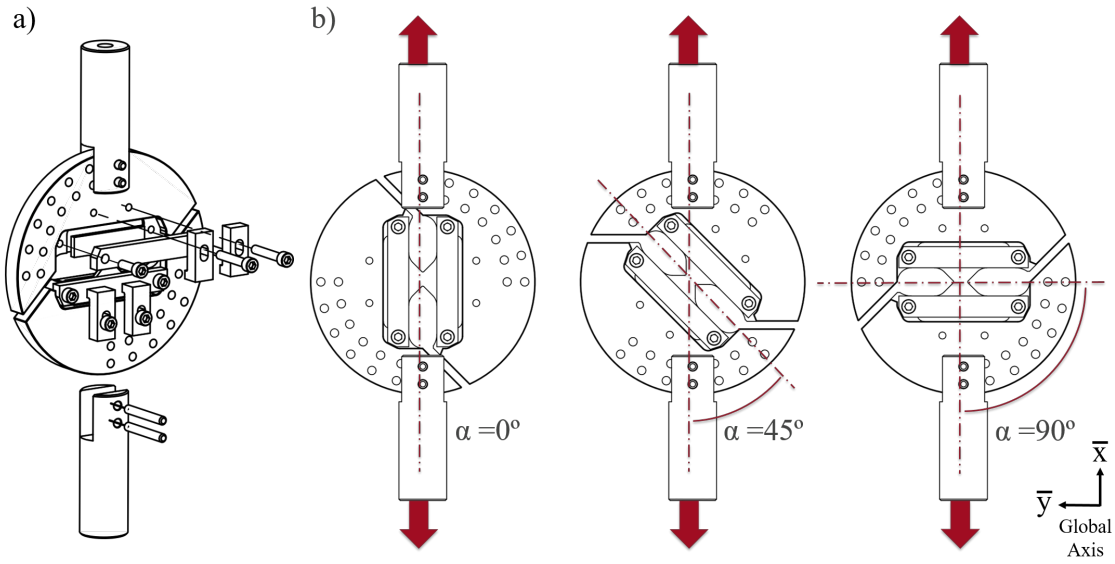


Figure 4.16: Arcan apparatus: (a) components and (b) selected test orientations.

As above-mentioned and depicted in figure 4.16a, the two-pin configuration was selected. Beyond the practicality that the rigid configuration offers in what concerns samples exchange, there is a more important benefit. Since these polymers are generally soft as compared to metals, a problem is usually observed, consisting in the deformation development localized in undesired locations of the test specimen. These deformations are generated by the rotation of the set (grips-specimen) when an angle different than α=90° is applied when a one-pin setup is utilized. Therefore, the two-pin configuration was selected. This type of assembly was previously tested by Doyoyo and Wierzbicki [2003], proving that it could overcome the lack of stress uniformity [Mohr and Doyoyo, 2009].

With the butterfly specimen and Arcan setup, it is possible to analyse distinct stress combinations, in the central interest section marked in red in Figure 4.17. By defining a local coordinate system, in which the interest area is parallel to the Y axis and perpendicular to the X axis, it is possible to obtain mean shear stress τ_{xy} and mean normal stresses σ_{xx}, following the equations in the Analytical formulation section.

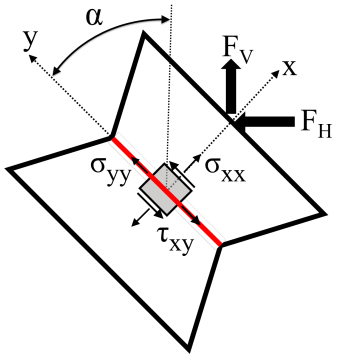


Figure 4.17: Biaxial state of stress at the gauge region of the test specimen, adapted from Mohr and Doyoyo [2009], Doyoyo and Wierzbicki [2003].

4.2.2.2 Test sample development

Butterfly test samples have been used in previous studies [Manaia, 2018, Hachour et al., 2014], with this type of grips. However, these specific specimens presented a section reduction in the gauge region, which was easy to produce using injection moulding. Due to the layer-by-layer fabrication method of the current study, this gauge geometry would complicate the specimen production. Thus, an alternative butterfly shaped specimen was developed (Figure 4.18c), maintaining the overall external dimensions of the samples used by Manaia [2018] as demonstrated in Figure 4.18b. This new sample was inspired in the original Arcan geometry (Figure 4.18a), excluding the thickness reduction at the gauge section, and thus allowing for a simple production process.

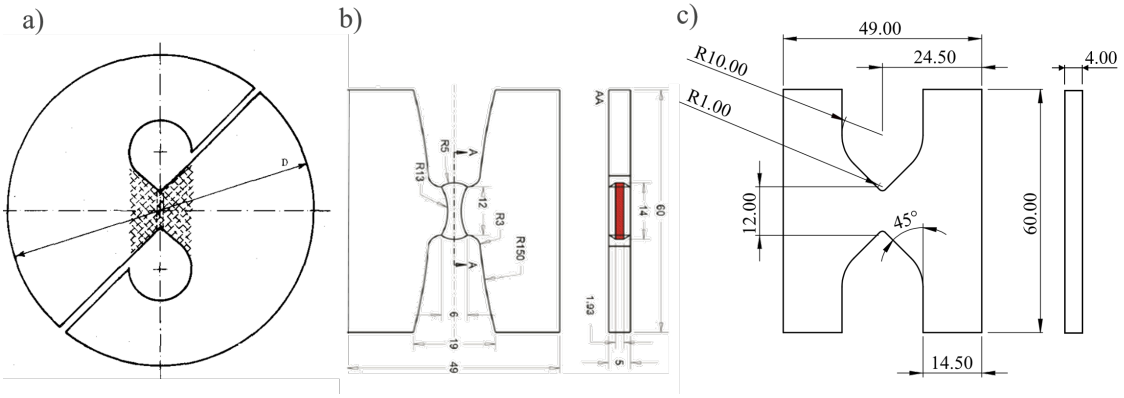


Figure 4.18: (a) Original Arcan sample configuration [Arcan et al., 1978], (b) butterfly specimen [Manaia, 2018] and (c) developed geometry.

The new developed specimen was subjected to Finite Element (FE) calculations using Abaqus, with four-noded plane stress quadrilateral elements with reduced integration (CPS4R), in the elastic regime. The material was assumed as isotropic with properties as obtained previously for CF15, through tensile tests. Boundary conditions were applied to one of the sample's arm locking its x and y displacements and rotations. The sample was placed at 0°, 45° and 90°, in which a displacement was applied to the other arm, in x direction as it can be observed in Figure 4.19. Von Mises stresses are presented, confirming that the higher stress values are located in the notch area, thus validating the geometry for an isotropic material hypothesis.

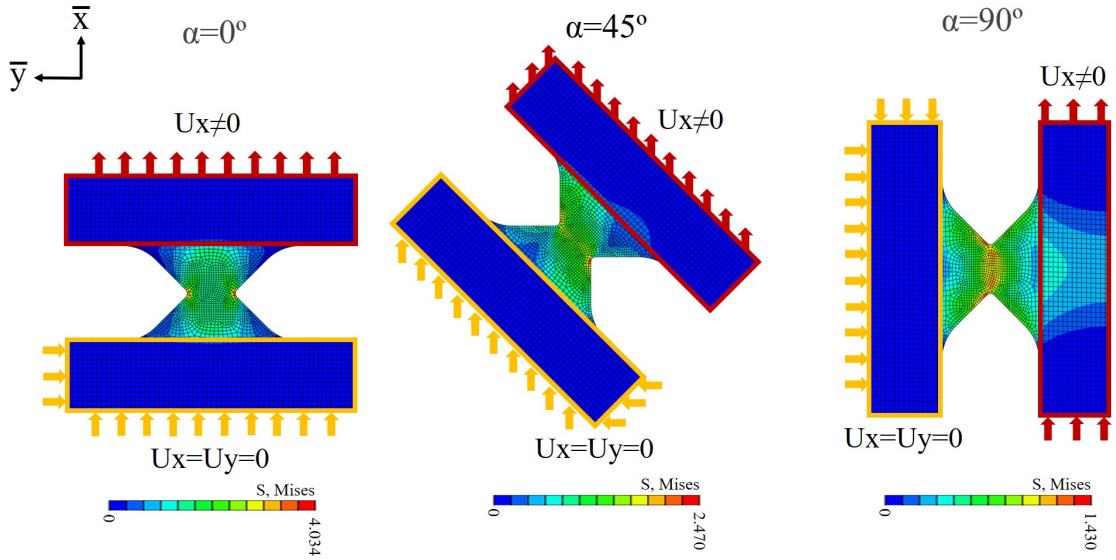


Figure 4.19: Von Mises stress simulation results for tensile, combined mode and shear tests.

4.2.2.3 Specimen building orientation

Taking into account the anisotropic studies presented in the literature review, the performance of FFF specimens produced according three distinct build orientations will be investigated. Figure 4.20 depicts the three build orientations as produced on the equipment tray. The sample 1 in Figure 4.20 is representative of the flat or horizontal samples denominated as H specimens, presenting an infill orientation of $\pm 45°$. Due to the flat build orientation, and alternate infill direction, these samples present, theoretically, the nearest to isotropic behaviour from the set. Samples 2 presented in Figure 4.20, which were built in the upright position are denominated as VT (vertical-transversal), V indicating the building orientation and T, the layer deposition orientation in a tensile loading scenario (α=90°). For this specific case, the interlayer adhesion is tested. The last type of sample (3) is denominated VL. Similarly to the previous, these specimens were printed vertically V, being rotated so that, in a tensile test scenario (α=90°), the deposition lines would be aligned with the loading axis as depicted in Figure 4.20.

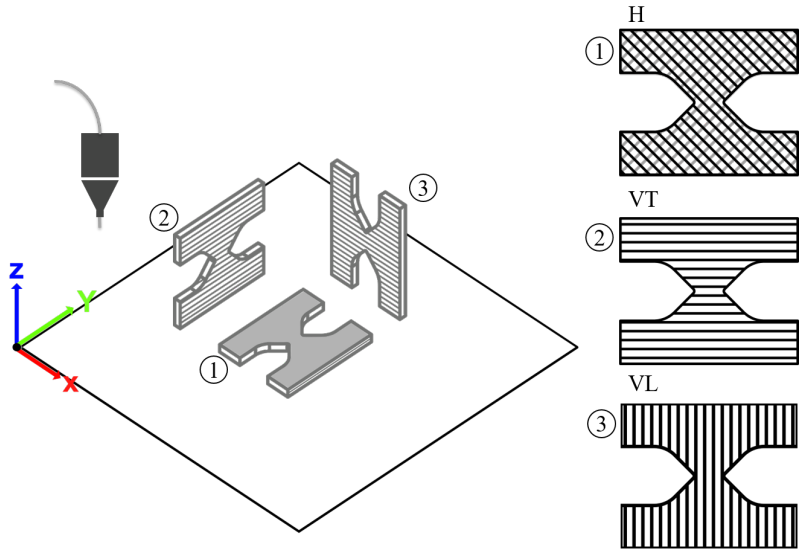


Figure 4.20: Specimen building orientation.

4.2.2.4 Arcan test - Analytical formulation

Considering the testing apparatus setup depicted in Figure 4.16a, two pins configuration was adopted, avoiding rotations of each grip; it is possible to detect that rotation movements are prone to occur for shear or combining mode tests and possible specimen misalignments. By applying the two-pins gripping, the lateral movements due to rotations are avoided, being ensured a test sample alignment with the loading axis [Manaia, 2018]. Nevertheless, a perpendicular to the loading direction reaction force is generated, differentiating from the one pin setup purposed by Arcan et al. [1978], in which this lateral reaction is converted into a rotation. To correctly measure this reaction value (Rload), a perpendicular to the loading axis load cell is needed and stress values calculated via equations 4.12 and 4.13 [Doyoyo and Wierzbicki, 2003]:

$$\sigma_{xx} = \frac{Fload}{Area} sin(\alpha) - \frac{Rload}{Area} cos(\alpha) \tag{4.12}$$

$$\tau_{yx} = \frac{Fload}{Area} cos(\alpha) + \frac{Rload}{Area} sin(\alpha) \tag{4.13}$$

However, if the material linear elastic properties are known, it is not necessary to measure this reaction force to determine the yield envelope (elastic limit) [Doyoyo and Wierzbicki, 2003]. Doyoyo and Wierzbicki [2003] derived expressions for shear and normal stresses at the centre of the specimen in the elastic regime using a theoretical and finite element analysis, assuming isotropic material:

$$\sigma_{xx} = \left(\frac{\beta_x sin\alpha}{(1-\beta_x)cos^2\alpha + \beta_x} \right) \frac{Fload}{Area} \tag{4.14}$$

$$\sigma_{yy} = \nu_{xy} \sigma_{xx} \tag{4.15}$$

$$\tau_{yx} = \left(\frac{cos\alpha}{(\beta_x - 1)sin^2\alpha + 1} \right) \frac{Fload}{Area} \tag{4.16}$$

Poisson ratio is a relationship between the transverse contraction and the longitudinal strain in the direction of the applied load, while in the linear elastic regime. Even though the samples are non isotropic, the measurements taken via Digital Image Correlation (DIC) allowed to calculate the Poisson ratio (ν) through the following equation 4.17:

$$\nu_{xy} = -\frac{\varepsilon_{xx}}{\varepsilon_{yy}} \tag{4.17}$$

For these measurements, the DIC data was obtained for a 90°(Tensile load), in which the global coordinate becomes coincident with the local system.

Isotropic materials

Equation 4.18 indicates the stiffness ratio (β_x) for isotropic specimens with Poisson ratio (ν) [Doyoyo and Wierzbicki, 2003, Manaia, 2018]:

$$\beta_x = \frac{2}{1 - \nu} \tag{4.18}$$

For an isotropic material, the relationship between shear modulus (G) and E is given by:

$$G = \frac{E}{2(1 + \nu)} \tag{4.19}$$

Anisotropic materials

Through equation 4.20 it is possible to compute the stiffness ratio (β_x) for anisotropic materials, being E_x the Young's modulus, while the G_{xy} is the shear modulus of the specimen for directions x, y;

$$\beta_x = \frac{E_x}{G_{xy}(1 - \nu_{yx}\nu_{xy})} \tag{4.20}$$

Anisotropic (orthotropic) elasticity theory indicates that through equation 4.21, it is possible to obtain relationship among these four elastic constants [Volokh, 2016]:

$$\nu_{xy}E_y = \nu_{yx}E_x \tag{4.21}$$

Which translates to:

$$\frac{\nu_{xy}}{E_x} = \frac{\nu_{yx}}{E_y} \tag{4.22}$$

Through these equations, it is possible to verify (considering both VT and VL) if the obtained elastic constants are accurate.

Due to the low stiffness of the test materials, shear (τ_{yx}) and direct stress values (σ_{xx} and σ_{yy}) can be obtained via equations 4.14 to 4.16, even with the absence of lateral reaction force loading cell for specific specimen to loading orientations.

Poisson ratios (ν) for H,VT and VL specimens were obtained via digital image correlation during the tensile test configuration of the Arcan setup (α=90°). Considering equations 4.14 and 4.16, which are related to tensile and shear stresses, it is possible to conclude that for a tensile test with the loading angle at 90°, the shear (τ_{xy}) becomes zero, and the component part of the equation 4.14 that depends on ν/elastic parameters becomes 1. This is and indicator that beyond the modulus, maximum (strength) stress values can be obtained. The same occurs, for different components when the angle is 0° (shear test): σ_{xx} becomes 0, while the angle/component is 1, thus indicating that τ_{xy} can be obtained. The same simplification does not happen for a 45° loading.

4.2.2.5 Test Procedure

The Arcan test was carried out on an INSTRON® 5900R (Illinois Tool Works Inc. USA) at a displacement rate of 0.5 mm/min with a 5 kN load cell in a controlled environment of 23°C and 50% humidity. Each specimen was tightened using a torque wrench adjusted at 4 Nm for the lateral screws, while the centre clamps were tightened at 8 Nm.

4.2.2.6 Materials and FFF configurations

FFF specimens were produced using two TronXY X5 (Shenzen TronXY Technology Co. LTD) printers. These are open chamber type machines, capable of a maximum production volume of 210 × 210 × 280 mm^3, reaching extrusion temperatures of 260 °C, and 100 °C for the tray. Two PA12 based 1.75 mm diameter filaments from Fillamentum ©, Parzlich s.r.o (Czech Republic) were used. The first PA12, a pure version, commercially named as Nylon FX256 and the second corresponding to a short fibre reinforced version (Nylon CF15) [Fillamentum, 2019b,a] were used. CF15 is reinforced with short carbon fibres with 100 μm length consisting in nearly 15 wt.% of the material, thus being expected a different mechanical behaviour from its unreinforced version, namely increased stiffness. The fibre orientation is aligned with the material deposition direction, following the material flow through the extruder, as shown by Ferreira et al. [2019b, 2020]. Therefore, the fibre disposition matches the printing pattern. Table 4.5 depicts some of the relevant material properties.

Table 4.5: Datasheet values and material specifications [Fillamentum, 2019b,a].

Property	CF15	FX256
Material density (g/cm^3)	1.08	1.01
Melt flow index ($g/10min$)	14.64	16.56
Glass transition temp. T_g (°C)	44.70	52.91
Thermal conductivity (10^{-3} W/m.k)	144.22	124.82
Tensile strength (MPa)	54.50	45.00
Tensile elastic modulus (MPa)	500	1400
Melting temperature (°C)	160	178
Print temperature (°C)	235-260	235-260

The printing parametrization and slicing methodology were defined with Simplify 3D®, 4.1.1 version, in which the parameters choice was defined considering previous tests, taking into account that the creation of fully dense samples usually leads to printing problems such as warping and bad visual appearance [Fonseca et al., 2019]. Table 4.6 depicts the parameters that allowed the best possible printing behaviour. Each batch of samples was produced simultaneously in both

Table 4.6: Selected printing parameters.

Extrusion Parameters	
Nozzle diameter (mm)	0.4
Nozzle material	brass/A2 steel
Layer height (mm)	0.2
Number of perimeters per layer	2
Infill percentage (%)	100
Infill pattern (°)	Rectilinear ±45
Skirt outlines	7
Extrusion temperature (°C)	260
Bed temperature (°C)	90
Bed surface	Tempered glass + CUBE®glue
Printing speeds (mm/s)	40

machines for CF15 and FX256, being printed six samples (one extra) per batch, according with the orientation. In total, ninety testes were performed (2 materials x 3 build orientations x 3 test orientations x 5 repetitions= 90). Material conditioning was done previously and after to the print process, being each feedstock spool dried during 8h at 70°C in a PrintDry™ (Canada) filament drier. After completing the print process, each set of samples was sealed in plastic bags with silica gel reducing the moisture presence. Once the printing process was completed, all samples with the same building orientation were stored together and posteriorly divided in sets of five.

4.2.2.7 Digital Image Correlation

DIC was used in order to understand how different the deformation fields are for the interest area of each sample. This method allowed to obtain the sample ε_{xx}, ε_{yy} and ε_{xy} (according to the global coordinate system, see Figure 4.16), making the comparison among distinct samples possible and to understand which areas were more susceptible to deformation. Considering the vast number of tests, only three, out of five samples, for each building orientation/test direction were prepared for DIC. In order to hide the layer effect and infill patterns, the samples were polished with 320 and 600 grit paper, creating an homogeneous surface required so the speckle can be detected correctly by image correlation. Matte white paint was applied via spray can, while the speckle was created with an Airbrush Iwata CM-B (Anesta Iwata Iberica SL, Barcelona, Spain). A Balser Ace acA2440 (Ahrensburg, Germany) camera was used, Fujifilm Fujinon coupled with a 1:2.3/50 mm (Toquio, Japan) lens, while the image processing was done with VIC-2D Correlated solutions (South Carolina, USA), with a subset size and step of 19 and 7 correspondingly. Images were captured at an acquisition frequency of 2 Hz.

As depicted in Figure 4.21, small central interest area was considered in the neck portion of the sample, so ε_{xx} (longitudinal), ε_{yy} (transversal) and ε_{xy} (shear) can be obtained. In addition to

the localized measurements, the deformation fields were obtained by defining and processing the visible part of the specimen, then converted into strains so the critical areas can be analysed.

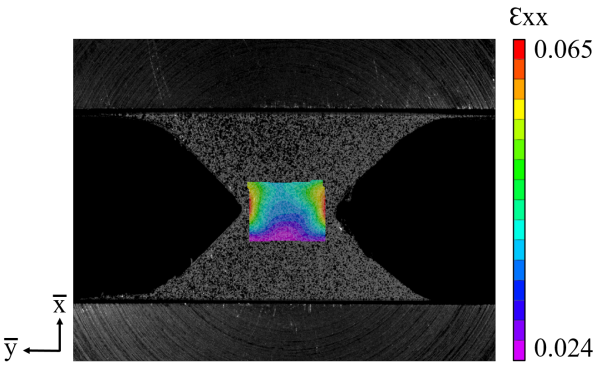


Figure 4.21: Longitudinal deformation field of a tensile *H* CF15 sample.

4.2.3 Results and discussion

4.2.3.1 Experimental curves

Figures 4.22 through 4.24 depict the load displacement behaviour of the Arcan testing samples at the different loading conditions tested. Figure 4.22 presents the behaviour of *H* printed samples. Considering the shear loading, it is possible to verify that the unreinforced samples sustained lower peak load values; however its displacement was 12.16±1.10 mm, which is significantly higher than observed so far for reinforced samples, that fractured at 3.39±0.25 mm, as it can be proved by the graph from Figure 4.25. Considering the combined loading, the reinforced material is more capable to whidstand higher loads but lower displacements than the unreinforced one. Tensile results show that *H* samples show almost similar behaviour for both materials as it can be seen in Figure 4.25.

Figure 4.23 represents the tests performed to *VT* samples. It is possible to assert that this printing orientation results in the lowest strength and ductility of all types of samples, for all the loading combinations. This build orientation tests the interlayer behaviour which is weaker. In addition, irregular fracture happened, in some of the cases, outside the neck area, mainly due to printing irregularities.

Figure 4.24 depicts the curves of the *VL* samples. It is possible to see that the unreinforced material can sustain higher levels of displacement for the three tests. Considering the load sustained, for shear and combined loading modes, higher ductility values are also obtained with the unreinforced PA version, yet the tensile strength was higher for CF reinforced sample set.

Through the results summary presented in Figure 4.25a it is possible to verify that even though CF15 is fibre reinforced, there is not a relevant gain in terms of strength. It is also possible to verify that *H* samples present the best overall behaviour. Even though these samples have a bi-directional orientation, unlike the traditional laminate composites in which the tensile strength and stiffness of the fibre is more than ten times higher than the surrounding matrix [da Silva et al., 2013], in

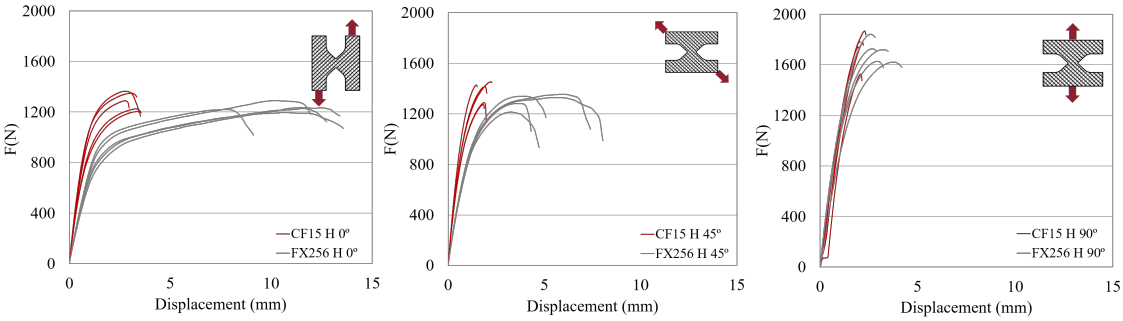


Figure 4.22: Arcan testing results of H samples at shear, combined mode and tensile loadings.

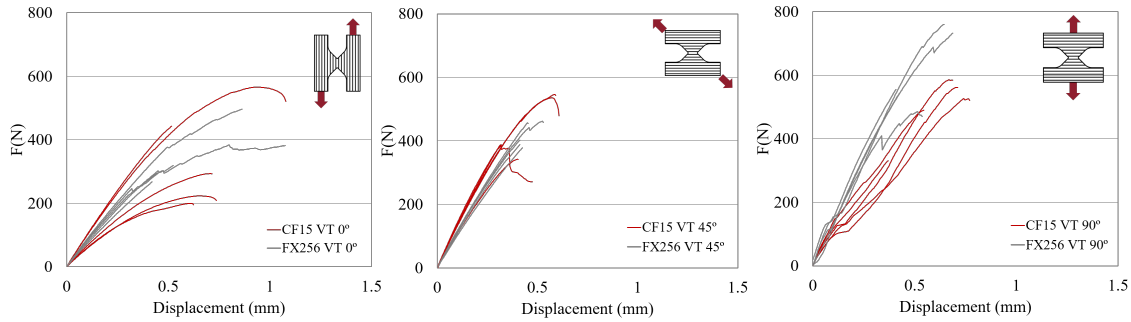


Figure 4.23: Arcan testing results of VT samples at shear, combined mode and tensile loadings.

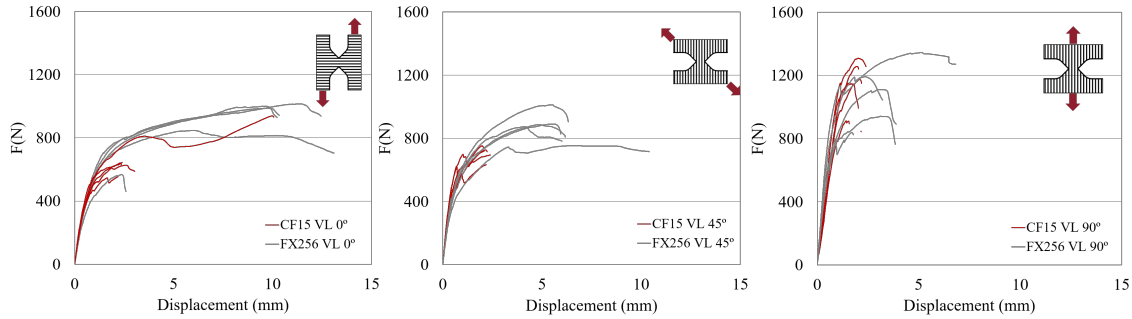


Figure 4.24: Arcan testing results of VL samples at shear, combined mode and tensile loadings.

this particular case, the longitudinal (VL) and transversal performance (VT) is not that different (doubling the force at best). In addition the alternated crossed pattern promotes better adhesion of the adjacent deposed layers since the previous and next layer is 90° rotated, thus improving the overall response of the sample while also promoting a more homogeneous behaviour (close to isotropic). Tensile VT FX256 samples show a higher strength than the reinforced version, which might occur due to the higher material fluidity during the deposition, being more capable to adapt and adhere to the previous layer geometry. This was not reflected for any other testing angle. VT tests indicate that the force needed to promote layer detachment occurred outside the neck area in some of the cases, which might happen due to printing defects. In addition, the similarity in maximum displacement results (between materials) dictates that is the layer interface performance that is being tested, instead of the material by itself (filament). As for VL samples, the deposition lines are oriented in the same direction as the tensile test, being those the best results from the set.

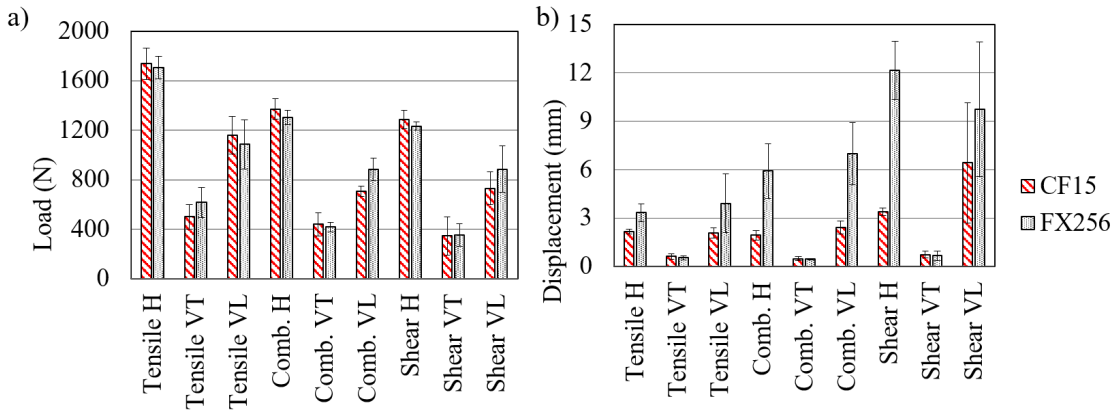


Figure 4.25: Average test values of (a) load and (b) displacement.

4.2.3.2 DIC Results

Two approaches were taken considering the DIC analysis. Firstly, a window in the centre of the sample's neck, averaging the strain values for the distinct strain component as mentioned above, reducing the influence of non-desired areas. For the second approach, all of the sample's visible area was selected and processed. This analysis was performed in order to understand which areas of the sample were more susceptible to the applied load. Figure 4.26 depicts the ε_{xx} (parallel to loading), ε_{yy} (transverse to loading) and ε_{xy} (shear) strain fields for the CF15 *H* samples, since these were the nearest to a homogeneous set of specimens. Figure 4.26a presents these fields for the tensile test. Longitudinal results indicate that there is no compressing areas, by presenting all positive values, being the the notch vertices the most critical areas. Transversal (ε_{yy}) shows that there is some lateral compression (Poisson effect) in the notch vertices, while expansion is observed in the centre of the sample.

For the combined mode results (Figure 4.26b) it is possible to observe that, in the loading direction, there is expansion of the sample, once again, with the vertices being the most affected areas, thus indicating that the fracture might occur parallel to the grips. It is also shown that lateral compression is generated in the notch area while the rest of the sample is being distended. Figure 4.26c depicts the shear strain results. It is important to refer that the right grip is static, while the left one is moving upwards. Thus, longitudinal results indicate the presence of compression in the upper part of the sample on both the static side and in the lower part of the moving side. Symmetrical results are observed in the opposite sides. The same effect is found laterally. Shear results evidence high localization values in the ligament of interest.

Considering the *VT* specimens in Figure 4.27, it is possible to observe overall lower strain values than for the *H* samples. This is due to the fact that since the samples have transversal layer deposition, the interlayer performance is being tested instead of the material itself. ε_{xx} in Figure 4.27a indicates that strain concentration points are present in the lateral notches similarly to *H* specimens, leading to a correct type of fracture in the gauge area; ε_{xy} presents similar behaviour to the previous type of sample, however less pronounced. As far as the combined mode results

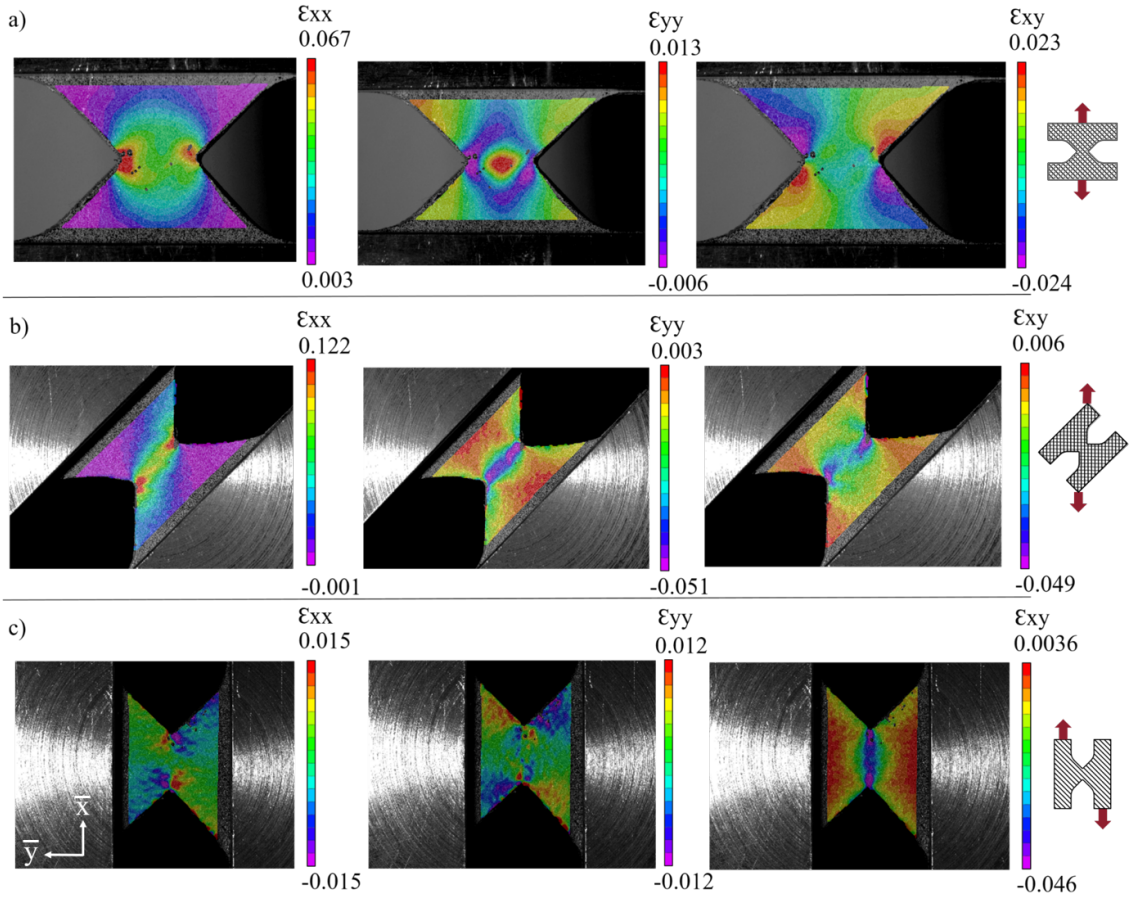


Figure 4.26: Deformation fields: (a) tensile, (b) combined mode and (c) shear for H specimens.

(Figure 4.27b), it is possible to observe an higher ε_{xx} strain out of the section of interest that was responsible for crack nucleation above the gauge area.

From the shear tests (Figure 4.27c), it is possible to detect a similar behaviour to the *H* specimens, despite the fact that a point with higher lateral (ε_{yy}) strain values in the inferior right part of the arm is detected, indicating a possible fracture nucleation point. Considering the shear strain ε_{xy}, it is shown that the central gauge area is the most loaded region of the sample.

Figure 4.28 depicts the DIC deformation fields for the *VL* specimens. Considering that the most irregular type of fracture was obtained using this type of sample, the deformation fields present some explanations, in which for the most samples, the fracture occurred not perpendicularly to the load but in the material deposition direction. For the ε_{xx} strain in Figure 4.28a, it is shown that the critical areas are, once again, the gauge extremities, suffering the most localized strain values. It is shown through ε_{yy}, that delamination is prompt to occur in the inferior left arm, since the highest strain values are presented in that point. For the combined mode (Figure 4.28b), similar nucleation points are observed through both ε_{xx} and ε_{yy} in the inferior right arm and superior left, which coincide with the ones being pulled as observed in testing. Thus, delamination occurs in the layer direction instead of a gauge fracture.

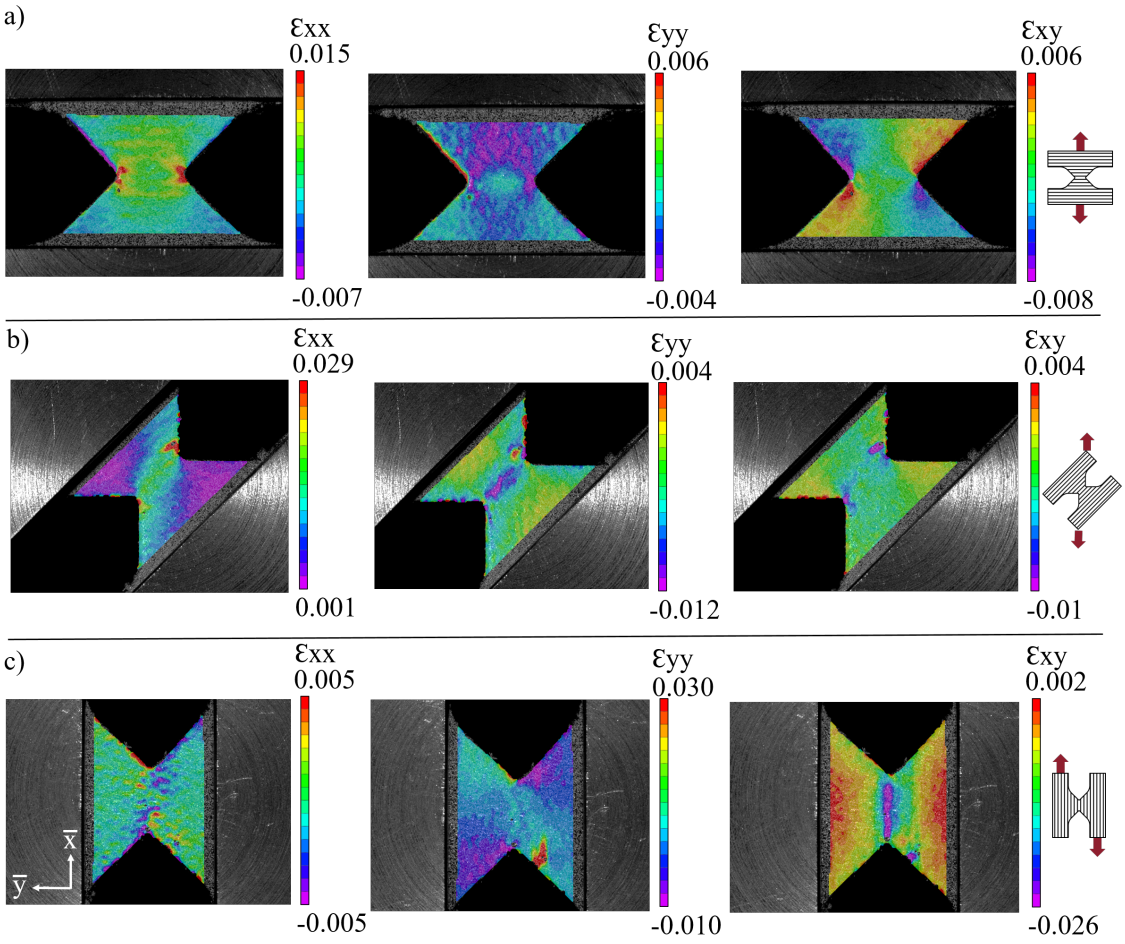


Figure 4.27: Deformation fields: (a) tensile, (b) combined mode and (c) shear for VT specimens.

The shear test results (Figure 4.28c) revealed the same trend in which cracking/delamination starts to occur perpendicularly to the gauge, aligned with the deposition. Regarding the shear strain ε_{xy}, the effect of delamination becomes clearer since unlike the previous H and VT, that presented higher shear strain values localized consistently in the gauge, in this type of samples, horizontal strain intensification areas indicate that layer detachment are likely to occur.

4.2.3.3 Fracture analysis

Figure 4.29 presents the after rupture view of the distinct types of CF15 samples obtained with the DIC setup, thus complementing the results discussed through DIC strain fields. Throughout the tests it was observed that these failure modes were similar for both materials. For H samples, localization of fracture occurred in the gauge area for all tests independently of loading direction. Only tensile tests presented a clear fracture, while for the combined loading and shear, yielding was observed in the gauge. These specimens orientation exhibited quasi-isotropic behaviour. For VT building orientation irregular fracture was observed. These samples were assumed as the most brittle ones, since the deposition was done parallel to the arms, resulting in a layer interface in the

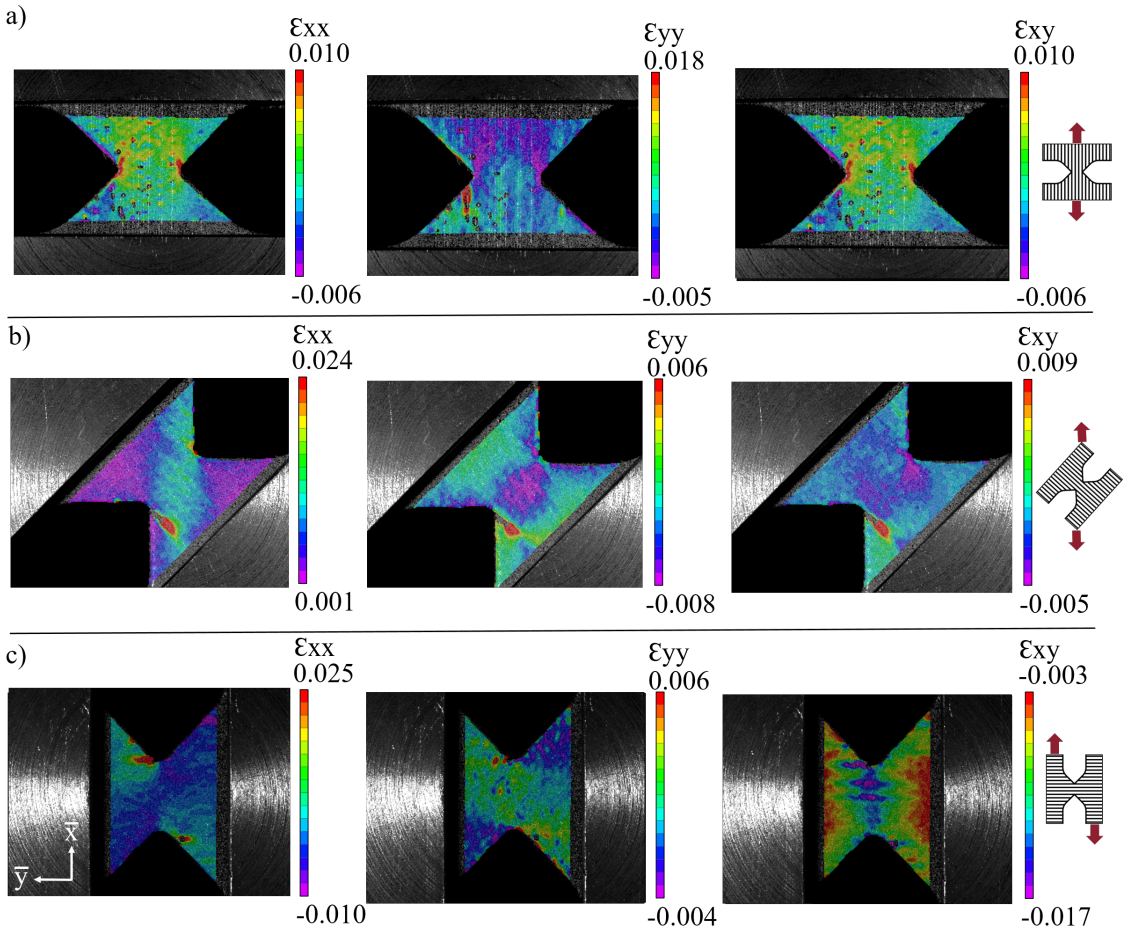


Figure 4.28: Deformation fields: (a) tensile, (b) combined mode and (c) shear for VL specimens.

gauge area parallel to the interest line. Through Figure 4.29 it is possible to observe fractures for tensile and shear. Delamination was found near the section of interest in parallel planes, for the combined mode as indicated in Figure 4.27b. However, the tests showed that this was not always the case, with the fracture happening also near the grips originated by the printing process. As it can be seen through Figure 4.30a, VT specimens were produced resorting to support material to provide structural support for the superior arm of the sample.

Since there is a gap between the support material and the upper area of the part (simplifying support removal), there is a lack of compression in the arm's first layer, and consequent stress concentration areas due to curved geometry as presented in Figure 4.30b. For this reason, some of the unexpected fractures occurred in this area.

VL samples show delamination of the layers for the distinct loading types. For the tensile tests, in some of the cases this delamination occurred in the gauge centre, while for the combined mode and shear, the top right and left lower arm were detached from the sample due to the loading direction.

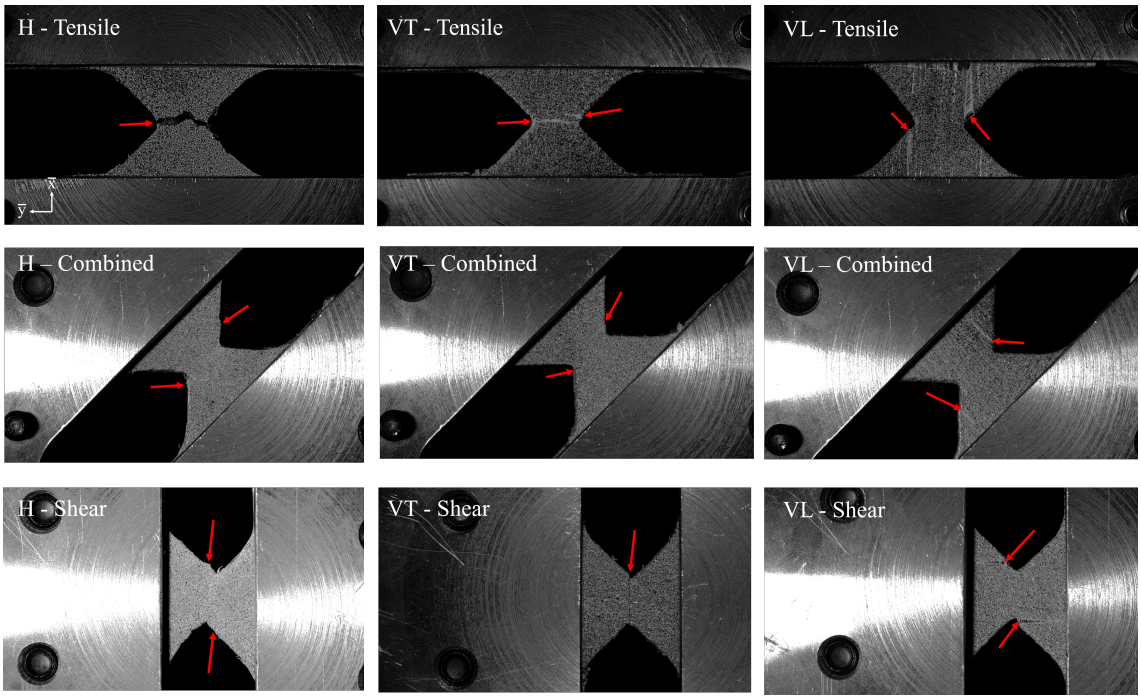


Figure 4.29: Fracture examples of CF15 for each type of test.

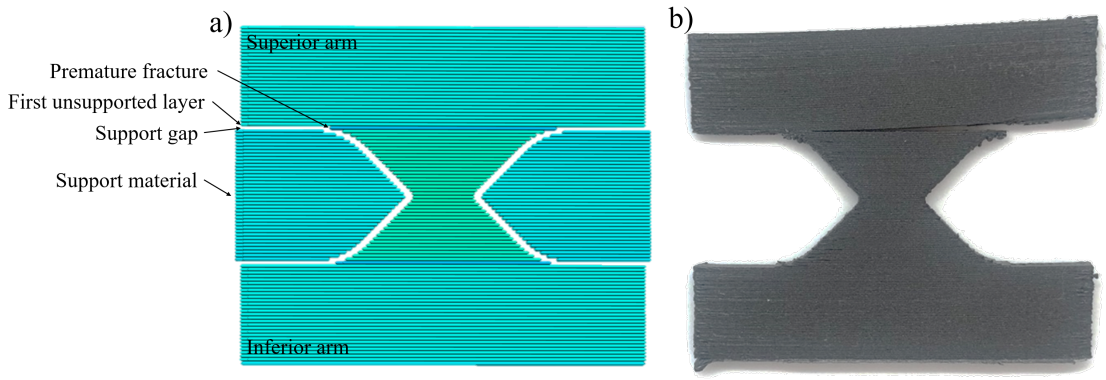


Figure 4.30: VT specimens: (a) printing scheme and (b) printed fractured sample.

4.2.3.4 Elastic and strength properties

Considering the three distinct building orientations, H samples, with its alternate $\pm 45°$deposition pattern may be distinguished from the others. H samples generate the nearest to isotropic behaviour, thus being assumed as such in the results analysis. Thus, for verification/comparison purposes, equation 4.18 can be used. Taking into account, the building type, this sample type could also be analysed by using the composites laminate theory. The other two (VL and VT) can be described as unidirectional, highly anisotropic material, longitudinally and transversally characterized to tensile and shear performance. Therefore, both VL and VT specimens can be

considered as one unidirectional material/structure tested in distinct orientations. Figure 4.31 indicates the different elastic and strength properties evaluated from the proposed tests, assuming the limitations regarding the absence of Rload measurement. From the vertical samples, it is possible to obtain longitudinal and transversal material properties. Taking into account these assumptions, the local coordinate system was adapted according to the deposition (long/transv) as presented in Figure (4.31b and c). The possibility of printing different orientations with Arcan orientation loadings maximizes the characterization possibilities.

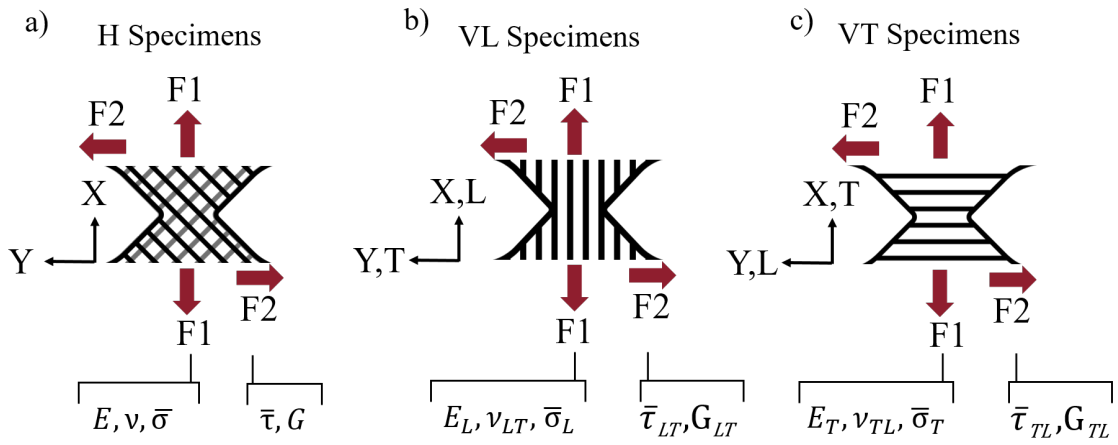


Figure 4.31: Obtained material properties: (a) H, (b) VL and (c) VT specimens.

By comparing the Poisson coefficient for both materials in Table 4.7, it is possible to conclude that the use of fibre leads to higher Poisson coefficients. VL samples, in which the material is deposited in the loading direction, present higher Poisson values for CF15. Since the presence of fibre leads to higher stiffness, it is possible to conclude that in order to achieve this high values, lower transversal contractions are also a consequence. Considering that VT samples present low and similar displacements for both materials (even though that ν is obtained in the linear elastic area) it is once again proven that fibre presence grant higher transversal stability. Thus, it is possible to assume that higher Poisson values are obtained in the longitudinal direction (ν_{LT}) rather than in the transversal one (ν_{TL}), and even more pronouncedly in the reinforced material.

Strength values shown in Table 4.7 were obtained according to the equations 4.14 and 4.16. As previously mentioned, strength and elastic modulus values were calculated for the pure solicitations (shear and tensile), since the stiffness ratio (β_x) dependant component did not present any influential effect. Tensile and shear modulus were calculated by plotting stress by the respective strains values which were obtained via DIC. The combined shear-tensile test results were not considered for this comparison, since the above mentioned formulation can only be applied during the linear elastic regime for isotropic materials, being the H specimens (assumed as near to isotropic) the only results to be considered.

Considering H samples, it is possible to observe that similarly to the loads in Figure 4.25a, both materials present analogous results as far as tensile strength, being CF15 slightly higher. Taking into account the shear strength values, once again the reinforced material is superior by a

residual advantage. The most notorious difference is presented by the Young's modulus results, being CF15 nearly three times higher than FX256, while the shear modulus is approximately 1.5 lower for the last.

Considering equation 4.19, shear modulus G was calculated for H samples in order to compare with the experimental results, assuming that the samples presented a quasi-isotropic behaviour. This theoretical values resulted in 1296.30 MPa and 503.87 MPa, while the experimental values were 597.09±54.54 MPa and 428.37±11.13 MPa for CF15 and FX256 respectively. Thus, it is possible to assess that FX256 presents a more consistent G value, therefore being possible to conclude that the unreinforced material present a more approximate to isotropic behaviour than the CF15, being the fibre the differential factor.

Due to its fabrication nature (deposition orientation), the results obtained from VT and VL specimens can be considered as two components of a unidirectional material like structure. Considering the transversal results (VT), it is possible to see that CF15 presents slightly lower values for all the properties (elastic and strength). However, these results are only indicative of how the interlayer performs, being that in this case, the fibre does not create any influence, since it is deposited with the layers in a perpendicular direction to the fracture. Instead, the difference in values is justified by the polymer intrinsic properties such as the FX256 lower viscosity/higher MFI which might promote a better interlayer adhesion.

As for the VL results, which represent the other component of this material/structure, tensile strength is slightly higher for the reinforced material, while the opposite happens for the shear strength. As expected, the CF15's Young's modulus (even with the high standard deviation) is more than double than FX256, justifiable by the fibre presence. However, the shear modulus presented similar values for both materials, with slight better performance for FX256. Once again, the similarity for this value is associated with the interlayer adhesion, which by analysing ε_{xy} from Figure 4.28c it is possible to observe that the layer effect on the strain is highly pronounced.

Since VT and VL are considered as the same unidirectional material tested in distinct orientations, $G_{LT} \approx G_{TL}$. By analysing the results in Table 4.7, the approximation is more notorious for the unreinforced material, while the reinforced specimens present a higher G_{LT}. This difference in behaviour may be related to with the longitudinal fibre orientation (along with the material deposition).

Table 4.7: CF15 and FX256 strength and elastic properties.

CF15

	$\overline{\sigma}$	$\overline{\tau}$	E	G	ν
H	43.48±3.19	32.16±1.81	3506.08±33	597.09±54.54	0.35
	$\overline{\sigma}_T$	$\overline{\tau}_{TL}$	E_T	G_{TL}	ν_{TL}
VT	12.48±2.52	8.62±3.89	1827.28±288.01	261.22±21.77	0.18
	$\overline{\sigma}_L$	$\overline{\tau}_{LT}$	E_L	G_{LT}	ν_{LT}
VL	29.02±3.82	18.26±3.34	5309.19±798.21	385.16±10.82	0.43
	[MPa]	[MPa]	[MPa]	[MPa]	

FX256

	$\overline{\sigma}$	$\overline{\tau}$	E	G	ν
H	42.68±2.25	30.85±0.88	1169±59.66	428.37±11.13	0.16
	$\overline{\sigma}_T$	$\overline{\tau}_{TL}$	E_T	G_{TL}	ν_{TL}
VT	15.39±3.08	8.81±2.28	1902.34±147.13	383.40±30.85	0.10
	$\overline{\sigma}_L$	$\overline{\tau}_{LT}$	E_L	G_{LT}	ν_{LT}
VL	27.15±5.01	22.10±4.72	1958.28±96.25	390.49±15.54	0.12
	[MPa]	[MPa]	[MPa]	[MPa]	

In addition, according to the orthotropic elasticity theory [Volokh, 2016], presented through equation 4.22, adapted to sample material coordinate system, it is possible to compare both V_{LT} and V_{TL} orientations through:

$$\frac{\nu_{LT}}{E_L} = \frac{\nu_{TL}}{E_T} \tag{4.23}$$

Through the results in Table 4.8 it is possible to observe that there is an approximate concordance indicating the congruence in separate sets of results (mechanical vs DIC). It is possible to verify once again an higher difference in results for the reinforced material, being this time not possible to relate to the fibre presence since this relationship takes into account the material properties in both directions (transversally and longitudinal). It is, however possible to verify that by approximation both materials comply with equation 4.23.

Table 4.8: Anisotropic elasticity relationship.

Material	$\frac{\nu_{LT}}{E_L(GPa)}$	$\frac{\nu_{TL}}{E_T(GPa)}$	Difference
CF15	0.10	0.08	0.02
FX256	0.06	0.05	0.01

4.2.4 Conclusions

FFF printed parts mechanical performance is considered as the weak point of this technology due to its high anisotropic structure and irregular behaviour. Even considering new and improved engineering polymer specially formulated to the process, both of these problems will remain due to the process intrinsic characteristics.

The scope of this work intends to obtain a grasp of how different building oriented printed parts react by comparing them, taking into account both reinforced and unreinforced materials. It was proven that in terms of strength, both materials revealed to have unexpected similar responses even though one being the short fibre reinforced version of the other. However, this same reinforcement caused a decrease in terms of ductility sustained confirmed in each variation of the test, thus justifying CF15 higher stiffness levels. It was also proven that FFF parts, regardless of the type of load that they are subjected to, will present the worst behaviour in the upright printing orientation (VT samples). In terms of maximum loads sustained, H samples with the $\pm 45°$infill pattern, proved to be the most capable taking into account the distinct types of single and combined loads, as well as the most regular/repeatable type of fracture.

It can be also assumed that H specimens present a near to isotropic behaviour for the unreinforced samples, while the fibre influence promotes an increased stiffness (E) which is not translated to shear values as expected through the theoretical formula. Finally, through the orthotropic elasticity theory it is proven that the consistency of E_L, E_T, V_{LT} and V_{TL} constants.

Due to its fabrication method in a context of application, FFF parts are hardly ever fully dense printed, which would increase anisotropy levels, particularly in the upright direction, since the inter-facial contact is much lower. Thus, in order to predict this behaviour, this type of study is of major concern.

Chapter 5

Post processing of printed samples

Post processing is an operation or set of operations that aims to a part's property improvement. In AM, post processing is used by few technologies mostly for cleaning processes. i.e, polyjet's water pressure washer and powder bed's pressurized air for powder removal and UV light is used for stereolitography parts to fully cure the part. Apart from the previous examples, polymer based post processing processes are not commonly used. For the most parts, FFF does not require post processing, being the most common scenario, support removal from more complex geometries. Nonetheless, FFF's two main problems are the inferior mechanical properties (facing other technologies) and the poor surface roughness, which in part results in a lack of geometrical accuracy. In this chapter, these two topics are addressed. In Section 5.1, the improvement of printed parts surface finishing is studied, by combining an additive technology with a subtractive process. In this section, the final surface roughness of the part is studied after being submitted to distinct combinations of machining parameters via design of experiments (DOE). Section 5.2 addresses the improvement of the mechanical performance by means of thermal treatments. Similarly to the previous section, a DOE was created in order to analyse the effect of temperature and time in tensile and flexural test specimens. With these studies, two of the process main flaws were addressed.

5.1 Machinability of PA12 and short fibre reinforced PA12 materials produced by Fused Filament Fabrication

The work described in the forthcoming section is presented in original article format, as submitted to the International Advanced Manufacturing Technology Journal, which has been published (January 2020) Ferreira et al. [2020].

Fused Filament Fabrication (FFF) is an extrusion-based process that allows quick and inexpensive part production, practically without any geometric limitations, offering flexibility, promoting reduction in costs and lead-time in an industrial scenario. Being one of the most widespread additive manufacturing techniques, the process has evolved introducing new and advanced materials (e.g. high-performance polymers and composites). Despite its advantages, the process is

vastly overlooked due to its high level of anisotropy, poor surface roughness and lack of geometric accuracy caused by the layer thickness. To reduce this effect, a sequence of laborious manual operations can be performed, which may result in time-consuming and inaccurate results. Therefore, efforts have been made towards the development of hybrid manufacturing technologies by combining FFF process and subtractive equipment, aiming to solve these limitations. In this work, two complementary methodologies analysing the behaviour of FFF PA12 and short fibre reinforced PA12 printed parts when subjected to a subtractive approach are presented. The first experimental plan took into account the final surface roughness (Ra and Rz) via full factorial design of experiments (DOE) and analysis of variance (ANOVA) considering the influence of distinct printing orientations, two types of cutting tools and machining parameters such as, cutting speed, feed and cutting depth. An analysis on tool wear and SEM microscopy to the machined surface were also performed. The second approach was carried out via Taguchi and ANOVA, considering the first experimental approach results. Thus, milling parameters were the focus, evaluating the final material surface roughness, being now monitored the cutting forces and tool wear analysis in order to understand their influence on the final results. It is shown that it is possible to machine PA12 based FFF printed parts without any major problems such as layer delamination. A decrease in Ra,t of 1931% to 0.99 μm for PA12CF and 2255% for PA12 to 0.96 μm was achieved, proving the overall machinability of the materials. It was found that PA12 creates higher levels of cutting loads and increased tool wear, thus indicating that short fibre presence improves the material machinability, while parameters such as building orientation do not possess any influence on the final surface roughness.

5.1.1 Introduction

Advances in additive manufacturing (AM) stand for a new era in fabrication, resulting in a fresh way of thinking, how people imagine and design parts for production. Due to its layer-by-layer approach, AM opens fabrication possibilities that conventional processes cannot respond to. Even though this process was initially intended for prototyping purposes, the subsequent evolution that the distinct techniques have been subjected to, opened the path for consumer ready parts. ISO/ASTM 52900:2015 [ISO/ASTM, 2015] divides AM technologies into seven distinct categories, among them, Material Extrusion, Powder Bed Fusion, Material Jetting, Binder Jetting, Direct Energy Deposition, Sheet Lamination and Vat Polymerization. All of these methods use similar approaches to part production, from the CAD model, to the parametrization selection and toolpath generation in slicing, beyond layer wise production and finishing post processing.

One of the most popular additive technologies, is commonly known as Fused Filament Fabrication (FFF), which is inserted in the Material extrusion branch. This technique consists into the liquification of a thermoplastic-based material, by raising its temperature and extruding it through a small diameter nozzle. Then the desired shape is created layer-by-layer, quickly solidifying the material by decreasing its temperature due to its contact with the surrounding air and the previously deposited material layers. FFF was one of the most widespread technologies in early 2000 for polymeric materials, becoming one of the broadest processes offering from

the low-cost to high-end industrialized equipment cost-effective solutions. With the evolution of technology, new material formulations were developed and a vast list of possible processable materials shows the technology's potential. Polylactic acid (PLA), the Acrylonitrile butadiene styrene (ABS), the Polyethylene terephthalate glycol (PETG) may be defined as the most common materials, followed by the engineering polymers such as Polyamides (PA), Polycarbonates (PC) and high-performance, high temperature polymers (i.e. Polyether ether ketone (PEEK) and Polyether Imide (PEI)). However, this meant that the hardware had to follow this evolution, fulfilling the material processing requirements. The creation of these high-performance materials was motivated by the usual low mechanical properties of the raw material. Following, this same evolution, composite materials have been adapted to the process being currently an important variant of the technology. With the addition of short fibres, nanotubes or continuous reinforcements to traditional matrix materials such as PA and PETG, an improvement in the final part mechanical behaviour has been achieved. Without these high-performance materials/composites, the process would still not be considered as a significant alternative by the industry, thus creating the possibility of new applications in aerospace [Williams et al., 2007],[Man Chun and Kowalik, 2018], automotive [Mayyas et al., 2012], sports [Ullah et al., 2015] and health [Singh et al., 2018].

Even though the advantages presented by the process, there are several challenges when facing other AM technologies. FFF parts present a higher level of anisotropy, partly due to the thermal residual stresses caused by successive heating/cooling cycles and its higher layer thickness. As a consequence of that layer thickness, the process typically originates poor surface finishing (e.g. pronounced staircase effect due to the rounded geometry of the deposed line [Singh et al., 2017b]). These issues tend to be accentuated for higher extrusion diameters or higher layer thicknesses as in big dimension parts. The thermal gradient created by the continuous material deposition can also influence the part dimensions, as well as the interlayer adhesion strength, since it dictates the type of connection between the adjacent layers [Zhang and Chou, 2008]. Moreover, the sequence of thermal cycles to which the material is subjected to, from polymeric expansion after leaving the nozzle, to the posterior shrinkage induced by the material cooling, create a unpredictable lack of precision and consequent poor geometric accuracy. Taking into account the process capabilities such as the wide range of materials, properties and low cost, the technology is now evolving towards the hybrid sector, where a machine can print and correct the part dimensions and surface quality via subtractive manufacturing.

Several studies have been developed in order to investigate the dimensional accuracy of FFF printed parts. Santana et al. [2017] studied the influence of layer thickness, infill density, deposition speeds, extrusion temperature and extrusion multiplier on the part dimensional accuracy in xyz directions. Through Taguchi method and ANOVA statistical analysis, it was possible to conclude that the infill density and extrusion multiplier are the most influential factors, being responsible for the printed samples distortions. Sood et al. [2009] analysed the influence of part orientation, raster width, layer thickness, air gap and raster angle on dimensional accuracy. By applying the Taguchi method, it was found that sample shrinkage was the most critical defect, since specimens were smaller in every direction. A final set of ideal parameters were developed

according to the statistical data analysis, reducing this phenomena. Peng et al. [2014] applied the same method in an equipment with fuzzy logic and analysed parameters as raster width, layer thickness, infill speeds and printing speeds. It was concluded that the most influential factor was raster width, followed by printing speed, layer thickness and infill speeds. Dimensional accuracy is also a consequence of the feedstock intrinsic properties, therefore its prediction is only possible through the complete characterization of the materials to be tested.

FFF is one of the additive processes that presents the weakest surface finishing. The surface of the final part depends upon how thin the layer thickness is, which is especially problematic in large volume parts. Higher levels of detail lead to increased print times and consequently higher costs. Low detail parts often require manual labour, which can be an imprecise and time-consuming operation. Beyond the manual treatment, chemical finishing and machining methods for improving final part quality have been studied. Galantucci et al. [2009] researched the link between FFF process parameters and surface roughness in a first step, and posteriorly tested the chemical bath finishing (acetone) on ABS printed parts. Singh et al. [2017b] also evaluated chemical (acetone) exposition technique via vapour smoothing station on parts roughness. A Design of Experiments (DOE) was carried out in order to identify the most influential parameters on the surface finishing. It was shown that surface finish was improved to nano-level without deviating from the initial dimensions. There have been several studies regarding ABS printed parts acetone bath/vapour smoothing techniques showing promising results [Lalehpour and Barari, 2016, Singh et al., 2016]. However, the finishing process using acetone is only possible for ABS and is extremely complex to control.

Machining a FFF printed part creates the possibility of benefiting from the accuracy provided by the subtractive process. The downfall of this technique is the need of specific hardware and all of the pre-machining routines involved in the process. As AM is the process of creating parts by adding layers of material upon itself, subtractive processes implicate the use of several techniques and processes into a piece of raw material, removing it until the desired shape is created. Since there is the need of post-processing FFF printed parts with inadequate dimensional accuracy and surface quality, further investigation towards the development of hybrid techniques is necessary, combining the material deposition with subtractive operations in a single machine. In a novel approach, Amanullah et al. [2017] developed a hybrid setup capable of both types of fabrication. This machine was composed by a FFF extruding head and a CNC cutting spindle in a cartesian three-axis kinematic, capable of one extra movement by rotating the tool plate (CNC Spindle/extruder) embedding both technologies with a single control panel. Lee et al. [2014] have shown prominent results in the development of an hybrid five-axis machine equipped with a rotating plate composed by a FFF extruder in one side and the spindle in the other. Case studies showed that by using a hybrid technique, the building time was reduced upwards 50%.

Considering this approach, machining parameters for printed parts need to be investigated. Since the parts are not made from a homogeneous block of material, the existing recommended parameters for polymeric solid materials are just a starting point. Beyond the influence of the printing process parameters and the material, the subtractive component presents challenges at

parameters and tools selection. Boschetto et al. [2016] addressed this topic by printing according to several deposition angles, square parallelepiped ABS samples, and posteriorly measuring surface roughness for different cutting depths for each sample. In a study developed by Tomal et al. [2018], a combination of FFF with abrasive milling was used to improve the dimensional accuracy and surface finish. The results showed an improvement in dimensional accuracy from 71% to 99% when comparing the original part with the milled one. In addition, the surface roughness (*Ra*) was measured presenting an improvement up to 91.3%.

To the best of author's knowledge, studies conducted earlier focused on face milling as the finishing technology are dedicated to more traditional materials such as ABS and PLA [Boschetto et al., 2016, Tomal et al., 2018], considering fewer machining parameters, (e.g. cutting depth, feed and cutting speed) aiming at improving surface roughness. In regards metallic materials, subtractive processes have been widely used for surface roughness enhancement. As shown by Kara [2017], Kara and Öztürk [2019] and Karabatak and Kara [2016], distinct process parameters were analysed, the Taguchi method coupled with ANOVA analysis being applied to obtain a combination of parameters allowing for an improved final surface roughness. Similarly to the above-mentioned researches, it is initially intended in this study to create the parameters window for a machining operation. For such purpose, the face milling operation is considered in machining both Polyamide 12 (PA12) and short fibre reinforced PA12 (PA12CF) printed parts are considered, taking into account that the abrasiveness of fibre reinforcement might present a challenge for the cutting tools. This study is seen by the authors as a required step to understand the behaviour of FFF parts when subjected to subtractive operations, leading the way towards the development of hybrid technologies possibilities. It is a purpose to allow the application of developed methodology in this study to other materials so that the adequate machining parameters may be obtained.

This paper is structured as follows: an introductory section addresses the FFF state-of-the-art, afterwards, a section presenting the materials and the additive production details which are common for both approaches. The research approach is divided into two major sections, representing the first and second approach. In each section, the experimental methods that describe the procedure are explained, followed by the results and discussion, being complemented by a final summary. Lastly, final conclusions concerning the whole work are presented.

5.1.2 Materials and specimens production

5.1.2.1 Materials

The material selection for this study consisted of two versions of Polyamide 12 (PA 12) ⌀1.75 mm filament from Fillamentum©, Parzlich s.r.o (Czech Republic). PA 12 - Nylon FX256 [Fillamentum, 2019b] from now on referred as PA12 and PA12-Nylon CF15 [Fillamentum, 2019a] (referred as PA12CF) as the reinforced version of the first brand. As indicated by the manufacturer datasheet, PA12CF is reinforced by 15 wt% of short carbon fibres with 100 μm in length and 10 μm in diameter. Table 5.1 depicts some of the relevant material properties. This type of

polymer is largely considered as an engineering thermoplastic, being suited for several load bearing applications. Its properties also include a high elastic modulus, as well as improved tensile strength, low friction coefficient and wear resistance. The application of this type of materials to the FFF technology allows an evolution in mechanical performance of the parts. Furthermore, most of the research in this field, considering the process of FFF, is done with commodity polymers such as ABS and PLA [Boschetto et al., 2016, Tomal et al., 2018], therefore it is of the most interest to develop knowledge with these new materials in order to further push the process.

Table 5.1: Datasheet values and material specifications [Fillamentum, 2019b,a].

Property	CF15	FX256
Material density (g/cm^3)	1.08	1.01
Melt flow index ($g/10min$)	14.64	16.56
Glass transition temp. T_g (°C)	44.70	52.91
Thermal conductivity (10^{-3} W/m.k)	144.22	124.82
Tensile strength (MPa)	54.50	45.00
Tensile elastic modulus (MPa)	500	1400
Melting temperature (°C)	160	178
Print temperature (°C)	235-260	235-260

5.1.2.2 Sample definition and production strategy

The developed specimen geometry for machinability testing (face milling with end cutters) was defined considering the following influential factors: i) The machinable face must have a minimal length of 60 mm in one direction, allowing stabilization of the milling process; ii) Each sample should maximize the number of tests, maintaining easy printability, while reducing material waste; iii) Since machining trials were performed at surface level, it is important to ensure a near 100% dense at surface level. The choice also took into consideration the tool diameter, the cutting tool overlapping between passes and finally, the printing capacity of the FFF machine. Thus, the selected geometry corresponded to a quadrangular prism with dimensions of 30x30x60 mm (Figure 5.1), with fully dense shells (bottom, top layers and perimeters) and internal infill of 15%.

The samples were manufactured in a Tronxy X5 3D printer from Shenzen Tronxy Technology Co. Ltd, and the process planning was performed with Simplify3D®4.0.1. Table 5.2 lists the parameters used in the production of the samples. The choice of the parameters was based on preliminary tests, which revealed to be the ones that presented increased printability, reduced warping and good visual aesthetics [Fonseca et al., 2019].

As previously mentioned, the surfaces to be machined were produced with a fully dense shell. Regardless of the printing orientation, and according to the parameters presented in Table 5.2, 15 top and bottom layers were needed to achieve the 3 mm machinable surface (0.2 mm layer height). For the lateral walls, the same shell thickness was achieved by using 8 perimeters (raster width of 0.4 mm, as shown in Figure 5.1).

Table 5.2: Fused filament fabrication parameters.

Extrusion Parameters	
Nozzle diameter	0.4 mm
Extrusion multiplier	1.05
Layer Parameters	
Layer height	0.2 mm
Raster width	0.4 mm
Top/bottom solid layers	15
Number of perimeters	8
Infill pattern	±45°
Infill percentage	15%
Temperatures	
Extrusion temp.	260°C
Bed temp.	90°C
Speed	
Printing speed	40 mm/s

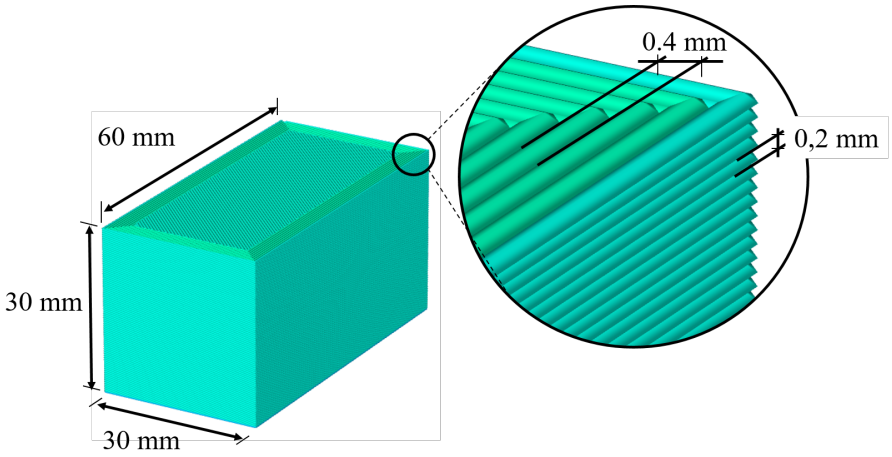


Figure 5.1: Sample dimensions and deposition strategy.

5.1.3 Research approach

As presented in Figure 5.2, this work describes two consequent approaches for the problem of machining FFF printed parts. The first approach is based on a full factorial design of experiments (DOE) and respective ANOVA analysis, considering four different types of variables, being those the material, cutting tool, machining parameters and building orientation. With this first approach to the problem, it was possible to create a first set of ideal parameters for optimized roughness. As a result, a second research was undertaken, disregarding some non-influential conditions, but keeping both materials and widening the milling parameter variables in a new Taguchi DOE and

statistical analysis. A new machining hardware setup (stiffer, more precise/stable machine) was also considered in order to compare possible machine influence on the final part properties. A multicomponent dynamometer was used for cutting forces measurement. As a result, surface roughness, cutting forces and tool edge microscopic analysis, for each set of variables, were obtained, allowing a better insight of the machining process. This study is seen by the authors as a step needed in the evolution of the process towards the development of a hybrid technique.

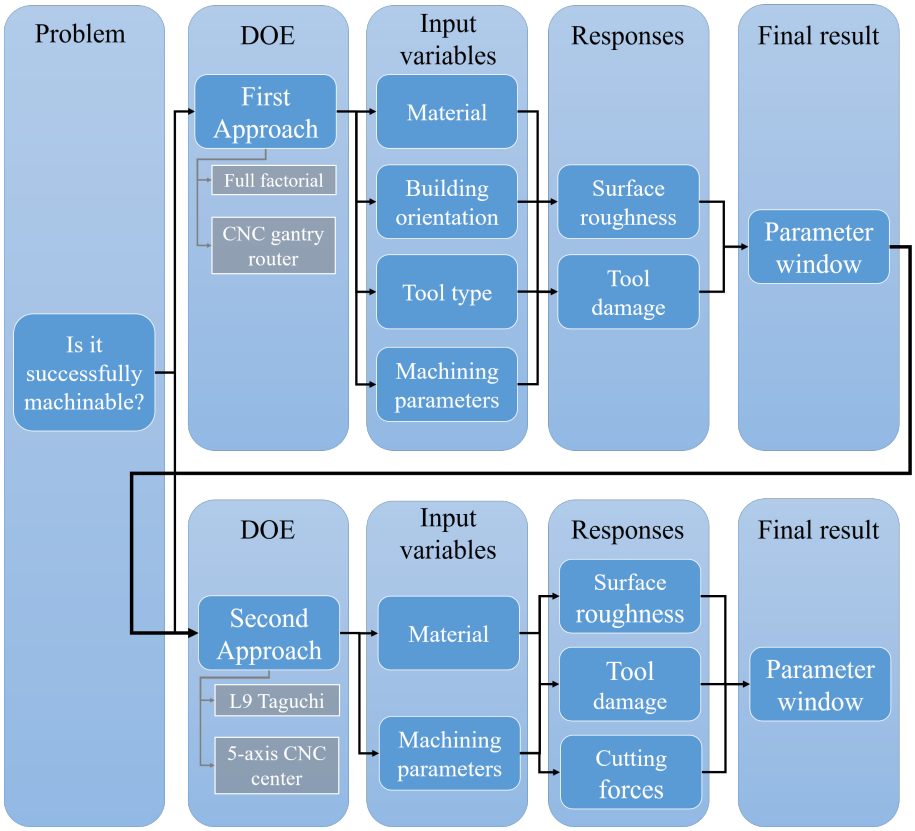


Figure 5.2: Work plan schematic.

5.1.3.1 Experimental approach 1

5.1.3.1.1 Methods

Within this section, experimental approach 1 is described in detail. The machining test hardware and protocol is presented, as well as the defined DOE and the surface roughness analysis prior and after the machining test. The main goal is to develop a machining parameters window for face milling finishing operations, improving the surface roughness by considering four types of variables: milling parameters (cutting speed, feed and depth of cut), material (PA12 and PA12CF), tool specification (2 or 4 flute) and print orientation.

Subtractive hardware

A Ouplan CNC Routers Checkbox 1008 was used. This milling machine presents a cartesian 3 axis gantry structure, with a maximum working size of 1100 x 850 x 200 mm, being capable of displacement speeds up to 25 m/min. It is equipped with a spindle that can achieve up to 24000 RPM, while the tool clamping is done by an ER-32 type system. This machine is recommended for light work and presents lower stiffness and stability than CNC machining centres as the one to be used in the second experimental approach.

DOE - First test programme

In order to combine all of these input values (A-Material, B-Tool, C-Building orientation, D-Cutting speed, E-Feed and F-depth of cut), a full factorial DOE was defined as the basis of this experimental analysis, resulting into ninety six different conditions, as presented in Figure 5.3. The experimental data obtained from tests (surface roughness) was investigated via ANOVA in order to identify the truly contributive parameters (using a confidence interval of 95%). This will allow further along the investigation path for a better parameter combination choice considering the obtained responses.

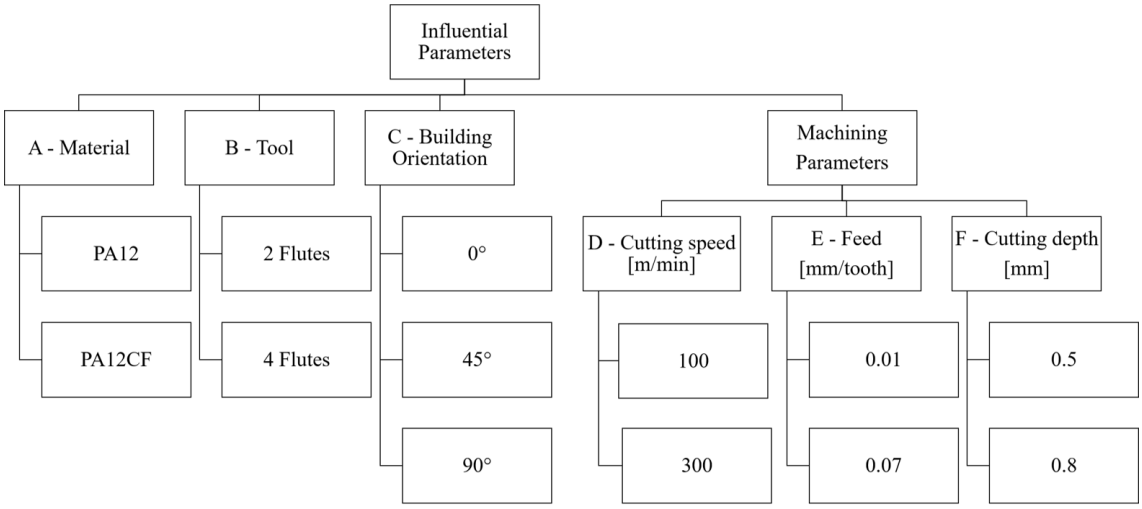


Figure 5.3: Approach 1 - Full Factorial DOE test matrix.

Building orientation: Concerning building orientation, horizontal specimens were produced at 0°, tilted at 45°, with support structures and upright position at 90°, as shown in Figure 5.4. By testing these three types of samples, it is possible to investigate how influential can the deposition orientation be on the machining process, since the tool will intersect shell lines deposed perpendicularly, parallel and 45° to its travelling path.

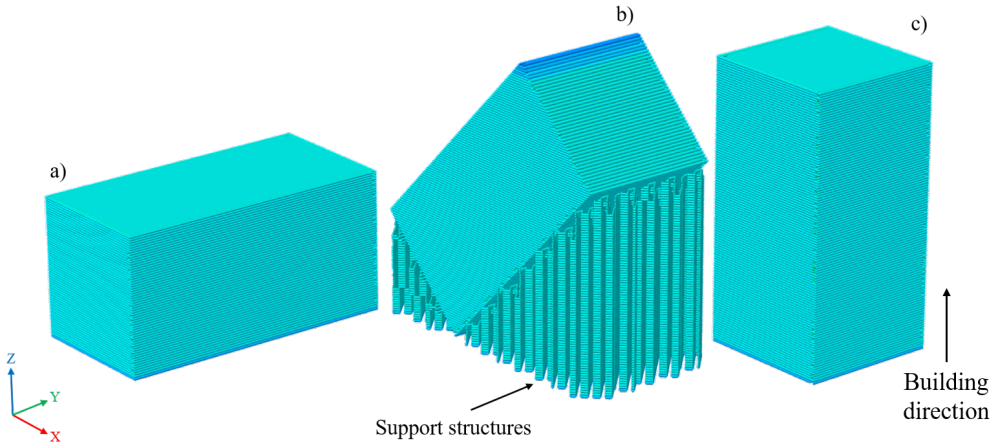


Figure 5.4: Different building orientations considered in this study: a) 0°(Horizontal/Flat position); b) 45° (tilted position) with support structures generated by Simplify3D; c) 90° (Up-right position).

Tool: Regarding the tool choice, two types of ⌀8 mm solid carbide end-mills supplied by Palbit, S.A. were used. A flat end two flute tool without coating, with an helix angle of 14° (HFMA200820-SOFTLINE) (Figure 5.5a) was selected. The second type was a flat end four flute tool, with 30° of helix angle and a diamond coating (HF30A400815 R050-KOPIEFR LINE) (Figure 5.5b). Both tools were subjected to two levels of three machining parameters, namely cutting speed, feed and depth of cut. The full set of experiments was performed using only two tools (one of each type).

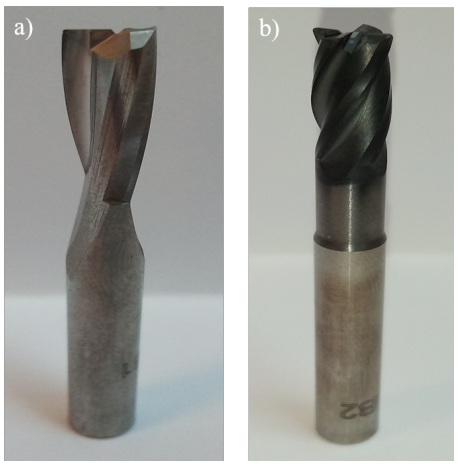


Figure 5.5: Cutting tools: a) flat end two flute and b) flat end four flute tool

Cutting Parameters: Prior to the first experimental plan, exploratory tests were performed by submitting the samples to a wide range of cutting speeds, based on the literature recommendation summarized in Table 5.3, defining a first estimate window for cutting parameters. Considering this

first analysis, cutting speed values process range were defined between 100 and 300 m/min, while the feed per tooth was 0.01 and 0.07 mm/tooth, the chosen cutting depth of 0.5 and 0.8 mm.

Table 5.3: Literature overview for cutting parameters for polymer machining.

Material	Type of tool			Cutting parameters			Reference
	Type/Material	Diameter (mm)	Cutting flutes	Cutting speed (m/min)	Feed (mm/tooth)	Cutting depth (mm)	
PA66, PA66-GF30 PA66-MoS2	Solid carbide inserts	121	8	186 to 294	0.100 to 0.157	1.00 to 1.56	Vasile et al. [2014]
PEEK	Solid carbide end mill	10	2	126 to 251	0200 to 0.300	4.00 to 8.00	Izamshah et al. [2013]
PA6G	End mill and solid carbide end mill	10, 14 and 18	4	100 to 140	0.008 to 0.015	1.00 to 2.00	Bozdemir and Aykut [2012]
CFRP	Solid carbide inserts	25	2	160 to 200	0.015 to 0.050	6.75	Voss et al. [2017]
ABS – P400	Solid carbide end mill	6	2	156 to 360	0.025	0.05 to 0.50	Boschetto et al. [2016]

Machining Strategy

Considering the high number of samples needed to accomplish the full factorial DOE, each face of the testing specimen was divided into two sectors and machined (end face milling) with a different set of cutting parameters, as illustrated in Figure 5.6. With this machining tool routine, an overlap of 2 mm between paths is observed, which corresponds to 25% of the tool diameter. The machining strategy was created via Mastercam Mill X9©.

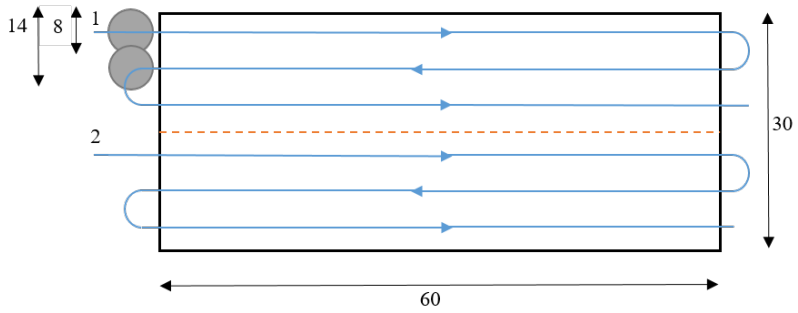


Figure 5.6: Machining strategy for the first methodology with two distinct parameter sets applied to each face.

Material and tool analysis

Roughness Measurement: The specimens surface roughness was measured using a profilometry Hommelwerle with a TK 300 tip (LV-50) with a diamond needle of ± 300 μm. The analysis was performed at an average speed of 0.5 mm/s for a total measuring length of 4.8 mm, according to ISO 4288 ISO 4288:1996 Geometrical Product Specifications (GPS) [1997]. For each specimen the surface roughness was assessed three times along two orthogonal directions: Ra,l (longitudinal) and Ra,t (transversal). Ra which is normally referred as roughness is characterized by the arithmetic mean of the ordinate's absolute (height values) within a base length. For comparison purposes, the measurements were taken prior and after the machining operation, as presented in

Figure 5.7. It is important to consider that Ra,l is measured in the machining feed/path direction, while Ra,t is across the machining path.

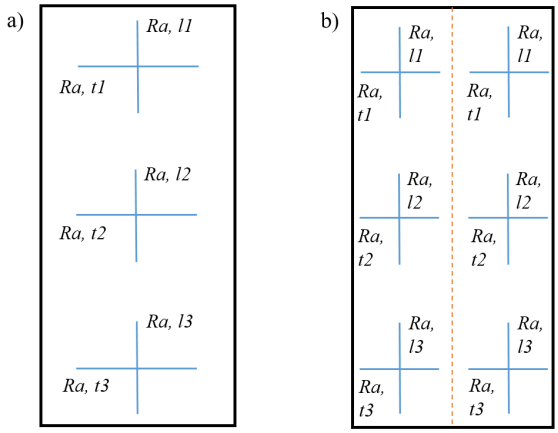


Figure 5.7: Measurement points for Ra,l and Ra,t prior a) and after b) machining.

SEM analysis: Scanning Electron Microscopy testing was performed in the machined samples using a Quanta 400FEG ESEM/EDAX Genesis X4M in order to understand the surface morphology of distinct processing variables combinations, fibre behaviour and polymer/fibre interaction.

5.1.3.2 Results and discussion - Experimental Approach 1

Pre-machining surface roughness

Table 5.4 depicts the roughness analysis results carried out prior to specimen machining. It is possible to observe a relationship between building orientation and Ra,l and Ra,t. Horizontally built samples (0°) present higher Ra,t than Ra,l for both materials, indicating that longitudinal measurements were made along the layers/deposition lines. The opposite behaviour is found for the upright samples (90°) in which longitudinal measurements are made perpendicularly to the layer deposition. For the tilted samples (45°), surface roughness is similar both longitudinally and transversally, since the measurement is done at 45° to the deposition direction. Therefore, it can be concluded that a 0.2 mm layer height leads to an average (perpendicular measurements to the deposed lines) roughness of 19.55±5.12 μm for PA12 and 19.01±0.25 μm for PA12CF.

ANOVA - Approach 1

Table 5.5 presents ANOVA results for the transversal roughness (Ra,t) analysis. Considering the above mentioned confidence interval (95%), if the P-Value is higher than 0.05, the parameter or combination of parameters is considered as non-influential to the final results, and consequently not presented in the model.

Building orientation and depth of cut do not show relevant influence on roughness results, nor some interactions between these parameters. From the remaining four input parameters, the results

Table 5.4: Surface roughness prior to machining tests, average values.

Building orientation	Material	$Ra,t(\mu m)$	$Ra,l(\mu m)$
0	PA12CF	19.12 ± 1.96	3.83 ± 0.53
45	PA12CF	16.88 ± 3.86	16.63 ± 4.30
90	PA12CF	6.13 ± 2.14	18.89 ± 1.61
0	PA12	21.65 ± 2.90	2.45 ± 6.19
45	PA12	13.63 ± 8.50	13.76 ± 3.38
90	PA12	2.61 ± 5.77	17.45 ± 10.14

show that the more significant one is the material with the highest contribution of 13.78%, followed by cutting speed (11.76%), then the feed (2.79%) and finally the tool with 2.76% of contribution, in a total of 31.09% of importance. There are six interactions presenting a total contribution of 51.42%, thus indicating the importance of the parameters combination, with the cutting speed/feed (D-E) being the most important (15.27%), followed by tool/feed (B-E) (13.17%), tool/cutting speed (B-D) (11.45%), material/tool (A-B) (5.51%), material/cutting speed (A-D) (4.75%) and finally material/feed (A-E) (1.27%). It is worth noting that some of these interactions present greater influence on Ra,t than each parameter alone.

Table 5.5: ANOVA *Ra,t* results (1st experimental approach).

Source	DF	SS	Contribution	F-Value	P-Value
A - Material	1	80.14	13.78%	71.18	0.000
B - Tool	1	16.05	2.76%	14.25	0.000
D - Cutting Speed	1	68.39	11.76%	60.75	0.000
E - Feed	1	16.21	2.79%	14.40	0.001
A-B	1	32.03	5.51%	28.45	0.000
A-D	1	27.64	4.75%	24.55	0.000
A-E	1	7.38	1.27%	6.55	0.012
B-D	1	66.55	11.45%	59.11	0.000
B-E	1	76.59	13.17%	68.03	0.000
D-E	1	88.80	15.27%	78.87	0.000
Error	85	93.45	17.47%		
Total	95	581.37	100%		

Through the main effects plot analysis in Figure 5.8, it is observable the influence of independent input variables. It can be perceived that the best transversal roughness is obtained with PA12CF material, processed with a two flutes tool, a cutting speed of 100 m/min and a feed of 0.07 mm/tooth.

Figure 5.9 presents the transverse roughness fitted interactions, with interactions, B-D, B-E and D-E as the most contributive ones. For B-D, the 2 flutes tool presents similar *Ra,t* for both cutting speeds, however, the 4 flutes tool presents better surface roughness with lower cutting

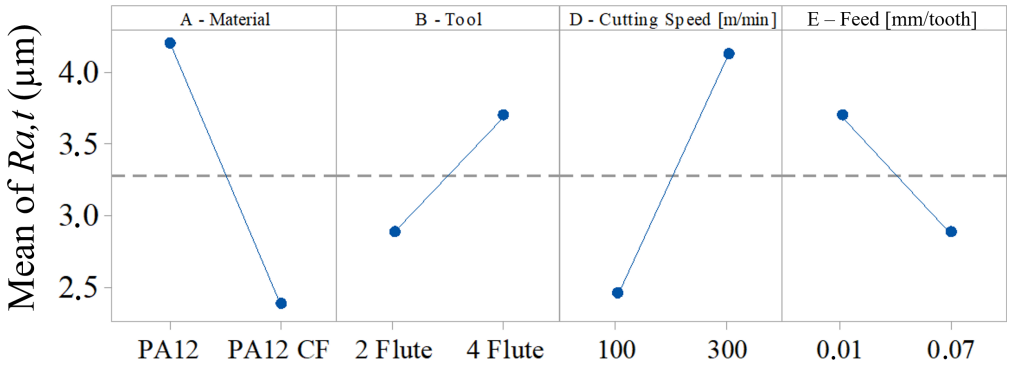


Figure 5.8: Main effects plot for *Ra,t*.

speeds 100m/min, while at 300 m/min the roughness is higher. B-E interaction indicates a better behaviour for the two flute tool at lower feeds, increasing the surface roughness for higher feeds (0.07 mm/tooth), while the 4 flute tool presents roughly the same behaviour at higher feeds than the two flutes tool at lower values. Finally, D-E, proving to be the most influential one, shows that at 0.07 mm/tooth (feed) the behaviour is roughly similar for both cutting speeds, while at lower feeds (0.01 mm/tooth) surface roughness is worst with the increase in the cutting speed from 100 to 300 m/min.

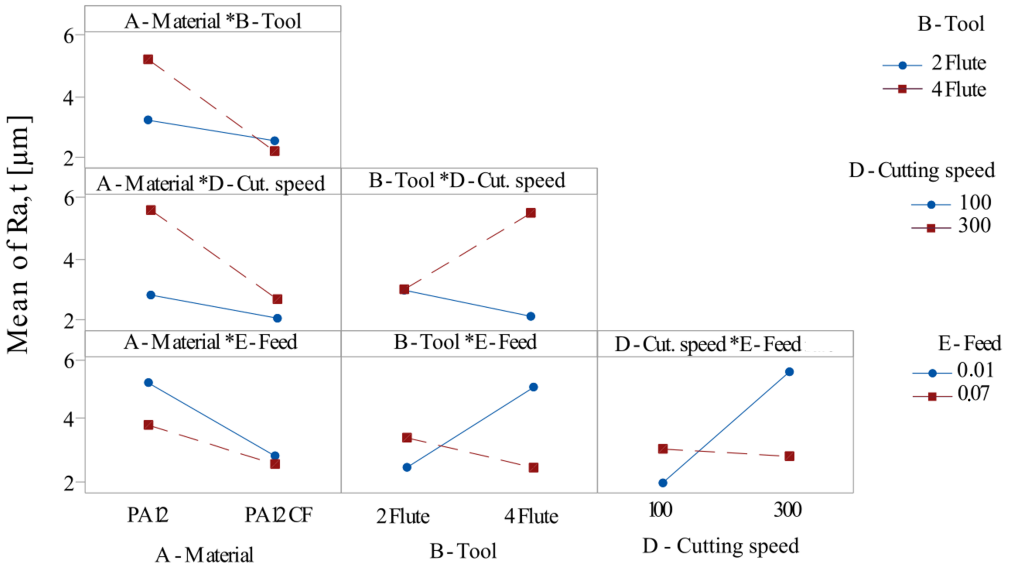


Figure 5.9: Two way interaction plot for *Ra,t*.

For longitudinal roughness (Ra,l), Table 5.6 depicts the results considering the same statistical analysis for the transverse roughness. In accordance with the Ra,t ANOVA's results, building orientation and depth of cut are not influential, nor the relative combinations. The independent parameters analysis, shows the feed as the most important contribution in this case (10.68%), followed by material (8.92%), cutting speed (8.86%) and the tool (1.59%), with a total contribu-

tion of 30.05%. Two way interactions present 47.04% and the most important contribution being the tool-feed (B-E) (17.84%), followed by cutting speed-feed (D-E) (14.24%), tool-cutting speed (B-D) (7.15%), material-feed (A-E) (3.75%), material-cutting speed (A-D) (2.24%) and finally material-tool (A-B) with 1.82% contribution. However, the error value is higher in longitudinal roughness results than what was presented in Table 5.5.

Table 5.6: ANOVA *Ra,l* results (1st experimental approach).

Source	DF	SS	Contribution	F-Value	P-Value
A - Material	1	95.72	8.92%	33.10	0.000
B - Tool	1	17.02	1.59%	5.89	0.017
D - Cutting Speed	1	95.00	8.86%	32.85	0.000
E - Feed	1	114.63	10.68%	36.64	0.000
A-B	1	19.48	1.82%	6.74	0.011
A-D	1	24.00	2.24%	8.30	0.005
A-E	1	40.25	3.75%	13.92	0.000
B-D	1	76.76	7.15%	26.54	0.000
B-E	1	191.42	17.84%	66.20	0.000
D-E	1	152.71	14.24%	52.81	0.000
Error	85	245.26	21.87%		
Total	95	1072.77	100.00%		

Main effects plot for *Ra,l* in Figure 5.6, shows that the ideal combination of parameters are in concordance with the ones obtained for the previous measurements. However, the major contribution is given by the feed (10.68%), contrasting with the 2.79% for Ra,t, with the optimal value not as low as in transverse direction.

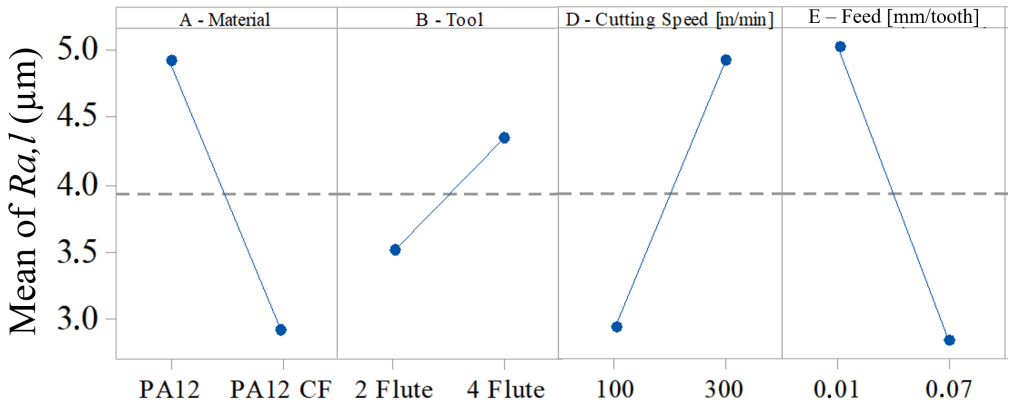


Figure 5.10: Main effects plot for *Ra,l*.

By comparing the two way interactions on Figure 5.11 for the transverse roughness, it is possible to observe that the trend is kept with very few differences. Once again, the three most influential interactions are B-D, B-E and D-E, which are the same most influential combination

in transversal roughness results. Considering B-E, which is the most statistically contributive (17.84%) interaction, it is possible to observe that for both speeds result in similar roughness for the two flute tool. The four flute tool presented improved roughness at lower speeds (100 m/min), while a worst response is shown for 300 m/min. Once more, for D-E interaction (second most important at contribution level), there is no significant difference in roughness at lower cutting speeds, despite that at higher cutting speed. For high feeds, the roughness is slightly improved, contrasting with lower values.

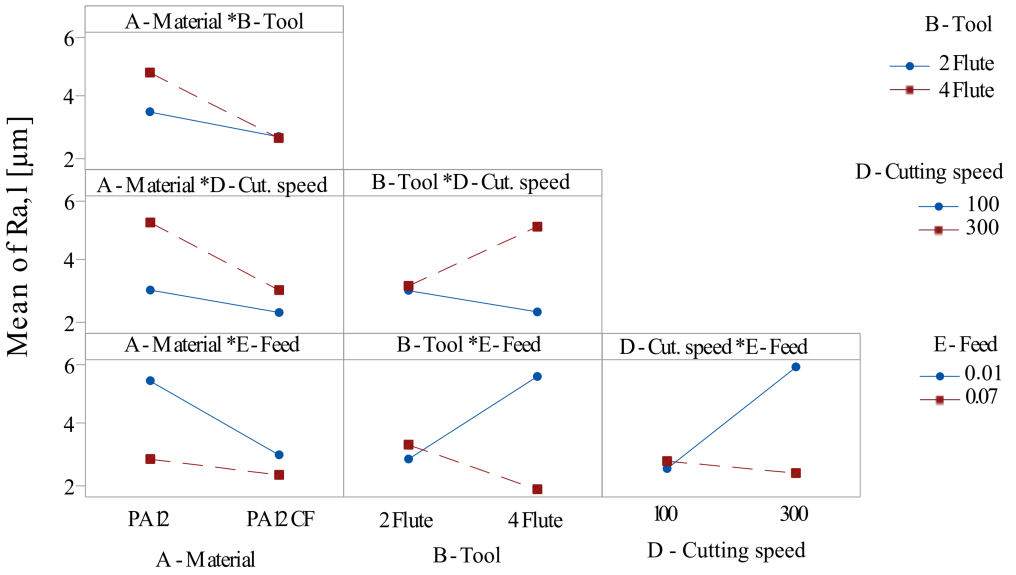


Figure 5.11: Two way interaction plot for *Ra,l*.

Considering the above mentioned factors, Figure 5.12a presents the *Ra,t* comparison of a PA12 CF, horizontally printed, prior and after the machining process with a two flute tool, cutting speed of 100 m/min, feed of 0.01 mm/tooth and cutting depth of 0.8 mm. An improvement is shown in transverse roughness from a 16.45±0.78 to 1.84±0.01 μm. Figure 5.12b presents the *Ra,l* comparison for PA12 CF, printed tilted at 45°, prior and posterior to machining process with a four flute tool, cutting speed of 300 m/min, feed of 0.07 mm/tooth and cutting depth of 0.8 mm. It is possible to identify an improvement in longitudinal total roughness from a 14.97±1.28 to 1.70±0.30 μm.

SEM analysis

Figure 5.13 depicts SEM results for a vertically printed PA12 CF sample after machining. Figure 5.13a presents three distinct areas, being the left side the end of the first parameters' set (check Figure 5.6); the right side shows the beginning of the second parameters' set, and the centre, which is marked with a white circle, it clearly shows the overlap area of the previous passes. Both paths were machined with a four flute tool, with a speed of 100 m/min and a cutting depth of 0.8 mm, however, in the left side (parameter set 1) the feed was 0.07 mm/tooth while in the

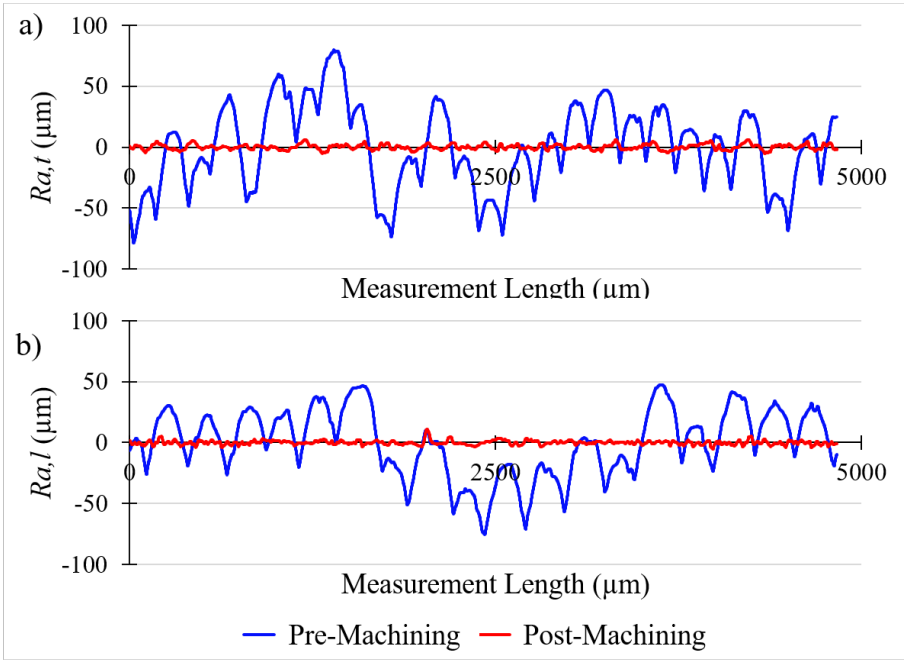


Figure 5.12: Roughness profile before and after machining: a)longitudinal and b)transversal.

right side a 0.01 mm/tooth was used (parameter set 2), presenting Ra,l values of 1.54±0.10 and 2.52±1.02 μm respectively, confirming the trend indicated in Figure 5.10. However, by analysing the Tool-Feed interactions it is possible to conclude that four flute tools require an higher feed to produce better roughness. This effect is seen for Ra,l and Ra,t. Lower feed rates, indicate lower displacement per tooth, thus, presenting a difference in behaviour for two and four flute tools. By imposing an higher number of rotations in the same area, could increase the sample's temperature and lead to irregular material removal. Figures 5.13b and c depict local magnifications of both machining parameter sets. Figure 5.13b exhibits a smoother surface, with diminutive fibre presence, thus indicating that the matrix polymer was removed and spread throughout the tool path. Figure 5.13c indicates a higher number of fibres, which are predominantly aligned with the tool rotation direction. This result reinforces the previous hypotheses that the polymer might have overheated at surface level, leaving the fibres broken and reordered.

Tool wear analysis

No protocol was taken concerning wear progression analysis; only two different tools were used to perform all the machining tests and the damage was verified in the end. Figure 5.14 shows the two tools the details of the worn out zone. Considering the two flute tool (Figure 5.14a and b) it is possible to observe chipping of the tool edge in one of the flanks. This type of damage might occur due to several reasons, such as the abrasiveness of the PA12 CF short fibres, a less stable spindle or machine axis and the consequent entrance and exit on the specimen, reasons which, cannot be confirmed with this first approach. Tool wear was found in the four flute tool (Figure 5.14c and d)

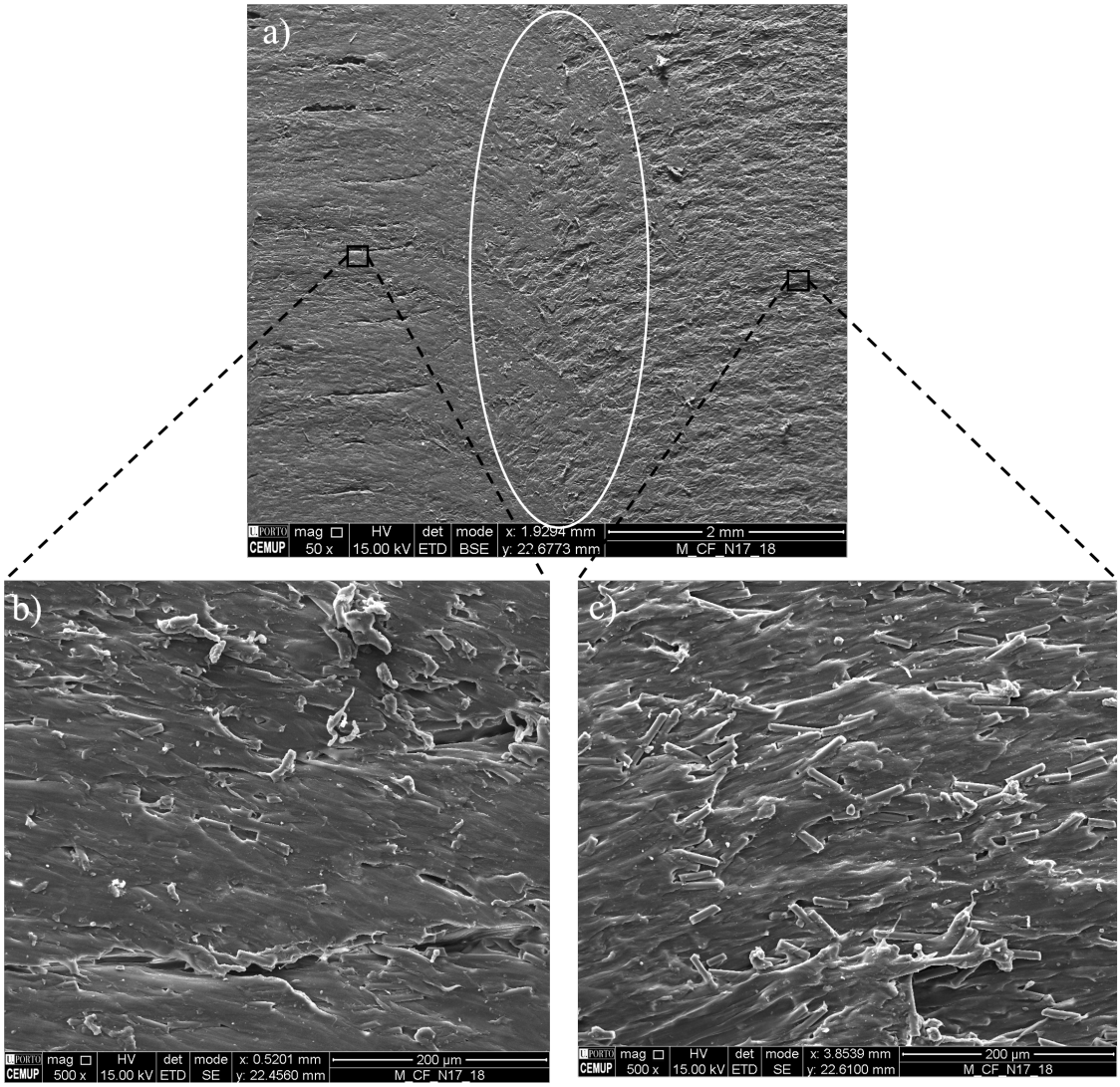


Figure 5.13: Surface analysis via SEM: a) Parameters set 1 and 2, b) Magnification of set 1 and c) Magnification of set 2.

in non advanced state due to its different characteristics (coating and number of flutes), presenting however coating abrasion..

5.1.3.3 Summary - Approach 1

In a general manner, this first approach allowed to demonstrate the possibility of machining FFF parts to improve their surface roughness/dimensional accuracy via CNC machining. An analysis of the material, building orientation, and machining parameters' influence on the overall printed part final surface roughness was performed for this specific subtractive setup. This study was able to indicate some guidelines for the next stage.

Considering the ANOVA analysis, the most influential parameters when taking into account *Ra*, are the material intrinsic properties, the cutting speed, the type of tool and the feed, thus

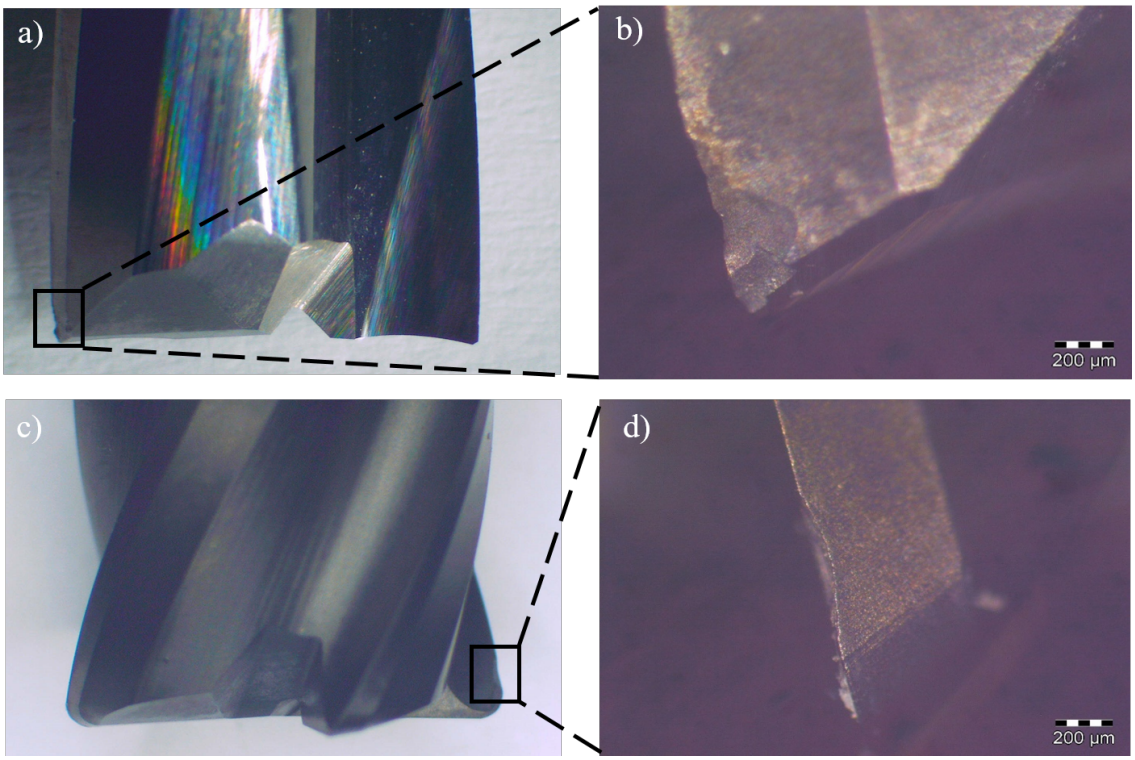


Figure 5.14: Tools wear (1st testing approach): a) two flute tool, b) two flute damage area magnification, c) four flute tool and d) four flute damage area magnification.

discarding building orientation and depth of cut. Building orientation was a chosen parameter since machining perpendicularly or parallel to the deposition paths was thought to be a critical parameter. However, being statistically proven non relevant after machining post-processing. The same was considered for the depth of cut, that removing more or less material at each tool pass might not influence the surface roughness.

PA12CF averages lower longitudinal and transverse roughness (1.84±0.11 μm and 2.01±0.34 μm) than its unreinforced version (2.80±0.54 μm and 2.18±0.20 μm), when considering the best combination of parameters (2 flute tool, lower cutting speeds and higher feed), hence leading to the conclusion that the presence of fibres improves the material stiffness, thus improving its machinability in terms of surface finishing.

The two way interactions present an higher level of statistical contribution (51.42% for Ra,t and 47.04% for Ra,l) for the final part finishing than the isolate input variables, since both presented approximately 20% of error.

Material-Tool interaction indicates that PA12 should be machined using a two flute, while for the reinforced material, surface finishing is roughly the same for both tools.

The same cutting speed of 100 m/min is advised for both materials, while higher feeds (0.07 mm/tooth) is advised for better surface finish. This result may be in contradiction with the expected for most metallic materials that show better roughness with reducing the feed. Higher feeds and lower cutting speeds results in less heating, less material softening and less material stir effect.

This goes against the literature values, which indicates that lower feeds lead to better surface finishing. It is also shown that improved roughness is obtained with lower cutting speeds, once again contrasting with literature values. In agreement with the literature results is the non-influence of the depth of cut [Alauddin et al., 1995].

Tool wear was detected in both tools, namely coating wear in the four flute tool, as well as chipping in the two flutes. This damage was likely caused by the impact in the multiple entries of the tool in the part and due to the presence of abrasive fibres in half of the samples. Outplan CNC machine, was considered as an influential factor, since its structure was susceptible to spindle vibrations during the longitudinal axis travel, which may lead to influenced results. Thus, the need for a newer and more robust hardware would be imperative for this parameter window verification.

SEM analysis showed the presence of a higher number of fibres at the surface for a certain set of parameters. This is caused by the tool edge movement, which allows to conclude that the tool either pulls the fibres out of the polymer or drags them to other zone embedding them into the matrix due to the temperature increase resultant of feed and cutting speed. In addition, it is visible that after the machining process, the fibre alignment is perpendicular to the tool advance direction, considering that originally the fibre orientation is the same of the polymer deposition (0, 45 and 90° with the tool trajectory).

In conclusion, the possibility of machining thermoplastic/reinforced with carbon fibre thermoplastics produced by additive manufacture was proven. Finally Table 5.7 shows the proposed parameters for this specific setup.

Table 5.7: Optimized processing window for PA12 and PA12CF machining targeting improved finishing - approach 1.

Parameters	PA12		PA12CF	
	Ra,t	Ra,l	Ra,t	Ra,l
Tool type	2 flutes	2 flutes	4 flutes	2 flutes
Cutting speed (m/min)	100	100	100	100
Feed (mm/tooth)	0.07	0.07	0.07	0.07
Building orientation (°)	Non significant			
Depth of cut (mm)	Non significant			

5.1.3.4 Experimental approach 2

5.1.3.4.1 Methods

Considering the conclusions and limitations identified by the first approach, a second experimental plan was conceived. For this test approach, both materials were once again considered, yet studied into separate DOE plans in order to better identify which feature most influences the final result. Since in the first approach, building orientation was statistically non-influential for the final results, it is not considered for this second test programme. As a result, all the samples were printed with the same horizontal orientation. Despite the cutting depth variable being not influencing to the

roughness in the first test campaign, it was considered in this second testing programme, since it is a machining parameter (building orientation is not). Thus, this new testing phase will be only focused into machining parameters. To eliminate the possible influence that the subtractive hardware could have on the results, a stiffer and more stable CNC machining centre was used. A tool variable was also kept, being the two flute tool, since it presented the best results in three out of four categories of first test setup (Table 5.7). Since some unexpected levels of tool wear were found in the first approach, a tool analysis was performed after each machining test. A load cell was added to measure the cutting loads and possibly identify the most critical parameters concerning this approach (Figure 5.15).

Subtractive hardware and load cell

This second trial was performed on a DMG Mori DMU 60 eVo 5 axis machine, with a working volume of 600x500x500 mm using a similar ER-32 clamping system. Since some tool wear (chipping and abrasion) was found in the first approach, which could be explained by the

fibres abrasiveness or due to undesired vibrations found in the first experimental setup, the second approach adopted a stiffer and stabler equipment. The three orthogonal cutting force components were measured with a Kistler multicomponent dynamometer type 9257B connected to a KISTLER 5070A 8-channel amplifier (Switzerland), then transmitted to an Advantech USB 4750A data acquisition card (Taiwan) with a sampling frequency of 4000 Hz. This setup was assembled in the CNC machine as seen in Figure 5.15. With this load cell, each milling operation produces a multi component load that will be measured, being the resultant force used as a response in the statistical analysis.

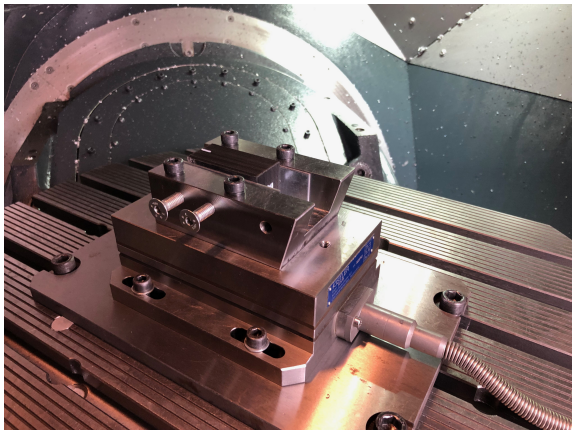


Figure 5.15: CNC setup with Kistler multicomponent dynamometer.

DOE - Second test programme

A Taguchi DOE was selected in order to minimize the number of printed samples and tools needed to perform the respective tests. As presented in Figure 5.16, separated DOE were performed for each material, focusing in machining parameters. A three level DOE was considered, introducing

intermediate values for cutting speed and feed, now including higher values for cutting depth than in previous testing programme. A L9 orthogonal array was used accordingly to Taguchi approach for DOE as seen in Table 5.8. Similarly to the first approach, an ANOVA (with a 95% confidence level) is conducted, determining the most contributive factors. In addition to ANOVA, the main effect plots are presented and, since there are three response levels, post-hoc pairwise comparisons analysis (Tukey HSD and Fisher LSD) are needed to identify the best combination of parameters, for each response type.

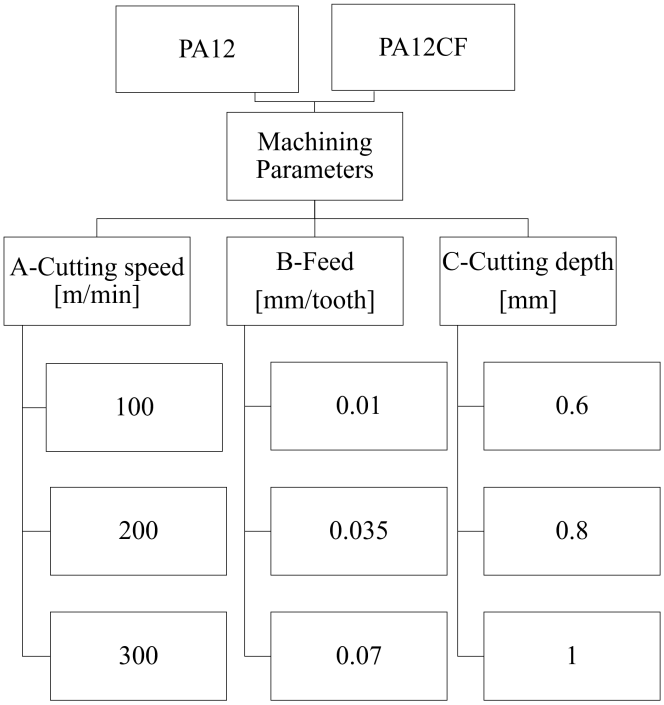


Figure 5.16: Approach 2 - Taguchi DOE with influential parameters and levels.

Table 5.8: Taguchi L9 orthogonal array used for the second testing programme.

Condition	Tool	Taguchi L9		
		Cutting Speed [m/min]	Feed [mm/tooth]	Depth of cut [mm]
1		100	0.010	0.6
2	1	100	0.035	0.8
3		100	0.070	1
4		200	0.010	0.8
5	2	200	0.035	1
6		200	0.070	0.6
7		300	0.010	1
8	3	300	0.035	0.6
9		300	0.070	0.8

Machining parameters

Regarding the cutting speed, maximum and minimum values were the same in the primary approach, corresponding to 100 and 300 m/min. Since this experiment is a three level Taguchi, an intermediate value of 200 m/min was introduced. The feed procedure included 0.035 mm/tooth as an intermediate value to the extremes of 0.01 and 0.07 mm/tooth. The cutting depths were 0.6, 0.8 and 1.0 mm.

Machining Strategy

Regarding the first experimental approach, the tool path in each specimen face was divided in two segments, thus allowing to test two different machining parameter combinations (Figure 5.6). In this trial (Figure 5.17), only one machining parameter set per face is used. The overlap in paths remains at 25%, and the tool starts and finishes the cycle 4 mm outside the sample (laterally). To increase the tool machining time, three faces per specimen were machined with the same parameters.

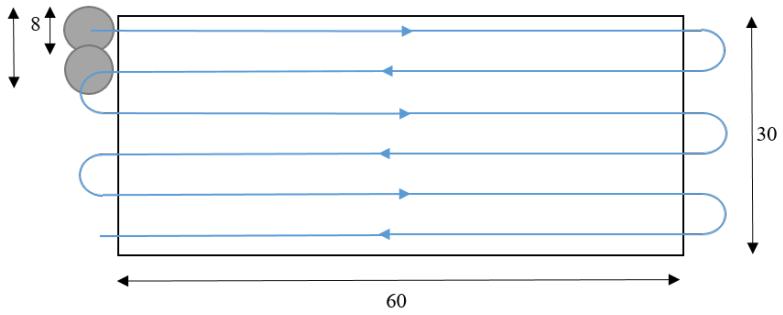


Figure 5.17: Tool path strategy for the second programme.

Tool and wear analysis

For this testing procedure, only the flat end two flute 8 mm diameter mill HFMA200820-SOFTLINE, supplied by Palbit, S.A., with an helix angle of 14°, was chosen. Contrarily to the first approach, one tool was used per each cutting speed, three tools in total (per material) were used as presented in the Taguchi's array (Table 5.8). The tool wear was evaluated by through microscopy observation of the cutting edges at the end of each Taguchi experiment condition.

Roughness Measurement

In addition to transverse and longitudinal *Ra* measurements, *Rz,t* and *Rz,l* were also measured posteriorly to the machining process as shown in Figure 5.18 according to ISO 4288 [ISO 4288:1996 Geometrical Product Specifications (GPS), 1997]. *Rz* value is obtained by measuring the vertical

distance from the highest to the lowest peak within five sampling lengths, averaging their distances, thus presenting another representative set of data for parameter evaluation. All of these measurements were taken in accordance with the first approach hardware and technique.

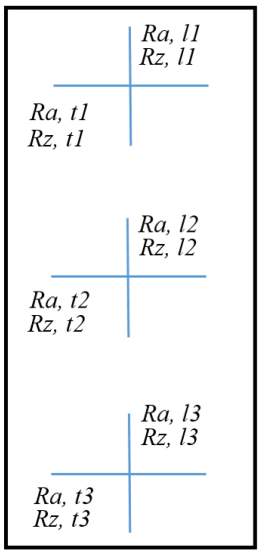


Figure 5.18: Measurement points for transversal and longitudinal *Ra* and *Rz*.

5.1.3.5 Results and Discussion - Approach 2

Figure 5.19 depicts the results in terms of *Ra,t*, *Ra,l*, *Rz,t*, *Rz,l* and cutting loads, obtained for the 9 Taguchi conditions (parameters combinations). It is important to refer that these are average values for each sample/condition of three machined faces. It is possible to observe some preliminary tendencies, even though the most definite results are only presented via main effect plots and ANOVA analysis.

Comparing *Ra,l* and *Ra,t* results, it is possible to observe the same trend. Apart from condition 9 (which contradicts the tendency), higher *Ra,l* values correspond to the higher *Ra,t* values for the same material. The results show lower PA12 roughness for the 1st, 4th, 6th, 7th, 8th and 9th (only in *Ra,t* with contrary behaviour in *Ra,l*) conditions. High standard deviation is also found in *Ra,t*, PA12, 5th and PA12, 8th condition. *Rz* values do not present similar tendency as the previous (*Ra*), showing also high level of deviation in some of the samples.

The most relevant result obtained from this preliminary data analysis is presented in cutting force graph of Figure 5.19e. Cutting forces for PA12 are much higher than in the reinforced material for all the conditions, doubling its value for some of the cases. Even though the unreinforced material shows higher deviation/result dispersion, the values are still superior than the forces obtained for PA12CF.

Considering the initial average values obtained for horizontal specimens, the improved results are shown for the conditions that correspond to the best final surface roughness. Since these samples were horizontally printed, longitudinal measurements ($Ra,l/Rz,l$) follow the deposition

lines, thus the worst and more significant results are presented in the transversal measurements. It is possible to identify in Table 5.9 that the improvement in surface roughness is 1931% for PA12CF and 2255% for PA12 in the transversal direction, while longitudinally, the increase is 479% and 318% for PA12CF and PA12, respectively. Since final Ra,l and Ra,t present similar results, it is possible to infer that the deposition orientation has no influence on the final surface roughness, agreeing with the data provided by the first approach that discards the building orientation as an influential factor on surface roughness.

Table 5.9: Improvement factor for machined specimens.

	PA12CF			
	Ra,t (μm)	Ra,l (μm)	Rz,t (μm)	Rz,l (μm)
Pre Machining	19.12±1.96	3.83±0.53	84.58±3.66	19.65±1.87
Machined (C5)	0.99±0.22	0.80±0.05	6.83±0.70	6.04±0.55
Improvement	1931%	479%	1238%	325%
	PA12			
	Ra,t (μm)	Ra,l (μm)	Rz,t (μm)	Rz,l (μm)
Pre Machining	21.65 ± 2.90	2.45 ± 6.19	84.05±6.07	8.70±0.96
Machined (C1)	0.96±0.14	0.77±0.10	6.75±0.40	4.88±0.88
Improvement	2255%	318%	1245%	178%

According to some findings available in research literature [Smith, 1989, Xiao and Zhang, 2002], it is claimed that the glass transition temperature (T_g) of a polymer is a crucial parameter concerning surface roughness. This implies that if the temperature of the machining area's surface is higher than the T_g, a good surface finish is likely to be obtained, since the material is removed in a ductile way. On the other hand, if the temperature is lower, a brittle material removal occurs and a rough surface is obtained. As presented in Table 5.1 both materials present T_g temperatures of approximately 50°C, that are possible to occur during the machining process, which was conducted without any kind of coolant (dry machining). Since, the reinforced material presents an higher thermal conductivity due to the fibres (Table 5.1), it could be easier to reach these temperatures than the unreinforced specimens.

ANOVA - second approach

Considering that five different responses were obtained for each material, ANOVA analysis was performed. The results are presented, considering that the factors showing no statistically significative influence were disregarded. In addition to ANOVA analysis, the main effect plots are presented, and since there are three response levels, Post-Hoc pairwise comparisons analysis (tukey HSD or fisher LSD) are needed to identify for each response type, the best parameter combination. Therefore, Tukey's test is used to complement ANOVA, in order to find means that are significantly different from each other, i.e. the most influential values of each parameter per response.

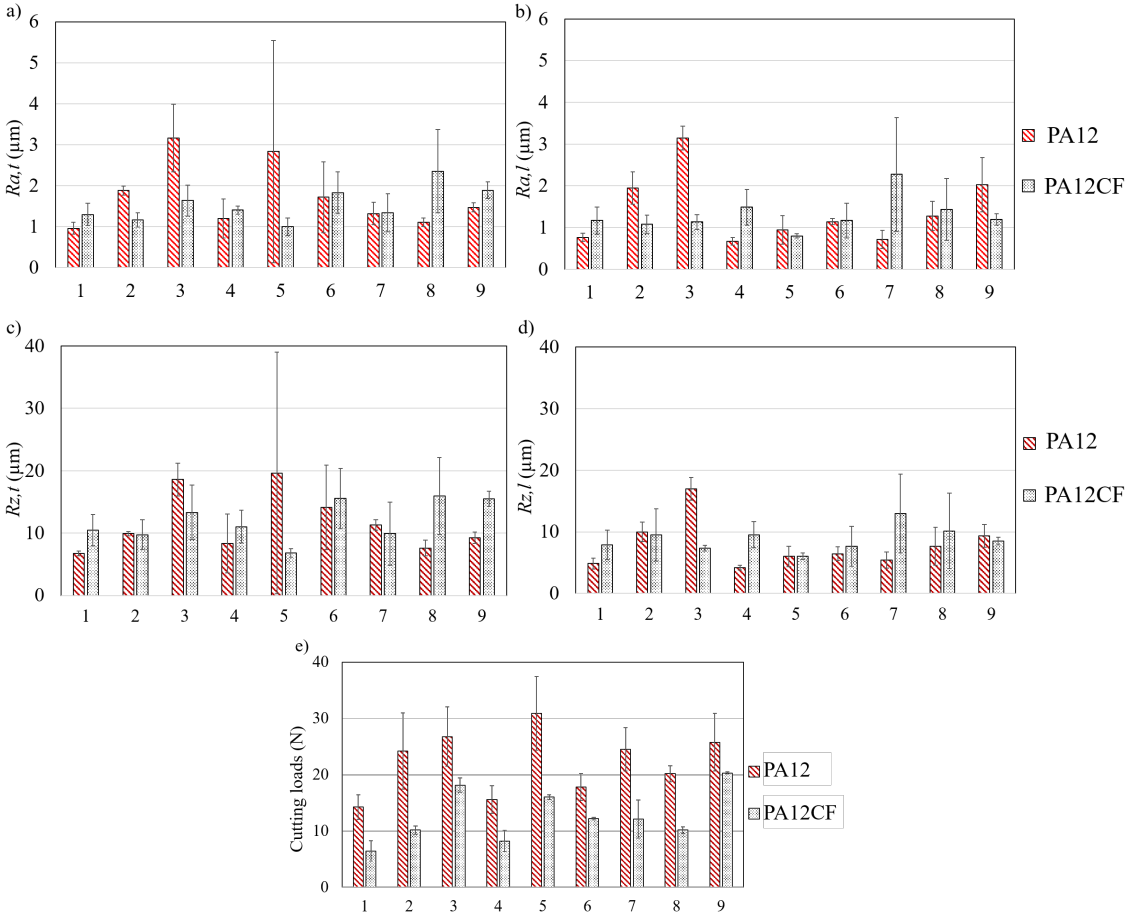


Figure 5.19: Taguchi matrix results: a) *Ra,t*, b) *Ra,l*, c) *Rz,t*, d) *Rz,l* and e) cutting forces.

The results show that for the reinforced material, no parameters presented acceptable p-values for *Ra,l, Rz,l, Ra,t* and *Rz,l* responses, being the cutting load the only result with statistically influential parameters. For PA12, similar results were found with non-influential responses in transversal roughness measurements, leaving longitudinal roughness response types and cutting loads to be analysed.

ANOVA analysis for *Ra,l* (Table 5.10) shows that all three considered inputs are statistically relevant, since an acceptable P-Value is presented. The most contributive set of parameters is the feed with 47.52%, followed by cutting speed (26.70%) and depth of cut (8.67%). As for *Rz,l* (Table 5.11), all three parameters are also considered influential, thus confirming the previous order with a slight change in the contribution percentages.

Figures 5.20 and 5.21 present the main effect plots for both *Ra,l* and *Rz,l*. *Ra,l* is composed by three relevant parameters. Based in Tukeys method, it is possible to say with 95% confidence that for cutting speeds of 200 and 300 m/min statistically similar means are presented, leading to conclude that between them, there is no relevant change in the response, being 100 m/min cutting speed the one that differences from the previous ones. Thus, to obtain better surface roughness (*Ra,l*), higher values of cutting speeds must be selected. Considering the same method

Table 5.10: PA12 *Ra,l* ANOVA (2nd experimental approach)

Source	DF	SS	Contribution	F-Value	P-Value
Cutting speed	2	4.871	26.70%	15.60	0.000
Feed	2	8.67	47.52%	27.76	0.000
Depth of cut	2	1.582	8.67%	5.07	0.017
Error	20	3.123	17.12%		
Total	26	18.246	100.00%		

for feed parameter, the three chosen values present significantly different means, indicating that 0.070 mm/tooth results in the worst finishing, and 0.010 mm/tooth in the best one, as confirmed by Figure 5.20. In the same way, the depth of cut of 0.6 mm is the only significantly different mean, resulting in the best values of roughness, while 0.8 and 1.0 mm have statistically identical means, resulting in similar roughness results. When considering *Rz,l*, the behaviour is similar to *Ra,l* except for the depth of cut, where there is an overlap in the terms, thus making it impossible to make an adequate conclusion using Tukey, Fisher or other pairwise comparisons.

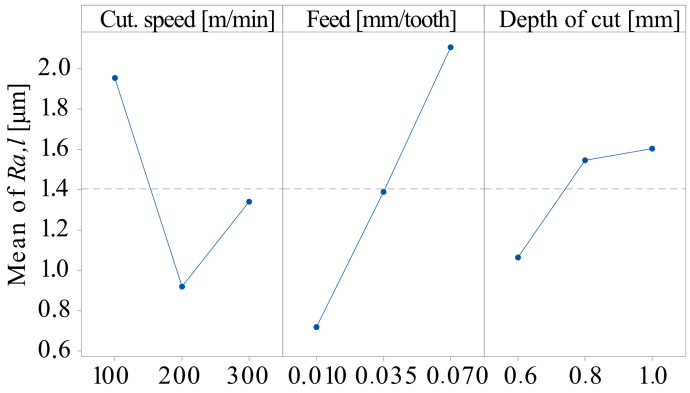


Figure 5.20: PA12 main effect plot for *Ra,l*.

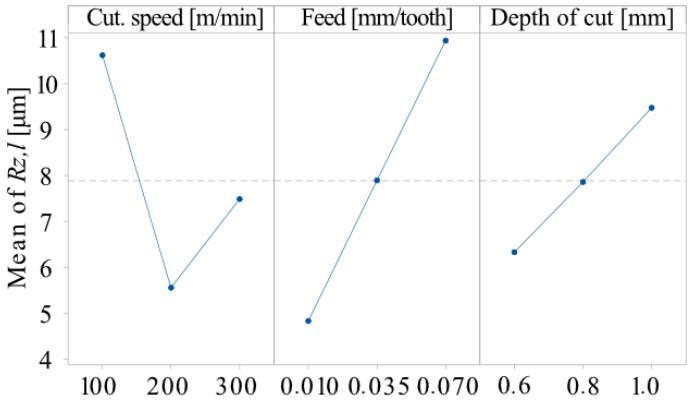


Figure 5.21: PA12 main effect plot for *Rz,l*.

Table 5.11: PA12 Rz,l ANOVA (2nd experimental approach)

Source	DF	SS	Contribution	F-Value	P-Value
Cutting speed	2	117.53	27.86%	12.75	0.000
Feed	2	167.63	39.74%	18.18	0.000
Depth of cut	2	44.44	10.54%	4.82	0.020
Error	20	92.2	21.86%		
Total	26	421.8	100.00%		

Cutting loads

PA12 cutting loads ANOVA analysis in Table 5.12 shows that the cutting speed was not statistically significant, since it was outside the confidence interval. Depth of cut presents 40.97% of the contribution in the final values, while feed is 21.82%. For PA12CF, as depicted in Table 5.13, all parameters are to be considered as equally influential. Depth of cut and feed defines the chip section, which leads to more or less proportional increase in the cutting loads.

Table 5.12: PA12 cutting loads ANOVA (2nd experimental approach)

Source	DF	SS	Contribution	F-Value	P-Value
Feed	2	239.63	21.82%	6.45	0.006
Depth of cut	2	450.07	40.97%	12.11	0.000
Error	22	408.77	37.21%		
Total	26	1098.47	100.00%		

Table 5.13: PA12CF cutting loads ANOVA (2nd experimental approach).

Source	DF	SS	Contribution	F-Value	P-Value
Cutting speed	2	33.66	6.08%	4.25	0.029
Feed	2	288.17	52.02%	36.39	0.000
Depth of cut	2	152.9	27.60%	19.31	0.000
Error	20	79.19	14.30%		
Total	26	553.93	100.00%		

Figures 5.22 and 5.23 present the main effect plots for cutting forces measured for both materials. Analysing PA12 first and basing these results on the Tukey's method it is possible to say with 95% confidence that higher feeds (0.070 and 0.035 mm/tooth) mean similar results, leading to conclude that there is no significant difference between them. As such, 0.010 mm/tooth is confirmed as the value that creates lower cutting forces as seen in Figure 5.22. The same methodology is used to understand the depth of cut results, indicating that 0.6 and 0.8 mm have similar means, leading both to identical lower cutting forces. On the other hand, the difference in means indicates that 1.0 mm cutting depth creates a significant increase in cutting forces, as presented in Figure 5.22. With regards to the reinforced material (PA12CF), the same overlap in the terms is encountered for the cutting speeds. As such, it is not possible to make adequate conclusions using Tukey's

pairwise comparison. However, through Fisher LSD, and using the same 95% confidence level, it is possible to infer that in this case 100 and 200 m/min have similar mean values, thus presenting no considerable difference in cutting force. 300 m/min presents a significantly different value, resulting in a considerable difference in results. This means that, in order to create lower cutting forces, 100 or 200 m/min should be used. Considering feed and cutting speed, Tukey's method was successfully applied, presenting significantly different means for all the cases, leading to conclude that every feed/depth of cut increment has effect, being exactly portrayed by the main effect plot in Figure 5.23.

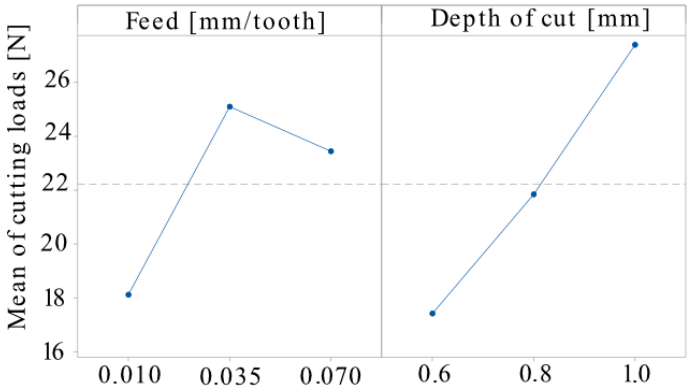


Figure 5.22: PA12 main effect plot for cutting forces.

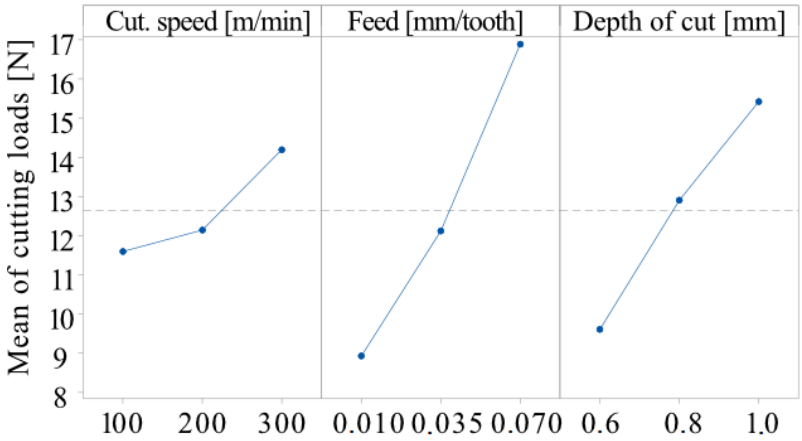


Figure 5.23: PA12CF main effect plot for cutting forces.

Tool wear analysis

Microscopic analysis was performed after the machining process for each Taguchi condition. Tables 5.14 and 5.15 show tool surfaces after conditions 3, 6 and 9, which correspond to the last usage of that tool for a specified cutting speed. Considering the parameters combinations, at the end of the 3rd condition (tool 1 - the tool has been subjected to the milling operation for 19 minutes and 32 seconds in 3 samples, 3 faces each). At the end of the sixth condition (second tool - the tool has milled during 9 minutes and 58 seconds), while for the third tool at the end of condition

9, the tool was used 6 minutes and 27 seconds. The presentation of only these final conditions was considered for the sake of conciseness. However, considering the results obtained, all of the conditions are discussed.

Regarding the unreinforced material, and following the same logic of the tables, microscopic observations show that, for the first condition, an abrasion is notorious in the cutting edge 1 and a small crater wear in edge 2. For condition number 2, the abrasion in cutting edge 1 is roughly the same. In the edge 2, beyond the crater wear, abrasion is now also visible along the edge for roughly 1 mm. The third condition shows an increase abrasion wear in both edges. At the end of the first condition of the second tool (condition number 4), chipping in cutting edges number 1 and 2 is notorious, a damage that was aggravated along the following two conditions, as presented in (C6) Table 5.14. The third tool showed some abrasion in cutting edge 1 and chipping in edge 2 after the 7th condition, which was not significantly increased by the following two conditions, as seen in condition 9 images.

Microscopical analysis of the tools used for the reinforced material depict a different behaviour with little to no damage (see images in Table 5.15). For the initial three conditions, the result is similar, presenting some abrasion wear in both cutting edges but no serious damage. The same result is found for the second tool, showing no signs of damage, even in the sixth condition. Condition number seven presents chipping in cutting edge 1 and 2, with the edge vertex missed. With test number 8, the damage seems to be accentuated for both edges, while also presenting an increased chipping area. Final condition shows an increase in the chipping area for edge 1 and a complete wear due to abrasiveness of the vertex in the second edge, as can be seen in Table 5.15.

By relating the tool wear analysis results with the cutting loads, it is possible to understand that the higher loads generated by machining increased the wear of the tool used in the unreinforced material.

5.1.3.6 Summary - Approach 2

This second approach allowed a deeper approximation to the machining parameter question. In addition, testing these parameters in a more precise and stable machine was a way of validating their application to different types of machines. As a consequence of the first approach, an higher number of responses was studied to better understand the material and tool behaviour. Taking into account the previous results, the following remarks were drawn:

Considering the five types of responses studied for each material, only cutting forces (for both materials) and the longitudinal roughness Ra,l and Rz,l for PA12 were statistically relevant, with at least one parameter contradicting the null hypotheses (P-value$<$95%). For PA12CF, Ra,l and Ra,t present an average value of 1.30$\pm$0.41 μm, in the 9 tests and 1.54$\pm$0.42 μm respectively, while PA12 presents 1.40$\pm$0.82 μm and 1.74$\pm$0.77 μm. It is possible to confirm that PA12CF presents a lower average, but also a lower standard deviation. This lower deviation, can relate to the fact that the parameter combinations present lower influence on the PA12CF, thus the lack of statistically contributive results, and consequently easier machining.

Table 5.14: Wear analysis for PA12 tools (40x magnification), 2nd testing approach.

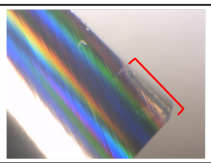
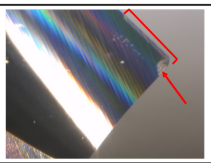
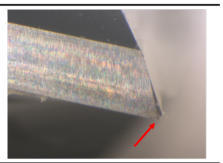
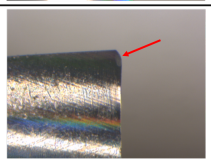
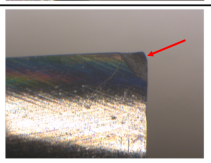
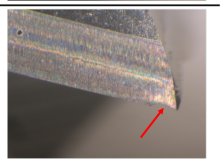
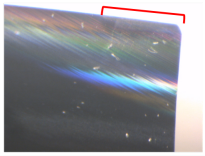
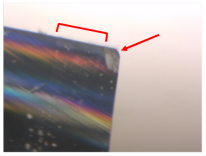
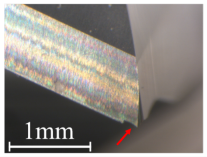
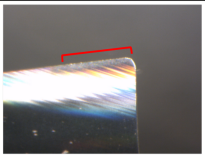
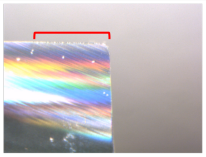
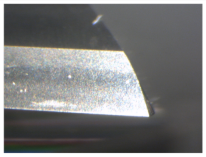
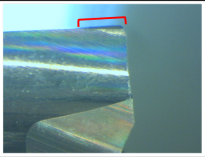
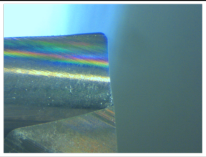
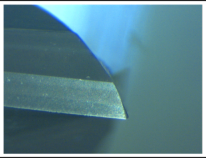
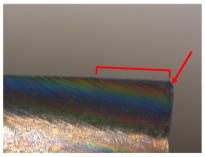
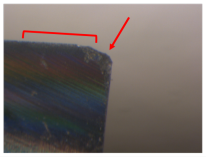
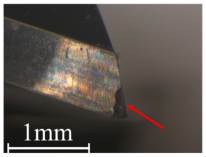
Condition	Cutting edge 1	Cutting edge 2	Lateral view
3			
6			
9			

Table 5.15: Wear analysis for PA12CF tools (40x magnification), 2nd testing approach.

Condition	Cutting edge 1	Cutting edge 2	Lateral view
3			
6			
9			

Through the ANOVA performed for PA12's Ra,l and Rz,l, it was possible to conclude that there is an agreement in the contributions, being the most significant parameter the feed, with 47.52% and 39.74%, respectively, followed by the cutting speed (26.70% and 27.86%) and the depth of cut (8.67% and 10.54%).

Considering Ra,l and Ra,t similar results (Table 5.9), it is possible to confirm that printing orientation is not an influential.

Considering the tool machining time, it is noticeable that for tool number 1 it is used more than double the time of tool number 2, and the triple of number 3, although it is not notorious a significant damage among the tools for PA12. On the contrary, PA12-tool 3 presents high abrasion wear levels and chipping that are not found in the first tool. This leads to the conclusion that there is no direct relationship between the machining time and tool wear for these specific approaches.

The analysis of the cutting loads showed that PA12CF values were much lower than for PA12, which reinforces the previous statement that PA12CF is easier to machine. In addition, microscope observations shows much faster/higher levels of tool wear in the ones used to machine the unreinforced samples. Table 5.16 presents a synthesis of the optimal parameters advised to machine this type of part with this specific setup.

Table 5.16: Optimized processing window for PA12 and PA12CF machining targeting improved finishing - approach 2.

Parameters	PA12CF		PA12	
	Cutting Force	Ra,l	Rz,l	Cutting Force
Cutting speed [m/min]	100/200	200/300	200/300	Non Significant
Feed [mm/tooth]	0.010	0.010	0.010	0.010
Depth of cut [mm]	0.6	0.6	-	0.6/0.8

5.1.4 Conclusions

This work intended to understand how PA12 based material printed parts behave in machining operations and what are the main influential factors, by defining a parameter operation window for surface analysis. Two subsequent experimental approaches were performed, showing different, but prominent results creating as such a progress towards hybrid manufacturing. While this first machining process was performed in less stiff/precise machine-tool, the second approach had its focus in exploring the best set of conditions in a more stiff precise machine. The results show that the purposed parameters combination for the first machine tool behave differently in the second hardware. As a consequence, results in tables 5.7 and 5.16 are different.

First approach ANOVA analysis proved that the building orientation influence was not relevant for the final surface roughness. Even though being a discarded parameter for the second test, this could be proved once again, since final Ra,l and Ra,t are similar for both materials in a longitudinal sample (0.80 ± 0.05 vs 0.99 ± 0.22 for PA12CF and 0.96 ± 0.14 vs 0.77 ± 0.10 for PA12).

In the first approach, the feed variable had contributions of 2.79% (Ra,t) and 10.68% (Ra,l), while with interactions the influence was over 30% for both cases. For the second approach, only PA12 presented significant values for surface roughness, yet, it is possible to observe that in this case the feed presented a 47.52% contribution. Thus, it can be concluded that feed rate is influential on surface roughness. As far as depth of cut, in the first approach it was not considered as a statistically relevant parameter. However, through the second approach, it is possible to perceive that this value influences on the PA12 material's final roughness. In addition, the PA12 and PA12CF cutting depth presented a contribution of 40.97% and 27.60% for the respective cutting forces generated, which is a surprising result since carbon fibres despite producing material reinforcement, their effects on machinability is not negative. It is also shown that for the same cutting depth, higher forces are exhibited by the unreinforced material, which justifies the higher levels

of damage found in the tools used in this material. Since tool wear (abrasion and chipping) was found in both approaches, the initial idea that the damage was created due to the hardware's lack of stiffness is discarded.

The second approach also implied that the best combination of parameters was different for both materials, yet reaching similar final material roughness. Since none of the inputs revealed to be statistically contributive for PA12CF, it is possible to affirm that the variation of parameters is less influential on the final result. This might occur due to higher machining temperatures created by the presence of fibres. The difference in parameter results considering both approaches is attributed to the machining hardware, leading to conclude, that the suggested parameters will vary with the type of hardware used.

In conclusion, it was proven that FFF PA12 and PA12CF printed parts can be machined to improve their final surface finishing, resulting in a roughness (Ra, t) decrease of 2255% and 1931% respectively.

Finally, this type of testing is essential for the development of a hybrid process, leading to conclude from both approaches to the problem that machining hardware is as crucial as the material to be machined.

5.2 Study of the annealing influence on the mechanical performance of PA12 and PA12 fibre reinforced FFF printed samples

The work described in the forthcoming section is presented in original article format, as submitted to the Rapid Prototyping Journal, being currently approved for publication.

Mechanical performance of Fused Filament Fabrication (FFF) parts vary with the type of feedstock, printing parameters, extrusion and platform temperatures. In this context, a study of the annealing treatment influence on the mechanical properties of parts produced with this process was carried out. For this, two different types of Nylon®(PA 12) were used, FX256 and CF15, being the second a short fibre reinforcement version of the first one. In this study, tensile and flexural properties of specimens produced via FFF were determined after being annealed at temperatures of 135, 150 or 165°C during 3, 6, 12 or 18 hours and compared with the non treated conditions. In addition, a thermal analysis was performed by Differential scanning calorimetry (DSC) to determine the degree of crystallinity of some of the annealed samples. In order to evaluate the annealing parameters influence on the mechanical properties, a full factorial design of experiments (DOE) was developed, followed by an analysis of variance (ANOVA), as well as Post-Hoc comparisons, to determine the most significative intervening factors and their effect on the results. The results indicate that CF15 material increased its modulus of elasticity, tensile strength, flexural modulus and flexural strength around 11%, while FX256 presented similar values for tensile properties, doubling for flexural results. It was also shown a decrease in tensile strain and flexural strain.

Overall, the annealing treatment causes a significant improvement in the mechanical performance of the material, with the exception of 165°C annealed samples, in which a decrease of the mechanical properties was observed, resultant of material degradation. The highest improvement was found in flexural strain, indicating an improved interlayer behaviour. Concerning the DSC and comparing the annealed and non-annealed samples, it was observed an increase in the degree of crystallinity. However, when comparing the annealed samples, it is verified that the change in the annealing temperature has a small influence on the degree of crystallinity.

5.2.1 Introduction

In an era of progress and innovation, the incessant demand for continuous improvement of the current technologies, as well as the introduction of new ones is a reality. Additive manufacturing (AM) is already well established as a production method, nonetheless the evolution and demand for better parts is continuously pushing the barrier on these processes and material properties [Wohlers, 2018]. According to ISO/ASTM 52900:2015 [ISO/ASTM, 2015] there are seven AM groups based on the different types of processing and materials, which comprise polymers, composites [Fonseca et al., 2019, Liu et al., 2019], metals [Gibson et al., 2018], ceramics [Chen et al., 2019], and glass [Dong et al., 2019]. Thus, with such an expressive growth of these technologies, it becomes important to analyse the possible post-processing techniques to improve the mechanical performance of the components produced by additive manufacturing. The FFF process is one

of the most widely used additive manufacturing techniques since it allows to produce highly flexible/customisable parts with complex geometries in a reduced period of time, at low cost, when compared to other polymer based AM techniques. FFF can process a wide range of materials, from the common use Polylactic acid (PLA) to engineering polymers as Polyamides (PA), high performance polymers such as Polyether ether ketone (PEEK) and composites, granting a full spectrum of mechanical properties. As the level of complexity of the material increase, also processing temperatures and consequently the difficulty of the process. The successive heating and cooling cycles inherent to the process, creates thermal residual stresses, leading to inadequate aesthetics and mechanical performance. Thus post processing thermal treatment of annealing is recommended in order to solve this type of problems. Annealing is a type of thermal treatment used to improve mechanical performance, thermal conductivity and stability in materials. For polymers, annealing induces a micro structural recrystallization and reorganization of the amorphous phase in the material via temperature increase during a certain period of time above its glass transition point (T_g) [Bai et al., 2011, Gogolewski et al., 1980, Fischer, 1972].

To the best of the author's knowledge, few studies have been conducted regarding thermal treatment influence on the mechanical performance of FFF printed parts [Dong et al., 2019, Rangisetty and Peel, 2017, Hart et al., 2018]. Dong et al. [2019] analysed the influence of the annealing process on the flexural behaviour of polylactic acid (PLA) and PLA grafted cellulose nanofibres. Both type of samples were thermally annealed above the glass transition temperature for a total of 6 temperature combinations. These samples were then submitted to flexural testing showing that the unannealed specimens were partly damaged, while the thermally treated samples preserved their structure enhancing the mechanical properties. Rangisetty and Peel [2017] studied the influence of the annealing process on tensile and flexural samples, considering different infill patterns. Samples were printed with commodity polymers such as PLA, Acrylonitrile Butadiene Styrene (ABS) and Polyethylene Terephthalate Glycol (PETG), along reinforced versions, even though provided by different feedstock producers. The samples were annealed 5°C above the glass transition temperature during one hour. The results present an increase in tensile strength for PLA and PET, sorting no effect on ABS. Young's modulus was also higher for PLA annealed samples (only unreinforced samples), while ABS presented a decrease in performance. Both PETG based materials presented an increase in modulus. Flexural strength increases significantly for PLA and PETG, while flexural modulus shows an improvement for pure PLA, reinforced ABS and considerable decrease in both PETG materials. As a result of the distinct materials, from different manufacturers, even considering the same type of polymer, may be the reason for the discrepancy in the results. Hart et al. [2018] studied the improvement of the interlayer fracture toughness of samples printed in ABS when annealed. Single edge notch bend fracture specimens were produced and submitted to several temperature/time conditions, however inserted in a specially developed aluminium fixture, which compresses the samples during treatment. Results show an increase in fracture toughness of 2500%.

In this work, the annealing of the same commercial unfilled PA 12 and short fibre reinforced FFF printed parts is studied via full factorial design of experiences (DOE) along with ANOVA

statistical analysis in order to analyse the influence of temperature and annealing time on tensile and flexural performance, along with thermal properties. The aim is to understand the fibre influence on the part properties when submitted to the temperature cycle and compare it with the pure matrix material.

This work is structured as follows: an introductory section that sums up the state of the art of the annealing treatment in FFF printed parts, afterwards, the experimental procedure is described in detail by addressing the materials, production method, annealing DOE and statistical analysis. Following, the results are analysed and lastly conclusions are drawn.

5.2.2 Experimental Procedure

5.2.2.1 Materials

Two versions of a commercial Polyamide 12 (PA 12) of ⌀1.75 mm feedstock were bought from Fillamentum©, Parzlich s.r.o (Czech Republic) and used as a basis of this study. CF15 is reinforced with short carbon fibres (100 μm in length and 10 μm in diameter) with a content of 15 wt.%. FX256 is the unreinforced version of CF15. Some of the datasheet material specifications are presented in Table 5.17, in which some unexpected values are presented, such as higher tensile modulus for the unreinforced material.

Table 5.17: Datasheet material specifications [Fillamentum, 2019b,a].

Property	CF15	FX256
Material density (g/cm^3)	1.08	1.01
Melt flow index ($g/10min$)	14.64	16.56
Thermal conductivity (10^{-3} W/m.k)	144.22	124.82
Tensile strength (MPa)	54.50	45.00
Tensile elastic modulus (MPa)	500	1400
Melting temperature (°C)	160	178
Print temperature (°C)	235-260	235-260

5.2.2.2 Material conditioning

PA based materials are highly hygroscopic and, hence, controlling the moisture content is demanded since it affects the mechanical performance of 3D printed parts, as has already been demonstrated by several scientific studies [Carrascal et al., 2005, Rajeesh et al., 2010, Do et al., 2015]. Thus, in both stages of printing and testing, the same material conditioning is required in order to non compromise the mechanical properties. Extruding a non dried out material through a nozzle will cause irregularities in the part surface, originated by vaporization of the moisture content. The materials were provided hermetically sealed with silica gel, however after each printing day, both materials were dried in a PrintDry^{TM} (Canada) filament drier at 70°C for 8 hours. After being printed, each set of samples was placed in a sealed bag with silica gel.

5.2.2.3 Preparation of the printed samples

Due to the large amount of samples needed for this study, two printing devices were used. FX256 sample production was performed in a Tronxy X5 3D printer from Shenzen Tronxy Technology Co. Ltd equipped with a brass nozzle. The reinforced samples, were printed in a Ratrig V-Core from Ratrig (Portugal) equipped with a hardened A2 steel, which is demanded due to the abrasiveness of the fibres. Both machines used the same extruder configuration, the same heated bed surface and the same slicing configuration designed in Simplify3D®4.1.1. Table 5.18 lists the parameters used in the production of the samples. Since printing 100% dense parts leads to high warping levels, extra (disposable) skirt outlines and glue were added to improve bed adhesion. The choice of the remaining parameters was based on preliminary tests, which revealed ideal for this type of samples, leading to improved printability, warping minimization and a better visual appearance [Fonseca et al., 2019].

Table 5.18: Selected printing parameters.

Parameter	Detail
Nozzle diameter	0.4 mm
Nozzle material	brass/A2 steel
Layer height	0.3 mm
Number of perimeters per layer	2
Infill percentage	100%
Infill pattern	Rectilinear ± 45 °
Skirt outlines	7
Extrusion temperature	260 °C
Bed temperature	90 °C
Bed surface	Tempered glass + CUBE®glue
Printing speeds	40 mm/s
Extrusion multiplier	1.04

5.2.2.4 Mechanical testing

Tensile samples were printed according to ISO 527-2 1A [International Organization for Standardization, 2012a], with the parameters mentioned in Table 5.18 in an INSTRON® 5900R (Illinois Tool Works Inc. USA) at 1 mm/min speed and a 5 kN load cell. Flexural samples were produced with same methodology and tested according to ISO 178 [International Standards Organization, 2010], in a TIRAtest 2705, Tira GmbH (Germany).

5.2.2.5 DSC analysis and Annealing conditions

DSC test

DSC (200 F3, Netzsch GmbH, Germany) was conducted at a heating rate of 10 °C/min under nitrogen purge. The samples were obtained from 10x10x4 [mm^3] printed parts with weights in the range of 10–20 mg. The temperatures varied from 30 °C to 220 °C, being performed two heating cycles along with the cooling scanning. For analysis purposes, the first heating cycle was not represented as it was performed to eliminate any possible effects of thermal history. A sample of each material was tested to define the temperature interval at which the annealing process should be done. Posteriorly to the annealing process, a treated sample of each temperature was also submitted to DSC testing in order to identify potential changes in the material thermal behaviour.

Annealing

The thermal treatment was performed in a POL-EKO Aparatura® SLW32 (Wodzislaw Slaski, Poland) drying oven, with a heating rate of 7 °C/min and a cooling rate of 1 °C/min. Annealing temperatures were defined considering the DSC results (performed previously to untreated samples) in order to avoid critical transition points. As demonstrated in Table 5.19, identical melting temperatures (T_m) are found in both polymers, while small differences are found for the other transition points, therefore the same temperatures were used. A 10 to 15 °C gap bellow (T_m) was considered and three stages of temperature were selected as the test values (165, 150 and 135°C) with a 15 °C interval, going bellow the crystallization temperature (T_c). The annealing time was 3, 6, 12 and 18h as presented in the experimental plan of Figure 5.24.

Table 5.19: FX256 and CF15 DSC results for the control samples.

Material	T_g [°C]	T_c [°C]	T_m [°C]	ΔH_f [J/g]	X[%]
FX256	44,7	143,2	176,3	35,5	16,9
CF15	52,9	150,4	178,5	14,9	6.10

In order to calculate the crystallinity percentage (X[%]), the following equation was used [V. and Canevarolo, 2002]:

$$X[\%] = \frac{\Delta H_f}{\Delta H_f^*} \tag{5.1}$$

Where ΔH_f is the material fusion enthalpy and ΔH^*_f is the fusion enthalpy of the 100% crystalline, values which can be found in literature [Blaine, 2002].

5.2.2.6 Design of Experiments and ANOVA

In order to better understand the results, a two factor (annealing temperature and time) full factorial DOE was developed where all the possible combinations were tested per material. For each condition, a sample for thermal analysis test, five flexural, five tensile samples per material were

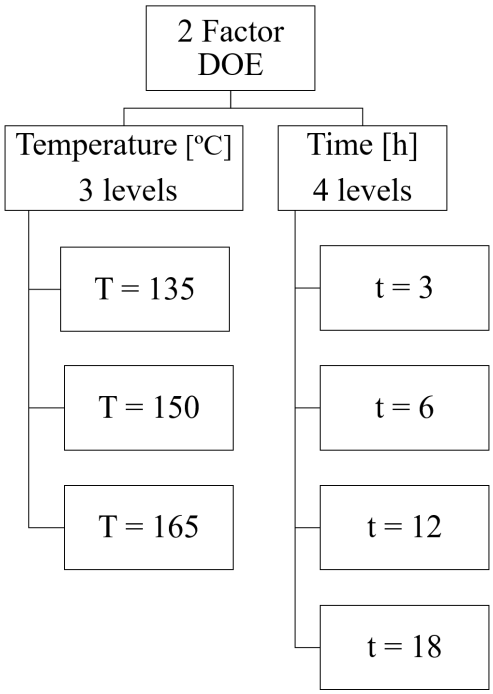


Figure 5.24: Experimental plan.

printed (beyond the non treated samples), then subjected to thermal treatment and consequent testing. Temperature, considered as the first factor, was tested for the three different levels, while the second factor (time) for four distinct time intervals were studied. The experimental data obtained from the mechanical tests was investigated via Analysis of Variance (ANOVA), in order to identify the truly contributive parameters considering a confidence interval of 95%. In addition to ANOVA, the main effect plots and interaction plots are presented, and since there are three and four response levels, Post-Hoc Fisher Least Significant Difference (LSD) pairwise comparisons (with a 95% confidence interval) were performed to the groups that presented p-value<.05 (except interactions), in order to identify the best parameter combination for each response group. An alternative to Fisher LSD was Tukey HSD Post-Hoc comparison method, which is a more rigorous method, however much harder to find the difference among results, and since a high number of tests was performed, the first method was preferred. This statistical analysis was performed with Minitab® 18. Table 5.20 depicts the full factorial DOE used for this test.

5.2.3 Results

5.2.3.1 DSC Results

DSC analysis was performed in both polyamide materials for the three test temperatures, being chosen the 6h time interval. Comparing the results for the control samples presented in Table 5.19 with the Table 5.21, it is possible to observe an unexpected decrease in T_g of almost 10°C for both types of material, which might be justified by some degradation. T_c and T_m showed an increase, which is not considered significant. The increase in ΔH_f[J/g] is directly related with the

Table 5.20: Full factorial DOE and condition 0.

Condition	Temperature -T [°C]	Time - t [h]
0	Control - Non treated samples	
1	135	3
2	135	6
3	135	12
4	135	18
5	150	3
6	150	6
7	150	12
8	150	18
9	165	3
10	165	6
11	165	12
12	165	18

X[%] values, as shown by Equation 5.1. Table's 5.21 last column presents the increase in crystallinity percentage facing the control samples, in which FX256 is approximately of 100%, while the reinforced material presents a increase above 400%. It is also shown that, as the annealing temperature increases, this percentage also grows, which can be explained by a longer cooling period, which allowed for the a better molecule organization. For the range of studied temperatures, non significant differences are reported.

Table 5.21: DSC results for annealed samples t=6h.

Condition	T_g[°C]	T_c[°C]	T_m[°C]	ΔH_f[J/g]	X[%]	↑[%] X[%]
			FX256			
T=135°C	36.77	146.98	180.71	85.19	34.77	105.74
T=150°C	37.66	146.79	181.07	86.51	35.31	108.94
T=165°C	37.96	148.49	180.24	94.67	38.64	128.64
			CF15			
T=135°C	36.84	154.68	180.40	80.25	32.76	437.05
T=150°C	39.81	154.62	180.47	81.55	33.29	445.74
T=165°C	41.76	155.36	179.97	81.66	33.33	446.39

5.2.4 Visual Analysis

Colour alteration can be seen as a sign of property change of specimens, evidencing chemical ageing, as seen in previous works [Sang et al., 2017]. This analysis was not performed in the reinforced samples due to the lack of transformation in its dark texture. Figures 5.25 and 5.26 depict a

tensile and flexural specimens per annealing condition. Specimen C0 indicates the original colour of the non treated samples. Considering the temperatures and time interval at which the specimens were exposed (see Table 5.20), at the lowest (C1-C4) and intermediate (C5-C8) temperature conditions, the colour of the samples evolved from white to light yellow and white to dark yellow, respectively, after increasing the exposure time. Furthermore, when using the highest temperature conditions (C9 to C12), yellowness becomes much more pronounced, going from light yellow to a dark brown. This change in colour is related to the oxidation of the PA resin [Sang et al., 2017, Fan et al., 2016]. Through the sample fracture, it is possible to observe that this change in colour is not only on the outside, but throughout its core. The tensile control sample C0 presented necking in the fracture area and a clear white colouration. From C1 until C6 overall elongation of the neck area is observed and an irregular fracture due to its $\pm 45°$pattern. From C7 onwards, it is possible to observe a slight elongation accompanied by fragile fracture perpendicular to the loading direction.

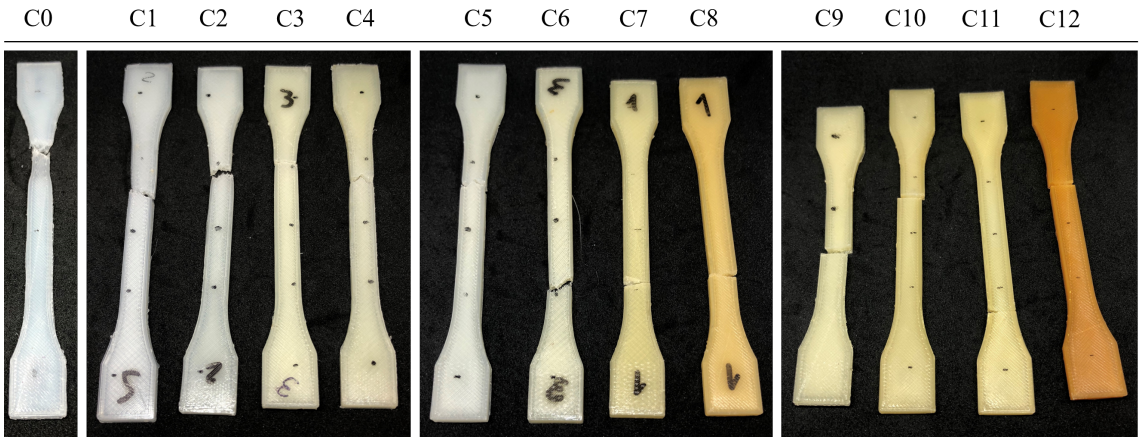


Figure 5.25: Tensile FX256 samples after test for each annealing condition.

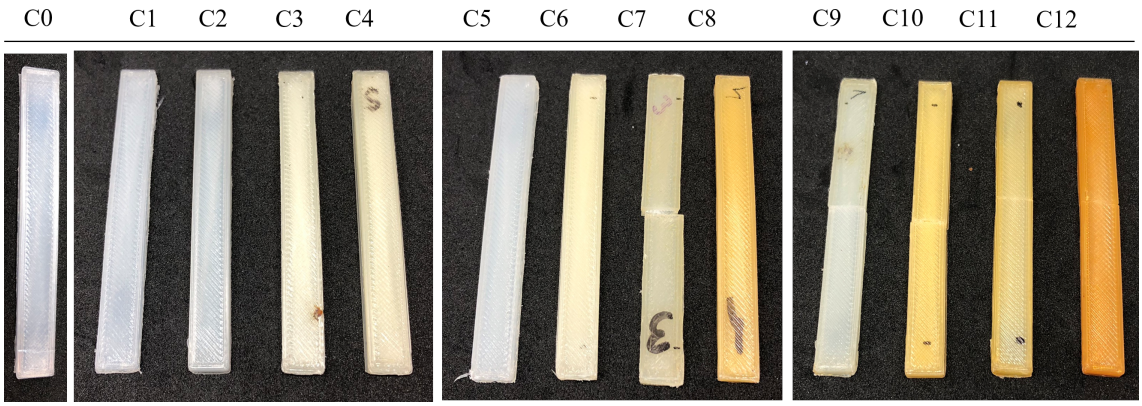


Figure 5.26: Flexural FX256 samples after test for each annealing condition.

5.2.4.1 Mechanical properties

Figures 5.27 and 5.28 represent the tensile and flexural results, respectively. Figure 5.27a depicts the Young's modulus results, in which it is possible to confirm that the reinforced parts present higher values than the unreinforced FX256. The CF15 control sample indicates 886 MPa, while the treated samples range from 780 to 980 MPa. FX256 results indicate a 450 MPa for the control and a range from 355 to 560 MPa. As for tensile strength (Figure 5.27b), the decrease is observed for higher temperatures for both materials, going from 45 to 30 MPa for the reinforced and 33 to 9 for the unreinforced. Considering the strain at break, FX256, as expected, presents much higher values, until T=150°C/t=12h, changing from 51 to 5% mainly due to material degradation as seen previously in literature [Abhari et al., 2017]. The reinforced material shows a constant decrease along the test conditions, varying from 25 to 4%.

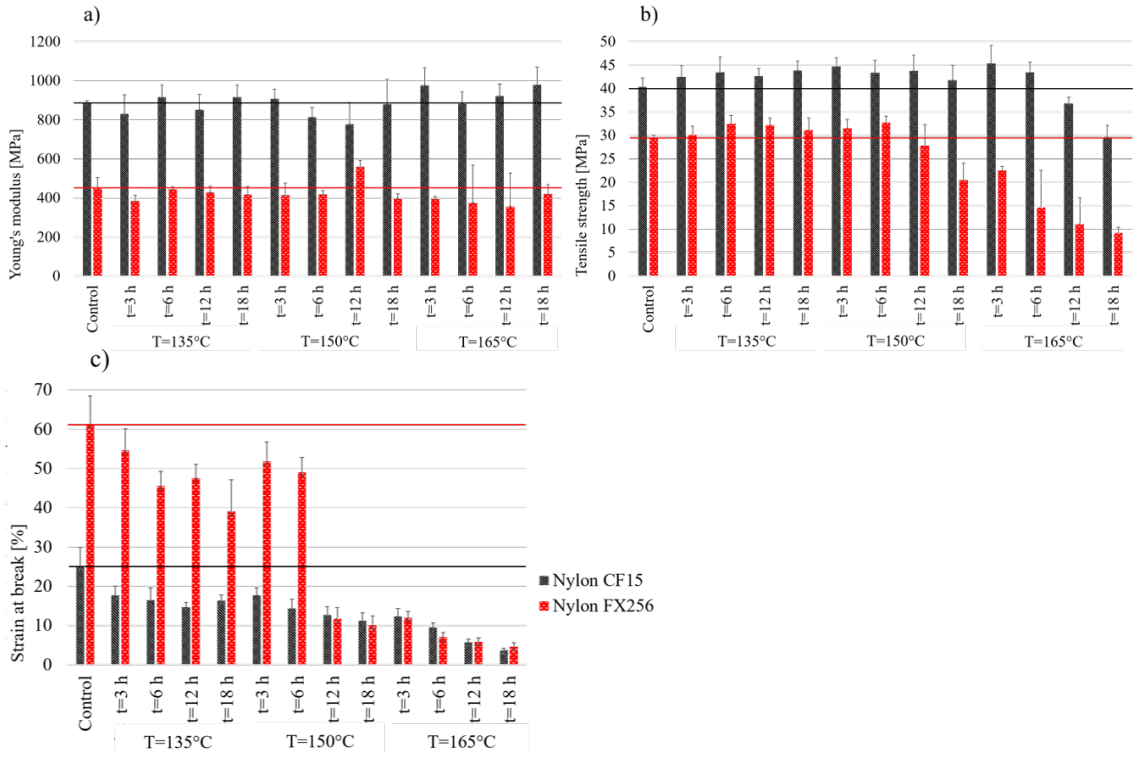


Figure 5.27: Tensile results comparison: a) Young's modulus, b) tensile strength and c) strain at break.

Flexural modulus (Figure 5.28a) shows that CF15 presents better results, ranging from 1500 to 2000 MPa, while FX256 presents values from 950 to 1400 MPa. In addition, it is notorious an increase in properties when facing the control sample for both materials. Considering flexural strength (Figure 5.28b), CF15 values are in the interval of 35 to 64 MPa, while for FX256 is 20 to 55 MPa. It was found that higher temperatures tend to result in lower values of strength for both materials. Flexural strain (Figure 5.28c) results show once again that higher temperatures are worst for the mechanical performance, being more susceptible the unreinforced material, ranging from 1.5 to 16% while CF15 varied from 2.4 to 15%.

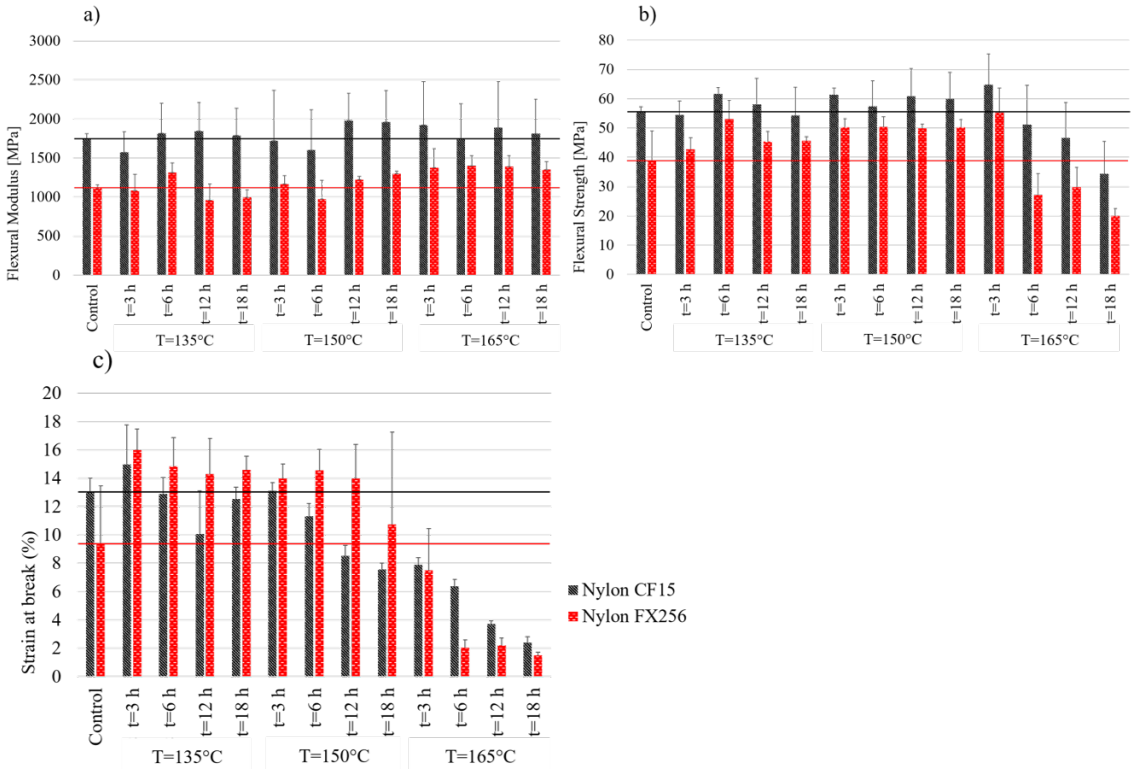


Figure 5.28: Flexural results comparison: a) flexural modulus, b) flexural strength and c) flexural strain.

5.2.4.2 ANOVA Results

In order to better interpret the results, with the purpose of finding the maximizing condition while considering the type of property needed, an ANOVA analysis was performed for each result obtained via tensile and flexural result (Modulus, strength and strain at break) for each material. To simplify the data presentation, ANOVA results are depicted in APA style (F(degrees of freedom, remaining degrees)=F value, p=value).

CF15 - Tensile

Through ANOVA analysis considering Young's modulus as a response, it is shown that only the temperature is statistically influential, with a contribution of 18.25% [F(2,48)=6.70, p=.003]. Post-Hoc Fisher LSD method with a confidence level of 95% indicates that all T=135/150°C have identical mean values, thus no significative difference between them. Through the main effect plot depicted in Figure 5.29, it is possible to verify that 165°C is the value that increases the most the modulus for this material.

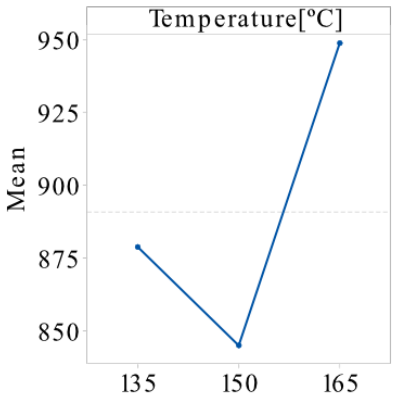


Figure 5.29: CF15 - Young's modulus main effects plot.

For tensile strength, ANOVA shows that the T [F(2,48)=13.95, p<.001] had a contribution of 16.42%, while t [F(3,48)=12.07, p<.001] 21.31% and the interaction T-t [F(6,48)=9.64, p<.001] a contribution of 34.03%, thus being the three most influential groups. Post-Hoc Fisher LSD comparison shows that temperatures of 150/135 °C have similar mean values and no significant difference between them, differentiating from 165 °C. For t=3 and 6h, means are also statistically similar, whereas for 12 and 18h present distinct mean results. This leads to conclude, according to the main effects plot of Figure 5.30, that higher strengths are obtained for the 135-150 °C at 3-6h intervals. The interaction plot shows that throughout the selected time intervals, T=135/150°C, strength decreases slightly, while for T=165°C, there is a significant decrease after 6h.

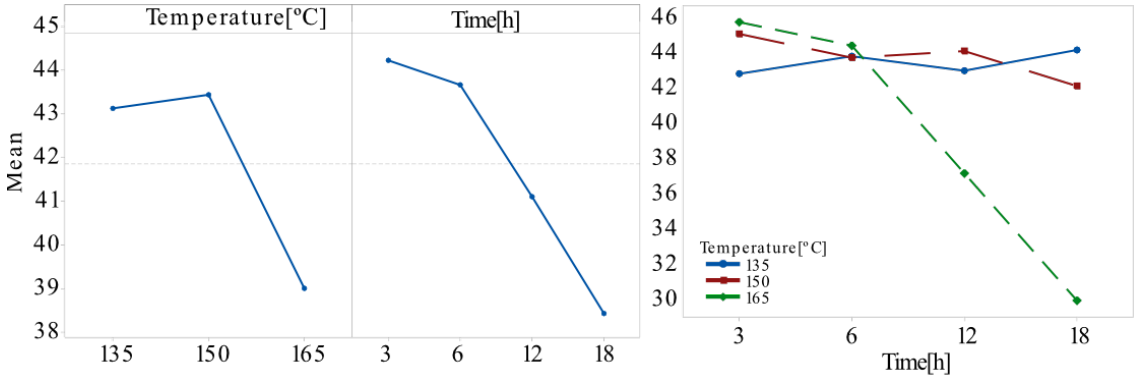


Figure 5.30: CF15 - Tensile strength main effects and interactions plots.

The ANOVA strain at break results show that, T [F(2,48)=94.93, p<.001] presented a contribution of 56.77% and t [F(3,48)=21.05, p<.001] a contribution of 21.11%, while T-t interaction [F(6,48)=13.51, p=.014] presented a contribution of 6.08%. Fisher LSD comparison shows that the three temperatures present significative different means, while for t=12 and 18h identical means are presented, and consequently no significative difference between the two occurs. Considering Figure 5.31 and the results obtained by the comparison method, it is possible to conclude that, the strain is maximized at T=135°C, t=3h. Interaction plot also shows that the general trend is

the decrease in strain at break for higher treatment durations, being the worst results obtained for T=165°C.

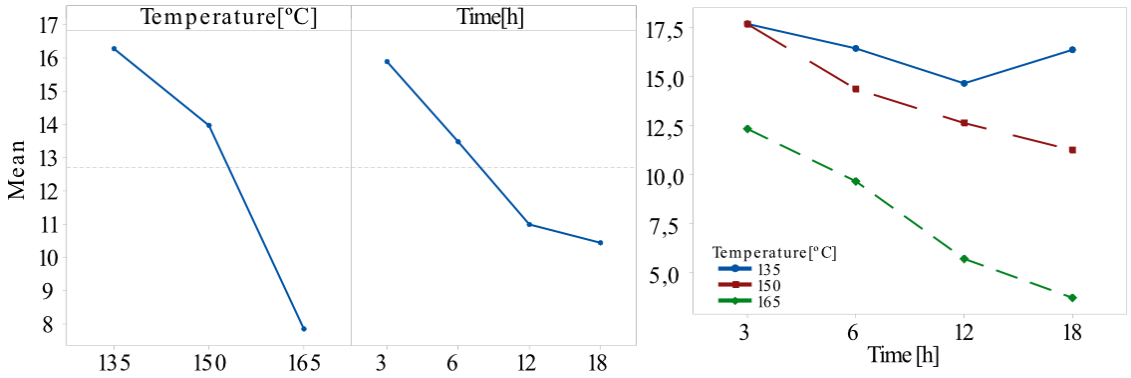


Figure 5.31: CF15 - Strain at break main effects and interactions plots.

CF15 - Flexural

ANOVA analysis to flexural modulus indicates that none of the variables are statistically influential since t, T and t-T p>0.05, not being possible to reject the null hypotheses.

In what concerns flexural strength, ANOVA analysis show that T [F(2,48)=5.79, p=.006] contributes 13.76%, t [F(3,48)=2.82, p=.049] with a contribution of 10.05%, while t-T interaction [F(6,48)=2.69, p=.025] contributes 19.16%. Through Fisher LSD Post-Hoc comparison it is possible to understand that for T=150 and 135°C have identical statistical means resulting in no significant difference between the two. Using the same comparison for the time group, it is possible to verify that 3/6/12h have similar statistical means, while 6/12/18h are also in other similar group, meaning that 3 and 18h are the only terms that do not present identical means, being statistically different. Main effect plots (Figure 5.32) demonstrate that higher flexural strain is obtained for T=135/150°C, while for t=3 is the best time interval for improved properties. Through the interactions plot, it is possible to observe that T=165 shows a decrease in behaviour as the annealing time increases, while the other two temperatures oscillate with higher treatment time.

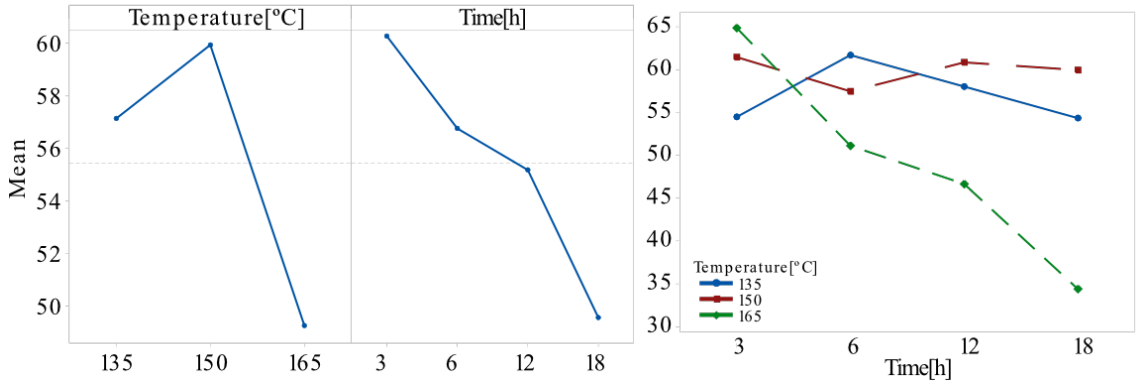


Figure 5.32: CF15 - Flexural strength main effects and interactions plots.

ANOVA flexural strain analysis indicates that T [F(2,48)=115.03, p<.001] contributes 62.08%, while t [F(3,48)=28.84, p<.001] contributes of 23.35%. As far as the interaction is concerned it was not considered statistically relevant since its p value was outside the confidence level of 95%. Given the Fisher LSD Post-Hoc comparison, it is possible to conclude that the three temperatures present distinct mean values, thus being all three statistically significant. As far as annealing time, only 18 and 12h present identical means, therefore no significative difference between both is found. Figure 5.33 shows that the higher flexural strain is found for the combination 135°C/3h.

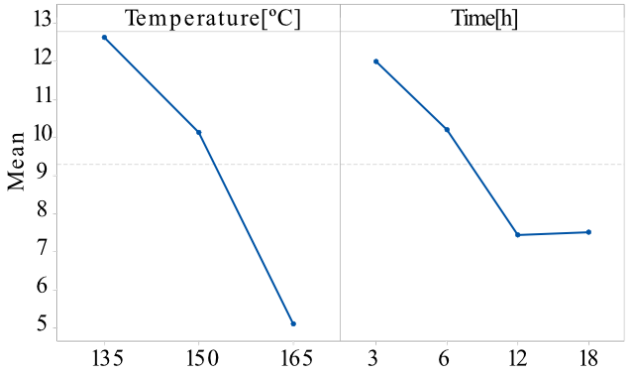


Figure 5.33: CF15 - Flexural strain main effects plots.

FX256 - Tensile

Through the ANOVA analysis to Young's modulus, it was shown that none of the variables are statistically influential since t, T and T-t p>0.05, not being possible to reject the null hypotheses at a confidence interval of 95%.

With regard to tensile strength, ANOVA shows that T [F(2,48)=106.57, p<.001] contributes 65.48% while, t [F(3,48)=11.49, p<.001] with a contribution of 10.60%, while the interaction T-t [F(6,48)=4.97, p<.001] gives a contribution of 9.17%. Taking into account Fisher comparison method, it is found that all three temperatures present statistically distinct means, therefore all three must be considered. With regards to time values, 3 and 6h present identical means, thereby no statistical evidences are shown that distinct one from the other. Through the main effect plot (Figure 5.34) and taking into account the previous considerations it is possible to ascertain that the best behaviour is found at 135°C/3-6h. Interaction plot depicts that T=135 shows minimal change for different treatment times, while for T=150°C a decrease is observed after t=6h. T=165°C presents a decreasing behaviour along the test time, being more pronounced at lower time intervals.

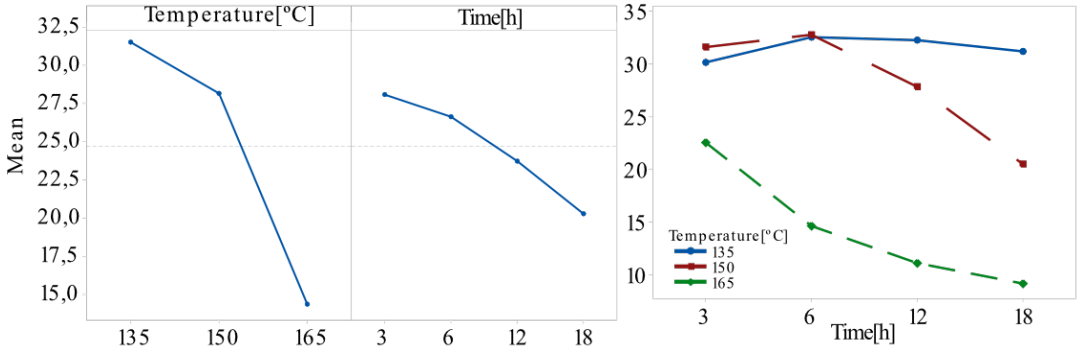


Figure 5.34: FX256 - Tensile strength main effects and interactions plots.

Considering the strain at break, ANOVA results indicate that T [F(2,48)=427.42, p<.001] contributes 62.28%, while t [F(3,48)=83.88, p<.001] with a contribution of 18.33%, whereas the interaction T-t [F(6,48)=36.35, p<.001] presents a contribution of 15.89%. Post-Hoc Fisher LSD showed that all temperature groups have distinct means, each one presenting relevant difference in the response. The same differences are found for all the time values. Main effect plot in Figure 5.35 shows that the improved performance is found at for 135°C/3h, whereas the combination plot shows a clear worst behaviour at T=165°C along the time, for T=135°C, a slight decrease along the time, while for T=150°C above 6h an abrupt decrease in strain at break is found.

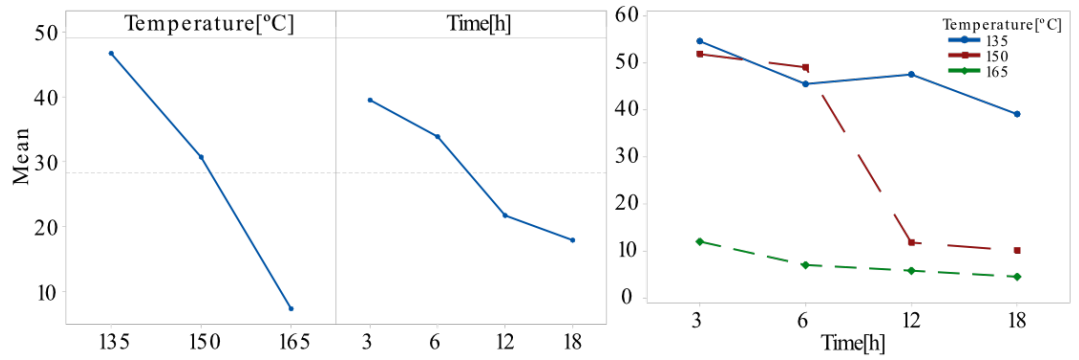


Figure 5.35: FX256 - Strain at break main effects and interactions plots.

FX256 - Flexural

For flexural modulus, ANOVA results show that T [F(2,48)=15.55, p<.001] contributes 30.49%, while t group does not fulfil the condition p<.05, thus not being considered for this set of results, whereas the interaction T-t [F(6,48)=3.76, p<.004] presents a contribution of 22.09%. A comparison using Fisher LSD method shows that T=135/150°C presents similar means, thus concluding that among the two there is no relevant change in the response. As far as the time, all of the terms share similar means, therefore, all values can have identical responses. Main effect plot in Figure 5.36 shows that the best behaviour is found at higher temperatures, regardless of the annealing time. Considering that t input variables do present evidences to deny the null hypotheses, the

variation through time is difficult to evaluate without more complex statistical analysis (e.g scott knot).

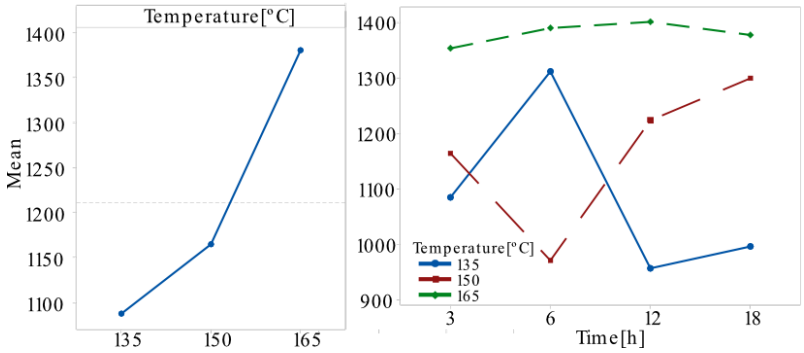


Figure 5.36: FX256 - Flexural modulus main effects and interactions plots.

Considering flexural strength, ANOVA results indicate T [F(2,48)=57.28, p<.001], which contributes 38.68%, while t [F(3,48)=10.77, p<.001] with a contribution of 10.91%, whereas the interaction T-t [F(6,48)=16.88, p<.001] presents a contribution of 34.20%. Post-Hoc Fisher comparison indicates that the three temperature stages present distinct means which translates into three different responses having to be considered. Time comparisons indicates that t=3h presents distinct mean from all of the samples, while 6 and 12h share similar means, as well as 12 and 18h, implying that only t=3h shows a relevant change in the response. Taking into consideration the main effect plots (Figure 5.37), it is perceived that the best flexural strength is achieved for 150°C/3h. The interaction plot shows a steady response along the time for T=150°C. However, T=135°C presents an increase in strength at t=6h and a consequent drop, while T=165°C presents an overall decrease in flexural strength as the time progresses.

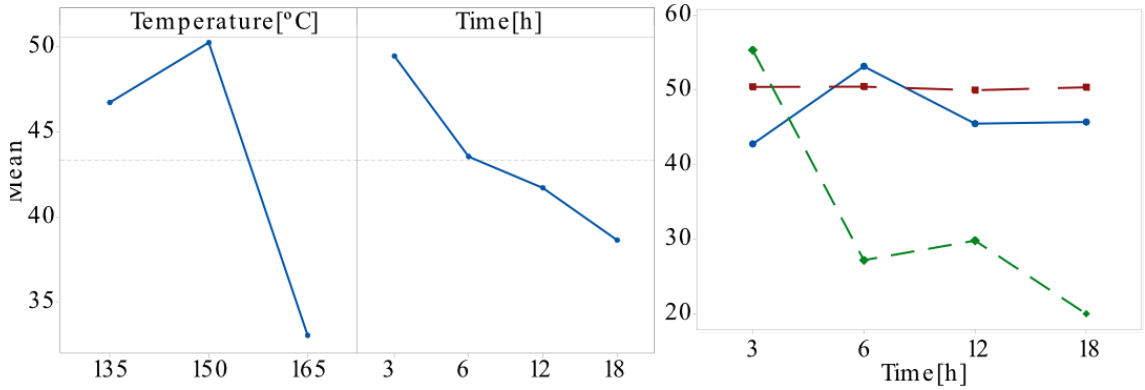


Figure 5.37: FX256 - Flexural strength main effects and interactions plots.

ANOVA results for flexural strain show that T [F(2,48)=96.51, p<.001] with a contribution of 74.57%, while t [F(3,48)=3.94, p=.014] contributing 4.56%, whereas the interaction T-t presented a p-value outside the confidence level thus being disregarded. Comparing the values inside the group with Fisher LSD it is possible to verify that T=135 and 150 °C present identical means, thus concluding that there is no relevant change in the response for those parameters. Comparing the

time responses, it is possible to identify two different stages of results. Identical means for 3 to 6h of treatment resulting in one stage, whereas 6, 12 and 18h also present identical means among them. Considering Figure 5.38 results, maximum flexural strain is achieved for 135-150°C/3h.

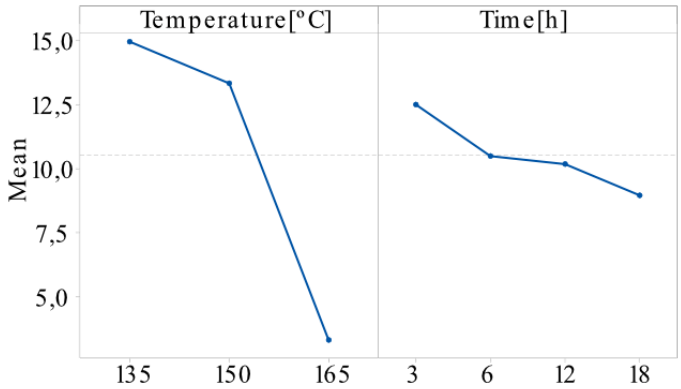


Figure 5.38: FX256 - Flexural strain main effects and interactions plots.

5.2.4.3 Discussion

Table 5.22 presents an overview of the results obtained through the statistical analysis, in which the best T/t interval is selected accordingly to the property. Through this table, it is possible to observe that t=3h interval is common to both materials' flexural and tensile responses with statistically significant results, indicating that t=3h is the ideal annealing time for an overall property increase. Considering annealing temperature, both materials' tensile and flexural properties apart from the modulus and σ_{flex}, present the common value of T=135°C for improved properties.

Table 5.23 depicts the property results in agreement with the statistical analysis. For the properties which ANOVA and Post-Hoc did not present any convergent solution, a maximized combination was selected, presenting the condition number (C) correspondent to the full factorial experience (Table 5.20). To summarize the results, improvement percentage for each property is also presented. It is also shown that, for the best conditions, the improvements were significantly higher for the unreinforced material, apart from the strain at break. In terms of flexural results, the improvement was also considerably higher for FX256, even though CF15 presented superior maximum values of flexural stress and modulus after treatment. Considering that both materials showed increase in flexural strain, it is possible that beyond the morphological alterations, the annealing process could promote a better interlayer behaviour.

Throughout the printing process, it became clear that the unreinforced material was more complex to print. This was corroborated by the DSC tests of the control samples, in which higher crystallinity percentage was present in FX256, thus justifying the higher contraction levels during production. The results presented in Table 5.21 indicate that the increase in annealing temperatures, allied to slower cooling rates, lead to an increase in crystallinity (more accentuated in the unreinforced material) as shown in literature [Fischer and Drummer, 2016]. It is also perceived

Table 5.22: Best annealing conditions according ANOVA's analysis.

	Tensile			Flexural		
Material	Property	Temperature [°C]	Time [h]	Property	Temperature [°C]	Time [h]
CF15	E [MPa]	165	-	E_{flex} [MPa]	-	-
	σ [MPa]	135-150	3-6	σ_{flex} [MPa]	135-150	3
	ε [%]	135	3	ε_{flex}[%]	135	3
FX256	E [MPa]	-	-	E_{flex} [MPa]	165	-
	σ [MPa]	135	3-6	σ_{flex} [MPa]	150	3
	ε [%]	135	3	ε_{flex}[%]	135-150	3

Table 5.23: Mechanical properties overview.

	Tensile					Flexural				
Material	C	Property	Control	Treated	Incr.[%]	C	Property	Control	Treated	Incr.[%]
CF15	12	E [MPa]	885.97±11.66	979.19±91.05	10.52	12	E_{flex} [MPa]	1748.48±60.95	1923.06±555.49	9.98
	5	σ [MPa]	40.36±1.93	44.75±1.87	10.88	5	σ_{flex} [MPa]	55.55±1.74	61.45±2.18	10.62
	1	ε [%]	25.04±4.88	17.67±2.30	-29.43	1	ε_{flex}[%]	13.06±0.96	14.99±2.79	14.78
FX256	6	E [MPa]	450.99±54.02	559.81±32.81	24.13	11	E_{flex} [MPa]	1114.31±38.98	1400.90±138.15	25.72
	2	σ [MPa]	29.49±0.59	32.52±1.79	10.27	6	σ_{flex} [MPa]	38.77±10.21	50.36±3.45	29.89
	1	ε [%]	61.19±7.31	54.592±5.52	-10.78	1	ε_{flex}[%]	9.40±4.08	16.00±1.48	70.21

that higher crystallinity levels lead to increased brittleness, justifying the decrease in strain along the defined conditions.

A decrease in performance was also found throughout the testing experiment matrix. Considering tensile strength results, it is possible to observe that FX256 performance starts to decay from C7 (in which higher change in colour is observable) onwards, while CF15 tensile strength kept higher than the control C0 until C10. As for the flexural strength, both presented decrease in performance after C10 being FX256, the most negatively influenced by the annealing condition. This decrease in properties may be also an indicative that thermal degradation of the polymer occurred at higher temperatures, most notoriously for higher treatment time periods indicating polymeric ageing possibility. A similar scenario was observed for the strain results, which allied to the increase in crystallinity might have originated the brittle behaviour.

5.2.5 Conclusion

In this work a full factorial DOE and statistical analyses were made in order to identify how PA12 and reinforced PA12 printed samples react to a wide range of temperatures and time conditions, considering mechanical behaviour as the response. This way, it was possible to define the best annealing conditions according with the type of property that is intended to maximise. Mechanical performance tests show that annealing theses materials can be in fact used as a method of increasing their mechanical properties. After thermal treatment, both materials showed similar crystallization degrees. Both materials show an increase in flexural properties for all properties studied. While CF15 improvement was from 10 to 15% for all properties, FX256 presented the bigger improvement of 26, 30 and 70% for E_{flex}, σ_{flex} and ε_{flex} correspondingly. Tensile tests

show that the best conditions present an increase from 11% (E and σ), while the strain is reduced 29% for CF15. FX256 shows an increase of 24% and 10% (E and σ),in spite of a decrease of 10% in strain being demonstrated. Flexural results show an improvement of all the properties, indicating that the annealing treatment promotes a relief of residual thermal stresses resultant of the 3D printing process and, at the same time, an enhanced inter-layer adhesion. Therefore, it can be stated that annealing in PA12 and short fibre reinforced PA12 printed parts leads to the improvement of their mechanical performance. In a general manner, as the mechanical properties of a polymer increase, their processing temperatures will most likely be higher. It was also found that T=165°C is not indicated for thermally treat these two types of polymers, since a decrease in properties was found by comparison with the C0 specimen. When considering a process such as FFF, in which successive heating and cooling cycles are a part of the process, residual stresses are created, distorting the part leading to warping and other defects. Thermal annealing is a process that beyond the intended increase in properties, can largely reduce internal stresses due to its slow heating, molecular relaxation and consequent slow cooling, leading to more stable parts.

Chapter 6

Conclusions

Being one of the most versatile technologies in terms of material range, scalability, cost effectiveness and easy to operate, FFF process is one of the most widespread AM processes, either in desktop or industrial environments. The complexity of the physical phenomena involved in the reshaping of a thermoplastic based polymer into a desired geometry, combined with the material intrinsic properties, as well as the right choice of parameters defines the behaviour of a part. In order to answer the industrial demands of lightweight functional parts with competitive performance, new and improved materials are constantly being developed, increasing not only the mechanical performance, but chemical and thermal capabilities. However, limitations are mainly centred in the anisotropic performance, or in the absence of homogeneity in the part's behaviour, which is an AM innate characteristic that depends on the internal patterns, but principally, the building orientation. This results in a gap of knowledge on the overall part behaviour that the designer needs to take into account. Other inherent drawback is the final surface finishing due to the visible layer lines, which compared to processes such as SLS falls short. The resolution of these process intrinsic challenges leads to the technology proliferation as a serious alternative production process. Considering FFF process is only useful for non functional parts is underestimating the technology. When integrated into other technologies, or process chain, the cost effectiveness in product development can be increased. Thus the hybridization concept presented and executed in Fibr3D project is a step towards this direction.

This study is motivated by the process drawbacks, intending to create an evaluation procedure that can analyse the part characteristics, and in some cases proposing a methodology to mitigate these gaps and even overcome them. Based on the motivation and work purpose, several open research questions were established to better comprehend the impact of these problematics. The main research findings generated by the imposed goals presented throughout this work, support the conclusions achieved, providing an answer to the original research questions.

6.1 Research Questions

Q1 - How much can fibre reinforcements improve the mechanical behaviour of an FFF part?

An extensive experimental mechanical testing campaign was carried out throughout the present PhD work, addressing in parallel both unreinforced and reinforced material, in accordance to all the proposed goals. Regarding the accomplished results, the following findings were obtained. In continuous fibre case, the change in behaviour is drastic, transforming the part from a ductile into a tough brittle polymer printed structure, reflecting the fibre behaviour. As far as short fibres, there are several factors influencing the part outcome, being the deposition direction/infill directly related to the material stiffness increase, as proven in section 3.4. The behaviour exhibited by short fibre reinforced parts and the unreinforced is similar, presenting identical maximum stress values for the most of the cases. However, higher stiffness modulus and lower strains are found with the presence of short fibre. It is also proven that when considering the strength and displacement between adjacent layers, the fibre presence has no effect what so ever, since those are aligned with the deposition direction. For a better understanding of this phenomena, other studies are necessary, suggested in the future work section. In regards to surface finish and machining operations, it is shown that the increased stiffness caused by the fibre presence results in improved surface finish.

Q2 - How does the printing conditions affect the mechanical behaviour?

This research question is directly related to the purpose of mechanical performances G2 and G3. It is successfully shown that performance is drastically changed by the specimen's internal infill. The mechanical performance is improved if the deposition is in line with the loading direction, an effect that is more pronounced if considering the reinforced samples stiffness. Even though the intercalate $\pm 45^{\circ}$ pattern presents the most homogeneous behaviour, the path disposition is inclined from the loading direction, thus not fully benefiting from the fibre presence, since the lateral adhesion of the deposited paths is also solicited. In what concerns the Arcan samples and building orientation, it is demonstrated the difference in behaviour, proving the claimed anisotropic properties. It is shown that the layer interface strength is by far the weakest property of an PA12 based FFF printed part. Thus, a method to improve the interlayer bonding is of the most interest (e.g. interlaminar mechanical testing with annealed specimens). In addition, due to irregular fracture areas caused by the sample geometry combined with the process, longitudinal samples presented inferior behaviour than the flat $\pm 45^{\circ}$. This variation in mechanical performance is mostly what limits the use of this technology in functional applications. To summarize, two remarks can be highlighted: (i) printing conditions affect significantly the mechanical performance of the part; (ii) the mechanical performance of FFF printed parts should be evaluated using structural characterization and considered as such.

Q3 - How can post processing be a beneficial complement to FFF process?

In order to answer this open question, two distinct studies were carried out, which cover the two types of finishing procedures (G1 and G2). Considering the machinability study, it was proven that the subtractive process originates homogeneous surfaces (with low surface roughness values).

Allied to the surface roughness improvement, the precision of the subtractive process grants the dimensional accuracy that even more expensive professional processes cannot provide. Taking into account an hybrid setup performance, subsequent additive and subtractive operations, the dimensional accuracy and finishing details can be applied with the same geometric freedom that the additive process by itself can provide, resulting in improved near to market parts. In regards to the annealing process, the increase in mechanical performance is significant. However to perform it in a separate operation, is not ideal, becoming time consuming and cost ineffective. If aligned with the productive process, i.e., performed inside the printer chamber, it is possible to avoid issues related to sudden cooling, reducing thermal stresses and consequently stabilizing the part. This method could be a major benefit as the complexity of the polymer increases (e.g. PEEK, PEI), since it decreases the occurrence of known issues, such as the lack of interlayer adhesion due to material contractions leading to warping.

6.2 Final Remarks

Fused Filament Fabrication is a technology with excellent capabilities, primarily due to its broadness and aptitude to be upgraded. It is in the author's main belief that the process is not industrially embraced due to the non professionalized stigma that comes along with it. Nonetheless, this work intends to enlighten that it is possible to produce cost effective, dimensionally accurate parts and mechanically robust parts. Thus, this work is also a further step towards proving how advantageous hybridization can be, by integrating a set of complex operations, all in one, which will allow for improved FFF manufactured parts.

6.2.1 Which are the guidelines for printing the best functional and structural thermoplastic based composites part through FFF?

From the author's point of view, the answer to this question can be given through the analysis of the following topics:

Hardware capabilities: If there is a possibility to take advantage of continuous fibre in a 3-axis manner, the performance of the part is going to be translated by the fibre's capability in plane, being the design, and consequent fibre positioning, of the most importance. In a 5-axis continuous fibre equipment, the part behaviour should be considered similarly to a traditional composite, prevailing the fibre performance, yet in a out-of-plane manner. For both cases, the polymeric matrix material is not the predominant element, since its purpose is to agglutinate the fibre layers. As for a non-continuous fibre deposition hardware, the prevailing performance is the one intrinsic to the feedstock type. Considering the data provided in section 3.1, it is known that higher performance materials imply the use of higher printing temperatures. Beyond the need for processing (extruding) the materials at higher temperatures, higher chamber temperatures are needed, thus resulting in more expensive and advanced hardware. Currently, most of low-cost equipment process materials up to 290°C, which allows for engineering thermoplastics such as PA,

in which the short fibres and nanotubes are included, leaving to the part designer to choose which capability it is of most importance, ranging from the more ductile to the electrically conductive, high service temperature or high strength.

Design for AM: It is important to consider that unlike continuous fibre, low infill percentages for a short fibre reinforced material decrease the mechanical performance. Material datasheets indicate the mechanical performance of a fully dense sample. Thus, the printed part will not reflect the load capabilities considered through that data. As far as the building orientation, the author's advice is that even if it is a complex geometry and support material is required, it should be adjusted so the load that the part is going to sustain should be parallel to the XY-axis, being those the preferential directions for mechanical solicitations.

Cost effectiveness: AM is a tool-less technique (does not require tool investment for each new part) that allows the production of 3D parts without significant waste generation, when compared to other traditional methods (subtractive). In an hypothetical scenario in which an advanced hardware is available, in which a 1 kg spool of PEEK (CarbonX 3DXtech[1]) costs near 445 €, and a 1 kg of PA12 (Fillamentum[2]) costs 55 €, the manufacturing cost is the same. It all depends on the part's requirements, the need for manufacture through this method and the size of the batch. For a small batch, considering that in traditional technologies, such as injection moulding, the mould itself might be more expensive than an advanced printer, the process could be a solution. However, for big series, considering that the process is slow, compared to injection moulding it will become less cost effective as the number of parts grows. It is a process indicated for iterative design, product development or a distinct sequence of parts, requiring no more financial effort for it. As far as post processing, thermal treatments are indicated to reduce thermal residual stresses, which are higher, for advanced polymers, since they require high processing temperatures. Thus it is considered that thermal treatment creates a more stable, with improved the mechanical behaviour part. Considering the subtractive processes, these should be used if high geometrical, dimensional tolerances, or improved surface behaviour is needed. It is necessary to consider that these operations increase the final part cost, since require extra labour, yet adding value to the part final overall outcome.

Considering the proposed guidelines to the composite FFF printed part, a flowchart is presented in Figure 6.1 that represents the assumptions made above, summarizing the process plan for printing functional and structural printed composites.

[1] https://www.3dxtech.com/carbonx-carbon-fiber-peek-3d-printing-filament/
[2] https://fillamentum.com/collections/technical-polymers/products/nylon-cf15-carbon?variant=31448674950

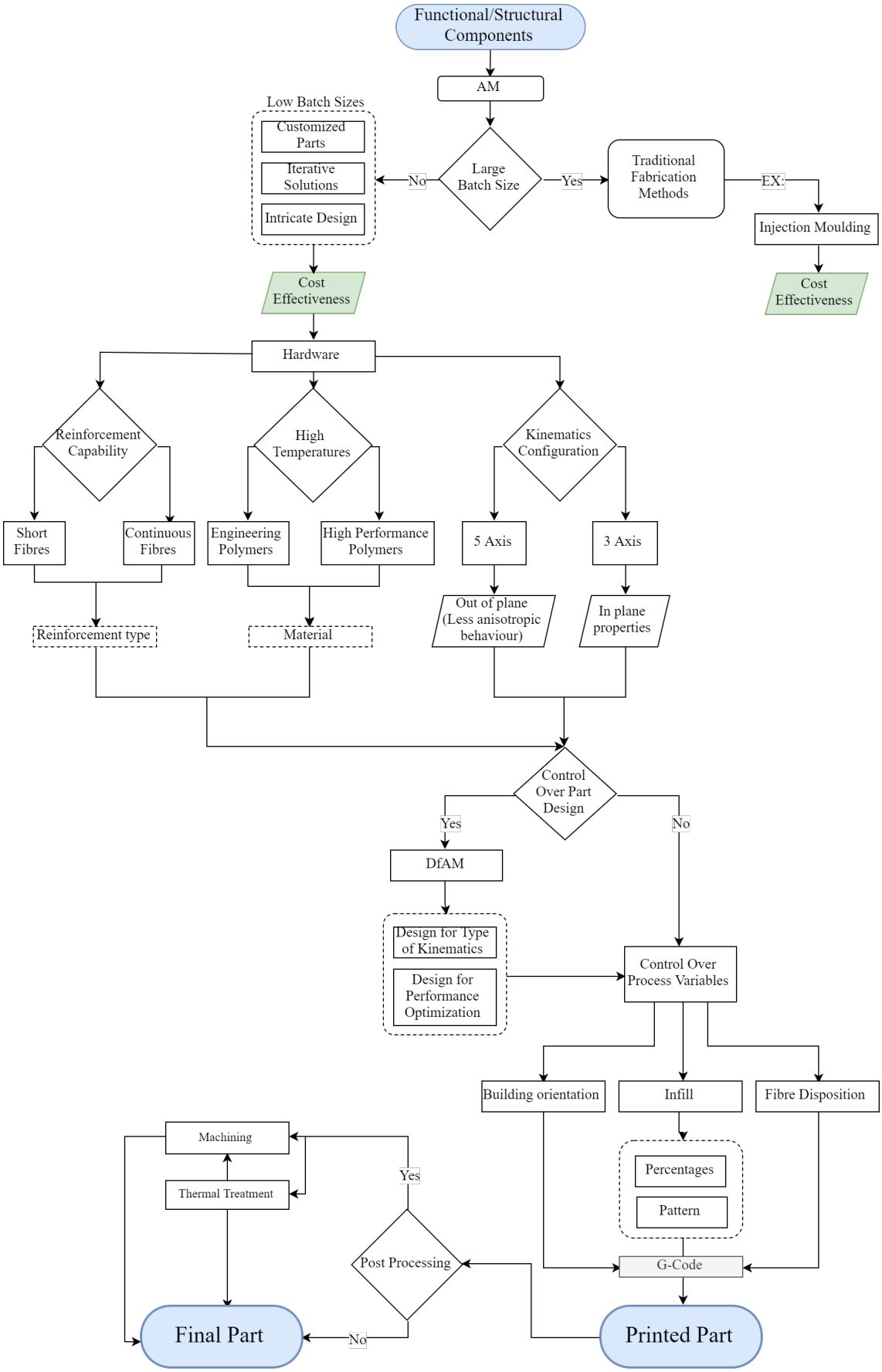


Figure 6.1: Guidelines for functional and structural component production.

6.3 Future Work

Regardless of the obtained results in this thesis, several ideas and concepts, that have not been pursued, are suggested as guidelines for future works.

Continuous Fibre samples: Due to the available equipment limitations, no further studies were pursued involving the continuous fibre deposition through FFF process. Considering the obtained results, future studies could include an evaluation of the increase in performance by augmenting the number of carbon fibre layers for these same geometries, obtaining a comparison among the distinct fibre types and available types of fibre infill patterns. Fibr3d project envisions the design and construction of a 5-axis capable, FFF printing machine using continuously reinforced thermoplastics. This equipment is also able to of achieving high chamber temperature (allowing the part annealing or slower cooling) and machining via a separate subtractive head. Considering a non restrictive hardware, as the previous or a commercial one, continuous fibre performance evaluating tests should be pursued, repeating some of the methodologies developed in this thesis, once again taking into account both non-reinforced and reinforced polymers, different building orientations, out-of-plane parts and distinct pattern schemes.

Interlaminary fracture mode II and mixed mode: Following the interlaminary fracture under mode I, distinct geometries were developed and tested under mode II. Due to the PA12 materials lack of stiffness, no progress was achieved. A new test campaign is suggested, redefining the test geometry, or by adding carbon fibre doublers bonded to the sample, forcing the fracture propagation in the desired area.

Interlayer strength: Considering the interlayer strength, preliminary tests were performed, using circular hourglass shaped specimens, which were printed in the upright position and bonded with a two component adhesive to aluminium machined grips, as presented in figure 6.2. For this geometry, it is proposed a test battery supported by a DOE and statistical analysis is proposed, considering as test factors the layer thickness, extrusion temperatures and printing speeds or extrusion multiplier variations. Taking into account the same type of test specimen, by submitting them to a thermal treatment, similar to the one presented in section 5.1, it would be possible to test its influence on the interlayer adhesion/strength, which would be a novel approach, and a relevant scientific contribution.

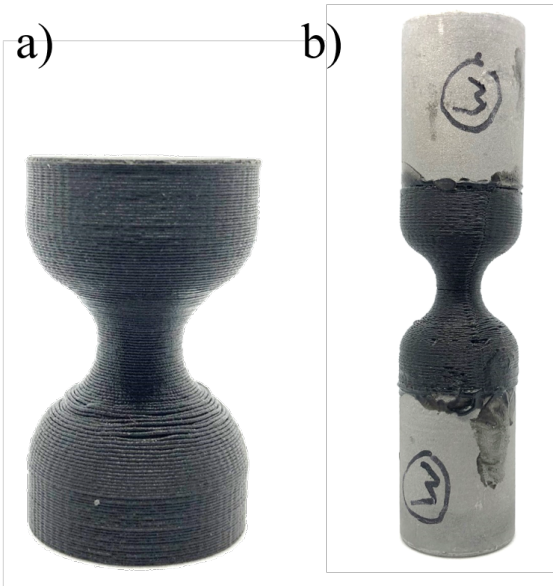


Figure 6.2: Interlaminar strength:(a)specimen and (b)specimen with aluminium bonded grips.

Off-axis test: The off-axis tension test is specially designed for determining the shear properties of unidirectional composite materials. Efforts have been made in the direction of using this method with the materials used in this thesis. Longitudinal and transversally patterned samples have been cutted out from a slate, and tensile tested in order to calculate the maximum shear angle of the off axis test. This work was not pursued until the end due to time constraints. This is a well-known characterization method for anisotropic materials and an innovative approach to additively printed parts.

Hybridization tests: Similarly to the work presented in Chapter 5, in which subtractive and annealing tests were performed in distinct equipments, other challenges arise, which can also be performed through this method. An example is the deposition and adhesion/performance upon a same material machined surface, which can be performed in the same line of thought as the previous. To quantify this adhesion test, a sample similar to the previously proposed above for interlayer strength could be printed up to over the middle point, machined, and resumed the printing process thus testing the capability of the material to adhere to a newly machined surface. Additional machining tests could be also performed for a similar approach to the one used in Section 5.1 for contour milling and hole correction.

Appendix A

Material and hardware selection

At the beginning of this study, a decision needed to be made in regards of which materials were to be used. Posteriorly to this feedstock analysis, some conclusions were taken regarding material selection. In order to better understand how these materials behave, it was defined that the supplier of the reinforced material that was being tested needed to provide an unreinforced version of the previous. Other factor that had to be considered was the available hardware, their respective temperature limitations and consequently its capability to process more complex materials. Throughout this work, two tronxy X5 were used, and finally a RatRig V-core machine, which are limited at 260°C, thus the usage of high performance polymers was not a possibility. Considering these restrictions, a PA based material, classified as an engineering polymer was the best option. However, when this study was began in 2016, the availability of a material which fulfilled these requisites was much more limited. Through the feedstock analysis, it was proven that both PA12 materials supplied from Fillamentum©, Parzlich s.r.o (Czech Republic) presented similar thermal behaviour and ideal processing temperatures, which was followed by brief contacts with the brand representatives, and then revealed that nylon based materials were a priority, and the plan was to keep producing it, thus being ensured enough quantities for the testing needed.

Nylon FX256

The PA12 unreinforced version is commercially known as Nylon FX256, provided by Fillamentum and presents high tensile strength, as well as toughness and impact resistance. It presents a low friction coefficient combined with a high operating temperatures, wear and chemical resistance. It is indicated for functional and technical part production from electronic components and equipments to bushings and gears. In addition, this material complies with the requirements for food contact applications [Fillamentum, 2019b].

Nylon CF15

Commercially known as Nylon CF15, this PA12 reinforced material presents similar thermal properties as the previous one, however it is characterized by an improved strength and rigidity due to

the presence of short carbon fibres. According to the datasheet, this fibres are 100μm in length and in conformance with the TGA analysis performed to both materials, its content ranges from 16 to 18wt.%. It presents higher stability and rheological behaviour, allied to a low thermal expansion due to the fibre presence and it is easily processed. It is indicated for bearings or cogwheels, as well as structural reinforcement parts. It is advisable the use of hardened steel nozzles in order to counteract the faster deterioration of normal brass nozzles, since CF15 presents highly abrasive behaviour due to the fibre presence [Fillamentum, 2019a].

CF15 Morphology analysis

A microscopic analysis was performed using an Olympus PMG 3 (Japan) inverted microscope with reflection light and an Olympus DP12 software and DP12 digital camera to capture magnifications at 23, 150, and 300x of the filament. Filamentar samples were inserted in the epoxy resin in both the axial and in the cross-sectional views, and posteriorly polished. With these images, material properties such as fibre orientation, distribution, and dimensions were determined using ImageJ software measuring tools [Schindelin et al., 2012]. Regarding the fibre content, whenever TGA test is not available/possible, an alternative methodology based on image analysis can be applied. For this specific case a fibre dimensional analysis was done in order to verify the datasheet values. Figure A.1a depicts a magnification of a filament cross section, while Figure A.1b shows magnification of the filament lateral section, both at 300x. Through these measurements, it was possible to obtain an average fibre length of 66$\pm$18 μm and a diameter of 6.4$\pm$11.91 μm.

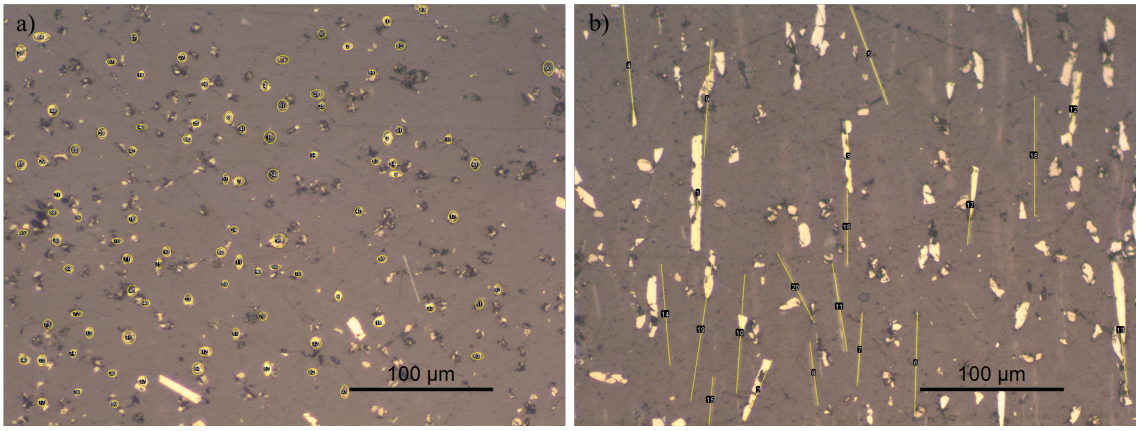


Figure A.1: Fibre dimensional analysis: a)cross section at

A further analysis to the CF15 filament morphology revealed that, dark spots or voids are observed in the central era of the filament. This can be seen in Figure A.2a and b, which represent a cross section magnification at 75x and lateral section at 23x. These voids might occur during the production process, where the humidity can be trapped in the centre of the filament. A posterior drying process is advised so this moisture would not cause printing irregularities, however the lack of material in those areas will be always be present.

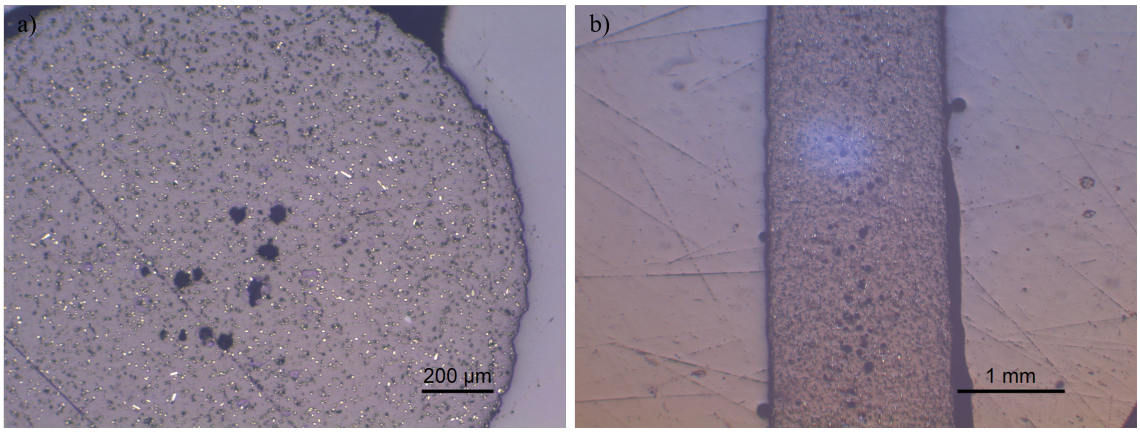


Figure A.2: Magnifications showing porosity in the filament: a)cross section 75x and b)lateral section at 23x.

Material Conditioning

PA based materials are highly hygroscopic. Several studies have shown that the presence of moisture in the material may cause a decrease in their mechanical performance [Carrascal et al., 2005, Rajeesh et al., 2010, Do et al., 2015]. When considering printing and testing phases, the same material conditioning is required in order to non compromise the mechanical properties. Extruding a non dried out material through a nozzle will cause irregularities in the part surface, originated by vaporization of the humidity content, causing material bubbling. The materials were provided by the seller, hermetically sealed with silica gel, however after each printing day, both materials needed to be dried in a PrintDry^{TM} (Canada) filament drier at 70°C for 8 hours (Figure A.3). After being printed, each set of samples, regardless of the type of test that they were submitted to, was placed in a sealed bag with silica gel.

Processability

As described in section 2.3.3, thermal residual stresses are a part of the process. Through the supporting studies detailed in this chapter it was possible to confirm that amorphous polymers such as PETG were easier to process, leading to warp free parts with accurate dimensions. On the contrary, semi-crystalline materials as PA presented a distinct behaviour, presenting the need for special cares so the specimens can be printed. Considering that all the samples planed for forthcoming and used in the supporting studies required the 100% dense infill percentage, thermal stresses generated are higher due to the higher number of cooling/heating cycles that they are subjected to, even if some measures were taken to minimize them. Firstly, the chosen extrusion temperature for both Fillamentum materials was 260°C, which was the higher value recommended by the seller datasheet. This temperature was chosen to increase the adhesion among the deposed lines. Since all of the available FFF machines did not have closed/heated chamber, the printing tray temperature was increased to the maximum at 90°C in order to compensate the lack of controlled environment, thus avoiding fast cooling cycles that result in warping. A 3 mm glass tray



Figure A.3: PrintDry^{TM} (Canada) filament drier.

was used as the printing surface, which despite its low conductivity reached similar temperatures than the tray, since its heating process was slow. On top of this glass surface, several types of adhesion improving materials were used. 3DLac®(Aragones, Spain), Magigoo from Thought3D LTD (Malta) and CUBE®glue from 3D Systems Inc. (Minnesota, USA) were tested, being applied in thin layers, directly over the glass surface. The best results were achieved by CUBE®glue. It was also found that sharp corners were the warping nucleation areas. To minimize this problem, a brim was created around each testing sample via slicing software, ranging from seven to eight paths (up to 10 mm) for one or two layers depending on the part. All of these features combined allowed to accurately print distinct geometries of samples. Furthermore, it was observed that the parts detached from the surface as the tray cooled down after print, even considering these features.

Slicing Software

The choice of the slicing software was narrowed to just three alternatives upon some research. Slic3r, Ultimaker Cura (Utrecht, Netherlands) and Simplify3D were taken into consideration. The first one, due to its simplicity, however, it is an open source platform implying a slow support through update and bug resolution. Cura proved to be the best free alternative, however the choice fell on Simplify3D due to previous experience with it.

Printing Hardware

In the beginning of this work, a Tronxy X5 3D printer, Shenzen Tronxy Technology Co. Ltd was acquired, which allowed to know both materials behaviour, and how this equipment reacted to continuously printing with the recommended settings. Since printing with these Nylon materials would require the maximum extrusion and heated bed temperatures allowed by the equipment for

long periods of time, major wear on the machine would be created. With this in consideration, a second same model machine was acquired, with exact same specifications in order to print simultaneously the same samples with the reinforced and unreinforced material. Tronxy X5 main specifications are presented in Table A.1.

Table A.1: Tronxy X5 3D Printer main specifications.

Brand Name	TRONXY
Model Number	X5
Max Printing Size	210*210*280mm
File Format	STL G-Code
Nozzle temperature	0-260°C
Heated bed	0-100°C
Print Speed	20-30 mm/s
Extruder diameter	Defaul 0.4 mm
XY Axis Positioning Accuracy	0.012 mm
Z Axis Positioning Accuracy	0.004 mm
Filament Diameter	1.75 mm
Printing Filament	PLA/ABS/TPU/FLEXIBLE/WOOD/PVA/PV/NYLON
Power supply	20 A 110 V/ 220 V
Machine Size	515*395*500 mm
Machine Net Weight	8.8 Kg
Operating System	Windows/ XP/ Mac

RatRig V-Core (described in Table A.2) was a secondary equipment acquired to RatRig (Algarve, Portugal), as mechanical component kit, since the manufacturer does not provide the full electronic components. Missing parts were acquired from E3D®[1] (United Kingdom) and OOZNEST[2] (United Kingdom). This machine was intended for other projects and maintained as backup throughout this work. When required, the same slicing specifications were used.

[1] https://e3d-online.com
[2] https://ooznest.co.uk

Table A.2: RatRig V-core 3D Printer main specifications.

Brand Name	RatRig
Model Number	V-Core
Max Printing Size	300*300*300 mm
File Format	STL G-Code
Nozzle temperature	0-300°C
Heated bed	0-100°C
Print Speed	30-40 mm/s
Extruder diameter	Defaul 0.4 mm
XY Axis Positioning Accuracy	0.012 mm
Z Axis Positioning Accuracy	0.004 mm
Filament Diameter	1.75 mm
Printing Filament	PLA/ABS/TPU/FLEXIBLE/WOOD/PVA/PV/NYLON
Power supply	30 A 220 V
Machine Size	570*506*560 mm
Operating System	Windows/ XP/ Mac

Bibliography

R. E. Abhari, P.-A. Mouthuy, N. Zargar, C. Brown, and A. Carr. Effect of annealing on the mechanical properties and the degradation of electrospun polydioxanone filaments. *Journal of the Mechanical Behavior of Biomedical Materials*, 67:127–134, 2017. ISSN 1751-6161. doi: https://doi.org/10.1016/j.jmbbm.2016.11.023. URL http://www.sciencedirect.com/science/article/pii/S1751616116304143.

S.-h. Ahn, M. Montero, D. Odell, S. Roundy, and P. K. Wright. Anisotropic material properties of fused deposition modeling ABS. *Rapid Prototyping Journal*, 8(4):248–257, 2002. ISSN 1355-2546. doi: 10.1108/13552540210441166.

M. Alauddin, I. A. Choudhury, M. A. El Baradie, and M. S. Hashmi. Plastics and their machining: A review. *Journal of Materials Processing Tech.*, 54(1-4):40–46, 1995. ISSN 09240136. doi: 10.1016/0924-0136(95)01917-0.

L. Alfonso, C. Badulescu, and N. Carrere. Use of the modified Arcan fixture to study the strength of bonded assemblies for automotive applications. *International Journal of Adhesion and Adhesives*, 80(November 2017):104–114, 2018. ISSN 01437496. doi: 10.1016/j.ijadhadh.2017.09.014.

N. Aliheidari, J. Christ, A. Ameli, R. Tripuraneni, and S. Nadimpalli. Measuring the interlayer fracture resistance of FDM printed thermoplastics. *SPE ANTEC Indianapolis*, pages 5–9, 2016.

A. N. Amanullah, Murshiduzzaman, T. Saleh, and R. Khan. Design and Development of a Hybrid Machine Combining Rapid Prototyping and CNC Milling Operation. *Procedia Engineering*, 184:163–170, 2017. ISSN 18777058. doi: 10.1016/j.proeng.2017.04.081. URL http://dx.doi.org/10.1016/j.proeng.2017.04.081.

R. Anitha, S. Arunachalam, and P. Radhakrishnan. Critical parameters influencing the quality of prototypes in fused deposition modelling. *Journal of Materials Processing Technology*, 118 (1-3):385–388, 2001. ISSN 09240136. doi: 10.1016/S0924-0136(01)00980-3.

M. Arcan, Z. Hashin, and A. Voloshin. A method to produce uniform plane-stress states with applications to fiber-reinforced materials - A specially designed specimen yields material properties under pure shear or uniform plane-stress conditions. *Experimental Mechanics*, 18(4): 141–146, 1978. ISSN 00144851. doi: 10.1007/BF02324146.

ASTM D5528-01. Standard test method for mode I interlaminar fracture toughness of unidirectional fiber-reinforced polymer matrix composites. *American Standard of Testing Methods*, 2014. doi: 10.1520/D5528-13.2.

ASTM International. F2792-12a - Standard Terminology for Additive Manufacturing Technologies. *Rapid Manufacturing Association*, pages 10–12, 2013. ISSN 1882-675X. doi: 10.1520/F2792-12A.2. URL http://www.ciri.org.nz/nzrma/technologies.html.

M. Attaran. The rise of 3-D printing: The advantages of additive manufacturing over traditional manufacturing. *Business Horizons*, 60(5):677–688, 2017. ISSN 00076813. doi: 10.1016/j.bushor.2017.05.011. URL http://dx.doi.org/10.1016/j.bushor.2017.05.011.

R. Auyeung, H. Kim, S. Mathews, N. Charipar, and A. Piqué. Laser additive manufacturing of embedded electronics. In *Laser Additive Manufacturing*, pages 319–350. Elsevier, 2017. doi: 10.1016/b978-0-08-100433-3.00012-9. URL https://doi.org/10.1016%2Fb978-0-08-100433-3.00012-9.

L. Bade, P. M. Hackney, I. Shyha, and M. Birkett. Investigation into the Development of an Additive Manufacturing Technique for the Production of Fibre Composite Products. *Procedia Engineering*, 132:86–93, 2015. ISSN 18777058. doi: 10.1016/j.proeng.2015.12.483. URL http://dx.doi.org/10.1016/j.proeng.2015.12.483.

H. Bai, F. Luo, T. Zhou, H. Deng, K. Wang, and Q. Fu. New insight on the annealing induced microstructural changes and their roles in the toughening of β-form polypropylene. *Polymer*, 52(10):2351–2360, 2011. ISSN 00323861. doi: 10.1016/j.polymer.2011.03.017. URL http://dx.doi.org/10.1016/j.polymer.2011.03.017.

C. Barnatt. *3D Printing: The Next Industrial Revolution*. ExplainingTheFuture.com, 2013. ISBN 9781484181768. URL https://books.google.pt/books?id=Tvb6nAEACAAJ.

J. Batchelder and S. Crump. Method for rapid prototyping of solid models, 1999. URL https://patents.google.com/patent/US5866058A/en. US5866058A.

C. Bellehumeur and L. Li. Modeling of Bond Formation Between Polymer Filaments in the Fused Deposition Modeling Process. *Journal of Manufacturing Processes*, 6(2):170–178, 2004. ISSN 15266125. doi: 10.1016/S1526-6125(04)70071-7.

P. Bettini, G. Alitta, G. Sala, and L. Di Landro. Fused Deposition Technique for Continuous Fiber Reinforced Thermoplastic. *Journal of Materials Engineering and Performance*, 2016. ISSN 1059-9495. doi: 10.1007/s11665-016-2459-8. URL http://link.springer.com/10.1007/s11665-016-2459-8.

R. L. Blaine. Thermal Applications Note - Polymer Heats of Fusion. *Thermal Applications Note*, pages 1–2, 2002. URL www.tainstruments.com/pdf/literature/TN048.pdf.

A. Boschetto, L. Bottini, and F. Veniali. Finishing of Fused Deposition Modeling parts by CNC machining. *Robotics and Computer-Integrated Manufacturing*, 41:92–101, 2016. ISSN 0736-5845. doi: http://dx.doi.org/10.1016/j.rcim.2016.03.004. URL //www.sciencedirect.com/science/article/pii/S0736584515300648.

M. Bozdemir and . Aykut. Optimization of surface roughness in end milling Castamide. *Int J Adv Manuf Technol*, pages 495–503, 2012. doi: 10.1007/s00170-011-3840-2.

B. Brenken, E. Barocio, A. Favaloro, V. Kunc, and R. B. Pipes. Fused filament fabrication of fiber-reinforced polymers: A review. *Additive Manufacturing*, 21(October 2017):1–16, 2018. ISSN 22148604. doi: 10.1016/j.addma.2018.01.002. URL https://doi.org/10.1016/j.addma.2018.01.002.

M. Buggy. Polymeric Materials. In *Reference Module in Materials Science and Materials Engineering*. Elsevier, 2016. ISBN 978-0-12-803581-8. doi: https://doi.org/10.1016/B978-0-12-803581-8.04104-7. URL http://www.sciencedirect.com/science/article/pii/B9780128035818041047.

M. A. Caminero, S. Pavlopoulou, M. López-Pedrosa, B. G. Nicolaisson, C. Pinna, and C. Soutis. Using digital image correlation techniques for damage detection on adhesively bonded composite repairs. *Advanced Composites Letters*, 21(2):51–57, 2012. ISSN 2633366X. doi: 10.1177/096369351202100203.

M. A. Caminero, M. Lopez-Pedrosa, C. Pinna, and C. Soutis. Damage assessment of composite structures using digital image correlation. *Applied Composite Materials*, 21(1):91–106, 2014. ISSN 0929189X. doi: 10.1007/s10443-013-9352-5.

M. A. Caminero, J. M. Chacón, I. García-Moreno, and G. P. Rodríguez. Impact damage resistance of 3D printed continuous fibre reinforced thermoplastic composites using fused deposition modelling. *Composites Part B: Engineering*, 148(March):93–103, 2018a. ISSN 13598368. doi: 10.1016/j.compositesb.2018.04.054. URL https://doi.org/10.1016/j.compositesb.2018.04.054.

M. A. Caminero, J. M. Chacón, and J. M. Reverte. Interlaminar bonding performance of 3D printed continuous fibre reinforced thermoplastic composites using fused deposition modelling M.A. *Polymer Testing*, 2018b. ISSN 0142-9418. doi: 10.1016/j.polymertesting.2018.04.038. URL https://doi.org/10.1016/j.polymertesting.2018.04.038.

T. Campbell, C. Williams, O. Ivanova, and B. Garret. Could 3D Printing Change the World? Technologies, Potential, and Implications of Additive Manufacturing. *Technologies, Potential, and Implications of Additive Manufacturing*, page 16, 2012.

O. Carneiro, A. Silva, and R. Gomes. Fused deposition modeling with polypropylene. *Materials & Design*, 83:768–776, oct 2015. doi: 10.1016/j.matdes.2015.06.053. URL https://doi.org/10.1016%2Fj.matdes.2015.06.053.

I. Carrascal, J. A. Casado, J. A. Polanco, and F. Gutiérrez-Solana. Absorption and diffusion of humidity in fiberglass-reinforced polyamide. *Polymer Composites*, 26(5):580–586, 2005. ISSN 02728397. doi: 10.1002/pc.20134.

C. Casavola, A. Cazzato, V. Moramarco, and C. Pappalettere. Orthotropic mechanical properties of fused deposition modelling parts described by classical laminate theory. *Materials and Design*, 90:453–458, 2016. ISSN 18734197. doi: 10.1016/j.matdes.2015.11.009. URL http://dx.doi.org/10.1016/j.matdes.2015.11.009.

J. M. Chacón, M. A. Caminero, E. García-Plaza, and P. J. Núñez. Additive manufacturing of PLA structures using fused deposition modelling: Effect of process parameters on mechanical properties and their optimal selection. *Materials and Design*, 124:143–157, 2017. ISSN 18734197. doi: 10.1016/j.matdes.2017.03.065. URL http://dx.doi.org/10.1016/j.matdes.2017.03.065.

M. Chanda. *Introduction to Polymer Science and Chemistry: A Problem-Solving Approach*. CRC Press, 2006. ISBN 9781420007329. URL https://books.google.pt/books?id=5GHLBQAAQBAJ.

Z. Chen, Z. Li, J. Li, C. Liu, C. Lao, Y. Fu, C. Liu, Y. Li, P. Wang, and Y. He. 3D printing of ceramics: A review. *Journal of the European Ceramic Society*, 39(4):661–687, 2019. ISSN 1873619X. doi: 10.1016/j.jeurceramsoc.2018.11.013.

K. Chin Ang, K. Fai Leong, C. Kai Chua, and M. Chandrasekaran. Investigation of the mechanical properties and porosity relationships in fused deposition modelling?fabricated porous structures. *Rapid Prototyping Journal*, 12(2):100–105, 2006. ISSN 1355-2546. doi: 10.1108/13552540610652447. URL http://www.emeraldinsight.com/doi/10.1108/13552540610652447.

N. Choupani. Experimental and numerical investigation of the mixed-mode delamination in Arcan laminated specimens. *Materials Science and Engineering A*, 478(1-2):229–242, 2008. ISSN 09215093. doi: 10.1016/j.msea.2007.05.103.

S. Christ, M. Schnabel, E. Vorndran, J. Groll, and U. Gbureck. Fiber reinforcement during 3D printing. *Materials Letters*, 139:165–168, 2015. ISSN 0167577X. doi: 10.1016/j.matlet.2014.10.065.

M. Cotteleer, J. Holdowsky, and M. Mahto. The 3D opportunity primer: The basics of additive manufacturing. *[Report]*, pages 1–17, 2014. ISSN 1431-8784. doi: 10.1007/0-387-28390-0. URL http://dupress.com/articles/the-3d-opportunity-primer-the-basics-of-additive-manufacturing/.

R. Créac'hcadec, L. Sohier, C. Cellard, and B. Gineste. A stress concentration-free bonded arcan tensile compression shear test specimen for the evaluation of adhesive mechanical response. *International Journal of Adhesion and Adhesives*, 61:81–92, 2015. ISSN 01437496. doi: 10.1016/

j.ijadhadh.2015.05.003. URL http://dx.doi.org/10.1016/j.ijadhadh.2015.05.003.

S. S. Crump. Apparatus and method for creating three-dimensional objects, 1992. URL https://www.google.nl/patents/US5121329.

L. F. M. da Silva, F. J. L. Alves, and A. T. Marques. *Materiais de Construção*. Publibdustria, 2013. ISBN 978-989-723-049-3.

P. Datta, B. Ayan, and I. T. Ozbolat. Bioprinting for vascular and vascularized tissue biofabrication. *Acta Biomaterialia*, 51:1–20, mar 2017. doi: 10.1016/j.actbio.2017.01.035. URL https://doi.org/10.1016%2Fj.actbio.2017.01.035.

A. C. De Leon, Q. Chen, N. B. Palaganas, J. O. Palaganas, J. Manapat, and R. C. Advincula. High performance polymer nanocomposites for additive manufacturing applications. *Reactive and Functional Polymers*, 103:141–155, 2016. ISSN 13815148. doi: 10.1016/j.reactfunctpolym.2016.04.010. URL http://dx.doi.org/10.1016/j.reactfunctpolym.2016.04.010.

A. de Morais, A. Pereira, M. de Moura, F. Silva, and N. Dourado. Bilinear approximations to the mixed-mode i?ii delamination cohesive law using an inverse method. *Composite Structures*, 122:361–366, 2015. doi: 10.1016/j.compstruct.2014.11.058. URL https://app.dimensions.ai/details/publication/pub.1048873712. Exported from https://app.dimensions.ai on 2018/10/30.

A. B. De Morais, M. F. De Moura, J. P. Gonçalves, and P. P. Camanho. Analysis of crack propagation in double cantilever beam tests of multidirectional laminates. *Mechanics of Materials*, 35(7):641–652, 2003. ISSN 01676636. doi: 10.1016/S0167-6636(02)00289-2.

M. F. de Moura, J. J. Morais, and N. Dourado. A new data reduction scheme for mode I wood fracture characterization using the double cantilever beam test. *Engineering Fracture Mechanics*, 75(13):3852–3865, 2008. ISSN 00137944. doi: 10.1016/j.engfracmech.2008.02.006.

G. Design. CES EDUPACK 2018, 2018.

G. F. Dias, M. F. de Moura, J. A. Chousal, and J. Xavier. Cohesive laws of composite bonded joints under mode I loading. *Composite Structures*, 106:646–652, 2013. ISSN 02638223. doi: 10.1016/j.compstruct.2013.07.027. URL http://dx.doi.org/10.1016/j.compstruct.2013.07.027.

V. T. Do, H. D. Nguyen-Tran, and D. M. Chun. Effect of polypropylene on the mechanical properties and water absorption of carbon-fiber-reinforced-polyamide-6/polypropylene composite. *Composite Structures*, 150:240–245, 2015. ISSN 02638223. doi: 10.1016/j.compstruct.2016.05.011. URL http://dx.doi.org/10.1016/j.compstruct.2016.05.011.

J. Dong, C. Mei, J. Han, S. Lee, and Q. Wu. 3D printed poly(lactic acid) composites with grafted cellulose nanofibers: Effect of nanofiber and post-fabrication annealing treatment on composite flexural properties. *Additive Manufacturing*, 28(February):621–628, 2019. ISSN 22148604. doi: 10.1016/j.addma.2019.06.004. URL https://doi.org/10.1016/j.addma.2019.06.004.

M. Doyoyo and T. Wierzbicki. Experimental studies on the yield behavior of ductile and brittle aluminum foams. *International Journal of Plasticity*, 19(8):1195–1214, 2003. ISSN 07496419. doi: 10.1016/S0749-6419(02)00017-7.

R. B. Dupaix and M. C. Boyce. Finite strain behavior of poly(ethylene terephthalate) (PET) and poly(ethylene terephthalate)-glycol (PETG). *Polymer*, 46(13):4827–4838, jun 2005. doi: 10.1016/j.polymer.2005.03.083. URL https://doi.org/10.1016%2Fj.polymer.2005.03.083.

R. O. Ebewele. *Polymer Science and Technology*. CRC Press, 2000. ISBN 9781420057805. URL https://books.google.pt/books?id=jzc0CwAAQBAJ.

J. Faludi, C. Bayley, S. Bhogal, and M. Iribarne. *Green Manufacturing and Sustainable Manufacturing Partnership Comparing Environmental Impacts of Additive Manufacturing vs . Traditional Machining via Authors University of California*. PhD thesis, University of California Berkeley, 2014.

W. Fan, J. L. Li, Y. Y. Zheng, T. J. Liu, X. Tian, and R. J. Sun. Influence of thermo-oxidative aging on the thermal conductivity of carbon fiber fabric reinforced epoxy composites. *Polymer Degradation and Stability*, 123:162–169, 2016. ISSN 01413910. doi: 10.1016/j.polymdegradstab.2015.11.016. URL http://dx.doi.org/10.1016/j.polymdegradstab.2015.11.016.

S. Fehri, P. Cinelli, M.-b. Coltelli, I. Anguillesi, and A. Lazzeri. Thermal Properties of Plasticized Poly (Lactic Acid) (PLA) Containing Nucleating Agent. *International Journal of Chemical Engineering and Applications*, 7(2):85–88, 2016. ISSN 2010-0221. doi: 10.7763/ijcea.2016.v7.548.

I. Ferreira, D. Vale, M. Machado, and J. Lino. Additive manufacturing of polyethylene terephthalate glycol /carbon fiber composites: An experimental study from filament to printed parts. *Proceedings of the Institution of Mechanical Engineers, Part L: Journal of Materials: Design and Applications*, 0(0):1–13, 2018a. ISSN 20413076. doi: 10.1177/1464420718795197.

I. Ferreira, M. Machado, J. Lino Alves, and A. T. Marques. A review on fibre reinforced composite printing via FFF. *Rapid Prototyping Journal*, 25(6):972–988, jan 2019a. ISSN 1355-2546. doi: 10.1108/RPJ-01-2019-0004. URL https://doi.org/10.1108/RPJ-01-2019-0004.

I. Ferreira, D. Vale, M. Machado, and J. Lino. Additive manufacturing of polyethylene terephthalate glycol /carbon fiber composites: An experimental study from filament to printed parts. *Proceedings of the Institution of Mechanical Engineers, Part L: Journal of Materials: Design and Applications*, 233(9):1866–1878, 2019b. ISSN 20413076. doi: 10.1177/1464420718795197.

I. Ferreira, R. Madureira, S. Villa, A. M. P. de Jesus, M. Machado, and J. Lino Alves. Machinability of PA12 and short fibre reinforced PA12 materials produced by fused filament fabrication. *The International Journal of Advanced Manufacturing Technology*, 2020. doi: https://doi.org/10.1007/s00170-019-04839-z.

I. A. Ferreira and J. L. Alves. Low-cost 3D food printing. *Ciência & Tecnologia dos Materiais*, 29(1):e265–e269, 2017. ISSN 0870-8312. doi: http://dx.doi.org/10.1016/j.ctmat.2016.04.007. URL http://www.sciencedirect.com/science/article/pii/S0870831217300538.

I. A. Ferreira, T. ting Shen, M. Machado, R. Neto, and A. Reis. Mechanical characterization of FDM parts reinforced with continuous carbon fibers. In *International Conference on Direct Digital Manufacturing and Polymers 2017*, number May 2017. Conference: International Conference on Direct Digital Manufacturing and Polymers 2017, 2017a. doi: 10.13140/RG.2.2.31637.27368/1.

I. A. Ferreira, F. J. Lino, and M. Machado. Effect of layer filling path on mechanical properties of PA and PA-reinforced FDM parts. In *PMI2018 - International Conference on Polymers and Moulds Innovations*, number September, 2018b. doi: 10.13140/RG.2.2.21586.61124. URL https://www.researchgate.net/publication/334194737_Effect_of_layer_filling_path_on_mechanical_properties_of_PA_and_PA-reinforced_FDM_parts.

R. T. L. Ferreira, I. C. Amatte, T. A. Dutra, and D. Burger. Experimental characterization and micrography of 3d printed PLA and PLA reinforced with short carbon fibers. *Composites Part B: Engineering*, 124:88–100, sep 2017b. doi: 10.1016/j.compositesb.2017.05.013. URL https://doi.org/10.1016%2Fj.compositesb.2017.05.013.

Fillamentum. Nylon cf15 carbon material datasheet, 2019a. https://www.dropbox.com/sh/v7pxxt4kp4bbq0d/AAC2Scjno5kWqnL5IKVtMWDEa/TDS{_}Nylon{_}CF15{_}Carbon.pdf?dl=0, last accessed 13/9/2019.

Fillamentum. Nylon fx256 material datasheet, 2019b. https://www.dropbox.com/sh/v7pxxt4kp4bbq0d/AAC8CNuvZ7ZHUGPjD5dfVUQ{_}a/TDS{_}Nylon{_}FX256.pdf?dl=0, last accessed 13/9/2019.

A. Fischer, S. Rommel, and T. Bauernhansl. New Fiber Matrix Process with 3D Fiber Printer ? A Strategic In-process Integration of Endless Fibers Using Fused Deposition Modeling (FDM), 2013. URL http://dx.doi.org/10.1007/978-3-642-41329-2{_}17.

C. Fischer and D. Drummer. Crystallization and Mechanical Properties of Polypropylene under Processing-Relevant Cooling Conditions with respect to Isothermal Holding Time. *International Journal of Polymer Science*, 2016, 2016. ISSN 16879430. doi: 10.1155/2016/5450708.

E. W. Fischer. Effect of annealing and temperature on the morphological structure of polymers. *Pure and Applied Chemistry*, 31(1-2):113–131, 1972. ISSN 1365-3075. doi: 10.1351/pac197231010113. URL https://www.degruyter.com/view/j/pac.1972.31.issue-1-2/pac197231010113/pac197231010113.xml.

J. Fonseca, I. A. Ferreira, M. F. S. F. D. Moura, M. Machado, and J. L. Alves. Study of the interlaminar fracture under mode I loading on FFF printed parts. *Composite Structures*, 214 (January):316–324, 2019. ISSN 0263-8223. doi: 10.1016/j.compstruct.2019.02.005. URL https://doi.org/10.1016/j.compstruct.2019.02.005.

FormFutura. Technical Data Sheet Product: Carbonfill, 2019. URL https://www.formfutura.com/page/downloads.

J. Frankland. Cooling Tips for Crystalline Polymers. Technical report, Frankland Plastics Consulting, LLC, 2013. URL https://www.researchgate.net/publication/296952296{_}Cooling{_}tips{_}for{_}crystalline{_}polymers.

K. Friedrich and A. A. Almajid. Manufacturing aspects of advanced polymer composites for automotive applications. *Applied Composite Materials*, 20(2):107–128, 2013. ISSN 0929189X. doi: 10.1007/s10443-012-9258-7.

S. Fu. Effects of fiber length and fiber orientation distributions on the tensile strength of short-fiber-reinforced polymers. *Composites Science and Technology*, 56(10):1179–1190, 1996. doi: 10.1016/s0266-3538(96)00072-3. URL https://doi.org/10.1016%2Fs0266-3538%2896%2900072-3.

L. M. Galantucci, F. Lavecchia, and G. Percoco. Experimental study aiming to enhance the surface finish of fused deposition modeled parts. *CIRP Annals - Manufacturing Technology*, 58(1):189–192, 2009. ISSN 00078506. doi: 10.1016/j.cirp.2009.03.071.

E. García-Tuñon, S. Barg, J. Franco, R. Bell, S. Eslava, E. D'Elia, R. C. Maher, F. Guitian, and E. Saiz. Printing in three dimensions with Graphene. *Advanced Materials*, 27(10):1688–1693, 2015. ISSN 15214095. doi: 10.1002/adma.201405046.

G. GARDINER. 3D printing composites with continuous fiber. *Composites World*, pages 3–11, 2018. URL https://www.compositesworld.com/blog/post/3d-printing-composites-with-continuous-fiber.

J. M. Gardner, G. Sauti, J. W. Kim, R. J. Cano, R. A. Wincheski, C. J. Stelter, B. W. Grimsley, D. C. Working, and E. J. Siochi. 3-D printing of multifunctional carbon nanotube yarn reinforced

components. *Additive Manufacturing*, 12:38–44, 2016a. ISSN 22148604. doi: 10.1016/j.addma.2016.06.008. URL http://dx.doi.org/10.1016/j.addma.2016.06.008.

J. M. Gardner, G. Sauti, J.-W. Kim, R. J. Cano, R. A. Wincheski, C. J. Stelter, B. W. Grimsley, D. C. Working, and E. J. Siochi. 3-d printing of multifunctional carbon nanotube yarn reinforced components. *Additive Manufacturing*, 12:38–44, oct 2016b. doi: 10.1016/j.addma.2016.06.008. URL https://doi.org/10.1016%2Fj.addma.2016.06.008.

J. Gausemeier, N. Echterhoff, and M. Wall. Thinking ahead the Future of Additive Manufacturing Analysis of Promising Industries. *University of Paderborn Direct Manufacuring Research Center*, page 103, 2012. URL https://www.rtejournal.de/ausgabe9/3355/view?set{_}language=de.

M. Gebler, A. J. Schoot Uiterkamp, and C. Visser. A global sustainability perspective on 3D printing technologies. *Energy Policy*, 74(C):158–167, 2014. ISSN 03014215. doi: 10.1016/j.enpol.2014.08.033. URL http://dx.doi.org/10.1016/j.enpol.2014.08.033.

I. Gibson, D. Rosen, and B. Stucker. *Additive Manufacturing Technologies: 3D Printing, Rapid Prototyping, and Direct Digital Manufacturing*. SpringerLink : Bücher. Springer New York, 2014. ISBN 9781493921133. URL https://books.google.pt/books?id=OPGbBQAAQBAJ.

M. A. Gibson, N. M. Mykulowycz, J. Shim, R. Fontana, P. Schmitt, A. Roberts, J. Ketkaew, L. Shao, W. Chen, P. Bordeenithikasem, J. S. Myerberg, R. Fulop, M. D. Verminski, E. M. Sachs, Y. M. Chiang, C. A. Schuh, A. John Hart, and J. Schroers. 3D printing metals like thermoplastics: Fused filament fabrication of metallic glasses. *Materials Today*, 21(7):697–702, 2018. ISSN 18734103. doi: 10.1016/j.mattod.2018.07.001. URL https://doi.org/10.1016/j.mattod.2018.07.001.

P. B. Gning, D. Delsart, J. M. Mortier, and D. Coutellier. Through-thickness strength measurements using Arcan's method. *Composites Part B: Engineering*, 41(4):308–316, 2010. ISSN 13598368. doi: 10.1016/j.compositesb.2010.03.004. URL http://dx.doi.org/10.1016/j.compositesb.2010.03.004.

S. Gogolewski, K. Czerntawska, and M. Gastorek. Effect of annealing on thermal properties and crystalline structure of polyamides. Nylon 12 (polylaurolactam). *Colloid and Polymer Science Kolloid Zeitschrift & Zeitschrift fibre Polymere*, 258(10):1130–1136, 1980. ISSN 0303402X. doi: 10.1007/BF01382456.

G. D. Goh, S. Agarwala, G. L. Goh, V. Dikshit, S. L. Sing, and W. Y. Yeong. Additive manufacturing in unmanned aerial vehicles (UAVs): Challenges and potential. *Aerospace Science and Technology*, 63(April):140–151, 2017. ISSN 12709638. doi: 10.1016/j.ast.2016.12.019. URL http://dx.doi.org/10.1016/j.ast.2016.12.019.

G. D. Goh, V. Dikshit, A. P. Nagalingam, G. L. Goh, S. Agarwala, S. L. Sing, J. Wei, and W. Y. Yeong. Characterization of mechanical properties and fracture mode of additively manufactured carbon fiber and glass fiber reinforced thermoplastics. *Materials and Design*, 137:79–89, 2018. ISSN 18734197. doi: 10.1016/j.matdes.2017.10.021. URL https://doi.org/10.1016/j.matdes.2017.10.021.

A. Greco, C. E. Corcione, A. Strafella, and A. Maffezzoli. Analysis of the structure and mass transport properties of clay nanocomposites based on amorphous PET. *Journal of Applied Polymer Science*, 118(6):3666–3672, jul 2010. doi: 10.1002/app.32401. URL https://doi.org/10.1002%2Fapp.32401.

D. Gu, H. Wang, F. Chang, D. Dai, P. Yuan, Y. C. Hagedorn, and W. Meiners. Selective laser melting additive manufacturing of TiC/AlSi10Mg bulk-form nanocomposites with tailored microstructures and properties. *Physics Procedia*, 56(C):108–116, 2014. ISSN 18753892. doi: 10.1016/j.phpro.2014.08.153. URL http://dx.doi.org/10.1016/j.phpro.2014.08.153.

N. Guo and M. C. Leu. Additive manufacturing: technology, applications and research needs. *Frontiers of Mechanical Engineering*, 8(3):215–243, Sep 2013. ISSN 2095-0241. doi: 10.1007/s11465-013-0248-8. URL https://doi.org/10.1007/s11465-013-0248-8.

Q. Guo. *Polymer Morphology: Principles, Characterization, and Processing*. Wiley, 2016. ISBN 9781118892763. URL https://books.google.pt/books?id=2OvbCwAAQBAJ.

A. Gupta and A. A. Ogale. Dual curing of carbon fiber reinforced photoresins for rapid prototyping. *Polymer Composites*, 23(6):1162–1170, 2002. ISSN 02728397. doi: 10.1002/pc.10509.

R. Gupta. *Polymer and Composite Rheology*. Plastics Engineering. CRC Press, 2000. ISBN 9781482273700. URL https://books.google.pt/books?id=0UZZDwAAQBAJ.

K. Hachour, F. Zaïri, M. Naït-Abdelaziz, J. M. Gloaguen, M. Aberkane, and J. M. Lefebvre. Experiments and modeling of high-crystalline polyethylene yielding under different stress states. *International Journal of Plasticity*, 54:1–18, 2014. ISSN 07496419. doi: 10.1016/j.ijplas.2013.06.004. URL http://dx.doi.org/10.1016/j.ijplas.2013.06.004.

K. R. Hart, R. M. Dunn, J. M. Sietins, C. M. Hofmeister Mock, M. E. Mackay, and E. D. Wetzel. Increased fracture toughness of additively manufactured amorphous thermoplastics via thermal annealing. *Polymer*, 144:192–204, 2018. ISSN 00323861. doi: 10.1016/j.polymer.2018.04.024. URL https://doi.org/10.1016/j.polymer.2018.04.024.

M. Hoffmann, K. Zimmermann, B. Bautz, and P. Middendorf. A new specimen geometry to determine the through-thickness tensile strength of composite laminates. *Composites Part B: Engineering*, 77:145–152, 2015. ISSN 13598368. doi: 10.1016/j.compositesb.2015.03.020.

T. Hofstätter, I. W. Gutmann, T. Koch, D. B. Pedersen, G. Tosello, G. Heinz, and H. N. Hansen. Distribution and orientation of carbon fibers in polylactic acid parts produced by fused deposition modeling. *ASPE/euspen 2016 Summer Topical Meeting on Dimensional Accuracy and Surface Finish in Additive Manufacturing*, pages 44–49, 2016. URL https://www.scopus.com/inward/record.uri?eid=2-s2.0-84983483211{&}partnerID=40{&}md5=01872b7ebe2ff6adbd008631a2c32dbe.

J. Holmström, J. Partanen, J. Tuomi, M. Walter, C. O. A. Ayodeji Emmanuel Oke, and M. M. Raphiri. Rapid manufacturing in the spare parts supply chain: Alternative approaches to capacity deployment. *Journal of Manufacturing Technology Management*, 21(6):687–697, jul 2010. ISSN 1741-038X. doi: 10.1108/17410381011063996. URL https://doi.org/10.1108/17410381011063996.

D. Horvath, R. Noorani, and M. Mendelson. Improvement of Surface Roughness on ABS 400 Polymer Using Design of Experiments (DOE). *Materials Science Forum*, 561-565:2389–2392, 2007. ISSN 1662-9752. doi: 10.4028/www.scientific.net/MSF.561-565.2389. URL http://www.scientific.net/MSF.561-565.2389.

Z. Hou, X. Tian, J. Zhang, and D. Li. 3D printed continuous fibre reinforced composite corrugated structure. *Composite Structures*, 184(October):1005–1010, 2018. ISSN 02638223. doi: 10.1016/j.compstruct.2017.10.080. URL http://dx.doi.org/10.1016/j.compstruct.2017.10.080.

K. Hu, D. D. Kulkarni, I. Choi, and V. V. Tsukruk. Graphene-polymer nanocomposites for structural and functional applications. *Progress in Polymer Science*, 39(11):1934–1972, 2014. ISSN 00796700. doi: 10.1016/j.progpolymsci.2014.03.001. URL http://dx.doi.org/10.1016/j.progpolymsci.2014.03.001.

Q. Hu, Y. Duan, H. Zhang, D. Liu, B. Yan, and F. Peng. Manufacturing and 3D printing of continuous carbon fiber prepreg filament. *Journal of Materials Science*, 53(3):1887–1898, 2018. ISSN 15734803. doi: 10.1007/s10853-017-1624-2.

C. W. Hull. Apparatus for production of three-dimensional objects by stereolithography. *US Patent 4,575,330*, pages 1–16, 1986. ISSN 13596462. doi: 10.1145/634067.634234. URL http://www.google.com/patents/US4575330.

D. Hull and T. W. Clyne. *An Introduction to Composite Materials*. Cambridge Solid State Science Series, 1996. ISBN 9781139170130. doi: 10.1017/cbo9781139170130. URL http://ebooks.cambridge.org/ref/id/CBO9781139170130.

E. Hull, W. Grove, M. Zhang, X. Song, Z. J. Pei, and W. Cong. Effects of process variables on extrusion of carbon fiber reinforced ABS filament for additive manufacturing. *Proceedings of the ASME 2015 International Manufacturing Science and Engineering Conference*, 1:1–9, 2015. doi: 10.1115/MSEC20159396.

S. C. Hung and K. M. Liechti. An evaluation of the arcan specimen for determining the shear moduli of fiber-reinforced composites. *Experimental Mechanics*, 37(4):460–468, 1997. ISSN 00144851. doi: 10.1007/BF02317314.

S. in Park, N. Watanabe, and D. W. Rosen. Estimating failure of material extrusion truss structures based on deposition modeling and a cohesive zone model. *Materials and Design*, 147:122–133, 2018. ISSN 18734197. doi: 10.1016/j.matdes.2018.03.034. URL https://doi.org/10.1016/j.matdes.2018.03.034.

D. S. Inc. End-of-vector laser power control in a selective laser sintering system, 2000. URL http://www.google.com/patents/US6085122. US6085122.

International Organization for Standardization. ISO 1133-1:2011 - Plastics – Determination of the melt mass-flow rate (MFR) and melt volume-flow rate (MVR) of thermoplastics – Part 1: Standard method. *Geneva*, 2011.

International Organization for Standardization. ISO 527-1:2012 - Plastics – Determination of tensile properties – Part 1: General principles, 2012a.

International Organization for Standardization. EN ISO 527-2 - Determination of tensile properties of plastics - Test conditions for moulding and extrusion plastics, 2012b.

International Standards Organization. ISO 178:2010 - Plastics – Determination of flexural properties, 2010.

M. S. Islam and P. Prabhakar. Interlaminar strengthening of multidirectional laminates using polymer additive manufacturing. *Materials and Design*, 133:332–339, 2017. ISSN 18734197. doi: 10.1016/j.matdes.2017.07.038. URL http://dx.doi.org/10.1016/j.matdes.2017.07.038.

ISO 4288:1996 Geometrical Product Specifications (GPS). Surface texture: Profile method-Rules and procedures for the assessment of surface texture (ISO 4288: 1996). In *German version EN ISO*. ISO, 1997. doi: 10.1186/s40557-016-0111-6.

ISO/ASTM. INTERNATIONAL STANDARD ISO / ASTM 52900 Additive manufacturing: General principles: Terminology, 2015. URL https://www.iso.org/obp/ui/{#}iso:std:69669:en{%}0Ahttps://www.iso.org/standard/69669.html{%}0Ahttps://www.astm.org/Standards/ISOASTM52900.htm.

R. Izamshah, M. A. Azam, M. Hadzley, M. A. Ali, M. S. Kasim, and M. S. Abdul. Study of surface roughness on milling unfilled- polyetheretherketones engineering plastics. *Procedia Engineering*, 68:654–660, 2013. ISSN 1877-7058. doi: 10.1016/j.proeng.2013.12.235. URL http://dx.doi.org/10.1016/j.proeng.2013.12.235.

A. Jansson and L. Pejryd. Characterisation of carbon fibre-reinforced polyamide manufactured by selective laser sintering. *Additive Manufacturing*, 9:7–13, 2016. ISSN 22148604. doi: 10.1016/j.addma.2015.12.003. URL http://dx.doi.org/10.1016/j.addma.2015.12.003.

D. Jiang and D. E. Smith. Anisotropic mechanical properties of oriented carbon fiber filled polymer composites produced with fused filament fabrication. *Additive Manufacturing*, 18:84–94, 2017. ISSN 22148604. doi: 10.1016/j.addma.2017.08.006. URL https://doi.org/10.1016/j.addma.2017.08.006.

R. Jones, P. Haufe, E. Sells, P. Iravani, V. Olliver, C. Palmer, and A. Bowyer. Reprap - The replicating rapid prototyper. *Robotica*, 29(1 SPEC. ISSUE):177–191, 2011. ISSN 02635747. doi: 10.1017/S026357471000069X.

J. Justo, L. Távara, L. García-Guzmán, and F. París. Characterization of 3D printed long fibre reinforced composites. *Composite Structures*, 185(November 2017):537–548, 2018. ISSN 02638223. doi: 10.1016/j.compstruct.2017.11.052. URL https://doi.org/10.1016/j.compstruct.2017.11.052.

K. K. Kar, R. Sharma, and K. K. Kar. *Composite Materials: Processing, Applications, Characterizations*. Springer Berlin Heidelberg, 2016. ISBN 9783662495148. doi: 10.1007/978-3-662-49514-8_17. URL https://books.google.pt/books?id=GqZDDQAAQBAJ.

F. Kara. Taguchi optimization of surface roughness and flank wear during the turning of DIN 1.2344 tool steel. *Materialpruefung/Materials Testing*, 2017. ISSN 00255300. doi: 10.3139/120.111085.

F. Kara and B. Öztürk. Comparison and optimization of PVD and CVD method on surface roughness and flank wear in hard-machining of DIN 1.2738 mold steel. *Sensor Review*, 39(1):24–33, 2019. ISSN 02602288. doi: 10.1108/SR-12-2017-0266.

M. Karabatak and F. Kara. Experimental Optimization of Surface Roughness in Hard Turning of AISI D2 Cold Work Tool Steel. *JOURNAL OF POLYTECHNIC-POLITEKNIK DERGISI*, 19 (3):349–355, 2016. ISSN 1302-0900.

M. Kattan, E. Dargent, and J. Grenet. Three phase model in drawn thermoplastic polyesters: comparison of differential scanning calorimetry and thermally stimulated depolarisation current experiments. *Polymer*, 43(4):1399–1405, feb 2002. doi: 10.1016/s0032-3861(01)00719-4. URL https://doi.org/10.1016%2Fs0032-3861%2801%2900719-4.

T. Kenneth. Method and apparatus for continuous composite three-dimiensional printing, 2014. URL https://patents.google.com/patent/US20140061974A1/en. US 2014/0061974 A1.

M. H. Khaliq, R. Gomes, C. Fernandes, J. Nóbrega, O. S. Carneiro, L. L. Ferrás, and F. Authors. On the use of high viscosity polymers in the fused filament fabrication process. *Rapid Prototyping Journal*, 23(4):727–735, may 2017. ISSN 1355-2546. doi: 10.1108/RPJ-02-2016-0027. URL https://doi.org/10.1108/RPJ-02-2016-0027.

J. H. Kim, W. S. Chang, D. Kim, J. R. Yang, J. T. Han, G. W. Lee, J. T. Kim, and S. K. Seol. 3D printing of reduced graphene oxide nanowires. *Advanced Materials*, 27(1):157–161, 2015. ISSN 15214095. doi: 10.1002/adma.201404380.

V. Kishore, X. Chen, C. Ajinjeru, A. A. Hassen, J. Lindahl, J. Failla, V. Kunc, and C. Duty. Additive Manufacturing of High Performance Semicrystalline Thermoplastics and Their Composites. *Proceedings of the 27th Annual International Solid Freeform Fabrication Symposium An Additive Manufacturing Conference*, pages 906–915, 2016.

F. V. D. Klift, Y. Koga, A. Todoroki, M. Ueda, and Y. Hirano. 3D Printing of Continuous Carbon Fibre Reinforced Thermo-Plastic (CFRTP) Tensile Test Specimens. *Open Journal of Composite Materials*, 6(January):18–27, 2016. doi: 10.4236/ojcm.2016.61003. URL http://www.scirp.org/journal/ojcm{%}5Cnhttp://dx.doi.org/10.4236/ojcm.2016.61003{%}5Cnhttp://creativecommons.org/licenses/by/4.0/.

H. Klug and L. Alexander. *X-ray Diffraction Procedures for Polycrystalline and Amorphous Materials*. Wiley, 1954. URL https://books.google.pt/books?id=VOVAqMOCUwAC.

C. Koch, L. Van Hulle, and N. Rudolph. Investigation of mechanical anisotropy of the fused filament fabrication process via customized tool path generation. *Additive Manufacturing*, 16: 138–145, 2017. ISSN 22148604. doi: 10.1016/j.addma.2017.06.003. URL http://dx.doi.org/10.1016/j.addma.2017.06.003.

J.-P. Kruth, M. Leu, and T. Nakagawa. Progress in additive manufacturing and rapid prototyping. *CIRP Annals*, 47(2):525–540, 1998. doi: 10.1016/s0007-8506(07)63240-5. URL https://doi.org/10.1016%2Fs0007-8506%2807%2963240-5.

J. P. Kruth, G. Levy, F. Klocke, and T. H. Childs. Consolidation phenomena in laser and powder-bed based layered manufacturing. *CIRP Annals - Manufacturing Technology*, 56(2):730–759, 2007. ISSN 00078506. doi: 10.1016/j.cirp.2007.10.004.

S. Kumar and J. P. Kruth. Composites by rapid prototyping technology. *Materials and Design*, 31 (2):850–856, 2010. ISSN 02641275. doi: 10.1016/j.matdes.2009.07.045.

A. Lalehpour and A. Barari. Post processing for Fused Deposition Modeling Parts with Acetone Vapour Bath. *IFAC-PapersOnLine*, 49(31):42–48, 2016. ISSN 24058963. doi: 10.1016/j.ifacol.2016.12.159. URL http://dx.doi.org/10.1016/j.ifacol.2016.12.159.

K. Lam, A. A. Bakar, and Z. M. Ishak. Effects of compatibilizer and testing speed on the mechanical and morphology behaviors of co-continuous amorphous copolyester-polyoxymethylene

blends. *Polymer Engineering & Science*, 45(5):710–719, 2005. doi: 10.1002/pen.20329. URL https://doi.org/10.1002%2Fpen.20329.

W. C. Lee, C. C. Wei, and S. C. Chung. Development of a hybrid rapid prototyping system using low-cost fused deposition modeling and five-axis machining. *Journal of Materials Processing Technology*, 214(11):2366–2374, 2014. ISSN 09240136. doi: 10.1016/j.jmatprotec.2014.05.004. URL http://dx.doi.org/10.1016/j.jmatprotec.2014.05.004.

J. Li, T. Monaghan, T. Nguyen, R. Kay, R. Friel, and R. Harris. Multifunctional metal matrix composites with embedded printed electrical materials fabricated by ultrasonic additive manufacturing. *Composites Part B: Engineering*, 113:342–354, mar 2017. doi: 10.1016/j.compositesb.2017.01.013. URL https://doi.org/10.1016%2Fj.compositesb.2017.01.013.

N. Li, Y. Li, and S. Liu. Rapid prototyping of continuous carbon fiber reinforced polylactic acid composites by 3D printing. *Journal of Materials Processing Technology*, 238:218–225, 2016. ISSN 09240136. doi: 10.1016/j.jmatprotec.2016.07.025. URL http://dx.doi.org/10.1016/j.jmatprotec.2016.07.025.

G. Liao, Z. Li, Y. Cheng, D. Xu, D. Zhu, S. Jiang, J. Guo, X. Chen, G. Xu, and Y. Zhu. Properties of oriented carbon fiber/polyamide 12 composite parts fabricated by fused deposition modeling. *Materials and Design*, 139:283–292, 2018. ISSN 18734197. doi: 10.1016/j.matdes.2017.11.027. URL https://doi.org/10.1016/j.matdes.2017.11.027.

H. Lipson and M. Kurman. *Fabricated: The New World of 3D Printing*. Wiley, 2013. ISBN 9781118410240. URL https://books.google.pt/books?id=IuOGAQP0CD8C.

R. Liu, Z. Wang, T. Sparks, F. Liou, and J. Newkirk. Aerospace applications of laser additive manufacturing. In *Laser Additive Manufacturing*, pages 351–371. Elsevier, 2017. doi: 10.1016/b978-0-08-100433-3.00013-0. URL https://doi.org/10.1016%2Fb978-0-08-100433-3.00013-0.

Z. Liu, Q. Lei, and S. Xing. Mechanical characteristics of wood, ceramic, metal and carbon fiber-based PLA composites fabricated by FDM. *Journal of Materials Research and Technology*, 8(5):3743–3753, 2019. ISSN 22387854. doi: 10.1016/j.jmrt.2019.06.034. URL https://linkinghub.elsevier.com/retrieve/pii/S2238785419301905.

C. Mahajan and D. Cormier. 3D Printing of Carbon Fiber Composites With Preferentially Aligned Fibers. *Proceedings of the 2015 Industrial and Systems Engineering Reserach Conference*, pages 2953–2963, 2015.

L. Man Chun and M. Kowalik. Preliminary studies for alternative lattice core design for FDM 3D Printed Sandwich Panels. *Materials Today: Proceedings*, 5(13):26519–26525, 2018. ISSN 22147853. doi: 10.1016/j.matpr.2018.08.110.

J. P. Manaia. *Deformation Behaviour of Semi Crystalline Polymers under Different Stress States*. PhD thesis, Faculdade de Engenharia Universidade do Porto, 2018.

J. P. Manaia, F. A. Pires, A. M. P. de Jesus, and S. Wu. Yield behaviour of high-density polyethylene: Experimental and numerical characterization. *Engineering Failure Analysis*, 97:331–353, 2019. ISSN 1350-6307. doi: https://doi.org/10.1016/j.engfailanal.2019.01.001. URL http://www.sciencedirect.com/science/article/pii/S1350630718313086.

G. P. Marinella Levi, Gabriele Natale. Apparecchiatura e metodo per la stampa tridimensionale di materiali compositi a fibra continua, 2015.

G. T. Mark. Methods for fiber reinforced additive manufacturing, dec 2014. URL https://www.google.com/patents/WO2014197732A2?cl=en.

G. T. Mark and A. S. Gozdz. Three dimensional printer with composite filament fabrication, oct 2015. URL https://www.google.com/patents/US9156205.

©Markforged. Mechanical Properties of Continuous Fibers Mechanical Properties, 2016.

A. T. Marques, J. Pereira, R. Neto, S. Esteves, R. Moreira, J. Matos, L. Reis, I. Ribeiro, M. Leite, I. Ferreira, M. Machado, R. Gomes, S. Mould, J. Pinto, T. G. Santos, B. Fernandes, M. T. Cidade, A. Velhinho, A. J. Pontes, J. P. Nunes, and F. Duarte. Additive Manufacturing Based Hybrid Process for Long or Continuous Fibre Reinforced Polymeric Matrix. In *XIII Iberoamerican Conference on Mechanical Engineering (CIBEM 2017)*, 2017.

B. Martin. Raw material pricing and Additive Manufacturing. *Engineering and Physical Sciences Research Council*, pages 1–13, 2014. URL http://www.3dprintingmaterialsconference.com/wp-content/uploads/2014/06/MB{_}Raw{_}Materials{_}3.pdf.

S. H. Masood. *Advances in Fused Deposition Modeling*, volume 10. Elsevier, 2014. ISBN 9780080965338. doi: 10.1016/B978-0-08-096532-1.01002-5. URL http://dx.doi.org/10.1016/B978-0-08-096532-1.01002-5.

S. H. Masood, K. Mau, and W. Song. Tensile Properties of Processed FDM Polycarbonate Material. *Materials Science Forum*, 654-656:2556–2559, 2010. ISSN 1662-9752. doi: 10.4028/www.scientific.net/MSF.654-656.2556. URL http://www.scientific.net/MSF.654-656.2556.

Mathematisch-naturwissenschaftliche Fakult. Advanced Lab: DSC Investigation of Polymers, 2015. URL https://polymerscience.physik.hu-berlin.de/docs/manuals/DSC.pdf.

R. Matsuzaki, M. Ueda, M. Namiki, T.-K. Jeong, H. Asahara, K. Horiguchi, T. Nakamura, A. Todoroki, and Y. Hirano. Three-dimensional printing of continuous-fiber composites by

in-nozzle impregnation. *Scientific reports*, 6(February):23058, 2016. ISSN 2045-2322. doi: 10.1038/srep23058. URL http://www.nature.com/srep/2016/160311/srep23058/full/srep23058.html.

A. Mayyas, A. Qattawi, M. Omar, and D. Shan. Design for sustainability in automotive industry: A comprehensive review. *Renewable and Sustainable Energy Reviews*, 16(4):1845–1862, 2012. ISSN 13640321. doi: 10.1016/j.rser.2012.01.012. URL http://dx.doi.org/10.1016/j.rser.2012.01.012.

P. McAlea, Kevin; Forderhase and B. Richard. SELECTIVE LASER SINTERING OF POLYMER POWDER OF CONTROLLED PARTICLE SIZE DISTRIBUTION. *United States Patent*, 53 (9), 1998. ISSN 00108049. doi: 10.1016/j.(73).

L. W. McKeen. 2 - Introduction to Plastics and Polymers. In L. W. McKeen, editor, *Permeability Properties of Plastics and Elastomers (Fourth Edition)*, Plastics Design Library, pages 21–40. William Andrew Publishing, fourth edition edition, 2017. ISBN 978-0-323-50859-9. doi: https://doi.org/10.1016/B978-0-323-50859-9.00002-6. URL http://www.sciencedirect.com/science/article/pii/B9780323508599000026.

W. Meiners, K. Wissenbach, and A. Gasser. Selective laser sintering at melting temperature, 2001. URL https://patentimages.storage.googleapis.com/89/28/63/fa9ae32a5e8098/US6215093.pdf.

G. W. Melenka, B. K. O. Cheung, J. S. Schofield, M. R. Dawson, and J. P. Carey. Evaluation and prediction of the tensile properties of continuous fiber-reinforced 3D printed structures. *Composite Structures*, 153:866–875, 2016. ISSN 02638223. doi: 10.1016/j.compstruct.2016.07.018. URL http://dx.doi.org/10.1016/j.compstruct.2016.07.018.

C. Melo. *Estudo da influência do pós-processamento de recozimento nas propriedades mecânicas de peças poliméricas fabricadas por impressão 3D*. PhD thesis, Master thesis of MIEM, Faculty of Engineering of the University of Porto, 2019.

A. Melocchi, F. Parietti, A. Maroni, A. Foppoli, A. Gazzaniga, and L. Zema. Hot-melt extruded filaments based on pharmaceutical grade polymers for 3D printing by fused deposition modeling. *International Journal of Pharmaceutics*, 509(1-2):255–263, 2016. ISSN 18733476. doi: 10.1016/j.ijpharm.2016.05.036. URL http://dx.doi.org/10.1016/j.ijpharm.2016.05.036.

C. Mims. 3D printing will explode in 2014, thanks to the expiration of key patents. *Quartz Media LLC.*, 2013.

V. Mirón, S. Ferrándiz, D. Juárez, and A. Mengual. Manufacturing and characterization of 3D printer filament using tailoring materials. *Procedia Manufacturing*, 13:888–894, 2017. ISSN 23519789. doi: 10.1016/j.promfg.2017.09.151. URL https://doi.org/10.1016/j.promfg.2017.09.151.

O. A. Mohamed, S. H. Masood, and J. L. Bhowmik. Optimization of fused deposition modeling process parameters: a review of current research and future prospects. *Advances in Manufacturing*, 3(1):42–53, 2015. ISSN 21953597. doi: 10.1007/s40436-014-0097-7.

N. Mohan, P. Senthil, S. Vinodh, and N. Jayanth. A review on composite materials and process parameters optimisation for the fused deposition modelling process. *Virtual and Physical Prototyping*, 12(1):47–59, 2017. ISSN 1745-2759. doi: 10.1080/17452759.2016.1274490. URL http://dx.doi.org/10.1080/17452759.2016.1274490.

D. Mohr and M. Doyoyo. Analysis of the Arcan Apparatus in the. *Journal of Composite Materials*, 36(22):2583–2594, 2009. ISSN 0021998027. doi: 10.1106/002199802027874. URL http://www.diapedia.org/other-types-of-diabetes-mellitus/4104085115.

R. Moreira. Conceiving a non-contact Measurement System for the Polymer Temperature at the Nozzle Exit of a FDM 3D Printer, 2016.

K.-I. Mori, T. Maeno, and Y. Nakagawa. Dieless forming of carbon fibre reinforced plastic parts using 3D printer. *Procedia Engineering*, 81(October):1595–1600, 2014. ISSN 18777058. doi: 10.1016/j.proeng.2014.10.196. URL www.sciencedirect.com.

Y. Nakagawa, K.-i. Mori, and T. Maeno. 3D printing of carbon fibre-reinforced plastic parts. *The International Journal of Advanced Manufacturing Technology*, pages 1–7, 2017. ISSN 0268-3768, 1433-3015. doi: 10.1007/s00170-016-9891-7. URL https://link.springer.com/article/10.1007/s00170-016-9891-7.

M. Namiki, M. Ueda, A. Todoroki, Y. Hirano, and R. Matsuzaki. 3D Printing of Continuous Fiber Reinforced. *Proceedings of the Society of the Advancement of Material and Process Engineering 2014, Seattle, 2-5 June 2014, 6*, pages 2–7, 2014.

T. Nancharaiah, D. R. Raju, and V. R. Raju. An experimental investigation on surface quality and dimensional accuracy of FDM components. *International Journal on Emerging Technologies*, 1(2):106–111, 2010.

R. Narang and D. Chhabra. Analysis of Process Parameters of Fused Deposition Modeling (FDM) Technique. *International Journal on Future Revolution in Computer Science & Communication Engineering IJFRCSCE*, 3(October 2017):41–48, 2017. ISSN 2454-4248. URL http://www.ijfrcsce.org.

C. Narsimlu, K; Pathak G. Arhendu; Mulky G. Avinash; Yavarna. A market analysis on the impact of additive layer manufacturing technologies on aerospace and defense supply chain. *Internationa Journal of Management*, 8(2):171–187, 2017.

T. D. Ngo, A. Kashani, G. Imbalzano, K. T. Nguyen, and D. Hui. Additive manufacturing (3D printing): A review of materials, methods, applications and challenges. *Composites Part B: Engineering*, 143(December 2017):172–196, 2018. ISSN 13598368. doi: 10.1016/j.compositesb.2018.02.012. URL https://doi.org/10.1016/j.compositesb.2018.02.012.

M. Nikzad, S. H. Masood, and I. Sbarski. Thermo-mechanical properties of a highly filled polymeric composites for Fused Deposition Modeling. *Materials and Design*, 32(6):3448–3456, 2011. ISSN 02641275. doi: 10.1016/j.matdes.2011.01.056. URL http://dx.doi.org/10.1016/j.matdes.2011.01.056.

F. Ning, W. Cong, J. Qiu, J. Wei, and S. Wang. Additive manufacturing of carbon fiber reinforced thermoplastic composites using fused deposition modeling. *Composites Part B: Engineering*, 80:369–378, 2015. ISSN 13598368. doi: 10.1016/j.compositesb.2015.06.013. URL http://dx.doi.org/10.1016/j.compositesb.2015.06.013.

J. Norman, R. D. Madurawe, C. M. Moore, M. A. Khan, and A. Khairuzzaman. A new chapter in pharmaceutical manufacturing: 3d-printed drug products. *Advanced Drug Delivery Reviews*, 108:39–50, jan 2017. doi: 10.1016/j.addr.2016.03.001. URL https://doi.org/10.1016%2Fj.addr.2016.03.001.

A. Peng, X. Xiao, and R. Yue. Process parameter optimization for fused deposition modeling using response surface methodology combined with fuzzy inference system. *The International Journal of Advanced Manufacturing Technology*, 73(1-4):87–100, 2014. ISSN 0268-3768. doi: 10.1007/s00170-014-5796-5. URL http://link.springer.com/10.1007/s00170-014-5796-5.

I. J. Petrick and T. W. Simpson. Point of View: 3D Printing Disrupts Manufacturing: How Economies of One Create New Rules of Competition. *Research-Technology Management*, 56(6):12–16, 2013. ISSN 08956308. doi: 10.5437/08956308X5606193. URL http://openurl.ingenta.com/content/xref?genre=article{&}issn=0895-6308{&}volume=56{&}issue=6{&}spage=12.

D. Phillips. Fiber-reinforced ceramics. In R. BROOK, editor, *Concise Encyclopedia of Advanced Ceramic Materials*, pages 155 – 160. Pergamon, Oxford, 1991. ISBN 978-0-08-034720-2. doi: https://doi.org/10.1016/B978-0-08-034720-2.50049-6. URL http://www.sciencedirect.com/science/article/pii/B9780080347202500496.

Politecnico Milano 1893. ATROPOS, Redefine Manufacturing, + LAB, 2014.

J. D. Prince. 3d printing: An industrial revolution. *Journal of Electronic Resources in Medical Libraries*, 11(1):39–45, 2014. doi: 10.1080/15424065.2014.877247. URL https://doi.org/10.1080/15424065.2014.877247.

H. Prüß and T. Vietor. Design for Fiber-Reinforced Additive Manufacturing. *Journal of Mechanical Design*, 137(11):111409, 2015. ISSN 1050-0472. doi: 10.1115/1.4030993. URL http://mechanicaldesign.asmedigitalcollection.asme.org/article.aspx?doi=10.1115/1.4030993.

K. R. Rajeesh, R. Gnanamoorthy, and R. Velmurugan. Effect of humidity on the indentation hardness and flexural fatigue behavior of polyamide 6 nanocomposite. *Materials Science and*

Engineering A, 527(12):2826–2830, 2010. ISSN 09215093. doi: 10.1016/j.msea.2010.01.070. URL http://dx.doi.org/10.1016/j.msea.2010.01.070.

S. Rangisetty and L. D. Peel. The effect of infill patterns and annealing on mechanical properties of additively manufactured thermoplastic composites. In *Proceedings of the ASME 2017 Conference on Smart Materials, Adaptive Structures and Intelligent Systems*, pages 1–12, 2017.

B. Redwood, F. Schöffer, and B. Garret. *The 3D Printing Handbook: Technologies, Design and Applications*. 3D Hubs B.V., 2017. ISBN 9789082748505. URL https://books.google.pt/books?id=R3OvswEACAAJ.

M.-j. J. Rietema. *Design of a prototype machine for 3D printing with continious fibre reinforcement*. PhD thesis, University of Twente, jun 2015. URL http://essay.utwente.nl/71622/.

D. Ronca, F. Langella, M. Chierchia, U. D'Amora, T. Russo, M. Domingos, A. Gloria, P. Bartolo, and L. Ambrosio. Bone Tissue Engineering: 3D PCL-based Nanocomposite Scaffolds with Tailored Properties. *Procedia CIRP*, 49:51–54, 2016. ISSN 22128271. doi: 10.1016/j.procir.2015.07.028. URL http://dx.doi.org/10.1016/j.procir.2015.07.028.

D. V. Rosato and M. G. Rosato. *Injection Molding Handbook*. Springer US, 2012. ISBN 9781461370772. URL https://books.google.pt/books?id=eihOnwEACAAJ.

D. B. Russell, T. Anderson, J. F. Bredt, M. J. Vogel, M. Seymour, W. J. Bornhorst, and M. I. Hatsopoulos. Method and apparatus for prototyping a three-dimensional object, 1999. URL https://www.google.com/patents/US6007318.

M. Rybachuk, C. Alice Mauger, T. Fiedler, and A. Öchsner. Anisotropic mechanical properties of fused deposition modeled parts fabricated by using acrylonitrile butadiene styrene polymer. *Journal of Polymer Engineering*, 37(7):699–706, 2017. ISSN 03346447. doi: 10.1515/polyeng-2016-0263.

Ryosuke Matsuzaki (Tokyo University). *3D Printer Using Continuous Carbon Fiber Composite Materials*. PhD thesis, Tokyo University of Science, Tokyo, 2013. URL http://www.nature.com/articles/srep23058.

E. M. Sachs, J. S. Haggerty, M. J. Cima, and P. A. Williams. Three-dimensional printing techniques, aug 1994. URL https://www.google.com/patents/US5340656.

A. Salem Bala, S. bin Wahab, and M. binti Ahmad. Elements and Materials Improve the FDM Products: A Review. *Advanced Engineering Forum*, 16:33–51, 2016. ISSN 2234-991X. doi: 10.4028/www.scientific.net/AEF.16.33. URL http://www.scientific.net/AEF.16.33.

S. Samborski. Numerical analysis of the DCB test configuration applicability to mechanically coupled Fiber Reinforced Laminated Composite beams. *Composite Structures*, 152:477–487,

2016. ISSN 02638223. doi: 10.1016/j.compstruct.2016.05.060. URL http://dx.doi.org/10.1016/j.compstruct.2016.05.060.

L. Sang, C. Wang, Y. Wang, and Z. Wei. Thermo-oxidative ageing effect on mechanical properties and morphology of short fibre reinforced polyamide composites-comparison of carbon and glass fibres. *RSC Advances*, 7(69):43334–43344, 2017. ISSN 20462069. doi: 10.1039/c7ra07884f.

L. Santana, J. Lino Alves, and A. da Costa Sabino Netto. A study of parametric calibration for low cost 3D printing: Seeking improvement in dimensional quality. *Materials and Design*, 135: 159–172, 2017. ISSN 18734197. doi: 10.1016/j.matdes.2017.09.020. URL https://doi.org/10.1016/j.matdes.2017.09.020.

J. Schindelin, I. Arganda-Carreras, E. Frise, V. Kaynig, M. Longair, T. Pietzsch, S. Preibisch, C. Rueden, S. Saalfeld, B. Schmid, J.-Y. Tinevez, D. J. White, V. Hartenstein, K. Eliceiri, P. Tomancak, and A. Cardona. Fiji: an open-source platform for biological-image analysis. *Nature Methods*, 9:676, jun 2012. URL https://doi.org/10.1038/nmeth.2019http://10.0.4.14/nmeth.2019https://www.nature.com/articles/nmeth.2019{#}supplementary-information.

C. A. Schneider, W. S. Rasband, and K. W. Eliceiri. NIH image to ImageJ: 25 years of image analysis. *Nature Methods*, 9(7):671–675, jul 2012. doi: 10.1038/nmeth.2089. URL https://doi.org/10.1038%2Fnmeth.2089.

F. Schoffer. How expiring patents are ushering in the next generation of 3D printing | TechCrunch, 2016. URL https://techcrunch.com/2016/05/15/how-expiring-patents-are-ushering-in-the-next-generation-of-3d-printing/.

A. T. T. Shen. Mechanical Characterization of Polymer Matrix Composites Produced by 3D Printing, 2017.

M. L. Shofner, K. Lozano, F. J. Rodríguez-Macías, and E. V. Barrera. Nanofiber-reinforced polymers prepared by fused deposition modeling. *Journal of Applied Polymer Science*, 89(11): 3081–3090, 2003. ISSN 00218995. doi: 10.1002/app.12496.

D. Singh, R. Singh, and K. S. Boparai. Development and surface improvement of FDM pattern based investment casting of biomedical implants: A state of art review. *Journal of Manufacturing Processes*, 31:80–95, 2018. ISSN 15266125. doi: 10.1016/j.jmapro.2017.10.026. URL http://dx.doi.org/10.1016/j.jmapro.2017.10.026.

J. Singh, R. Singh, and H. Singh. Repeatability of linear and radial dimension of ABS replicas fabricated by fused deposition modelling and chemical vapor smoothing process: A case study. *Measurement: Journal of the International Measurement Confederation*, 94:5–11, 2016. ISSN 02632241. doi: 10.1016/j.measurement.2016.07.064. URL http://dx.doi.org/10.1016/j.measurement.2016.07.064.

R. Singh and S. Singh. Additive Manufacturing: An Overview. In *Reference Module in Materials Science and Materials Engineering*, number May, pages 1–8. Elsevier, 2017. ISBN 978-0-12-803581-8. doi: 10.1016/b978-0-12-803581-8.04165-5. URL https://www.researchgate.net/publication/312005775_Additive_Manufacturing_An_Overview.

R. Singh, R. Kumar, and M. S. J. Hashmi. Friction Welding of Dissimilar Plastic-Based Material by Metal Powder Reinforcement. In *Reference Module in Materials Science and Materials Engineering*. Elsevier, 2017a. ISBN 978-0-12-803581-8. doi: https://doi.org/10.1016/B978-0-12-803581-8.04159-X. URL http://www.sciencedirect.com/science/article/pii/B978012803581804159X.

R. Singh, S. Singh, I. P. Singh, F. Fabbrocino, and F. Fraternali. Investigation for surface finish improvement of FDM parts by vapor smoothing process. *Composites Part B: Engineering*, 111:228–234, 2017b. ISSN 13598368. doi: 10.1016/j.compositesb.2016.11.062. URL http://dx.doi.org/10.1016/j.compositesb.2016.11.062.

E. Smith. *Single-point turning of amorphous thermoplastic polymers*. PhD thesis, North Carolina State University, 1989.

P. Song, Z. Cao, Y. Cai, L. Zhao, Z. Fang, and S. Fu. Fabrication of exfoliated graphene-based polypropylene nanocomposites with enhanced mechanical and thermal properties. *Polymer*, 52 (18):4001–4010, 2011. ISSN 00323861. doi: 10.1016/j.polymer.2011.06.045. URL http://dx.doi.org/10.1016/j.polymer.2011.06.045.

A. K. Sood, R. K. Ohdar, and S. S. Mahapatra. Improving dimensional accuracy of Fused Deposition Modelling processed part using grey Taguchi method. *Materials and Design*, 30 (10):4243–4252, 2009. ISSN 02641275. doi: 10.1016/j.matdes.2009.04.030. URL http://dx.doi.org/10.1016/j.matdes.2009.04.030.

A. K. Sood, R. K. Ohdar, and S. S. Mahapatra. Parametric appraisal of mechanical property of fused deposition modelling processed parts. *Materials and Design*, 31(1):287–295, 2010. ISSN 02641275. doi: 10.1016/j.matdes.2009.06.016. URL http://dx.doi.org/10.1016/j.matdes.2009.06.016.

A. Sorrentino, I. National, F. D. Santis, and G. Titomanlio. *Progress in Understanding of Polymer Crystallization*. Number April. Springer, 2007. ISBN 3540473076. doi: 10.1007/3-540-47307-6.

M. Spoerk, F. Arbeiter, H. Cajner, J. Sapkota, and C. Holzer. Parametric optimization of intra- and inter-layer strengths in parts produced by extrusion-based additive manufacturing of poly(lactic acid). *Journal of Applied Polymer Science*, 134(41):1–15, 2017. ISSN 10974628. doi: 10.1002/app.45401.

Stratasys. PC (polycarbonate) Data Sheet.

L. J. Struble and X. Ji. 9 - rheology. In V. Ramachandran and J. J. Beaudoin, editors, *Handbook of Analytical Techniques in Concrete Science and Technology*, pages 333 – 367. William Andrew Publishing, Norwich, NY, 2001. ISBN 978-0-8155-1437-4. doi: https://doi.org/10.1016/B978-081551437-4.50012-6. URL http://www.sciencedirect.com/science/article/pii/B9780815514374500126.

W. J. Swanson and P. Hopkins. Thin-wall tube liquifier, 1991. ISSN 2004001828.

R. Swartz, B. CRIST, and J. Fallon. Methods and apparatus for 3d fabrication, mar 2013. URL https://www.google.pt/patents/WO2013033273A2?cl=en.

Taulman3D. Alloy 910 Datasheet, 2019. http://taulman3d.com/alloy-910-spec.html, last accessed 13/9/2019.

H. L. Tekinalp, V. Kunc, G. M. Velez-Garcia, C. E. Duty, L. J. Love, A. K. Naskar, C. A. Blue, and S. Ozcan. Highly oriented carbon fiber?polymer composites via additive manufacturing. *Composites Science and Technology*, 105:144–150, 2014. ISSN 02663538. doi: 10.1016/j.compscitech.2014.10.009.

©Markforged Inc. FFF Nylon Filament Safety Data Sheet, 2015. URL http://ww3.cad.de/foren/ubb/uploads/4M/FFF{_}Nylon{_}Filament{_}SDS{_}US{_}111915{_}Draft.pdf.

J. L. Thomason. The influence of fibre length and concentration on the properties of glass fibre reinforced polypropylene: 5. Injection moulded long and short fibre PP. *Composites Part A: Applied Science and Manufacturing*, 33(12):1641–1652, 2002. ISSN 1359835X. doi: 10.1016/S1359-835X(02)00179-3.

E. T. Thostenson, W. Z. Li, D. Z. Wang, Z. F. Ren, and T. W. Chou. Carbon nanotube/carbon fiber hybrid multiscale composites. *Journal of Applied Physics*, 91(9):6034–6037, may 2002. doi: 10.1063/1.1466880. URL https://doi.org/10.1063%2F1.1466880.

X. Tian, T. Liu, C. Yang, Q. Wang, and D. Li. Interface and performance of 3D printed continuous carbon fiber reinforced PLA composites. *Composites Part A: Applied Science and Manufacturing*, 88:198–205, 2016. ISSN 1359835X. doi: 10.1016/j.compositesa.2016.05.032. URL http://dx.doi.org/10.1016/j.compositesa.2016.05.032http://dx.doi.org/10.1016/j.jclepro.2016.11.139.

A. Tomal, T. Saleh, and M. Khan. Combination of fused deposition modelling with abrasive milling for attaining higher dimensional accuracy and better surface finish. *IIUM Engineering Journal*, 19(2):221–231, 2018. doi: 10.31436/iiumej.v19.i2.960. URL https://www.scopus.com/inward/record.uri?eid=2-s2.0-85057986620&doi=10.31436%2fiiumej.v19.i2.960&partnerID=40&md5=733cb764d959c7f470258db285471767. cited By 0.

B. M. Tymrak, M. Kreiger, and J. M. Pearce. Mechanical properties of components fabricated with open-source 3-D printers under realistic environmental conditions. *Materials and Design*, 58:242–246, 2014. ISSN 18734197. doi: 10.1016/j.matdes.2014.02.038. URL http://dx.doi.org/10.1016/j.matdes.2014.02.038.

H. Ullah, A. R. Harland, and V. V. Silberschmidt. Dynamic bending behaviour of woven composites for sports products: Experiments and damage analysis. *Materials and Design*, 88:149–156, 2015. ISSN 18734197. doi: 10.1016/j.matdes.2015.08.147. URL http://dx.doi.org/10.1016/j.matdes.2015.08.147.

C. J. S. V. and S. V. Canevarolo. *Ciência dos polímeros: um texto básico para tecnólogos e engenheiros*. Artliber, 2ª edição edition, 2002. ISBN 9788588098107. URL https://books.google.pt/books?id=Vm0OAQAACAAJ.

A. Valerievich, M. Valerievich, F. Konstantinovich, and K. A. RAVKATOVICH. WO2018190750 (A1) - Print head for additive manufacturing of articles, 2018. URL https://patentimages.storage.googleapis.com/86/48/0b/c6de19f0b021b5/WO2018190750A1.pdf.

A. A. VALERIEVICH, V. V. VITALIEVICH, R. A. FEDOROVICH, and S. V. ALEKSEEVICH. WO2017188861 (A1) - Composite reinforcing thread, prepreg, tape for 3d printing and installation for preparing same, 2017. URL https://patentimages.storage.googleapis.com/e9/38/fe/42ae766d276a9c/WO2017188861A1.pdf.

T. H. Vaneker. Material Extrusion of Continuous Fiber Reinforced Plastics Using Commingled Yarn. *Procedia CIRP*, 66:317–322, 2017. ISSN 22128271. doi: 10.1016/j.procir.2017.03.367. URL http://dx.doi.org/10.1016/j.procir.2017.03.367.

A. B. Varotsis. 3D Printing vs. CNC machining. *3D Hubs*, 2018.

G. Vasile, C. Fetecau, and A. Serban. Experimental Research on the Roughness of Surfaces Processed Through Milling Polyamide Composites. *MATERIALE PLASTICE*, 1(2):205–212, 2014.

K. Volokh. *Anisotropic Elasticity*, pages 77–90. Springer Singapore, Singapore, 2016. ISBN 978-981-10-1599-1. doi: 10.1007/978-981-10-1599-1_5. URL https://doi.org/10.1007/978-981-10-1599-1_5.

A. Voloshin and M. Arcan. Failure of unidirectional fiber-reinforced materials - new methodology and results. *Experimental Mechanics*, 20(8):280–284, 1980. ISSN 0014-4851. doi: 10.1007/BF02328412.

R. Voss, T. D. If, L. Seeholzer, F. Kuster, and K. Wegener. CIRP Journal of Manufacturing Science and Technology Influence of fibre orientation , tool geometry and process parameters on surface quality in milling of CFRP. *CIRP Journal of Manufacturing Science and Technology*, 18:75–91,

2017. ISSN 1755-5817. doi: 10.1016/j.cirpj.2016.10.002. URL http://dx.doi.org/10.1016/j.cirpj.2016.10.002.

R. M. Wang, S. R. Zheng, and Y. P. Zheng. *Polymer matrix composites and technology*. Woodhead Publishing, 2011. ISBN 9780857092212. doi: 10.1533/9780857092229.

T. M. Wang, J. T. Xi, and Y. Jin. A model research for prototype warp deformation in the FDM process. *International Journal of Advanced Manufacturing Technology*, 33(11-12):1087–1096, 2007. ISSN 02683768. doi: 10.1007/s00170-006-0556-9.

Z. Weng, Y. Zhou, W. Lin, T. Senthil, and L. Wu. Structure-property relationship of nano enhanced stereolithography resin for desktop SLA 3D printer. *Composites Part A: Applied Science and Manufacturing*, 88:234–242, 2016. ISSN 1359835X. doi: 10.1016/j.compositesa.2016.05.035. URL http://dx.doi.org/10.1016/j.compositesa.2016.05.035.

C. Wilkening and A. Lohner. APPARATUS FOR PRODUCING ATHREE DIMENSIONAL OBJECT, 1998.

J. William D. Callister. *Fundamentals of Materiales Science and Engineering*. John Wiley & Sons, Inc, 2001. ISBN 978-1-118-06160-2. doi: 10.1007/978-981-10-2529-7_2. URL https://linkinghub.elsevier.com/retrieve/pii/B9780444828774500196.

G. Williams, R. Trask, and I. Bond. A self-healing carbon fibre reinforced polymer for aerospace applications. *Composites Part A: Applied Science and Manufacturing*, 38(6):1525–1532, 2007. ISSN 1359835X. doi: 10.1016/j.compositesa.2007.01.013.

W. W. Wits, J. R. R. García, and J. M. Becker. How Additive Manufacturing Enables more Sustainable End-user Maintenance, Repair and Overhaul (MRO) Strategies. *Procedia CIRP*, 40:694–699, 2016. ISSN 22128271. doi: 10.1016/j.procir.2016.01.156. URL http://dx.doi.org/10.1016/j.procir.2016.01.156.

W.J. Sichina. Characterization of Polymers Using TGA. Technical report, University of Washington, 2011. URL http://depts.washington.edu/mseuser/Equipment/RefNotes/TGA{_}Notes.pdf.

T. Wohlers. Wohlers Report 2018: Additive Manufacturing and 3D printing State of the Industry Annual Worldwide Progress Report. *Wohlers Associates*, 2018.

T. T. Wohlers, W. Associates, R. I. Campbell, and T. Caffrey. *Wohlers Report 2016: 3D Printing and Additive Manufacturing State of the Industry : Annual Worldwide Progress Report*. Wohlers Associates, 2016. ISBN 9780991333226. URL https://books.google.pt/books?id=YHUJkAEACAAJ.

T. T. Wohlers, W. Associates, R. I. Campbell, and T. Caffrey. *Wohlers Report 2017: 3D Printing and Additive Manufacturing State of the Industry : Annual Worldwide Progress Report*. Wohlers

Associates, 2017. ISBN 9780991333226. URL https://books.google.pt/books?id=YHUJkAEACAAJ.

G. Wypych. Handbook of Polymers. In G. Wypych, editor, *Handbook of Polymers*. Elsevier, Oxford, 2012. ISBN 978-1-895198-47-8. doi: https://doi.org/10.1016/B978-1-895198-47-8.50001-1. URL https://www.sciencedirect.com/science/article/pii/B9781895198478500011.

J. Xavier, J. Morais, and F. Pereira. Non-linear shear behaviour of bovine cortical bone by coupling the Arcan test with digital image correlation. *Optics and Lasers in Engineering*, 110(February): 462–470, 2018. ISSN 01438166. doi: 10.1016/j.optlaseng.2018.07.004. URL https://doi.org/10.1016/j.optlaseng.2018.07.004.

K. Q. Xiao and L. C. Zhang. The role of viscous deformation in the machining of polymers. *International Journal of Mechanical Sciences*, 44(11):2317–2336, 2002. ISSN 00207403. doi: 10.1016/S0020-7403(02)00178-9.

X. Yao, C. Luan, D. Zhang, L. Lan, and J. Fu. Evaluation of carbon fiber-embedded 3D printed structures for strengthening and structural-health monitoring. *Materials & Design*, 114:424–432, 2016. ISSN 02641275. doi: 10.1016/j.matdes.2016.10.078. URL http://dx.doi.org/10.1016/j.matdes.2016.10.078.

D. Young, N. Wetmore, and M. Czabaj. Interlayer fracture toughness of additively manufactured unreinforced and carbon-fiber-reinforced acrylonitrile butadiene styrene. *Additive Manufacturing*, 22(November 2017):883–890, 2018. ISSN 22148604. doi: 10.1016/j.addma.2018.02.010. URL https://doi.org/10.1016/j.addma.2018.02.023.

Y. Zhai, D. A. Lados, and J. L. LaGoy. Additive manufacturing: Making imagination the major limitation. *JOM*, 66(5):808–816, mar 2014. doi: 10.1007/s11837-014-0886-2. URL https://doi.org/10.1007%2Fs11837-014-0886-2.

W. Zhang, C. Cotton, J. Sun, D. Heider, B. Gu, B. Sun, and T. W. Chou. Interfacial bonding strength of short carbon fiber/acrylonitrile-butadiene-styrene composites fabricated by fused deposition modeling. *Composites Part B: Engineering*, 137(August 2017):51–59, 2018. ISSN 13598368. doi: 10.1016/j.compositesb.2017.11.018. URL https://doi.org/10.1016/j.compositesb.2017.11.018.

Y. Zhang and K. Chou. A parametric study of part distortions in fused deposition modelling using three-dimensional finite element analysis. *Proceedings of the Institution of Mechanical Engineers, Part B: Journal of Engineering Manufacture*, 222(8):959–967, 2008. ISSN 09544054. doi: 10.1243/09544054JEM990.

W. Zhong, F. Li, Z. Zhang, L. Song, and Z. Li. Short fiber reinforced composites for fused deposition modeling. *Materials Science and Engineering A301*, 301:125–130, 2001. ISSN 09215093. doi: 10.1016/S0921-5093(00)01810-4. URL www.elsevier.com/locate/msea.

C. Ziemian, M. Sharma, and S. Ziemi. Anisotropic Mechanical Properties of ABS Parts Fabricated by Fused Deposition Modelling. *Mechanical Engineering*, 2012. ISSN 9789533070865. doi: 10.5772/34233.

S. Ziemian, M. Okwara, and C. W. Ziemian. Tensile and fatigue behavior of layered acrylonitrile butadiene styrene. *Rapid Prototyping Journal*, 21(3):270–278, 2015. ISSN 1355-2546. doi: 10.1108/RPJ-09-2013-0086. URL http://www.emeraldinsight.com/doi/abs/10.1108/RPJ-09-2013-0086.

R. Zou, Y. Xia, S. Liu, P. Hu, W. Hou, Q. Hu, and C. Shan. Isotropic and anisotropic elasticity and yielding of 3D printed material. *Composites Part B: Engineering*, 99:506–513, 2016. ISSN 13598368. doi: 10.1016/j.compositesb.2016.06.009. URL http://dx.doi.org/10.1016/j.compositesb.2016.06.009.